



**University
of Brighton**

**Experimental analysis of two-phase flows
in the context of Pulsating Heat Pipes for
space applications**

Luca Pietrasanta

Thesis submitted in partial fulfilment of the
requirements of the University of Brighton
for the degree of Doctor of Philosophy

September 2018

Supervisors:

Prof. Marco Marengo

Dr. Nicolas Miche'

Abstract

The constant demand for innovation in heat transfer solutions for compact and more powerful electronics is driving the research towards new technologies able to dissipate more power in reduced dimensions. In the field of thermal management in space, a new generation of two-phase passive devices able to fulfil severe requirements of compactness, performance and reliability is emerging. Vapor–liquid two-phase flows are commonly found in many applications such as chemical engineering processes, nuclear reactors, and heat exchangers. For this reason, they have been investigated for decades. However, due to the complexity of the physical phenomena involved, predictions are largely in terms of empirical or semi-empirical correlations, based on specific test conditions (e.g. controlled unidirectional mass flow rate). The extrapolation of these correlations to other operating conditions may not be valid, particularly when the mass flow rate is unknown because it is either the result of thermal induced phenomena or it is operated for instance in hyper and micro-gravity environments. In the field of two-phase passive wickless heat transfer devices such as Pulsating Heat Pipes, flow pattern transitions from slug-plug to semi-annular induce a significant variation of the highly-coupled thermo-hydrodynamic behaviour of the device, thus affecting the overall thermal performance.

In the present work, a Pulsating Heat Pipe in its simplest configuration of a Single Loop, has been tested under the varying gravity levels available on a parabolic flight (normal gravity, hyper gravity and micro gravity). After the design and realisation of

an aerospace-standard compliant test rig, the fluid flow high-speed imaging obtained has been processed. Using the frames acquired, a software tool has been developed and validated to estimate vapor bubbles velocity, length and void fraction in the channel portion observed (adiabatic section). The aim is to investigate the flow pattern transition and bubble break-up limits. Modified versions of the well-known Froude, Weber and Bond number have been introduced, considering the actual acceleration of the fluid rather than a constant value of g (gravitational acceleration) and the length of the bubble as characteristic length. Finally, based on the above non-dimensional analysis, a novel flow pattern map, valid for an accelerated Taylor flow and obtained under the three different gravity levels available on a parabolic flight, has been proposed.

This new map can be useful to the development of comprehensive designing tools for passive two-phase device for both ground and space applications, via the selection of the proper manufacturing parameters and fluid properties that guarantee the desired flow pattern and to identify operational limits of Pulsating Heat Pipe.

Additional activities related to novel investigations of flow pattern and heat transfer in Pulsating Heat Pipes carried out *a latere* are also presented. Medium Wave Infra-Red imaging of the working fluid through a sapphire tube of a functioning Pulsating Heat Pipe and the attempt to solve the Inverse Heat Conduction Problem to obtain the fluid-side heat transfer coefficient are presented in Appendix.

Acknowledgments

I would like to express my gratitude to the many people involved, at different levels, in this scientific and personal journey that is a PhD. In particular, I owe my gratitude to Prof. Marengo for all the opportunities and incredible experiences I had the chance to make in the past three years under his supervision, for his invaluable scientific support and for his way of letting things always appear “easy”; to Dr. Mauro Mameli, that I am proud to call a friend, and from which I have learned not just a big share of my technical knowledge but also how to survive a PhD and the passion and dedication for the scientific research: you have been of great inspiration to me.

I would also like to thank all the remarkable researchers and scientists I met along my journey and with whom I shared conferences, thoughts, parabolic flights or paper preparation with: Prof. Sauro Filippeschi, Prof. Paolo Di Marco, Dr. Anastasios Georgoulas, Dr. Vincent Aysel, Dr. Nicolas Miche’, Dr. Lucio Araneo, Dr. Wassilis Tzevelecos and Dr. Manolia Andredaki: thanks for every moment you have dedicated to me, for your help and your precious example. Hope to keep on having the pleasure to work with you. I cannot forget who shared the PhD life with me: Cristina Boscariol, Luke Poulton, Paul McGinn, Filippo Gerbino and Dan Sykes, whom I also want to acknowledge for his help in “putting into code” some ideas that have become part of this research work.

I cannot forget whom I owe the greatest gratitude to, and probably will not understand a single line of this work: Laura, Mamma, Beppe, Babbo, Piera, Marcello, Rachele and Arianna. You have shaped me over the years, you have always supported me, and you always will: you are the energy of my life.

Thanks to all my “Brightonians” friends, you never made me feel far from home.

And to myself: *spiral out, keep going!*

Contents

Abstract	I
Acknowledgments	III
List of figures	VIII
List of tables	XIV
List of acronyms	XVI
Nomenclature	XVIII
Declaration	XX
1 Introduction.....	1
1.1 Motivations	1
1.2 Objectives	3
1.3 Impact of the Research.....	3
2 Passive Two-Phase Heat Transfer Devices	6
2.1 Introduction.....	6
2.2 The Thermosyphon (TS) and the Closed Loop Two-Phase Thermosyphon (CLTPT)	11
2.2.1 The Thermosyphon	11
2.2.1.1 Transport limitations.....	14
2.2.2 The Closed Loop Thermosyphon.....	15
2.3 The Heat Pipe (HP)	16

2.3.1	Transport limitations	18
2.3.2	Performance and operating conditions	20
2.4	The Loop Heat Pipe (LHP) and Capillary Pumped Loops (CPL)	23
2.5	The Pulsating Heat Pipe (PHP).....	26
2.5.1	Operating mechanism.....	27
2.6	PHP Technologies applications	28
2.7	Classification based on TRL for space applications	29
3	The Pulsating Heat Pipe for heat transfer on Earth and in space.....	34
3.1	Introduction.....	34
3.2	Micro-scale two-phase flows	35
3.3	Investigating a two-phase flow in capillary devices	37
3.3.1	The Critical Heat Flux (CHF).....	38
3.3.2	Two phase flow instabilities	39
3.3.3	Useful Non-dimensional Numbers.....	40
3.4	PHP working principles.....	42
3.4.1	The start-up.....	46
3.4.2	Thermal performance	48
3.5	Parameters affecting the functioning of a PHP.....	49
3.5.1	Performance of a tilted PHP	53
3.6	Role of the liquid film	54
3.6.1	Dynamics of menisci.....	55
3.6.2	Observing oscillatory component	56
3.6.3	Evaporation and condensation associated with a self-sustained thermally driven oscillation.....	59
3.7	PHP research for Space applications.....	63
4	Experimental set-up and Methods.....	67
4.1	Introduction.....	67

4.2	Local scale investigation and single loops	68
4.3	The Single Loop Pulsating Heat Pipe (SLPHP) test rig.....	69
4.4	Liquid bulk velocity estimation method.....	71
4.5	Void fraction and bubble length estimation method.....	75
4.6	Parabolic flight investigation.....	78
4.6.1	Platform for Parabolic Flights investigation.....	80
4.6.1.1	Liquid Cooling System (LCS).....	85
4.6.1.2	Visualization (High speed visible spectrum camera)	88
4.6.1.3	Visualization (infrared).....	89
4.6.1.4	Results of the rack design and construction.....	90
5	1-g, Micro-g and Hyper-g tests.....	91
5.1	Introduction.....	91
5.2	SLPHP: On ground characterisation	92
5.2.1	SLPHP start-up with different fluids.....	95
5.3	SLPHP: μ -g and Hyper-g characterisation.....	98
5.3.1	Experimental procedure	98
5.3.2	Temperature, pressure and visual data	99
5.3.3	Start-up in micro-gravity	107
5.3.4	Void fraction evolution in the SLPHP	109
6	Developing flow pattern maps of an accelerated two-phase flow	111
6.1	Flow pattern in two-phase flows.....	111
6.1.1	Two-phase flow pattern maps.....	113
6.2	Flow pattern transition in the context of Pulsating Heat Pipe	117
6.2.1	Critical velocity theory verification - Inertial effects on the flow pattern transitions	121
6.2.2	Role of velocity, acceleration and bubble length in flow pattern transitions and bubble break up.....	127
6.2.3	The proposed flow pattern map	131

7	Conclusions and future developments.....	140
7.1	Conclusions.....	140
7.2	Future developments	141
7.2.1	Liquid direct temperature measurement via MWIR imaging.....	142
7.2.2	Inverse heat conduction problem in the context of Pulsating Heat Pipes 144	
	Bibliography.....	146
	List of publications	156
	Appendix A: Infrared analysis in the context of PHP	158
	Appendix B: The Inverse Heat Conduction Problem (IHCP).....	162
	B.1 Formulation of the problem.....	163
	Appendix C: Code for the estimation of Void Fraction and bubble length.....	165

List of figures

Figure 1 Analysis of typical electrical energy consumption in data centre [2].....	5
Figure 2 Order of magnitude of heat transfer coefficient achievable with different cooling technologies	7
Figure 3 Comparison of various heat transfer technologies [3]	8
Figure 4 General functioning schematic of two-phase capillary driven heat transfer device	9
Figure 5 The air preheater for baking ovens proposed by Gay and based on finned, partially filled thermosyphons [4]	12
Figure 6 Gravity assisted wickless two-phase closed thermosyphon [5].....	12
Figure 7 Schematic of a CLTPT for components cooling [9].....	16
Figure 8 Heat Pipe and its main regions [4].....	16
Figure 9 Radii of curvature of the liquid-vapour interface in evaporator and condenser [10].....	17
Figure 10 Fluid pressure along the structure of a HP	18
Figure 11 Performance map of HP with limits [4]	19
Figure 12 Selection of wick structures [4]	20
Figure 13 Temperature drops and equivalent thermal resistance of a HP [10].....	21
Figure 14 Loop Heat Pipe and Capillary Pumped Loop in their schematic view [11]	23
Figure 15 General scheme of a LHP [12]	24
Figure 16 Detail of a typical LHP evaporator [4].....	24
Figure 17 Operating cycle of a LHP [12].....	25

Figure 18 Schematic of a conventional Closed Loop Pulsating Heat Pipe [14]	27
Figure 19 Heat and mass processes involved in a Taylor flow, dominant flow pattern in the PHP [16]	28
Figure 20 Defence Program Satellite (DPS) sensor detail.....	33
Figure 21 Example of Heart Pipe radiator panel. Please refer to [19] for an exhaustive description of the sub-systems.....	33
Figure 22 Mechanisms believed responsible of initiating CHF in flow boiling, with local increasing (CHF+) and decreasing (CHF-) of the critical heat flux [36]	39
Figure 23 Three configurations of PHP. From left to right: Open Loop, Closed Loop, Closed Loop with check valves	43
Figure 24 Evolution from oscillating to circulating motion with increasing of power input [42].....	44
Figure 25 Evaporator temperature during a typical transient behaviour due to a step change in the heat input [43]	45
Figure 26 Thermodynamic of a PHP on a Pressure-Enthalpy diagram[42].....	46
Figure 27 Example of start-up for different fluids [44]	47
Figure 28 Effect of inclination angle from Vertical (90°) to horizontal (0°) for a 1.1mm PHP filled with FC-72 (50% FR) [48].....	53
Figure 29: a) Capillary resistance due to dynamic contact angle; b) Influence of several plugs in a tube on resistance to movement [69]	56
Figure 30: Experimental set-up for investigation of capillary pressure difference effects on oscillations [72]	58
Figure 31: a) Schematic of the experimental set-up for self-sustained thermally driven oscillating flow in a “unit-cell”; b) Unit-cell details and relevant parameters [74] ...	60
Figure 32: Variation of vapour mass during one cycle of induced oscillation, separating the four different contributions, and position of the interface in the channel [74].....	61
Figure 33: a) Schematic of one cycle of the meniscus motion b) Time evolution of the meniscus position related to the pressure field [74].	62
Figure 34 Wickless heat pipe working principles variation increasing the internal diameter and decreasing the gravity level.....	64
Figure 35 Single Loop Pulsating Heat Pipe (SLPHP) with position and numbering of thermocouples and pressure transducers.....	70
Figure 36 Velocity nodes grid overlapped on a frame and position of the radial averaging sections.....	72

Figure 37 Error between the imposed velocity (V^*) and the velocity estimated by the filtered PIV method (V_{PIV})	74
Figure 38 Prediction of fluid velocity variation with the heating power input, for different liquid quality (x_0) and ratio of evaporative heat to the total heat (β) from the analytical model presented in [90].....	74
Figure 39 Binarization process of the original frame and successive estimation of a bubble volume as sum of infinitesimal disks	77
Figure 40 Weightlessness platforms available and their principal characteristics [98]	79
Figure 41 Parabolic flight manoeuvre description [98], [99].....	80
Figure 42 Logic of the Experimental Rack	80
Figure 43 Rendering of the primary structure	81
Figure 44 General layout of connections as per PFC67 th	83
Figure 45 Rack modules description. All sub-systems included in the rack, as per 67 th ESA PFC, with a weight breakdown as required by Novespace.....	84
Figure 46 Description of the Liquid Cooling System.....	85
Figure 47: Description of the TECS assembly.....	86
Figure 48: LCS assembly and double containment	86
Figure 49: Position of the cooling stage assembly in the rack.....	86
Figure 50 High-speed visible spectrum Ximea XIQ camera	89
Figure 51: ESA MWIR Camera specifics	89
Figure 52 The University of Brighton parabolic flight rack in its final configuration	90
Figure 53 Relevant thermophysical properties of the selected working fluids in a temperature range of interest. a) Surface tension b) Liquid density, c) Latent heat of vaporisation, d) Dynamic viscosity	92
Figure 54 Comparison of critical diameter according to Bond criterion for ethanol and FC-72 varying the temperature in a relevant range for the tested device.	93
Figure 55 Global thermohydraulic behaviour of the system varying power distribution, working fluid and inclination angle of the SLPHP: no symbol = not tested; - = no fluid motion in the transparent tube; S = start-up or shut down (unstable); O = oscillating (stable); C= circulating (stable); D = dry-out risk.	94

Figure 56 Start-up characteristics of the SLPHP with a) FC-72 and b) Ethanol. From top to bottom of each figure: Power input, Pressure signals, Evaporator temperatures. Activation delay reported. c) Position of the thermocouples in the evaporator zone.	97
Figure 57 Complete tack of temperature, pressure and z-axis acceleration for ethanol during the 66th ESA PFC. In the temperature plot, Yellow\red colour shade = Evaporator temperatures; Blue colour shade = Condenser temperatures	99
Figure 58 Ethanol, detail of parabolae 0 to 6, low heating power. From top to bottom: z-axis acceleration, heating power, pressure signals, temperature signals.	100
Figure 59 Ethanol, detail of parabolae 26 to 30, low heating power. From top to bottom: z-axis acceleration, heating power, pressure signals, temperature signals..	100
Figure 60 Typical flow pattern obtained with ethanol for low power input (9W). Evaporator side in red, condenser side in blue	101
Figure 61 Typical flow pattern obtained with ethanol for medium power input (18W). Evaporator side in red, condenser side in blue	101
Figure 62 Typical flow pattern obtained with ethanol for high power input (24W). Evaporator side in red, condenser side in blue	102
Figure 63 Complete tack of temperature, pressure and z-axis acceleration for FC-72 during the 66th ESA PFC. In the temperature plot, Yellow\red colour shade = Evaporator temperatures; Blue colour shade = Condenser temperatures	103
Figure 64 FC-72, detail of parabolae 0 to 6, low heating power. From top to bottom: z-axis acceleration, heating power, pressure signals, temperature signals.	104
Figure 65 FC-72, detail of parabolae 26 to 30, high heating power. From top to bottom: z-axis acceleration, heating power, pressure signals, temperature signals.	104
Figure 66 Typical flow pattern obtained with FC-72 for low power input (9W). Evaporator side in red, condenser side in blue	105
Figure 67 Typical flow pattern obtained with FC-72 for medium power input (18W). Evaporator side in red, condenser side in blue	105
Figure 68 Typical flow pattern obtained with FC-72 for high power input (24W). Evaporator side in red, condenser side in blue	106
Figure 69 Position of evaporator thermocouples and colours adopted in Table 25 .	108
Figure 70 Comparison of evolution of average void fraction with standard deviation during parabolic flight for two working fluids.	109
Figure 71 Basic flow pattern in vertical tubes [105]	112

Figure 72 Schematic of flow patterns and the corresponding heat transfer mechanisms and qualitative variation of the heat transfer coefficients for flow boiling in a horizontal tube [106]	113
Figure 73 Flow pattern map in 1-g vertical upward air–water flow in 25mm i.d. tube [105].....	114
Figure 74 Experimental flow pattern map with transition curves for R236fa, D = 1.03mm channel at $T_{sat}=31$ C, $T_{in}=27$ C and $Co = 0.83$ [108].....	115
Figure 75 Experimental flow pattern map with transition curves for R134a, D = 3.04mmchannel at $T_{sat}=31$ C, $T_{in}=27$ C and $Co = 0.27$ [108].....	115
Figure 76 The quantitative transition criterion for physical confinement in flow boiling in relation to Bo and Re number proposed by Harirchian and Garimella [109]	116
Figure 77 Critical diameter curve for common working fluids in static conditions and in a 230 K to 350 K temperature application range	118
Figure 78 a) Map of critical diameter according to Weber number criterion and b) Garimella number criterion for Ethanol at Earth gravity level.....	119
Figure 79 Critical velocity according to Garimella criterion for a 2 mm I.D. tube filled with Ethanol at varying gravity level and over a 140K temperature range	120
Figure 80 Critical velocity according to Garimella criterion for a 2 mm I.D. tube filled with FC-72 at varying gravity level and over a 140K temperature range.....	120
Figure 81 Velocity signal obtained for FC-72 at 9W and 15W under varying gravity levels and critical velocity thresholds (in red).....	123
Figure 82 Velocity signal obtained for FC-72 at 18W and 24W under varying gravity levels and critical velocity thresholds (in red).....	124
Figure 83 Velocity signal obtained for Ethanol at 9W and 15W under varying gravity level and critical velocity thresholds (in red).....	125
Figure 84 Velocity signal obtained for Ethanol at 18W and 24W under varying gravity levels and critical velocity thresholds (in red).....	126
Figure 85 Ratio between estimated velocity and critical velocity for 2mm sapphire tube filled with FC72, during 1g period; all properties evaluated at 23°C. Frames a) and d) shown non-accurate prediction while frames b) and c) truly describe the flow pattern. Acquisition frequency: 100fps.	127
Figure 86 Effect of initial bubble length on the liquid dynamics, responsible for break-up phenomena [111]	128
Figure 87 Break up event during a reverse flow. Ethanol, 1g, 18W power input....	130

Figure 88 Ethanol flow pattern map in terms of dynamic non-dimensional groups with bubble length as characteristic; adiabatic section of a single loop PHP.....	133
Figure 89 Statistic of the bubble length to diameter ratio for ethanol in 1g at four power level. Sampling period 5 s at 100 fps, HFOV = 50mm.....	133
Figure 90 Statistic of the bubble length to diameter ratio for ethanol in Hy-g at four power level. Sampling period 10 s at 100 fps, HFOV = 50mm.....	134
Figure 91 Statistic of the bubble length to diameter ratio for ethanol in μ -g at four power level. Sampling period 10 s at 100 fps, HFOV = 50mm.....	134
Figure 92 FC-72 flow pattern map in terms of dynamic non-dimensional groups with bubble length as characteristic length; adiabatic section of a single loop PHP	135
Figure 93 Statistic of the bubble length to diameter ratio foe FC-72 in 1g at four power level. Sampling period 5 s at 100 fps, HFOV = 50mm.....	136
Figure 94 Statistic of the bubble length to diameter ratio foe FC-72 in Hy-g at four power level. Sampling period 10 s at 100 fps, HFOV = 50mm.....	136
Figure 95 Statistic of the bubble length to diameter ratio foe FC-72 in μ -g at four power level. Sampling period 10 s at 100 fps, HFOV = 50mm.....	137
Figure 96 Flow pattern map for Ethanol and FC-72 in terms of dynamic non-dimensional groups with bubble length as characteristic length; adiabatic section of a single loop PHP	137
Figure 97 Flow Pattern map of an accelerated slug-plug flow independent from the fluid and the diameter of the tube obtained under three different gravity level.....	138
Figure 98 MWIR visualization of a FC-72 slug-plug flow through a sapphire insert during the 68 th ESA parabolic flight campaign.....	143
Figure 99 a) Gravity level, b) External tube temperatures at the edges of the sapphire, c) Pressure difference, d) Liquid velocity and void fraction and e) time-space temperature map of the fluid synchronized during microgravity oscillations.....	144
Figure 100 Global emissivity of FC-72, methanol and ethanol as a function of the optical thickness of the fluid in a wavelength of 3–5 μ m [124].....	160
Figure 101 Schematisation of the problem and equivalent electric scheme for the lumped parameter model resolution	161
Figure 102 Schematisation and formulation of the IHCP.....	163
Figure 103 Schematisation of the resolution procedure	164

List of tables

Table 1 Classification of passive two-phase devices on the method of condensate return.....	10
Table 2 Maximum thermosyphon merit number for common fluids [4].....	13
Table 3 Typical operating characteristics of HP working fluid pairing with shell/wick material.....	22
Table 4 Classification of LHP [12].....	26
Table 5 Comparison between main technologies available	29
Table 6 Technology Readiness Level summary and milestones [17]	30
Table 7 EADS ASTRIUM Heat Pipe qualification and Space application history [18]	32
Table 8 Equivalent thermal resistance for different geometries, reprinted from [43]	48
Table 9 Effect of dimensions, working fluid and filling ratio on operating limit	52
Table 10 Effect of orientation on PHP performances.....	54
Table 11 Relevant works done on PHP in Micro-g and Hyper-g.....	65
Table 12 Simplified geometry approach in Pulsating Heat Pipe research. Geometry: Single Loop (SL), Single Channel (SC). Flow type: Pulsating (P), Mechanically induced oscillation (MIO). Area of study: Entire Loop (EL), Evaporator (EVA), Condenser (COND), Adiabatic section (ADB).....	69
Table 13 Samples of the main flow patterns identified during the experimental campaigns.....	72
Table 14 Void fraction estimation and measure techniques selection.....	76
Table 15 Parabolic flight rack sub-system description in its final configuration as per PFC67 th and PFC68 th	82
Table 16: Description of the Liquid Cooling System main components.....	87

Table 17: LCS hydraulic pressure components list.	88
Table 18: Fast speed visualization system elements.....	88
Table 19 Cases tested during ground test characterization [88].....	94
Table 20 Start-up performance comparison between working fluids.....	96
Table 21 Uncertainty calculated on different heat input steps.....	96
Table 22 Fluids properties at the start of the heating period.....	97
Table 23 PFC 66 th experimental matrix	99
Table 24 Activation energy detail in micro-gravity conditions for ethanol and FC-72	107
Table 25 Start-up behaviour during a micro-gravity period for ethanol and FC-72	108
Table 26 Statistic of prediction accuracy of semi-annular flow pattern and slug-plug flow pattern with the presented velocity code (considering a 10% error on the velocity estimation) and according to the critical velocity criterion. ‘N\A’= Flow pattern not present;’-‘=Data not available.	122
Table 27 Innovative techniques of temperature measurement applicable in local scale, milli/micro-channels	159
Table 28 Medium Wave Infra-Red camera specifics	161

List of acronyms

CFD	Computational Fluid Dynamic
CHF	Critical Heat Flux
CPL	Capillary Pumped Loop
ESA	European Space Agency
FDM	Finite Difference Method
FEM	Finite Element Method
FPPHP	Capillary Closed Loop Flat Pulsating Heat Pipe
FR	Filling Ratio
HFOV	Horizontal Field Of View
HP	Heat Pipe
HTC	Heat Transfer Coefficient
IHCP	Inverse Heat Conduction Problem
ISS	International Space Station
LHP	Loop Heat Pipe
OHP	Oscillating Heat Pipe
OLPHP	Open Loop Pulsating Heat Pipe

PF Parabolic Flight

PHP Pulsating Heat Pipe

Space PHP: A PHP with a hydraulic internal diameter bigger than d_{crit} on ground

TC Thermocouple

THM Top Heating Mode

TPHP Capillary Closed Loop Tube Pulsating Heat Pipe

TS Thermosyphon

VOF Volume Of Fluid

WF Working Fluid

Nomenclature

Bo	Bond number [-]
Ca	Capillary number [-]
c_p	Specific heat capacity at constant pressure [J/kg K]
d	Diameter [m]
Fr	Froude number [-]
g	Gravity acceleration [m/s ²]
Ga	Garimella number [-]
h	Convective heat transfer coefficient [W/m ² K]
h_{lv}	Latent heat of vaporisation [J/kg]
k	Thermal conductivity [W/m K]
M	Merit figure
m	Mass [kg]
Nu	Nusselt number [-]
P	Pressure [Pa]
\dot{Q}	Heat power input [W]
R	Thermal resistance [K/W]

Re	Reynolds number [-]
T	Temperature
t	Time [s]
V	Volume [m ³]
u	Liquid phase velocity [m/s]
We	Weber number [-]

Greek symbols

α	Void fraction [-]
δ	Liquid film thickness [m]
ε	Error [%]
μ	Dynamic viscosity [Pa s]
ρ	Density [kg/m ³]
σ	Surface tension [N/m]
τ	Wall shear stress [Pa]
ϕ	Ratio between actual and critical velocity [-]

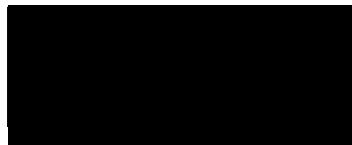
Subscript

c	Condenser
e	Evaporator
l	Liquid, Length of the bubble
v	Vapour

Declaration

I declare that the research contained in this thesis, unless otherwise formally indicated within the text, is the original work of the author. The thesis has not been previously submitted to this or any other university for a degree and does not incorporate any material already submitted for a degree.

Signed



Dated Brighton, 05/10/2018

Chapter 1

Introduction

1.1 Motivations

The constant demand for innovation in heat transfer solutions for compact and more powerful electronics is driving the research towards new technologies able to dissipate more power in less space and with high reliability standards. The research in the field of Thermal Management has been pushed towards the development of a new generation of techniques based on two-phase technologies to fulfil stringent requirements of compactness and high heat fluxes, to achieve an effective, reliable and cheap heat transfer in harsh conditions such as space. These advantages are realised by order of magnitude enhancement in heat transfer coefficient achieved with flow boiling and condensation compared to single phase systems.

In space applications, the main goal of thermal management is to maintain temperatures of a sensor, component, instrument, spacecraft, or space facilities within the required limits, regardless of the external environment or the thermal loads imposed from operations. Typical gravity levels for objects inside the Space Shuttle range from 10^{-2} to 10^{-5} g. For the International Space Station, the gravity level would range between 10^{-3} and 10^{-6} g. Effective heat removal from electronic chips is required for ensuring their reliability and preventing premature damage. Heat dissipation in very compact assemblies (like microelectronics), combined with high heat flux density

is difficult to achieve using conventional cooling methods. Considering the past years' trend, the complexity of the cooling system given by the improvement in electronics, is going to increase. In the field of space applications, with the increasing size of space platforms for future exploration missions, large amounts of heat need to be dissipated or transferred in gravity conditions very different from earth and with reduced or no maintenance allowed. A reduction of moving mechanical elements become crucial.

Two-phase passive device, like Heat Pipes (HP) or Thermosyphons (TS), exploit both sensible and latent heat to passively transfer heat from a heat source to a heat sink. They have been widely used for their proven capability to meet general requirements of high heat fluxes dissipation in many electronic-related applications with no external work needed and no moving parts required. Because of the physical phenomena involved, HPs and TSs have shown some limitations during the demanding conditions encountered in very small devices (i.e. new generations of Ultrabook, mobile phones) and in systems non-gravity assisted (i.e. satellites, spacecrafts). A new generation of devices, Pulsating Heat Pipes (PHPs) or Oscillating Heat Pipes (OHP) were proposed in the late '90s to extend the field of applicability of two-phase passive systems and keep pace with demands and requirements of Thermal Management. PHPs can be considered the last frontier of the two-phase passive heat transfer devices. Due to their construction simplicity, the ability to dissipate heat also in microgravity, and high heat transfer capability, PHPs could represent a new alternative cooling system in the near future, both for ground and space applications.

Despite the extensive data present in literature (pressure and temperature trends, flow visualisation) a shortage of useful correlations, mechanistic and computational models, is available in literature. PHP technology is still far from industrialisation due to complex phenomena involved. PHPs are mainly based on phase change phenomena and capillary forces; the fluid motion is inherently non-stationary and chaotic, thus difficult to understand and to model. The characteristic Taylor flow, also called slug/plug flow, is considered the basis of the proper functioning of the device, but it is still not clear which are the relevant parameters that mark the transition to a different flow pattern, reducing the overall circulation of fluid and hence the thermal performance and the range of applicability.

Two-phase passive heat transfer devices can be useful in various heat transfer problems, such as in laser diodes, photovoltaic cells, infrared detectors. In recent years, numerous works have been proposed but many fundamental questions still need to be

addressed in order to reach industrialization phase and a full space qualification. Among the main issues, the basic understanding of the effects of flow pattern transitions (under different boundary conditions and heat load) on the local heat transfer are worthy of further investigation. In addition, new investigation techniques need to be developed and tested, in order to answer specific questions that conventional methods have been unable to do.

1.2 Objectives

Considering the work on PHPs available in literature, a gap in the basic research emerged in the characterization of the conditions that guarantee a PHP to work under confined slug-plug flow. The main purpose of this study is then to characterize the fluid-dynamics of the oscillating /circulating flows in a wickless two-phase heat transfer device based on the working principles of the PHP. The conventional static confinement criteria will be discussed, and new dynamic criteria introduced and explored. A new approach to flow pattern map making, taking into account new parameters as the actual fluid acceleration and the length of the vapour bubbles, will be investigated.

This thesis also intends to determine the effect of varying gravity level on the resulting flow pattern and on the start-up phase of a PHP, being a potential candidate for thermal management in space applications. In order to test the device in a space relevant environment, reduced and increased gravity levels will be obtained through the microgravity platform known as Parabolic Flight. A suitable test rig will be design and realised to accommodate the experiments onboard of the platform.

1.3 Impact of the Research

Gas–liquid (or vapor–liquid) two-phase flows are commonly found in many industrial processes and engineering applications. Due to their important applications in chemical engineering processes, nuclear reactors, refrigeration systems, and heat exchangers, two-phase flows have been actively investigated for several decades. Valuable experimental data were collected on-ground for different flow orientations and flow passage geometries. Theories and correlations were developed to predict the engineering parameters of gas–liquid flows in conduits in terms of flow pattern

transitions, pressure drops, void fraction, heat-transfer rates, etc. However, due to the complexity of the flow, predictions were largely in terms of empirical or semi-empirical correlations, which were for the most part based on specific test conditions; e.g., conduit size and shape, adiabatic or boiling flows, method of heating or gas injection, etc. Extrapolation of these correlations to other conditions may not be valid, particularly when gravity is significantly reduced and in new categories of devices.

Space agencies worldwide are actively exploring the implementation of two-phase thermal management to support astronauts' life onboard future space vehicles and planetary bases. According to NASA Technology Roadmap on Thermal Management Systems [1], a Heat Transport System should: *“Allows safe, reliable, and reduced-mass transport loop designs for human missions. Allows more efficient and reliable systems that reduce power requirements and permits heat transport against a steeper thermal gradient, thus allowing spacecraft to operate in a wider range of environments. Provides more efficient heat switches and heat straps and insulations that provide more reliable and efficient passive thermal control of spacecraft.”*

Heat Pipe Capillary-Based Loops are included in the list of technology that are worthy of further investigation to enhance Crewed Planetary Exploration Missions.

Of high interest is also the development of PHPs for ground applications. For instance, the cooling of the battery packs of Hybrid or Full Electric vehicles, to cut any parasite energy consumption (i.e. working fluid pumping energy in conventional single-phase loops), would increase autonomy and avoid over dimensioning in the battery capacity.

Another field of interest for ground two-phase passive system is the cooling of datacentre where, as shown in Figure 1, the 38% of the electrical power is absorbed by the cooling of the units [2]. For both fields, On-ground and In-Space, a design tool is mandatory to guide engineers in the design of the proper thermal solution, pass through innovation in research techniques and reliable data collection to support the modelling phase. This will make it possible to increase the Technology Readiness Level (TRL), obtain the Space Qualification and start the industrialization process for a new generation of PHPs. The impact of the present work is then considered substantial.

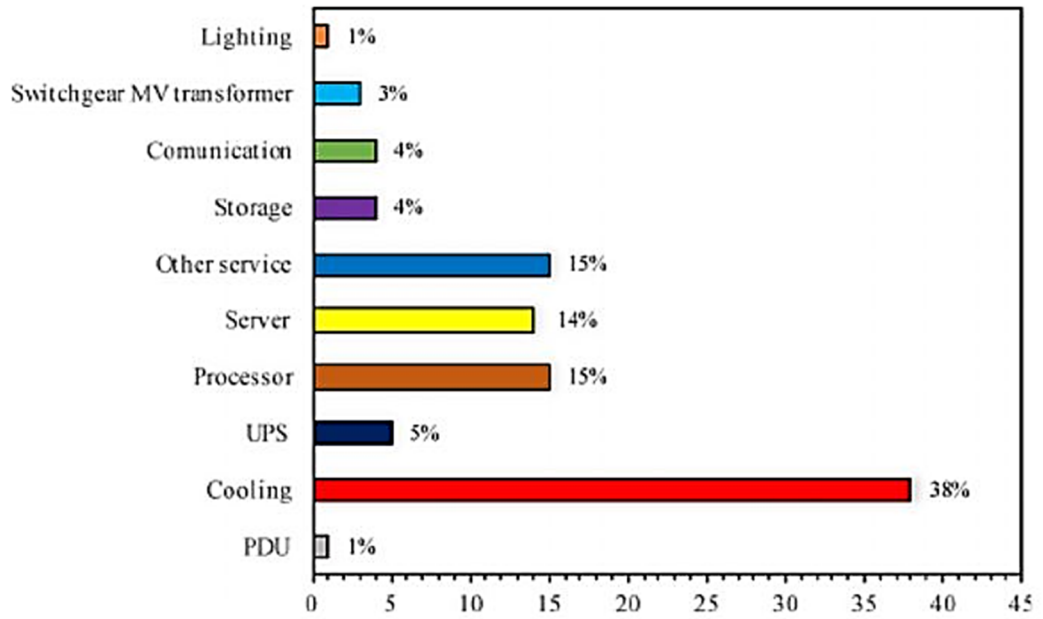


Figure 1 Analysis of typical electrical energy consumption in data centre [2]

Chapter 2

Passive Two-Phase Heat Transfer Devices

2.1 Introduction

The best way to introduce the concept of passive two-phase heat transfer devices and then Pulsating Heat Pipes as members of this family, is to provide an overall perspective on the principal ideas behind the various heat transfer technologies available. This will establish the position of PHP among several available thermal management solutions. If a heated object has to be cooled to prevent overheating and to be kept at a design value of temperature, various cooling methods can be adopted (Figure 4). A conventional general classification proposes six categories:

- Radiation
- Natural gas cooling
- Natural liquid cooling
- Forced gas cooling
- Forced liquid cooling
- Two-phase cooling

Assuming the external heat transfer coefficient is known and fixed (e.g. by convective air cooling), the easiest way to increase the effectiveness of the cooling

process is to extend the exchange surface via a series of solid fins. In this case the thermal conductivity of the material will define the limit in the heat transfer, together with the extension of the exchange surface. Another strategy to effectively cool the object, is to let a fluid circulate in a closed loop that connects the heat source (object) and a heat sink, exploiting the sensible heat transfer (single phase pumped loop) or allowing the fluid to vaporise in order to exploit both sensible and latent heat (two-phase pumped loop); increasing the Reynolds number forcing the circulation with a pump, the heat transfer will increase. Forced convection is not restricted by the orientation of the system but increases the system cost and decreases its reliability and compactness. If the solid conductive fins can be replaced with a passive two-phase device, like a thermosyphon, thermal conductivity can be greatly enhanced exploiting both conductive and latent heat transfer mechanism. Thermosyphon are gravity assisted devices and they will encounter issues related to the orientation of the device. A Heat Pipe can overcome this limitation using a porous media to guarantee the return of the condensate to the evaporator whatever the inclination, although with a reduction of the performance. Pulsating Heat Pipes can exploit both sensible and latent heat transfer, eliminating the pump and the wick to reduce the complexity and achieve thermal a thermal management almost independent from the orientation.

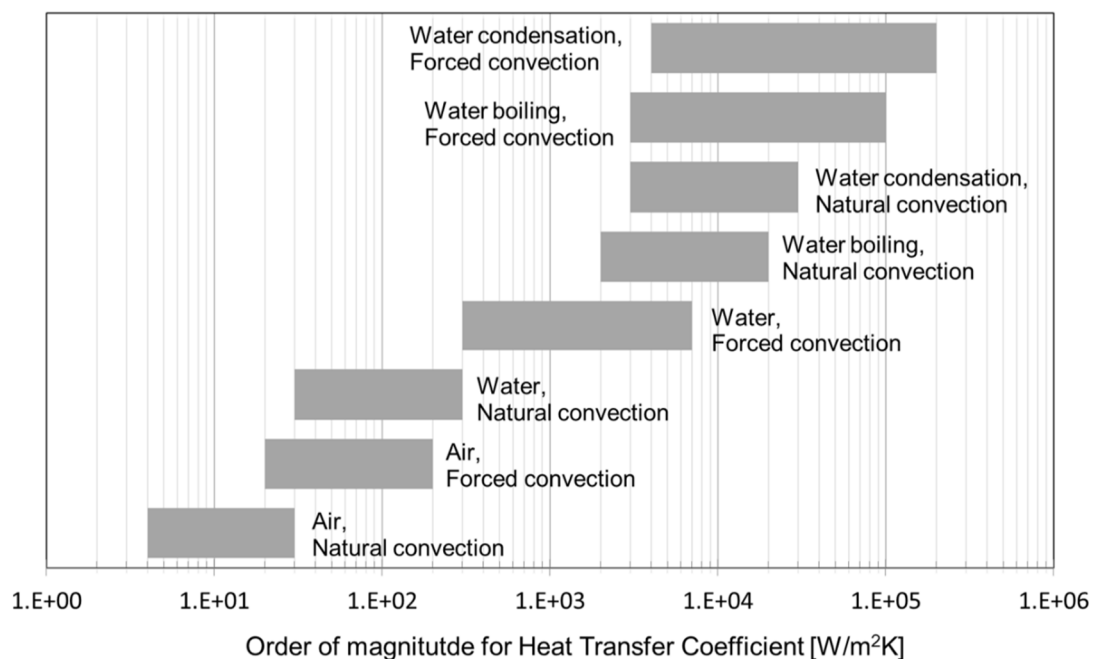


Figure 2 Order of magnitude of heat transfer coefficient achievable with different cooling technologies

The order of magnitude for heat transfer coefficients depending on the physics mechanism is shown in Figure 2. The increasing of the thermal capacity associated

with the phase change means considerably smaller mass flow rate with respect to standard single-phase cooling. On the other hand, two-phase systems show typical limitations that set a cap to the maximum power transferable, like the dry-out conditions.

The performance of a passive two-phase device is often expressed in terms of equivalent thermal conductivity. A device filled with water at the proper filling ratio (FR), defined as the volume occupied by the fluid over the total volume available in the device, would have a thermal conductivity several hundred times the one of pure copper. By using a proper combination of WF and material of the containment (pipework), the temperature of use can range from cryogenic applications (5-10K) to high temperature applications (above 2000K).

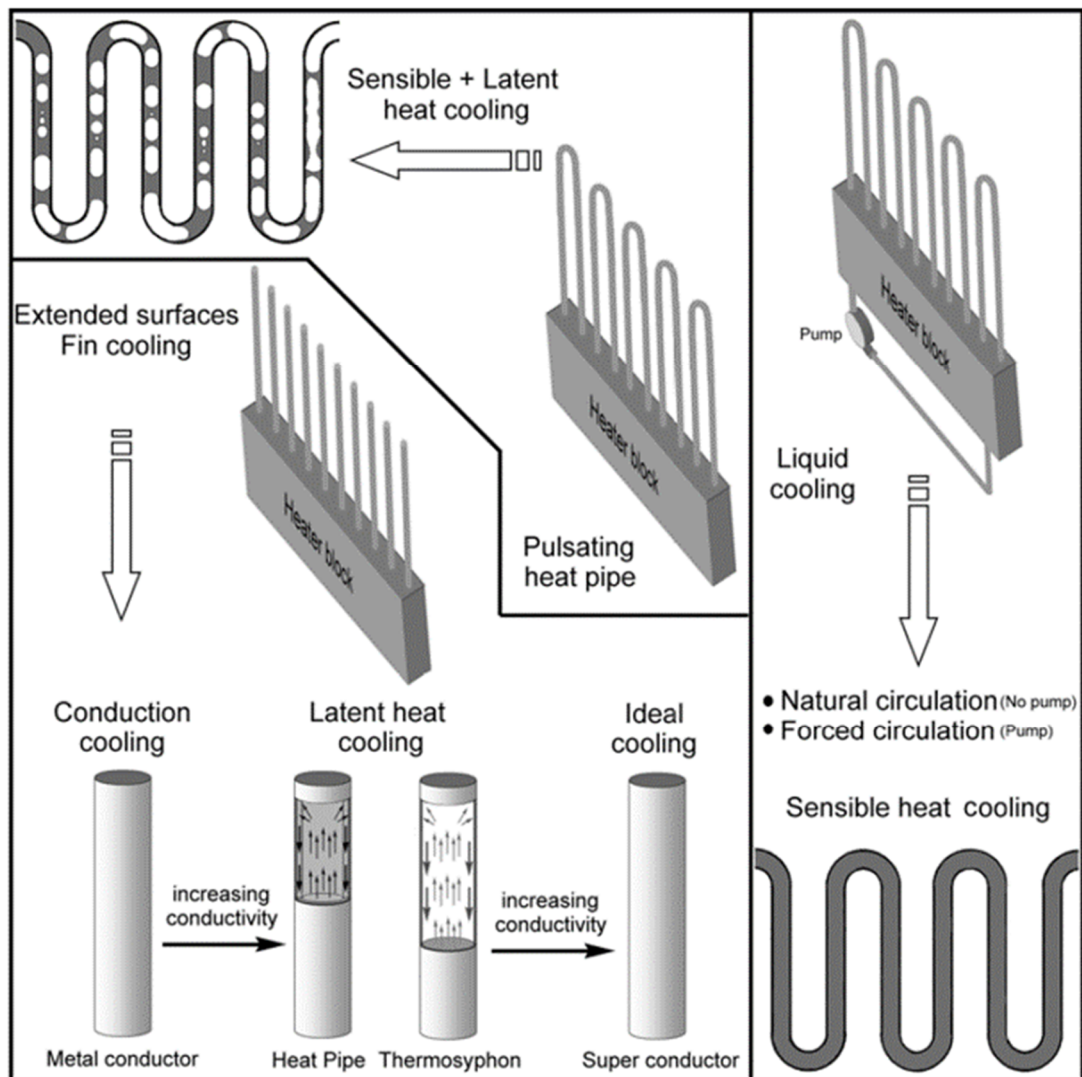


Figure 3 Comparison of various heat transfer technologies [3]

The present research deals with two-phase fluid flow and the process of transferring heat from a hot source and a cold source as an effective and reliable alternative to purely conductive or forced single phase heat transfer. The process involves evaporation and condensation through the addition of heat to a fluid in such a way to increase the vapour quality and subtraction of heat to the fluid to decrease the vapour quality. In evaporation and condensation, the hydrodynamic and the heat transfer process have a high level of coupling. This coupling is much higher than the one existing in single phase flows because the addition/removal of heat causes a variation in the amount and distribution of each phase and the flow pattern or topology of the fluid flow. In multiphase applications, the distribution of phases in the channel defines the characteristic of the structure of the flow pattern. The dominance of surface tension forces in small channels results in flow patterns different to those found in macro scale flows. A stratified flow in a capillary channel can rarely be observed. When the flow rate is low enough, the bubbles are contained in a continuous liquid phase. The Taylor flow forms as the flowrate increase and elongated bubbles with equivalent spherical diameter. Two-Phase Passive Systems exploit the thermally induced circulation/oscillation of the working fluid to transfer heat from a heat source to a heat sink without any external work. The term Passive refers to the absence of any pumping device or external source of energy other than the thermal sources given by the subject of the cooling, and the ambient where to release the heat. When these boundary conditions are constantly provided, the physical phenomena required are activated and the heat transfer takes place. In general, the operation of a common passive heat transfer device is based on the interdependent effect of three physical phenomena:

- Phase change
- Gravity
- Capillarity

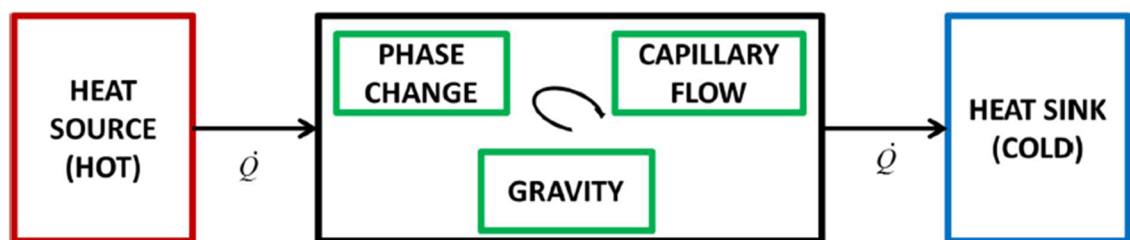


Figure 4 General functioning schematic of two-phase capillary driven heat transfer device

Assuming the phase change always happening in a two-phase device, the relevance of the other two phenomena changes with the type of devices. For instance, in a Thermosyphon the effect of the capillary forces is negligible, given the diameters involved and the absence of small porous structures. In a Heat Pipe, instead, the effect of gravity is the less relevant because the return of condensate to the evaporator relies on the capillary flow in the wick structure located in the circumferential section of the pipe. Transferring heat with a passive two-phase system is a very effective process that allows small temperature gradient to drive the heat flux over considerable distances and nearly isothermal operations regardless of variation in the thermal load. Simple construction and exceptional flexibility are additional strengths of these devices. The phase change of a fluid allows high thermal capacity devices. Compared to standard technologies such as air natural convection cooling, water forced convection cooling, this results in a considerably smaller mass flow rate required and a high specific HTC.

A variety of cross section areas and lengths have been the object of passive two-phase devices design, from microscale (100 μ m x 20mm) to macroscale (10 m long). Common features of all devices are the evaporation and condensation area. Many of them also have an adiabatic section, which separates evaporator and condenser sections by an appropriate distance, intended to satisfy the design constraints of the application. A given passive two-phase device can sometimes have the evaporator section divided into subsections, in the form of a multi-evaporator. The same can happen with the condenser. The main driving force for the return of the condensed working fluid can be capillary and/or gravitational even though centrifugal, electrostatic and osmotic forces can be used in special applications [4].

A useful classification of passive two-phase devices can be done according to the method of condensate return:

Table 1 Classification of passive two-phase devices on the method of condensate return

Wicked devices	Wick-less devices
<ul style="list-style-type: none"> • Heat Pipe (HP) • Loop Heat Pipe (LHP) 	<ul style="list-style-type: none"> •Thermosyphon (TS) •Pulsating Heat Pipe (PHP)

2.2 The Thermosyphon (TS) and the Closed Loop Two-Phase Thermosyphon (CLTPT)

2.2.1 The Thermosyphon

Two-phase natural circulation devices or Thermosyphons or Closed two-phase thermosyphons and gravity-supported heat pipes are highly effective heat transfer elements which become increasingly applied in terrestrial heat transport and heat recovery systems. The Perkins tube, as an essential part of the history of two-phase natural circulation devices, dates back to 1831 (UK Patent No. 6146) with a first patent of a system for heating by small bore wrought iron pipes. The first use of the Perkins tube containing only a small quantity of water and operating on a two-phase cycle, is described in the 1936 patent by Perkins (UK Patent No. 7059). An improved version of the Perkins tube that uses external finning on the tubes to improve the tube-to-gas heat transfer is shown in the air-to air heat exchanger proposed by F.W. Gay (US Patent No. 1725906) dated 1929 (Figure 5).

TSs are wickless gravity assisted devices with the condenser always located above the evaporator to let the condensate returns by gravity. They are used in many applications including snow-melting and de-icing, waste heat recovery heat exchangers, solar energy systems and in high-performance electronics thermal management for fixed orientation gravity-assisted application. The thermosyphon (Figure 6) consists of an evacuated sealed tube filled with a working fluid in saturated equilibrium and in a precise quantity related to the application. It is composed by an evaporator, a condenser and an adiabatic section. The heat flux, applied to the lower end of the pipe, causes boiling and evaporative phenomena in the liquid pool existing at the bottom and in the liquid film along the pipe wall. The working fluid in the evaporator is at a higher pressure than in the condenser section causing the vapour to flow upwards.

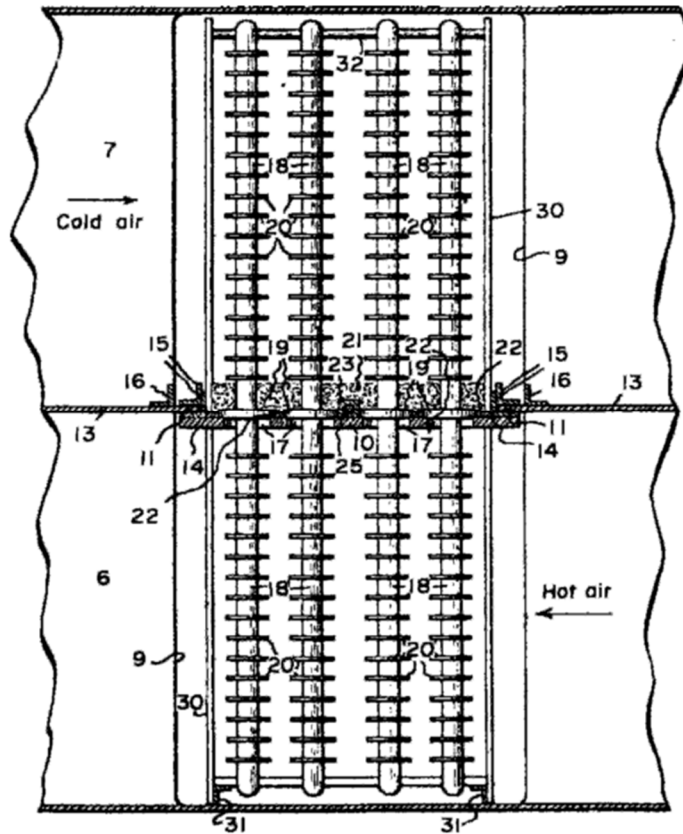


Figure 5 The air preheater for baking ovens proposed by Gay and based on finned, partially filled thermosyphons [4]

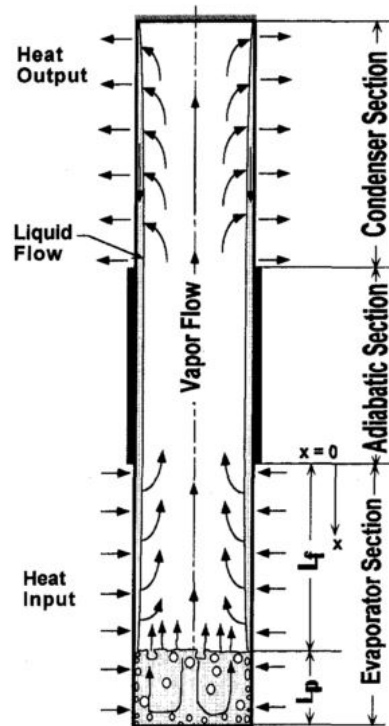


Figure 6 Gravity assisted wickless two-phase closed thermosyphon [5]

The heat transfer rate, which can be established between evaporator and condenser, mainly depends on the diameter of the pipe, the working fluid, the adiabatic section length, the operative temperature and the orientation with respect to the gravity. The performance of the TS is significantly affected by the inclination angle, to the extent where the device can stop working, and from the filling ratio (FR). A FR that is too low can lead to dry-out of the evaporator while an excess of liquid can lead to quantities being carried up to the condenser, where blockage of surface for condensation can result. A commonly adopted rule for avoiding dry-out and condenser blockage is to fill the device according to the following [4]:

$$V_l = 0.001D(l_e + l_a + l_c) \quad (2-1)$$

Where D is the diameter of the thermosyphon and l_e , l_a and l_c are the length of evaporator, adiabatic and condenser zones, respectively. For identifying the proper working fluid able to minimise the temperature drop along a device, a figure of merit M' has been introduced. This figure of merit can be defined as [4]:

$$M' = \left(\frac{h_{lv} k_l^3 \sigma_l}{\mu_l} \right) \quad (2-2)$$

Where h_{lv} is the latent heat of vaporisation, k_l is the thermal conductivity of the liquid phase, σ_l the surface tension and μ_l the dynamic viscosity of the liquid. The group defined in (2-2) depends only on the properties of the working fluid and the conditions that maximise M' define the theoretical optimum performance. The way M' varies with working fluid and the temperature at which it is maximised is shown in Table 2.

Table 2 Maximum thermosyphon merit number for common fluids [4]

Fluid	Temperature (°C)	$M' \max \left(\frac{\text{kg}}{\text{K}^{3/4} \text{S}^{5/2}} \right)$
Water	180	7542
Ammonia	-40	4790
Methanol	145	1948
Acetone	0	1460
Toluene	50	1055

Due to its high figure of merit, availability, cost and non-toxicity, the most common working fluid for thermosyphons is water. Other fluids investigated [6][7] belong to

the chlorofluorocarbons (CFC) refrigerant fluid family (R11, R12, R22, R113) for intermediate operating temperature and the R134a as a replacement of the Freon range. Ethanol and FC-72 have also been investigated for high thermal power applications. In terms of materials used for the pipe, copper and stainless steel are the most common. Some characteristics of TSs for microelectronics applications has been reported to vary between the following limits [5]:

- Wall heat fluxes of 1–52 kW/m²;
- Filling ratios of 0.1–0.62;
- Inner diameters of 6–37 mm;
- Evaporator section height of 50–600mm;
- Vapor temperature of 260–350 K.

A detailed review of experimental works on thermal resistance and heat transfer coefficient can be found in the work of Jafari et al. [8].

2.2.1.1 Transport limitations

Two-phase thermosyphons can be performance-limited in different ways. The type of heat transport limitation depends on geometric dimensions (e.g. diameter, evaporator length), working fluid fill charge and radial heat flux. In most cases, one of the three following performance limits can occur:

- *Dry out limit:* The dry-out limit occurs at the bottom of the evaporator in the liquid falling film mode. This limit prevails for very small liquid filling ratio and relatively small radial evaporator heat fluxes. As the heat transport is increased the quantity of working fluid required for the circulation of vapor and condensate increases. If the available amount of fluid returning from the condenser is too small for the given heat input, the bottom of the evaporator starts to dry out and the wall temperatures are slowly rising. The dry-out limit is established when the friction losses of the condensate flow and the shear forces at the vapor/liquid interface are exceeding the pumping force.
- *Boiling limit:* This limit prevails for relatively large filling ratios, when a pool of liquid is present at the bottom of the evaporator, and high radial evaporator heat fluxes. Vapor bubbles are generated in the liquid pool, and this nucleate boiling becomes more intense with increasing heat flux. At a certain critical radial heat flux individual vapor bubbles are combined to form rather rapidly a vapor film at the wall. This vapor film is insulating the evaporator surface from

the evaporating liquid. Due to the poor thermal conductivity of the vapor only part of the heat input to the wall is transferred to the liquid, the rest is stored in wall material, thus causing a sudden increase of the evaporator wall temperature.

- *Entrainment limit:* This limit occurs for large filling ratios, high axial heat flows, but small radial evaporator heat fluxes. The high axial heat flow causes a high relative velocity between the counter-current flows of vapor (rising) and liquid (descending), and consequently an increase of the shear stresses at the vapor/liquid interface. Thereby, large surface waves are induced at the vapor/liquid interface causing instability of the liquid flow which leads to an entrainment of liquid. The entrained liquid is transported to the condenser by the vapor flow and collected there. The high shear stresses can also cause the returning of the condensate to be completely stopped. The intense entrainment or *flooding* causes an insufficient liquid supply to the evaporator. This leads to a local dry-out and ultimately to a complete dry-out of the evaporator.

2.2.2 The Closed Loop Thermosyphon

Two-phase natural circulation loops or Closed Loop Two Phase Thermosyphons (CLTPT) represents a particular version of a thermosyphon. These systems work under gravity with the condenser above the evaporator and do not require pump or capillary action of a wick structure to allow the heat transfer fluid to be returned to the evaporator. They consist of four major components; the evaporator, the riser tube, the condenser, and the down-comer tube. The terms “riser” and “down-comer” describe the general fluid flow direction through the connecting tubes in a natural circulation thermosyphon where condenser is placed at a higher elevation than the evaporator. The heat transfer rate mainly depends on the diameter of the pipes, the working fluid, the adiabatic section length and the orientation with respect to the gravity. The operating principle compared to the single tube thermosyphons is to separate the paths of the returning condensate liquid from the path of the vapor leaving the evaporation zone. In this way, a significant increase of heat transport with respect to the conventional two phases closed thermosyphons can be achieved. The extent of the increase in performance is higher as the size of the devices decrease.

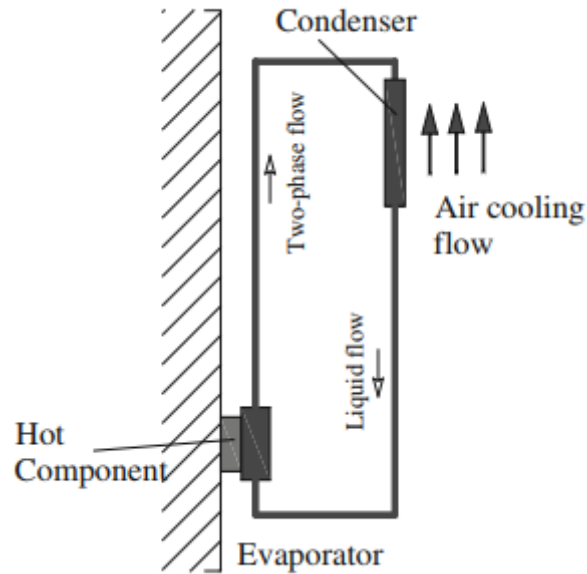


Figure 7 Schematic of a CLTPT for components cooling [9]

2.3 The Heat Pipe (HP)

The basic heat pipe differs from the thermosyphon in the way the condensate returns to the evaporator. A HP consists of a sealed tube containing a wick in contact with the inner surface of the pipe wall. The role of the wick structure is to provide a preferential path for the condensate, while the vapour phase flows in the middle of the tube core. The main regions of a HP are shown in Figure 8

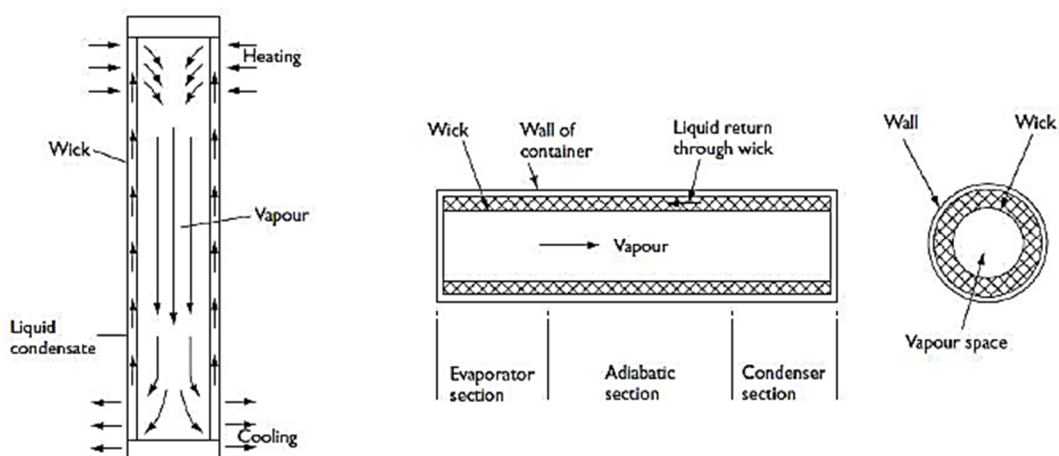


Figure 8 Heat Pipe and its main regions [4]

The pressure difference that drives the liquid from the condenser through the porous structure and eventually to the evaporator, allowing a continuous process, is generated by a difference in the capillary radii (advancing and receding meniscus) at evaporator and condenser ends (Figure 9).

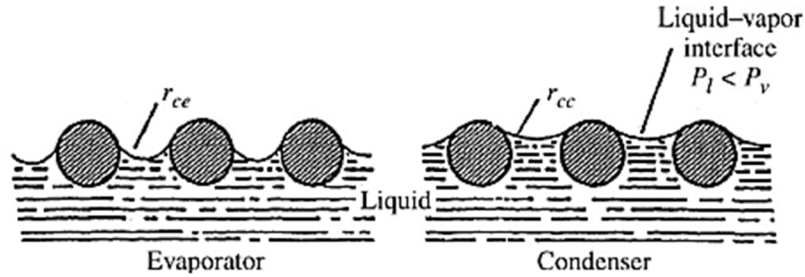


Figure 9 Radii of curvature of the liquid-vapour interface in evaporator and condenser [10]

The capillary pressure is usually obtained by means of the Young-Laplace equation [10]:

$$\Delta P_c = \frac{2\sigma \cos\theta}{r_{eff}} = (\Delta P_c)_{evap} - (\Delta P_c)_{cond} \quad (2-3)$$

where r_{eff} is the effective radius of curvature, assumed as the inner radius of a circular tube, and θ is the apparent contact angle, function of the combination fluid-wick material used; σ is the surface tension. To activate the device, the maximum capillary pumping pressure $\Delta P_{c,max}$ must be greater than the total amount of pressure drop in the pipe [10]:

$$\Delta P_{c,max} \geq \Delta P_l + \Delta P_v + \Delta P_g \quad (2-4)$$

Ideally, the maximum value of capillary pressure occurs when the values of the contact angle at the evaporator and at the condenser are respectively $\theta_e = 0^\circ$ and $\theta_c = 90^\circ$. When this condition is verified, no dry out occurs at the evaporator region and the HP can operate, allowing the fluid to circulate overcoming friction losses and adverse body forces such as gravity. The contributions to this pressure drop are:

- ΔP_l Pressure drop required to return the liquid from the condenser to the evaporator
- ΔP_v Pressure drop necessary to cause the vapour flow from the evaporator to the condenser
- ΔP_g Pressure due to hydrostatic head of liquid

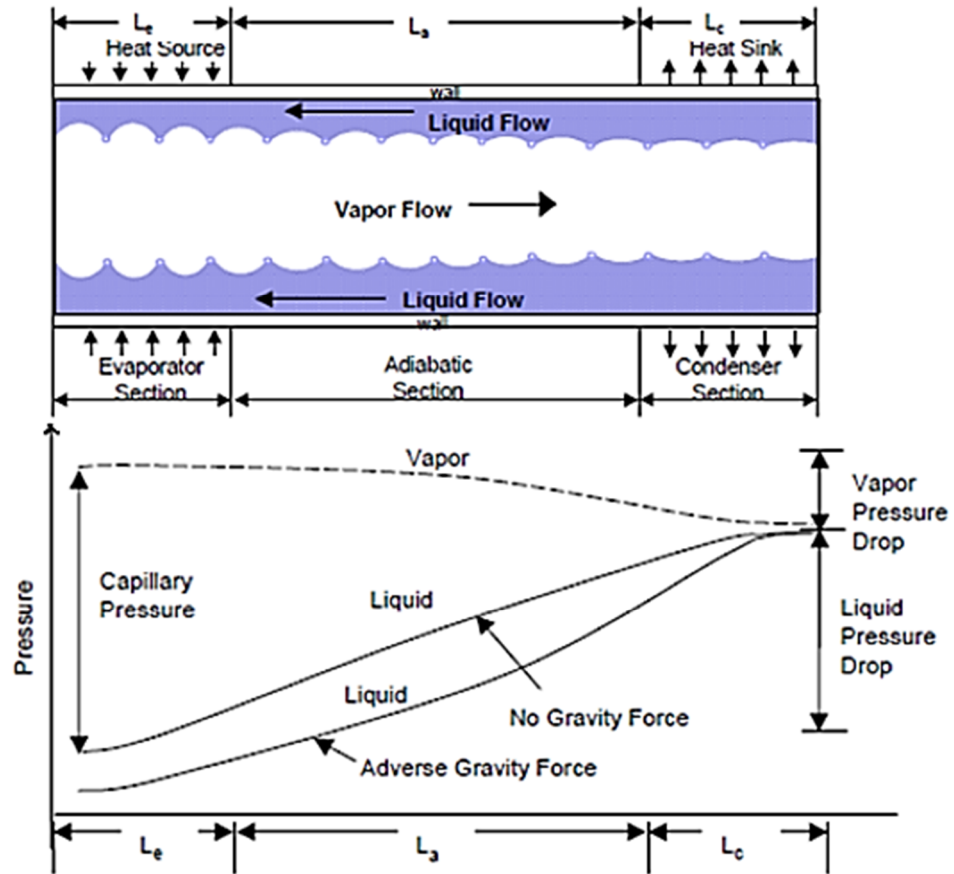


Figure 10 Fluid pressure along the structure of a HP

The value of ΔP_g is expressed by the following relation:

$$\Delta P_g = \rho_l g l \sin \Phi \quad (2-5)$$

where ρ_l is the liquid density, g the acceleration due to gravity, l the length of the HP and Φ the angle between the HP and the horizontal position. This term can be zero, positive or negative depending on the inclination of the device.

2.3.1 Transport limitations

The existence of a maximum pressure drop condition implies the existence of limitations to heat transport in a HP. Limitations of the maximum heat input can be divided into two categories: events that lead to a failure of the device and events that do not lead to a failure. The failures are characterized by insufficient liquid flow to the evaporator for a given heat input or dry out. The heat input is related to the mass flow rate of the working fluid that circulates and its latent heat. A non-failure of the device

means that the HP is going to work at an increased temperature for an increasing value of the heat input (Figure 11).

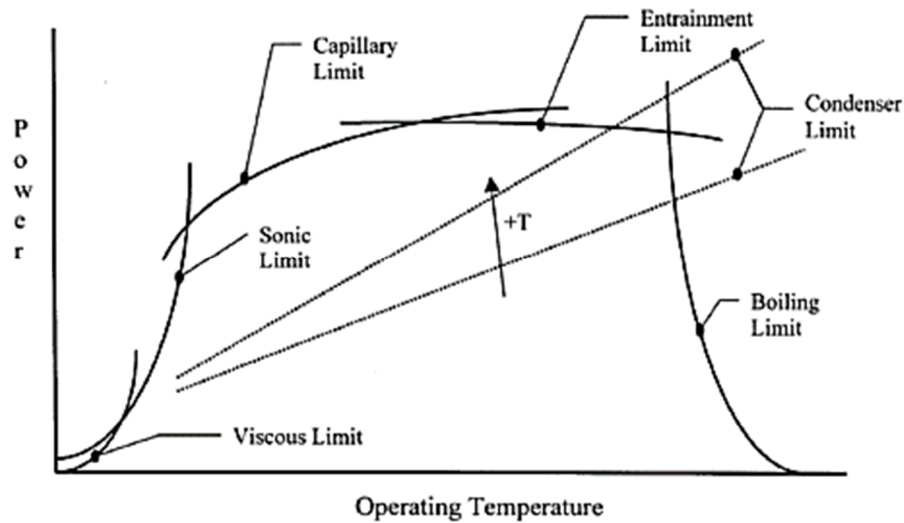


Figure 11 Performance map of HP with limits [4]

Some of these limitations are defined as limitations causing a failure:

- *Capillary Limit*: Relates to the development of capillary pressure difference across the liquid-vapour interfaces. It occurs when the capillary pressure is insufficient to provide enough liquid to the evaporator and leads to dry-out conditions in the evaporator. It's the primary maximum heat transport limitation of a HP
- *Boiling Limit*: Occurs when the applied heat flux is sufficient to cause nucleate boiling in the wick in the evaporator zone. This creates vapour bubbles that partially block the liquid return and evaporator dry-out can occur. This is sometimes referred to as the heat flux limit
- *Entrainment Limit*: High shear forces caused by the counter-flow passage of vapour over the liquid saturated wick. The liquid can be entrained by the vapour and return to the condenser, causing insufficient flow in the wick.

Other limitations are defined as not leading to failure of the device:

- *Viscous limit*: Occurs at low operating temperatures, where the saturation vapour pressure may be comparable to the pressure drop required to drive the vapour flow in the HP. Also called the vapour pressure limit.

- *Sonic Limit*: At low vapour densities, the mass flow rate in the HP reaches high vapour velocities; choked flow in the vapour passage may occur.
- *Condenser Limit*: Caused by cooling limitations of the condenser; for instance, a low exchange surface area can lead to this limitation.

2.3.2 Performance and operating conditions

For a given geometry of HP, its performance is heavily affected by the morphology of the wick structure. There are three principal capillary geometries (Figure 12):

- Wick structures consisting of a porous structure made up of interconnecting pores (Homogeneous Wicks);
- Open grooves;
- Covered channels consisting of an area for liquid flow closed by a finer mesh capillary structure (Composite Wicks).

The heat pipe temperature range depends mainly on the pairing of working fluid with the material of the shell and of the wick, as shown in Table 3.

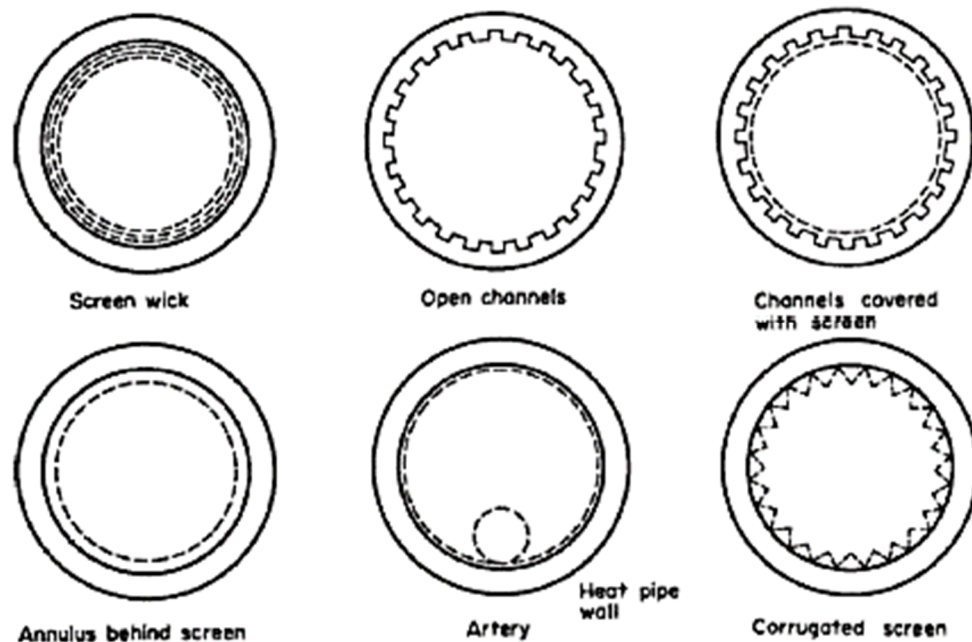


Figure 12 Selection of wick structures [4]

The overall temperature difference between heat sink and heat source is an important characteristic for HPs thermal control systems; it defines the thermal resistance of the device. An electrical resistance analogy (Figure 13) can be used to evaluate the value of the thermal resistance; each part of the HP can be separated into an individual thermal resistance. The combined resistance provides a mechanism to model the overall resistance and temperature drop from the heat sink to the heat source associated to a given heat input. From this analogy, it is also possible to extrapolate the mean operating adiabatic vapour temperature, needed to define the transport limit at given operating conditions.

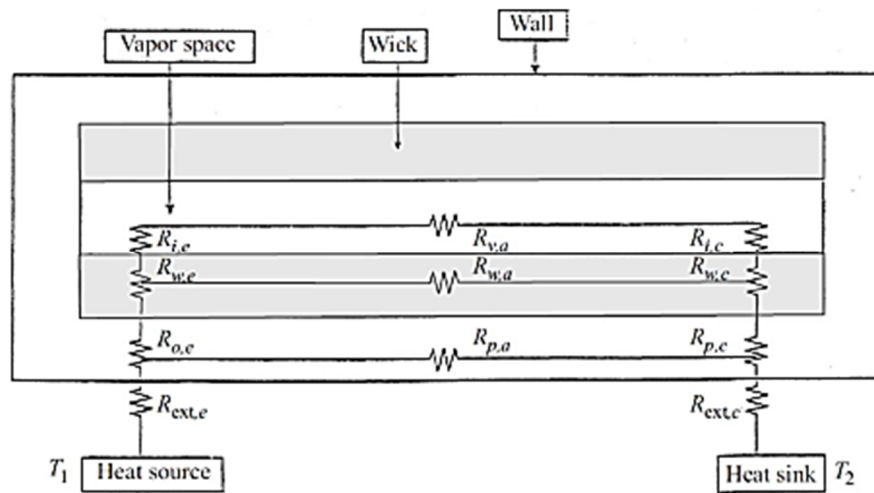


Figure 13 Temperature drops and equivalent thermal resistance of a HP [10]

By examination of typical range of resistance values, several simplifications are possible. Due to comparative magnitudes, the axial resistance of the pipe and the liquid-wick combinations, may be treated as open circuits and neglected. The liquid-vapour interface resistances and the axial vapour resistance can both not be considered. After all these simplifications, a general equation for evaluation of the overall thermal resistance of a HP can be expressed as:

$$R_{th} = \frac{T_e - T_c}{Q} \quad [\text{K/W}] \quad (2-6)$$

where T_e and T_c are respectively the evaporator and the condenser temperature, Q is the heat power input.

Working Fluid	Temperature Range [°C]	Shell Material	Measured axial heat flux [W/cm ²]	Measured radial heat flux [W/cm ²]
Low Temperature or Cryogenic Heat Pipe Working Fluids				
Helium	-271 to -269	SS, Ti		
Hydrogen	-260 to -230	SS		
Methane	-180 to -100	SS		
Neon	-240 to -230	SS		
Nitrogen	-200 to -160	SS	67 @ -163°C	1.01 @ -163°C
Oxygen	-210 to -130	Al, Ti		
Carbon Dioxide	-50 to 30	Al, SS, Ti		
Mid Range Heat Pipe Working Fluids				
Acetone	-48 to 125	Al, SS		
Ammonia	-75 to 125	Al, SS	295	2.95
Ethane	-150 to 25	Al		
Methanol	-75 to 120	Cu, Monel, Ni, Ti	450 @ 100°C	75.5 @ 100°C
Methylamine	-90 to 125	Al		
Pentane	-125 to 125	Al, SS		
Propylene	-150 to 60	Al, SS		
Water	1 to 325	Cu, Monel, Ni, Ti	670 @ 200°C	146 @ 200°C
High temperature heat pipe fluids				
Mercury +0.02% Magnesium +0.001%	190 to 550	SS	25100 @ 360°C	181 @ 360°C
Cesium	350 to 925	SS, Inconel, Haynes		
NaK	425 to 825	SS, Inconel, Haynes		
Potassium	400 to 1025	Stainless Steel, Inconel, Haynes	5600 @ 750°C	181 @ 750°C
Sodium	500 to 1225	SS, Inconel, Haynes	9300 @ 850°C	224 @ 850°C
Lithium	925 to 1825	W, Nb	2000 @ 1250°C	207 @ 1250°C
Silver	1625 to 2025	W, Mo	4100	4.13

Table 3 Typical operating characteristics of HP working fluid pairing with shell/wick material

2.4 The Loop Heat Pipe (LHP) and Capillary Pumped Loops (CPL)

A main drawback of the conventional heat pipe is the presence of the wick along the entire internal surface, which causes increased pressure losses in the liquid flow. Moreover, the manufacturing of high-quality wick structures requires specific competences and technologies and represent the most expensive component of Heat Pipes. For this reason, in the last few decades, attention has been given to devices able to operate separation of the vapor passage from the liquid passage and reducing the presence of the wick in the heat pipes. This resulted in the loop heat pipe (LHP), developed primarily in the former Soviet Union, and capillary pumped loops (CPL), developed primarily in the United States (Figure 14). The nature of an LHP and a CPL are actually the same, the major difference being that the LHP usually operates in a constant-conductance mode, while a CPL usually operates in a variable conductance mode by keeping the operation temperature unchanged. Like conventional HPs, a Loop Heat Pipe (LHP) exploits capillary action to circulate the working fluid in a closed loop by effect of the thermal input (Figure 15). A LHP, differently to an HP, has a wick structure confined only to the evaporator section (Figure 16). The evaporator also contains a compensation chamber, which serves as an accumulator for the fluid during the operation of the device. Another important component is the condenser, whose shape and size depend on the heat sink nature and on the cooling conditions. Evaporator and condenser are connected on one side by a liquid line and on the other side by a vapour line: both lines are made of a smooth, small diameter pipe.

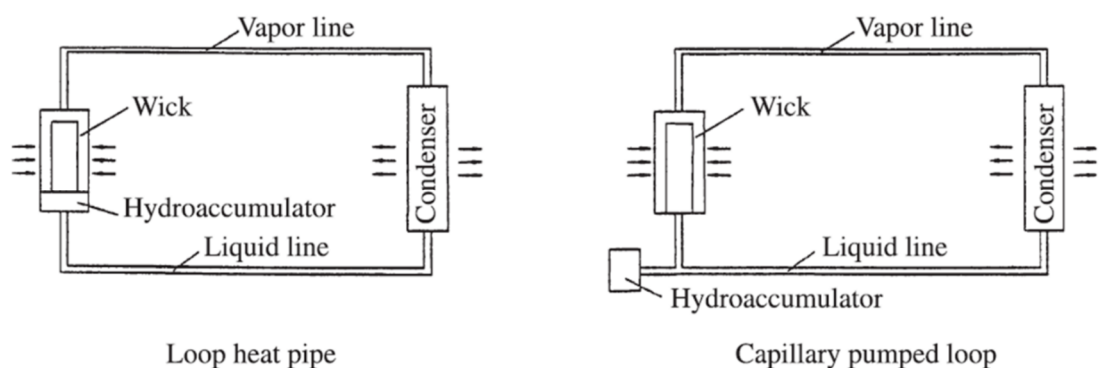


Figure 14 Loop Heat Pipe and Capillary Pumped Loop in their schematic view [11]

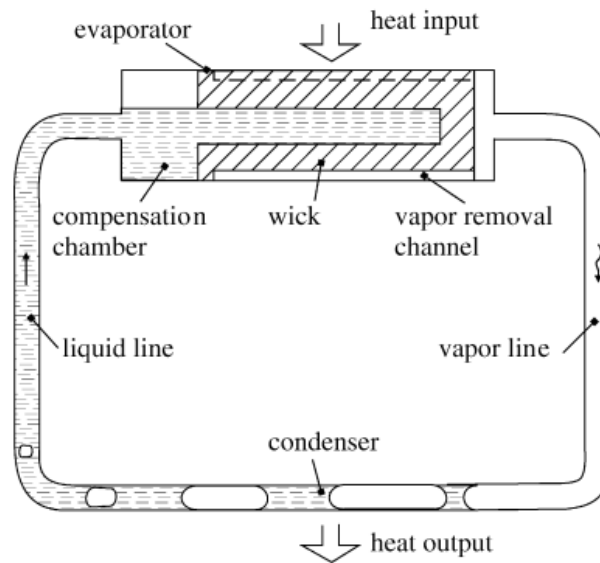


Figure 15 General scheme of a LHP [12]

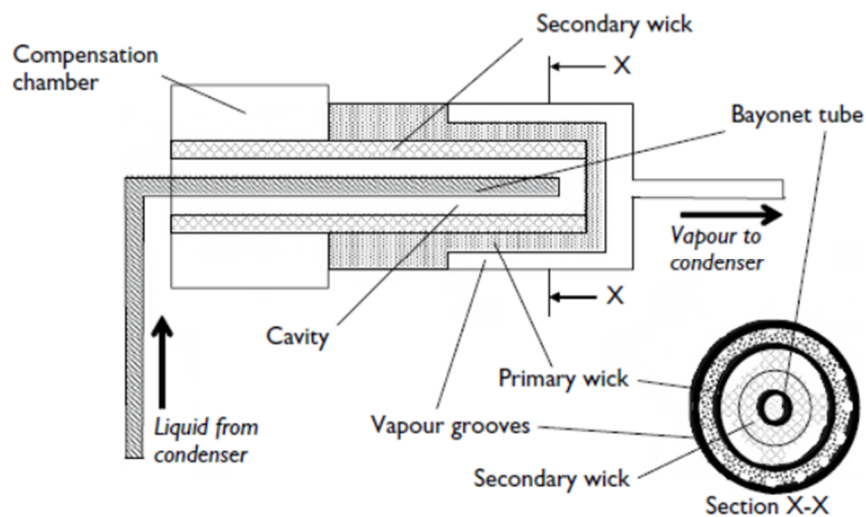


Figure 16 Detail of a typical LHP evaporator [4]

Like conventional heat pipes, LHPs/CPLs are subjected to limitations. The operating cycle, described by Maidanik, is reprinted in Figure 17. Along the saturation line, point 1 corresponds to the vapour conditions just above the vaporising meniscus surface on the wick, as the working fluid vaporises into the vapour passage. The section 1-2 is the pressure loss associated with vapour flow and direction changes through the vapour grooves and vapour header (vapour removal channels). The difference in temperature between the outside of the evaporator and the surface of the wick causes an increase in vapour temperature. Section 2-3 is the assumed pressure drop due to the adiabatic motion of vapour through the vapour line. Section 3-5 is the

isobaric (pressure losses in the condenser are usually negligible) heat transfer process that take place in the condenser, divided in vapour-liquid condensation up to T_4 (3-4) and liquid subcooling down to T_6 (4-5). The section 5-6 represents the isothermal pressure loss due to the gravitational head associated with the liquid return from the condenser to the evaporator through the liquid line. From 6 is the sensible liquid heating in the compensation chamber that ends in 7 when the saturation conditions are reached. The process of the liquid going through the wick structure (7-8) into the evaporator is associated with a pressure drop (P_6 to P_8) and a liquid superheating without boiling (due to the short duration of this phase) until reaching point 8, which is the state of the working fluid in the proximity of the evaporating menisci. The pressure drop ΔP_c between 1 and 8 corresponds to the value of the total pressure losses in all the sections of the LHP.

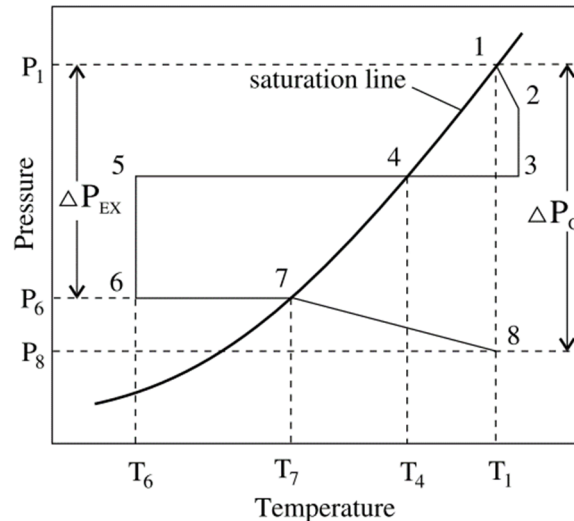


Figure 17 Operating cycle of a LHP [12]

Similar to the functioning limit of an HP, the capillary pressure generated in the wick (ΔP_c) has to exceed the sum of the pressure losses due to the motion of working fluid in the vapour phase (ΔP_v) in the liquid phase (ΔP_l) and the pressure losses caused by the hydrostatic resistance of the liquid column (ΔP_g). Due to the various designs of LHPs (Table 4), this limitation may have different magnitudes and characteristics.

Table 4 Classification of LHP [12]

LHP design	LHP dimensions	Evaporator shape	Evaporator design
<ul style="list-style-type: none"> • Conventional (diode) • Reversible • Flexible • Ramified 	<ul style="list-style-type: none"> • Miniature • All the rest 	<ul style="list-style-type: none"> • Cylindrical • Flat disk-shaped • Flat rectangular 	<ul style="list-style-type: none"> • One butt-end compensation chamber • Two butt-end compensation chambers • Coaxial
Condenser design	Number of evaporators and condensers	Temperature range	Operating-temperature control
<ul style="list-style-type: none"> • Pipe-in-pipe • Flat coil • Collector 	<ul style="list-style-type: none"> • One • Two and more 	<ul style="list-style-type: none"> • Cryogenic • Low-temperature • High-temperature 	<ul style="list-style-type: none"> • Without active control • With active control

2.5 The Pulsating Heat Pipe (PHP)

The Pulsating Heat Pipe (PHP) is the last evolution of wickless Passive two-phase devices. The novel concept of a wickless device, was firstly introduced by Akachi [13] in the early '90s. These devices function via thermally excited motion induced by the cyclic phase change of the working fluid. Differently from wicked HPs, the capillary effect is in this case provided by the small dimensions of the channel rather than an additional structure inside the shell. The result is a device solely consisting in a bended tube with a diameter able to provide capillary conditions for the selected WF and for the gravity field in which the device needs to operate. The PHP is partially filled with a WF to a specific Frilling Ratio (FR). The result of this filling is very peculiar and distinctive of these devices: the two-phase fluid inside the PHP consists of a random distribution (a train) of liquid slugs alternate to vapour plugs. A typical PHP presents the three sections characteristic of Passive two-phase devices (Figure 18): an evaporating section, an adiabatic section, and a condensing section. The PHP functions by receiving heat from the section in contact with the heat source (this is generally the turns section, the result of the bending in a serpentine of the entire tubing) and rejecting the heat in a condensing area.

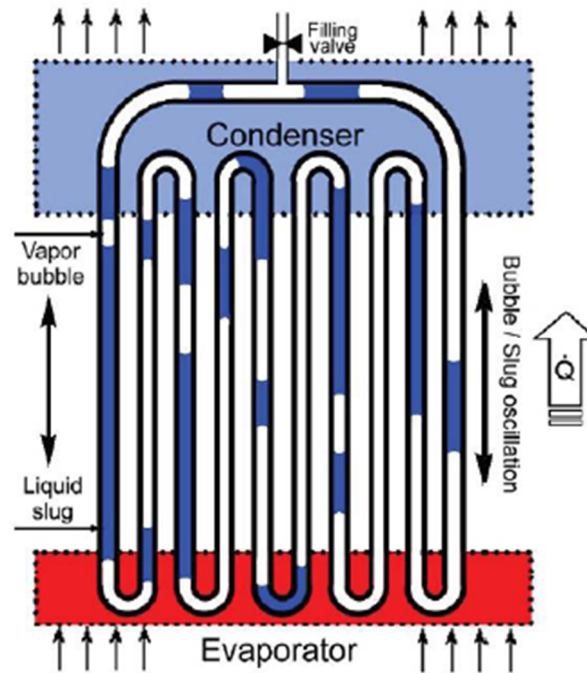


Figure 18 Schematic of a conventional Closed Loop Pulsating Heat Pipe [14]

2.5.1 Operating mechanism

The evaporation and condensation of the working fluid is the continuous process which creates a pulsating non-equilibrium vapour pressure that drives fluid motion between adjacent tube sections. This results in a complex global motion of two-phase fluid, characterised by oscillatory and circulatory components activated by both sensible and latent heat transfer. The phase change helps to generate the oscillation motion and a great part of the job of transferring heat is accomplished by the sensible heat transfer. The device can work against gravity if the evaporation area is well designed (sufficient number of turns, non-uniformity of the heating) as long as the non-equilibrium conditions are continuously established within the system.

Heat and mass processes and forces acting on the fluid at a macro-level are illustrated in Figure 19. The dominant flow pattern in a PHP can be defined as Taylor flow [15] or slug-plug flow.

The flow pattern can be defined axisymmetric with a slip ratio between the two phases generally >1 . Due to the capillary dimension of the channel, the shape of the edges of the vapour bubble is the classical meniscus, formed due to surface tension. A liquid film is encapsulating the bubble and its thickness and stability depend on the solid-fluid contact angle at the menisci.

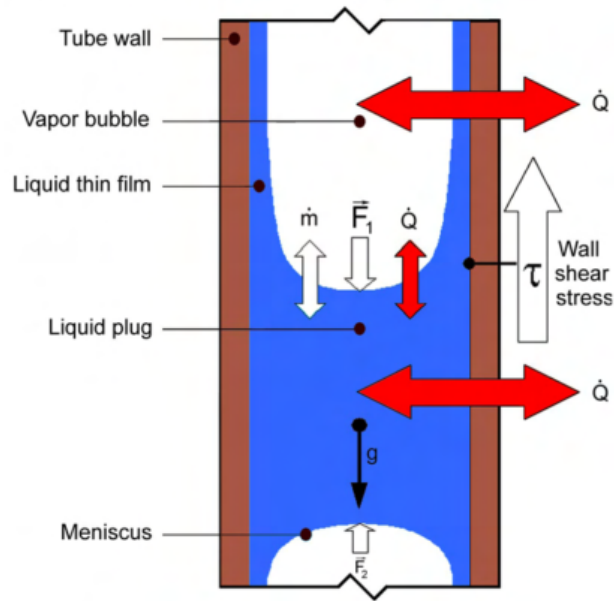


Figure 19 Heat and mass processes involved in a Taylor flow, dominant flow pattern in the PHP [16]

A capillary pressure, caused by adjacent slug/plug and linked to the curvature of the menisci, is acting on the liquid plugs. During the movement of the fluid, slugs and plugs experience internal viscous dissipation as well as shear stress. The predominant force will affect the hydrodynamic and the heat transfer property of the PHP.

The activities at the evaporator can follow this flow: heat transfer from the wall to the liquid, evaporation mass transfer to the neighbour vapour bubbles or breaking up of the liquid plug with creation of new bubbles as a result of nucleate boiling in the slug. The saturation properties, P and T , increase locally. The saturated vapour plugs can receive heat from the liquid film in direct contact with the channel wall. In this case, evaporation mass transfer from the film takes place, as well as from the liquid plugs. All the mentioned thermo-dynamic transformations take place in an isochoric way. The reverse processes take place in the condenser. The classical concept of steady-state is not applicable to the PHP, where thermally driven pressure waves and pulsations are generated in each branch of the device, which interact with the adjacent.

2.6 PHP Technologies applications

Although PHPs are being widely studied in the academic community, the commercial availability of pulsating heat pipes is limited. Thermacore, Inc. and the Rockwell Scientific Co. have done research regarding pulsating heat pipes, but do not currently manufacture PHPs as standard items. Two companies that do offer PHPs for

sale are TSheatronics Co., Ltd. of Japan and Advanced Cooling Technologies, Inc. (ACT) in the United States. TSheatronics calls their technology Heatlane. Heatlane AL-EX is an aluminium flat plate PHP that can be manufactured in different configurations.

	Sintered HP	TS	PHP
Application	Ground/Space	Ground	Ground/Space
Radial/surface Heat Flux	High up to 200 W/cm ²	High up to 100 W/cm ²	Medium up to 30 W/cm ²
Total Power per unit (depends on the geometry)	High up to 1kW	High up to 3kW	Medium up to 0.5kW
Thermal Resistance	Very Low down to 0.01 K/W	Very low down to 0.05 K/W	Very Low down to 0.08 K/W
Start Up Time (depends on the geometry)	Fast Few seconds	Medium 2-3minutes	Medium 2-3 minutes
Effect of inclination angle	Medium Depending on the wick structure type	Gravity is necessary	Critical A proper design may avoid strong effects, top heating mode is difficult
3D space adaptability	Medium Relatively foldable	Medium gravity limit	High highly foldable
Thermally controlled surface	Medium	Medium/Low	High
Operation reliability	High	High	Medium
Cost	Medium/High	Medium/Low wickless	Low wickless

Table 5 Comparison between main technologies available

The working fluids used are butane and HFC-134a. The Heatlane AL-EX can be combined with aluminium fins and used as a heat sink to cool power semiconductors, laser generators, and CPUs. A similarly finned PHP can be used as a heat absorber. Applications for aluminium Heatlanes without fins include cooling plasma screens and LCD monitors. TSheatronics also makes a stainless-steel version of their product with water as the working fluid. This style PHP has found uses in the food service industry.

2.7 Classification based on TRL for space applications

The Technology Readiness Levels (TRLs), initially adopted by NASA, were introduced in ESA in order to enable discipline-independent assessments of the maturity of a particular technology and the consistent comparison of maturity between different types of technology, all in the context of a specific system, application and operational environment.

Table 6 Technology Readiness Level summary and milestones [17]

TRL	TRL Description	Milestone achieved
1	Basic principles observed and reported	Potential applications are identified following basic observations, but element concept not yet formulated.
2	Technology concept and/or application formulated	Formulation of potential applications and preliminary element concept. No proof of concept yet
3	Analytical and experimental critical function and/or characteristic proof-of-concept	Element concept is elaborated, and expected performance is demonstrated through analytical models supported by experimental data/characteristics.
4	Component and/or breadboard functional verification in laboratory environment	Element functional performance is demonstrated by breadboard testing in laboratory environment.
5	Component and/or breadboard critical function verification in a relevant environment	Critical functions of the element are identified, and the associated relevant environment is defined. Breadboards not full-scale are built for verifying the performance through testing in the relevant environment, subject to scaling effects.
6	Model demonstrating the critical functions of the element in a relevant environment	Critical functions of the element are verified, performance is demonstrated in the relevant environment and representative model(s) in form, fit and function.
7	Model demonstrating the element performance for the operational environment	Performance is demonstrated for the operational environment, on the ground or if necessary, in space. A representative model, fully reflecting all aspects of the flight model design, is build and tested with adequate margins for demonstrating the performance in the operational environment.
8	Actual system completed and accepted for flight (“flight qualified”)	Flight model is qualified and integrated in the final system ready for flight.
9	Actual system “flight proven” through successful mission operations	Technology is mature. The element is successfully in service for the assigned mission in the actual operational environment.

The technical maturity of instruments and spacecraft sub-systems with respect to a specific space application are classified according to a "Technology Readiness Level" (TRL) on a scale of 1 to 9. ESA uses the ISO standard 16290 Space systems – Definition of the Technology Readiness Levels (TRLs) and their criteria assessment [17].

Both Heat Pipes (Table 7) and Loop Heat Pipes have reached the flight proven status throughout many successful missions. Heat Pipes have been implemented in Defence Program Satellites (DPSs) for the cooling to approximately 150 K of IR telescope (Figure 20) that detects and tracks missiles by the heat emitted from their rocket plumes.

Other fields of application of HP and LHP, together with batteries isothermalisation, are the “body-mounted” radiator panels for applications that require a radiator that is not part of the vehicle structure: heat is transported from the heat-

dissipating components to the radiator (Figure 21) using fixed or variable-conductance heat pipes or loop heat pipes/capillary pumped loops.

As a result of the increasing demand of technical solutions for a widening range of thermal management problem, HPs and LHPs continue to be active subjects of research and development. Current areas of research include:

- reliable lightweight low-pressure-drop parallel condensers;
- freeze-tolerant radiators;
- advanced high-performance, low-conductivity wicks;
- evaporators of different aspect ratios (long, thin, flat, miniaturized, etc.)
- heat-transfer performance improvements;
- miniature systems
- simplification of the technology, for adaptation to mass production;
- multi-evaporator and multi-condenser systems, including reversible loops and large-scale isothermalizers;
- cryogenic systems;
- high-temperature systems.

In this context, Pulsating Heat Pipes can find a role especially in terms of simplification of the manufacturing process and for multi-evaporator/condenser. The next step will be to support the PHPs development from functional verification in laboratory environment TRL4 to a critical function verification in relevant environment, TRL5, through a long-term microgravity investigation onboard the International Space Station.

Table 7 EADS ASTRIUM Heat Pipe qualification and Space application history [18]

ASTRIUM Heat Pipe Qualification and Space Application Programmes		81	82	83	84	85	86	87	88	89	90	91	92	93	94	95	96	97	98	99	00	01	02	03	04	05	06	07	08	09		
		Heat Pipe Project																														
Qualifications	[Qualification bars: 81-82, 84-85, 87-88, 90-91, 93-94, 96-97, 99-00, 02-03, 05-06, 08-09]																															
ESTEC Lifetest, Start 2/78	[Lifetest bar: 81-99]																															
Inhouse Lifetest	[Lifetest bar: 81-99]																															
OLYMPUS	[Application bar: 85-86]																															
EUROSTAR	[Application bar: 83-84]																															
ERS-1 / ERS-2	[Application bars: 85-86, 89-90]																															
MAS	[Application bar: 85-86]																															
TELECOM 2	[Application bar: 88-89]																															
RADARSAT HPMC	[Application bars: 89-90, 91-92]																															
APCF / BDPU (Fluorocarbon)	[Application bars: 90-91, 92-93]																															
POLAR PLATFORM	[Application bars: 91-92, 93-94]																															
GOME-1 / GOME-2	[Application bars: 92-93, 99-00]																															
AMOS N/S PANEL	[Application bars: 92-93, 94-95]																															
HEAT PIPE UNITS	[Application bars: 89-90, 93-94, 96-97, 99-00]																															
SILEX GEO	[Application bars: 94-95, 96-97]																															
SCIA RADIATOR "A"	[Application bars: 94-95, 96-97]																															
SCIA TBU 7/8 (Methane)	[Application bar: 95-96]																															
ADM BB	[Application bar: 00-01]																															
EOS COOLING UNIT	[Application bars: 01-02, 03-04]																															
CRYOSAT-1 / 2	[Application bars: 02-03, 04-05]																															
TERRASAR-X LCT Radiator	[Application bars: 03-04, 05-06]																															
OPTICAL HEAD	[Application bars: 04-05, 06-07]																															
Tandem-X LCT Radiator	[Application bars: 05-06, 07-08]																															
ESA MINI HEAT PIPE	[Application bars: 06-07, 08-09]																															
KOMPSAT K3A KISS	[Application bar: 08-09]																															

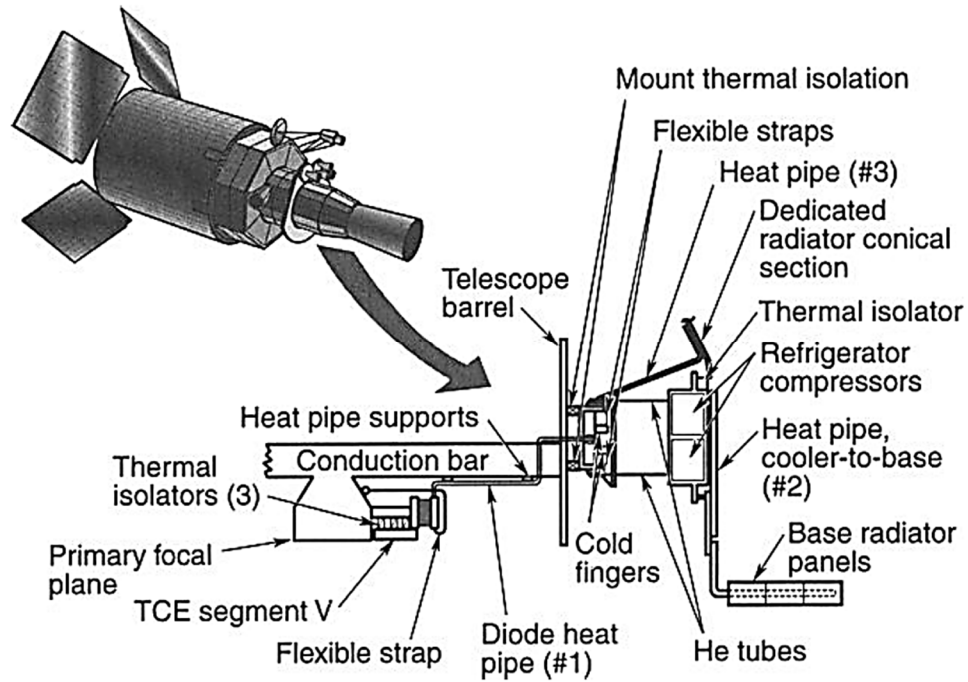


Figure 20 Defence Program Satellite (DPS) sensor detail

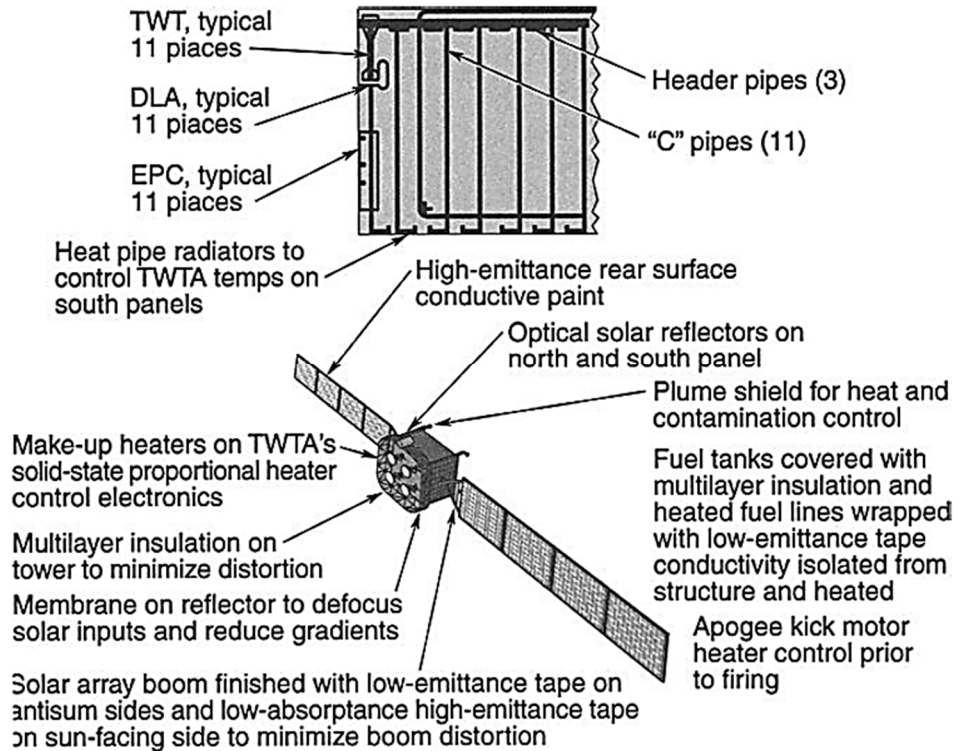


Figure 21 Example of Heat Pipe radiator panel. Please refer to [19] for an exhaustive description of the sub-systems.

Chapter 3

The Pulsating Heat Pipe for heat transfer on Earth and in space

3.1 Introduction

The PHP device belongs to a special category of two-phase Wickless Heat Pipes that operate thanks to the capillary conditions established in its meandering tube. PHPs have been originally described in a series of patents during the 90's [20] [13]. From a technological point of view, an PHP is very simple and cost effective compared to other heat transport device. It is composed by a small diameter tube arranged in a serpentine, evacuated, partially filled with a incondensable-free working fluid, with thermo-physical properties suitable to maximise the heat transfer, and eventually sealed [21]. This fluid, defined as the working fluid (WF), resides into the PHP in the form of liquid slugs and vapour plugs train because of the dominant effect of capillary forces with respect to the buoyancy forces.

A PHP can be considered a non-equilibrium heat transfer system where a steady state is never achieved, and its functioning is chaotic. Three main section can be identified in a PHP: evaporating, adiabatic and condensing section. PHPs are designed with numerous points of condensation and evaporation (the turns in its serpentine) that reach from the evaporator to the condenser to introduce as many local perturbations as

possible. Thanks to that, the working fluid contained inside the device is exposed to continuous phase changes, resulting in a pulsating pressure field induced during evaporation and condensation processes. The fluid motion as well as the transition of the flow pattern is highly chaotic and oscillating but the system is able to reach several steady state conditions over a wide range of operating conditions [14]. The fluctuation of pressure inside the PHP drives a self-excited oscillating motion of liquid plugs and vapour bubbles significantly enhancing the convection and consequently promoting the heat transfer between a thermal source (evaporator) and a thermal sink (condenser) [22] both of sensible and latent heat. The resulting flow of phases can be defined co-current dominant even though the numerous flow reversal and the difference in density of liquid and vapour, induce inertial effects that result in a counter-current flow in the instants right after the flow reversal.

Their advantages with respect to the standard technologies of heat transfer are mainly related to the exploitation of the high heat transfer rates associated with the phase change phenomenon but also sensible heat, the compactness and the possibility to be operated passively, avoiding the use of pumps and against gravity. For these reasons PHPs are considered promising heat transfer device [22].

Despite the attractive and motivating advantages of the PHP systems, the understanding of the fundamental hydrodynamic and thermal transport mechanisms of PHPs is far from satisfactory. Principal opposition to industrial applications is the lack of phenomenological comprehension of heat transfer mechanism in capillary oscillating flows, especially along the time-varying thin film wetting process.

3.2 Micro-scale two-phase flows

It is very important to understand the difference between the physical mechanisms involved in a macro-scale two phase flow rather than in a micro-scale. For millimetric channels, capillary force becomes non-negligible and starts playing an important role compared to inertia and viscous forces. As the channel diameter becomes smaller, like in micro-channels, surface tension becomes the predominant force. This means effects on the flow pattern transition and, in particular on, the existence and thickness of a thin liquid film on the pipe wall. The film thickness and its length at a given time determine the overall dynamics of the meniscus. It has been observed analysing a non-boiling two-phase flow in a circular channel of 1.5mm diameter, that when a slug reaches a length equal to the capillary channel diameter in which is flowing, the Nusselt number

can rise up to an order of magnitude over the single-phase limit [23]. There is still little systematic information available on the two-phase flow patterns in a microchannel [24][25]. Four flow patterns have been identified in microchannels: slug flow, liquid-ring flow, gas core flow surrounded by a serpentine-like liquid film, and semi-annular flow, but did not observe the dispersed bubbly and liquid droplet flows [26].

A classification based on the channel dimension has been proposed by Kandlikar et al. [27]:

- Macro channels: $D \geq 3\text{mm}$;
- Mini-channels: $3\text{mm} \geq D \geq 200\mu\text{m}$;
- Micro-channels: $200\mu\text{m} \geq D \geq 10\mu\text{m}$;
- Transitional Micro-channels: $10\mu\text{m} \geq D \geq 1\mu\text{m}$;
- Transitional Nano-channels: $1\mu\text{m} \geq D \geq 0.1\mu\text{m}$;
- Nano-channels: $0.1\mu\text{m} \geq D$

This classification, based only on hydraulic diameter, is not useful and merely conventional. The above-mentioned criterion does not take into account the working fluid properties therefore does not reflect properly the influence of the physical mechanism as flow regime transition. More effective is a classification based on the analysis of geometry of the capillary (cross section and diameter), fluid properties and bubble growth, in particular, on the bubble departure diameter. The threshold between macro and micro scale has been sets as the point at which the diameter of a growing bubble reaches the channel dimension before detachment; at this point, only one bubble can exist into the channel and can only grow in length. Beyond this threshold, macro-scale theory is no longer applicable[28].

A classification that includes working fluid properties has been proposed by Cheng and Wu[29] on the base of the Bond number $Bo = g(\rho_l - \rho_v)d_h^2/\sigma$. Bond number is the ratio of the surface tension to the body forces. A high Bond number indicates that the system is relatively unaffected by surface tension. The classification is the following:

- Micro-channel: $Bo < 0.05$;
- Meso-channel: $0.05 < Bo < 3$;
- Macro-channel: $Bo > 3$;

A low Bo number (< 1) indicate that the surface tension is strongly dominating. For practical uses, the capillary limit for the channel diameter is evaluated at ground gravity level by the criterion of $Bo < 4$ formulated by Kew and Cornwell [30].

Rearranging the Bond number equation can be obtained the so-called *critical diameter* of the capillary:

$$d_{crit} \leq \sqrt{\sigma Bo / g(\rho_l - \rho_v)} \quad (3-1)$$

However, defining the right length scale for a transition between macro and micro scale could still not be sufficient. For example, the discussion on Bo number does not consider the additional effect of the inertial forces that affect the formation of the plugs and slugs train. Therefore, it is better to focus on the transition of different patterns of fluid flow rather than on the channel dimension and redefine macro and micro scales as confined and unconfined bubble regimes [31]. More recently, a new semi-empirical transition criterion considering both inertial and viscous effects based on the Garimella Number (Ga) has been proposed [31]: $Ga = \sqrt{Bo} \cdot Re_l \leq 160$ where Re_l is the Reynolds number associated with the liquid phase. The corresponding critical diameter, more suitable for defining the limit for space applications, can be calculated as [32]:

$$d_{Ga} \leq \sqrt{\frac{160\mu_l}{\rho_l U_l} \sqrt{\frac{\sigma}{(\rho_l - \rho_v) \cdot g}}} \quad (3-2)$$

where U_l , μ_l and ρ_l are the velocity, viscosity and density of the liquid phase; ρ_l is the density of the vapour phase, σ the surface tension and g the gravitational acceleration.

When surface tension dominates over gravitational forces, slug flow occurs in mini/micro channels, called Taylor bubble train flow. Taylor bubbles adopt a characteristic capsular shape, with a liquid thin film separating the vapour phase from the wall [33].

3.3 Investigating a two-phase flow in capillary devices

Gas-liquid two-phase flows are very complex physical processes combining thermodynamics, fluid mechanics and heat transfer. They are affected, among other parameters, by a liquid-gas-solid interface, channel shape, flow characteristics (velocity, acceleration and direction). A main categorization of flows is according to the presence or absence of heat transfer: adiabatic or diabatic two-phase flows. In diabatic two-phase flows, phase change can take place: vaporization or condensation.

Phase change can also take place, however, in adiabatic flows due to pressure changes. The direction of the flow marks a distinction too: the role played by gravity in vertical, horizontal and inclined flows is fundamental when the difference in density between phases can be of the order of 10^3 .

A two-phase flow shows some peculiarity if compared to a single-phase or phenomena not unique to two-phase that can become much more complex. In two-phase microchannel flows one important difference with respect to macro-channel flows is that the liquid flow is laminar at most but not all the test conditions, which is quite rare in macro-channel studies. The typical range of interest in microchannel flows are liquid Reynolds numbers from 100 to 4000. Hence, flow pattern transition theories with turbulent liquid flows cannot be expected to apply directly to the similar transition for laminar conditions. In addition to inertia, viscous and pressure forces present in a single-phase flow, two-phase flows are also affected by the interfacial tension forces, wetting characteristics of the combination liquid-tube wall and the exchange of mass, momentum, and energy between the phases. Capillary (surface tension) forces become important in small diameter tubes, eliminating stratification of the liquid and hence channel orientation is at most only of secondary importance in microchannels.

3.3.1 The Critical Heat Flux (CHF)

The Critical Heat Flux (CHF) refers to the heat transfer limit causing a sudden rise in surface temperature. This very large, sudden rise in wall temperature, results most likely in a dry-out of the channel (liquid no longer wetting the tube wall) and the vapour phase is the only responsible for the cooling, with a dramatic drop of the heat transfer coefficient. The coexistence of the two phases does not imply any equilibrium: the gas and the liquid have different average velocities and temperatures.

A large volume of experimental and theoretical studies on the CHF phenomenon have been carried out by many researchers, starting with the work that led Nukiyama [34] in the early 30s to formalize the pool boiling curve, and resulting in numerous empirical correlations and mechanistic models for the definition of the critical heat flux in pool boiling and flow boiling conditions. A review from Hall and Mudawar [35], identified over 100 CHF correlations focused on just subcooled water flow in uniformly heated round tube. Although there is much debate concerning the precise mechanism for flow boiling CHF, researchers concur that, for heat flux-controlled

systems, this phenomenon is associated with a sharp rise in wall temperature and drastic reduction in the local heat transfer coefficient resulting from inadequate liquid access to the wall. Published literature includes numerous CHF databases and empirical correlations for specific fluids, flow geometries and operating conditions. Unlike single-phase correlations, flow boiling CHF correlations often provide inaccurate predictions. An alternative to empirical CHF correlations is to develop mechanistic theoretical models based on a postulated or visually confirmed CHF trigger mechanism.

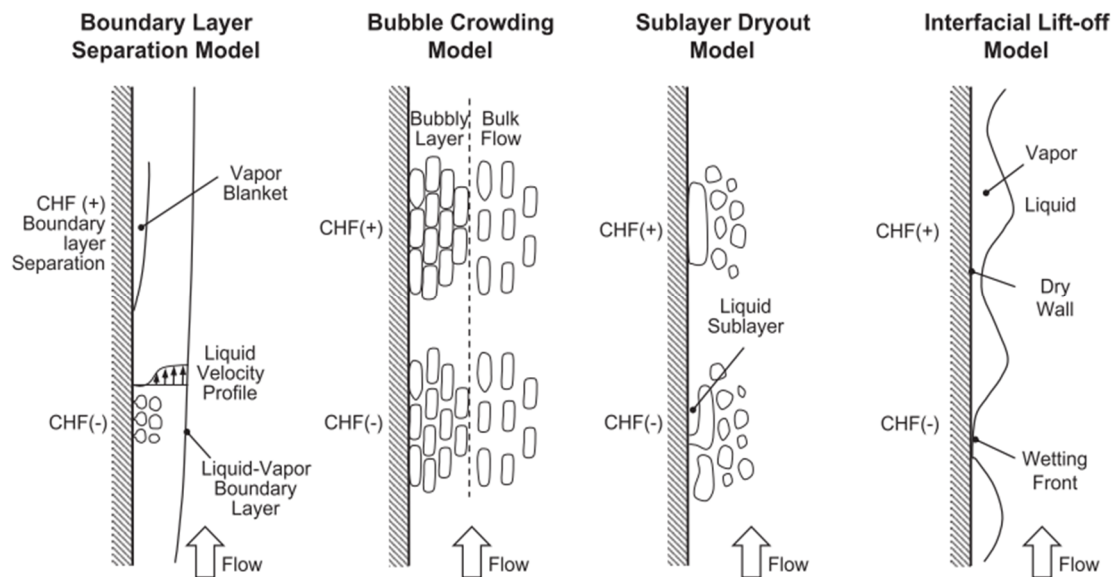


Figure 22 Mechanisms believed responsible of initiating CHF in flow boiling, with local increasing (CHF+) and decreasing (CHF-) of the critical heat flux [36]

In Figure 22, for instance, the main mechanisms believed responsible for the initiating of CHF in flow boiling are presented, with indication of where specific phenomena causes a local non-uniformity in the critical heat flux.

In a PHP, reaching the critical heat flux is quite common during its normal functioning. When this happens for a prolonged period, the vapour stagnates in one or more evaporator curves, with a sudden drop of the heat transfer coefficient that can lead to dry-out conditions, losing the temperature control function of the thermal management system.

3.3.2 Two phase flow instabilities

Another characteristic of two-phase flows is that they often show instabilities that have no equivalent in single-phase flow. As a result, large pressure, flow rate or volume fraction oscillations that disrupt the expected behaviour of the flow can occur.

The classification of two-phase flow instabilities as static and dynamic is most widely used as suggested by Boure' et al. [37]:

- Static instabilities:
 - Ledinegg instability or flow excursion;
 - Critical heat flux or boiling crisis;
 - Flow pattern transitions;
 - Bumping instability;
 - Chugging instability or geysering.
- Dynamic instabilities:
 - Density waves;
 - Acoustic oscillations;
 - Thermal oscillations;
 - Pressure drop oscillations;
 - Parallel channel.

An exhaustive description of the theory of instabilities lies outside the scope of this work even if of high interest for two-phase passive devices like Thermosyphons and Pulsating Heat Pipes. The reader can refer to Kalac and Bon [38] and Ruspini et al. [39] for detailed general reviews and to Saha and Celata for instabilities in microchannels [40].

Dynamic two-phase instabilities are present in a PHP and the number of turns increases the level of internal perturbations. It may be concluded that thermo-mechanical interactions and instabilities in a PHP as well as in capillary sized tubes (mini-micro channels), is quite complex and further investigations are needed. The fact that PHPs are closed systems in which the velocity scale is dependent on the imposed thermal boundary conditions (and is not known a priori) makes it more difficult for analysis.

3.3.3 Useful Non-dimensional Numbers

Non-dimensional groups are useful in arriving at key basic relations among system variables that are valid for various fluids under various operating conditions. A few dimensionless numbers or groups of variables that are very often used will be introduced. For the meaning of letters and symbols, please refer to the Nomenclature.

- Bond number (Bo):

$$Bo = \frac{gd^2(\rho_l - \rho_g)}{4\sigma} \quad (3-3)$$

represents the ratio of gravitational (buoyancy) and capillary force scales. The length scale used in its conventional definition is the pipe radius. When $Bo \ll 1$, gravitational forces in microchannels can be neglected. As a result, the other forces like surface tension force, the gas inertia and the viscous shear force exerted by the liquid phase are found to be the most critical forces in the formation of two-phase flow patterns.

- Capillary number (Ca):

$$Ca = \frac{\mu_l U}{\sigma} \quad (3-4)$$

is a measure of the relative importance of viscous forces and capillary forces. In the case of liquid plugs in a capillary tube, the Ca can be viewed as a measure of the scaled axial viscous drag force and the capillary or wetting force. It controls principally the liquid film thickness (δ) surrounding the gas phase in gas-liquid two-phase plug.

- Froude number (Fr):

$$Fr = \frac{\rho U^2}{\rho g d} \quad (3-5)$$

represents a measure of inertial forces and gravitational forces.

- Reynolds number (Re):

$$Re = \frac{\rho U d}{\mu} \quad (3-6)$$

is traditionally defined as the ratio of inertial to viscous force scales. It is mostly used to determine whether the flow is laminar or turbulent.

- Weber number (We):

$$We = \frac{\rho U^2 d}{\sigma} \quad (3-7)$$

represents a measure of inertial forces to interfacial forces.

3.4 PHP working principles

A PHP behaves as a spring-mass-damper system composed by a train of liquid plugs and vapour bubbles. Complex oscillating motion of working fluid occurs inside PHP. When the liquid plug moves to the evaporating section the heat addition causes the increase in vapour volume and pressure. Under Taylor bubble train flow conditions, the bubble velocity will not be equal to the slug velocity due to the lower friction given by the presence of the thin liquid film. This pressure waves speed difference generates an exciting force. This force helps to start up the oscillating motion and when the liquid plug moves to the evaporation section the plug stops and start to move back. When this spring-mass system disappears, the oscillating motion of the PHP will stop. This can happen when the rise of the heat transfer rate causes an increase in the oscillating motion as well as of the heat transfer and in the velocity field; the length of the liquid plugs on the other hand decreases and when the vapour velocity reach a critical value, the flow pattern changes into an annular flow, caused by the penetration of the liquid plug by the vapour. The train of plugs and bubbles disappears, and the oscillation are no longer present. The PHP reaches its maximum heat transport capability, called the PHP's operation limit [22]. In order to generate the oscillation or the circulation motion, the liquid slug has to be pushed by the vapour plugs; the ideal flow pattern for this kind of behaviour is the Taylor bubble train flow [41]. There is a meniscus region on either end of a slug caused by surface tension at the solid/liquid/vapour interface. Near to the pipe wall, the vapour plug is surrounded by a thin liquid film where the phase change takes place. Also, the meniscus region, between slugs and plugs participates to the phase change heat transfer. Thus, a lot of parameters need to be considered during PHP investigation [21].

Although many PHP designs can be found in literature, the basic classification consists of three planar layouts (Figure 23):

- Open Loop, where the ends of the pipe are closed, not connected to each other. The working fluid is only able to oscillate, not circulate;
- Closed loop, where the ends are joined together, allowing oscillation and circulation of fluid;
- Closed loop with check valve, where one or more check valves are used to force the fluid to circulate in one preferential direction;

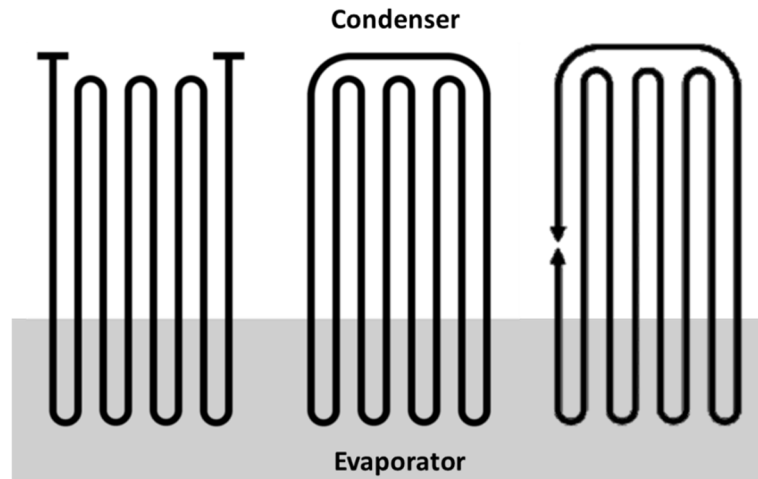


Figure 23 Three configurations of PHP. From left to right: Open Loop, Closed Loop, Closed Loop with check valves

The complex phenomena of evaporation and condensation and the dynamics of the internal flows make it difficult to obtain a clear representation of the heat transfer characteristics of a PHP. However, if we increase the heat power input to a PHP stepwise from cold, the operating regimes observable are now well known, and they can be classified as follows:

- *Pure conduction*: Characterised the heat transfer mode of a PHP not activated, before the start-up, or of a PHP during the last phase of the switching off. Increasing the power load causes an increase of the evaporator temperature, but no fluid fluctuation can be appreciated, resulting in no motion of vapour bubbles and liquid slugs. The pressure at the condenser is stable and corresponds to the saturation temperature;
- *Weak Pulsation*: evaporator and condenser do not show temperature fluctuations. Only some small amplitude pressure fluctuation can be measured, and few seconds can pass between pulsations of relevant entities;
- *Start-Up*: Temperature oscillations are measurable in some of channels; the temperatures at the evaporator does not stabilize, showing increases and decreases linked to stop-over of the fluid alternated to sudden oscillations;
- *Full activation*: the thermal energy provided to the system is now sufficient to cause major thermal instabilities, resulting in strong pressure oscillations, repeated with high time-density. A proper frequency of oscillation is not recognisable, given the chaoticity of the events. All the temperatures at the

evaporator zone decrease abruptly and a vigorous two-phase flow motion can be observed. This motion may have two characteristics, and/or an alternation of the two (Figure 24):

Oscillation: is an alternation of direct and reverse flow with significant amplitude, caused by local thermal instabilities.

Circulation: the fluid has a preferential direction, having a beneficial effect on the heat transfer.

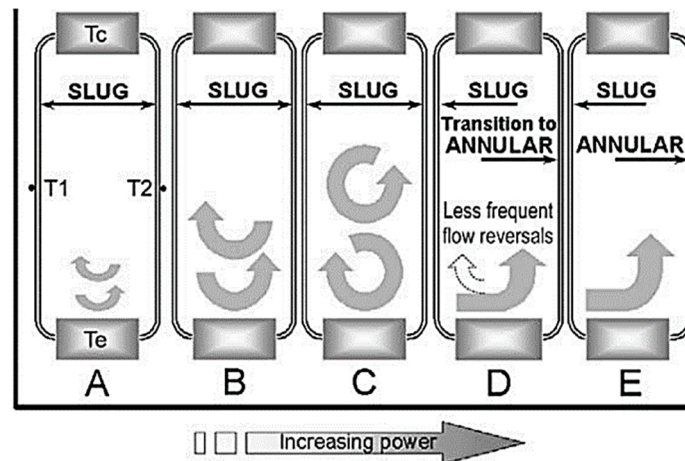


Figure 24 Evolution from oscillating to circulating motion with increasing of power input [42]

When the system is fully activated, and the power input kept constant for a sufficient amount of time (thermal transient), a pseudo steady-state can be achieved. It should be noted that the classical usage of the term ‘steady states’, which refers to truly equilibrium solutions, does not apply to the case of a PHP, that explains the “pseudo”. It is more like a thermally efficient steady state, strongly depending on the whole complexity of boundary and starting conditions. The transient period can last for a few hundred seconds, depending essentially on the thermal inertia of the evaporator (Figure 25) [1].

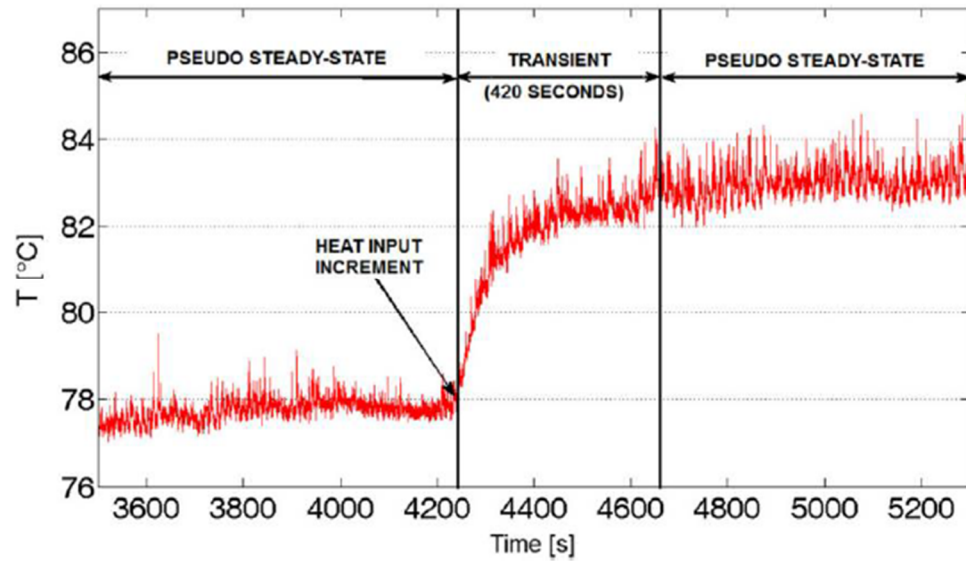


Figure 25 Evaporator temperature during a typical transient behaviour due to a step change in the heat input [43]

- *Dry out*: the thermal energy provided to the PHP is now too high causing the liquid film to evaporate from the evaporator zone, leaving the vapour phase responsible for the cooling, defining the thermal crisis of the system. Evaporator temperatures increase rapidly, causing the failure of the PHP.

The pressure differentials registered during the functioning of a PHP are caused by expanding bubbles in the evaporator and contracting bubbles in the condenser. The system PHP can be considered isochoric with no associated external work. Local control volumes in the evaporator and condenser are involved with work interactions, having reverse signs, with adjoining fluid particles. Heat addition along with ‘positive pumping’ by the expanding bubbles is taking place in the evaporator. In the condenser, the bubbles collapse giving up the heat and in turn do a ‘negative pumping’ work on the adjoining fluid particles. Having this in mind, the features of the thermodynamic cycle described by a PHP have been investigated by Khandekar and Groll [42], who proposed a general terms thermodynamic cycle using a Pressure-Enthalpy (P-h) diagram (Figure 26), based on the outcomes of the investigation of a simplified loop. When the fluid is moving, the vapour quality of the mixture coming out from the condenser X_c is lower than X_e at the outlet of the evaporator. At the same time, the fluid pressure is lower at the condenser compared to the evaporator. The thermodynamic transformation that takes place in the adiabatic zones, is defined as an isenthalpic pressure drop, defining also the inlet conditions for both evaporator and condenser. The complex processes taking place at the evaporator and at the condenser

can be simplified by subdividing into two thermodynamic processes, constant pressure heat addition/condensation and isentropic pumping/ negative isentropic work up by the bubbles.

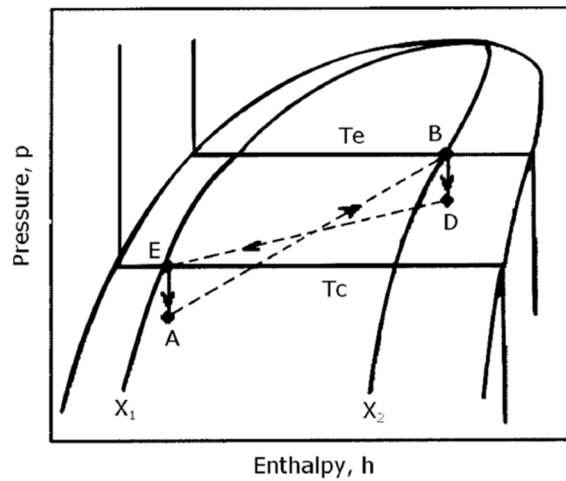


Figure 26 Thermodynamic of a PHP on a Pressure-Enthalpy diagram[42]

3.4.1 The start-up

The start-up mechanism involves the onset of two-phase flow pulsations that allows an estimation of the thermal performance of a PHP. The onset of pulsations at lower heat input depends on the thermo-physical properties of working fluid and it's strongly affected by the initial distribution of phases in the evaporator zone. Under the adiabatic condition, the PHP is in overall thermal equilibrium and all the thermocouples indicate the same initial temperature. Applying heat power to the evaporator, the temperature of the working fluid increases; when this amount is low, there is not sufficient energy to generate vapour bubbles and no pulsation is observed in the PHP. Increasing the heat load, the onset of the oscillation can be observed and associated to fluctuations of the values of pressure. When the onset of pulsation occurs, heat is transferred passively from evaporator to condenser. Therefore, evaporator temperature decreases and condenser temperature increases. Comparing the behaviour of different fluids with the same heat input (Figure 27 [44]), the minimum zone width of steady state condition is observed for acetone and the maximum for water, which has the highest thermo-physical properties and lowest dP/dT ratio when compared to ethanol, methanol and acetone. A high value of dP/dT ratio, reveals that a small change in temperature can generate a large pressure difference, which drives the early pulsation. This is mainly the result of different specific heat, boiling temperature and surface tensions. The high value of surface tension increases the interfacial force which opposes the pulsation in

capillary dimension channels. Therefore, water has a late start-up time, highest start-up temperature and start-up heat input in comparison to other pure fluids. Great impact on the start-up is also caused by the dynamic viscosity; it increases shear stress along the wall and consequently increases pressure drop in the capillary tube, demanding more heat to start the pulsation. The start-up mechanism also requires low capillary resistance. Capillary resistance depends on capillary diameter, contact angles and surface tension.

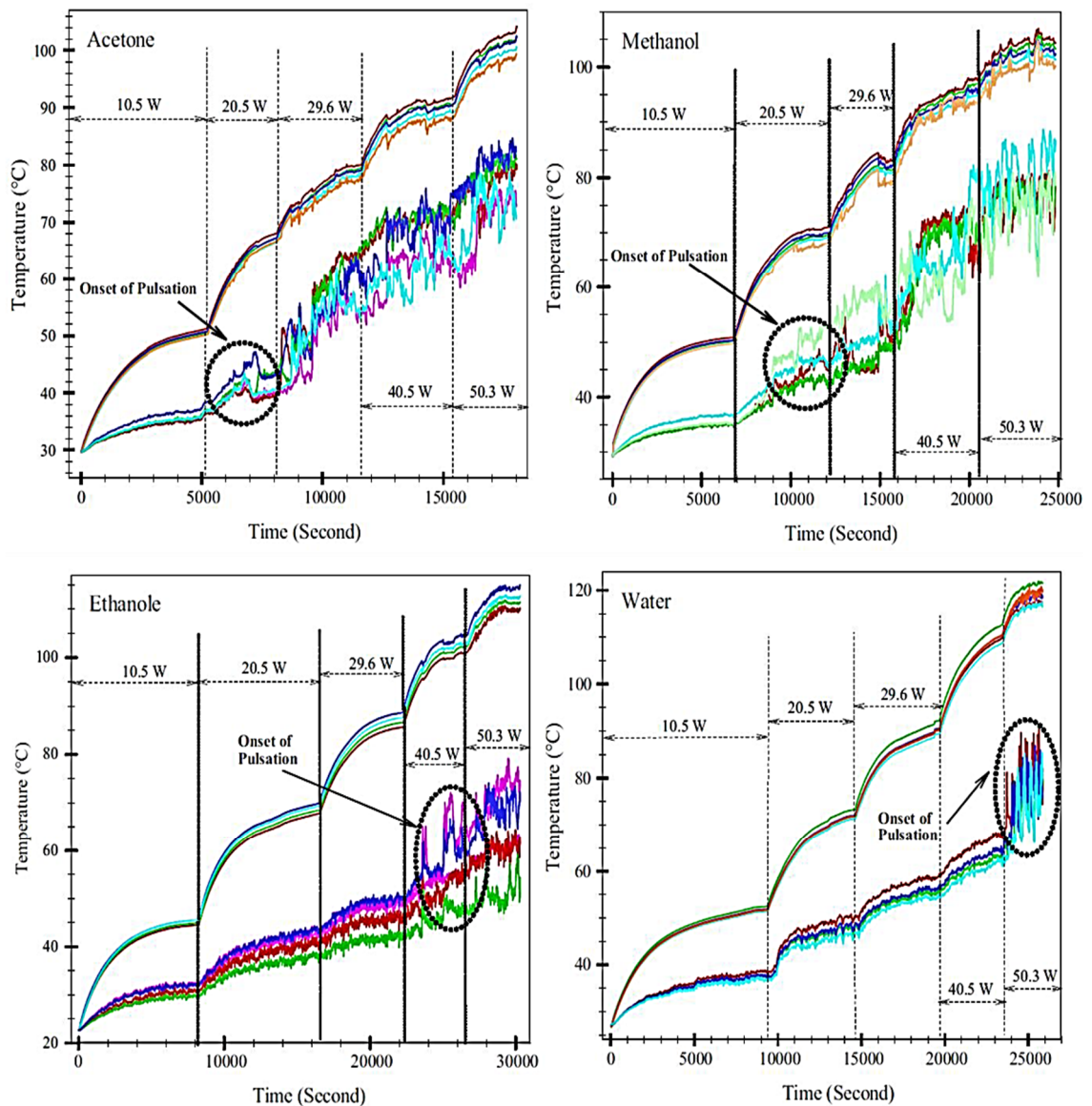


Figure 27 Example of start-up for different fluids [44]

For a fixed combination of working fluid and tube material, the surface contact angles are constant. When the capillary diameter is fixed, the capillary resistance mainly depends on the surface tension of the working fluid. The oscillation inception

in the single-branch pulsating heat pipe [45] and in multi-branch pulsating heat pipe [46] has been investigated numerically by Nikolayev in the presence of the heat conduction along the PHP tube. The start-up power has been observed scaling like the square root of the tube heat conductivity. The liquid viscous dissipation is found to be much less important than the energy dissipation via the fluid and solid heat transfer.

3.4.2 Thermal performance

When in a full activation phase, and a pseudo-steady state has been reached after the transient period (the time-averaged component of the temperature settles), the overall thermal performance of the PHP can be estimated. The thermal performance is estimated as standard by the overall equivalent thermal resistance in [K/W] between evaporator and condenser:

$$R_{eq} = (\bar{T}_{w,e} - \bar{T}_{w,c}) / \dot{Q}_t \quad (3-8)$$

where $\bar{T}_{w,e}$ is the average of the measured values in the zone where the wall temperature reaches its maximum (evaporator) and $\bar{T}_{w,c}$ is the average of the measured values in the zone where the wall temperature reaches its minimum (condenser). Thermal resistance is observed to decrease with increase in heat input irrespective of working fluids. This value can be easily compared with other PHP of different geometry and different working fluid, as reported in the work of Mameli et al. [43]

Table 8 Equivalent thermal resistance for different geometries, reprinted from [43]

Author	PHP geometry	L_{tot} [m]	n [-]	A_{cr} [m ²]	Q_{max} [W]	ΔT_{w-c} [K]	R_{eq} [K/W]
Akachi [13]	Copper tube O.D. 3mm	0.46	160	0.00113	2000	90	0.045
Yang et al.[14]	Copper tube O.D. 3mm	0.12	40	0.00028	400	123	0.3075
Yang et al.[47]	Aluminium Plate	0.18	66	0.00036	400	75	0.1875
Mameli et al.[43]	Copper tube O.D.4mm	0.2	4	5e-5	100	80	0.84

Referring to Table 8, L_{tot} is the distance between the heat source and the heat sink, n is the number of turns, $A_{cr} = \frac{n\pi d_{OD}^2}{4}$ is the total PHP cross-section.

As stated before, the overall thermal resistance can be estimated only after the end of a transient period, when the temperature has settled. From what is presented in

Chapter 3, it can be argued that the available micro-g period obtained throughout a parabolic flight is not enough to define an overall thermal resistance. In fact, 20s of μ -g are not sufficient to lead the fluid through the start-up phase and reach a full activation. The absence of an overall motion in the PHP, will return a value of equivalent thermal resistance with a lower limit identified only by the conduction phenomena in the solid domain of the tube and in the liquid domain of the working fluid.

3.5 Parameters affecting the functioning of a PHP

The oscillating motion and therefore the thermal performance of a PHP are affected by numerous parameters, including the following:

Working fluids specifics

- Filling Ratio (FR, percentage of the PHP volume occupied by the working fluid): It has been established that the zone of interest for a PHP operation is achieved when the FR is between about 20 to 80% [48]. Below a 20% FR, there are not enough distinct liquid plugs and the operation becomes ‘unstable’ resulting in large unacceptable variations in the average evaporator temperature. Above 80% there are not enough bubbles to provide the pumping action and so the performance drastically deteriorates.
- Surface tension: Surface tension is necessary for the formation of the liquid plugs and vapour bubbles in the pipe [49]. Fluids with higher surface tension cause an increase of the maximum allowable diameter but also increase the capillary pressure in the tube. Larger diameters will allow an increased mass flow rate and consequently an increased heat transfer rate. An increase of the capillary pressure, on the other hand, requires greater bubble pumping and thus a higher heat input to maintain the pulsating flow [50];
- Latent heat of vaporisation: A low latent heat causes the liquid to evaporate more quickly at a given temperature and a higher vapor pressure, facilitating the start-up process. The liquid slug oscillating velocities will be increased, improving the heat transfer performance of the PHP; but the dry-out will occur at an earlier stage compared to a high latent heat of vaporisation fluid [51];

- Specific heat: A high specific heat will increase the amount of sensible heat transferred. Because a great share of the total heat transfer in a PHP is considered due to sensible heat, a fluid with a high specific heat is desirable[51]. On the other hand, with a low specific heat value, a shorter time of heating is required for the working fluid to reach superheat and boiling, resulting in a faster start-up with a lower maximum temperature reached [52];
- Viscosity: A low dynamic viscosity will reduce shear stress along the wall and will consequently reduce pressure drop in the tube. This will reduce the heat input required to maintain a pulsating flow;

Geometrical Design of the PHP

- Number of turns in the PHP: This affects thermal performance [53] and may negate the dependence from gravity [54]. By increasing the number of turns, there are more distinct locations for heat to be applied, increasing the thermodynamic instabilities that promote the fluid movement. In fact, if the number of turns is too small, there is a minor alternation of hot and cold zones and a reduced presence of local pressure drops (the driving force acting on the fluid). When the number of turns is increased, the PHP is able to work also in the horizontal heat mode, its thermal resistance decreases and there are less evident differences between working fluids in terms of overall efficiency, as numerically investigated by Mameli et al. [55]. For practical application, a low number of turns should be avoided [43], Depending on the inner diameter and on the evaporator temperature, a number of turns greater than 14-16 tends to guarantee complete independence from the gravity level.
- Size of condenser and evaporator: Can affect the overall heat transfer of the PHP and change in the flow patterns. Below a particular activation heat flux from the evaporator, the fluid in the PHP will not pulsate. If the condenser is under-dimensioned, designed with a capability not sufficient to dissipate the max heat input intended for the PHP, the range of functioning of the device will be reduced by early dry-out phenomena. For a fixed filling ratio and heat input condition, reducing the length of condenser within would accelerate the start-up process and decrease the thermal resistance while the dry-out occurred easily at low filling ratio [56].

- Effect of tube inner diameter: Sufficient small inner diameters establishes a slug-plug flow. Decreasing the inner diameter, the effect of surface tension on the slug/plug flow and thermal performance increases, while the effect of gravity becomes relatively small and even insignificant [57]. Beyond a specific limit, the working fluid will tend to stratify under the effect of gravity and the device will stop functioning as a ‘pulsating’ heat pipe, behaving like a closed two-phase thermosyphons [58].

Heat power input

When working fluid and geometrical parameters have been defined, the resulting flow pattern is directly related to the heat input. Power input strongly affects the overall thermal performance of a PHP because plays a key role in the following phenomena:

- Vapour bubble size and velocity
- Flow instabilities
- Bubble break up
- Evaporator dry-out

Surface characteristics

- Wettability: The effect of pipe internal surface property, has a potential crucial role on the thermo-fluid-dynamic performance of an oscillating meniscus device. A small contact angle is shown when the liquid spreads on a surface. When the contact angle is $<90^\circ$ a liquid film is wetting the surface (hydrophilic) while when the contact angle is $>90^\circ$ a liquid film is not spreading on the surface (hydrophobic). The wettability of a solid surface is affected by two factors: the surface energy and surface roughness. The surface energy is an intrinsic property of a material that can be controlled by chemical modification. In a hydrophobic channel, the capillary forces will resist the flow of the liquid. For the hydrophilic case, the gas bubble slides over the liquid film reducing the energy dissipation. A PHP function with a super-hydrophilic chemical treatment of the entire device has been tested, showing an increase in thermal resistance compared with the non-treated case [59]. A hybrid treatment, with super-hydrophilic evaporator and super-hydrophobic condenser, presented a

stronger oscillating motion in comparison with that of copper PHP [60]. In this case, the thermal resistances of the functional PHP was found to be reduced by about 5-20%.

Working fluid and filling ratio significantly affects the maximum heat transfer capability, known as operating limit. When a PHP receives an increasing amount of heat, the internal vapor pressure subsequently increases. If this vapor pressure is too high, the liquid slugs will be retarded and prevented from returning to the evaporator section, causing the internal thermal resistance to increase rapidly. Therefore, the heat from the evaporator cannot be transferred to the condenser section, causing dry-out in the evaporator section. The state at which dry-out occurs is called critical state. The connection between the critical heat flux increase with an increase in the latent heat of vaporization of the working fluid has been highlighted [41]. A completely filled PHP (FR = 1) is identical in operation to a single-phase thermosyphon; only very few bubbles are present, not sufficient to generate the required fluid motion. Within the operating range of the filling ratio various flow patterns may exist depending on the boundary conditions. The effect of dimensions, working fluid, filling ratio and heat flux level on operating limit has been extensively investigated. For a given working fluid with the same filling ratio, same total tube length but different number of turns of the PHP, the operating limit increases with the number of turns increase. Also, the working fluid and filling ratio significantly affects the operating limit. Working fluid with low volumetric filling ratio FR (30-40%) occupies a small volume of the PHP.

Table 9 Effect of dimensions, working fluid and filling ratio on operating limit

Author	PHP Description	Dimensions	Working fluid	Filling ratio	Operating limit
Cao et al. [61](2004)	Flat PHP	180x54x4	FC72	20%	60W
Cao et al. [61](2004)	Flat PHP	180x54x4	FC72	30%	110W
Yang et al. [14] (2008)	Copper 20 turn PHP, BHM	I.D. 1mm	R123	50%	390W
Yang et al. [14] (2008)	Copper 20 turn PHP, BHM	I.D. 2mm	R123	50%	540W
Ji et al. [62] (2014)	Copper 6 turns PHP, BHM and HHM, Operating temperature: 20°C and 60°C	I.D./O.D. 1.65/3.18	Water	From30%to70%	600- 900W
Ji et al. [62] (2014)	Copper 6 turns PHP, BHM and HHM, Operating temperature: 20°C and 60°C	I.D./O.D. 1.65/3.18	HFE7100	From30%to70%	300- 400W

Too little mass is not able to carry appreciable amount of heat from the evaporator to the condensing section. When the FR is too high (>80%) and the heat load is low, the PHP is not able to reach the activation; on the other hand, when the heat load is high, too many bubbles are generated, and the higher pressure impedes the liquid plugs to move toward the condenser. The optimum FR of a PHP may vary with: number of turns, length and inner diameter. The heat transfer capability of an PHP is affected by the heat flux level, due to the stronger oscillating motion generated by higher power input and the consequent thermo-hydraulic instabilities.

3.5.1 Performance of a tilted PHP

The performance of a PHP, in terms of overall thermal resistance, can be heavily affected by the inclination of the device, especially for simpler designs as shown in Figure 28. Charoensawan and Terdtoon [63] found that the evaporator length does not have any effect on the thermal performance of an inclined PHP, but a minimal number of turns is needed to operate in the horizontal position.

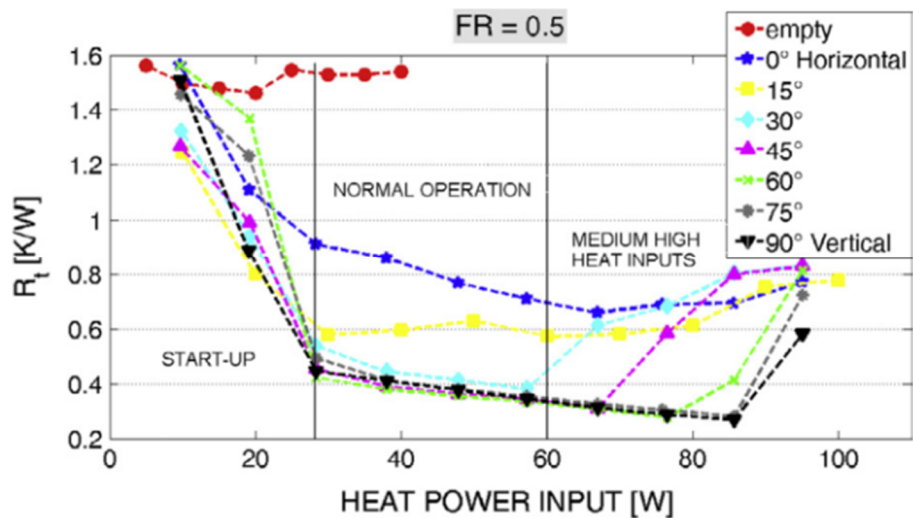


Figure 28 Effect of inclination angle from Vertical (90°) to horizontal (0°) for a 1.1mm PHP filled with FC-72 (50% FR) [48]

A tilting angle means a different degree of assistance from gravity forces. One of the aims of good CLPHP design is to make the thermal performance, as far as possible, independent of the operating orientation. The way orientation affects heat transfer performance can be alleviated with appropriate design consideration: increasing the number of turns and decreasing the channel diameter has been proven lessening gravity dependence, increasing the pressure perturbations. In addition, the input heat flux is

also a strong parameter, which affects dynamic instability and a series of test with different inclination of the PHP has been performed as reported in Table 10.

Table 10 Effect of orientation on PHP performances

Author	PHP Description	Working Fluid	Orientation Effects
Khandekar et al. (2002) [64]	3xFP-CL-PHP set-ups machined into aluminium substrate and covered with a glass plate; #1: 2.2 x 2mm ² , 11 turns; #2: 1.5 x 1mm ² , 11 turns; #3: Circular 2 mm, 9 turns;	Water Ethanol	Vertical Operation: (1) Largest d _{hyd} (2mm) shows the highest heat throughput at the lowest thermal resistance; (2) Rectangular cross section has lower thermal resistance than circular cross section although both have the same d _{hyd} ; (3) Circular cross section has lowest heat transport capability but a small thermal resistance; Horizontal Operation: (Between 5° to 15° to horizontal) Any kind of oscillations stop; Heater dry out and steep increase in thermal resistance.
Chien et al. (2012) [65]	2xCopper FP-CL-PHP #1: Uniform diameter, 16 channels 2x2mm ² ; #2: Non-uniform diameter: 8channels 2x2mm ² + 8 channels 1x2mm ² ;	Water; FR from 40% to 70%;	4 inclination tested: HHM (0°), 30°, 60°, BHM (90°); At lower power input, gravity adversely affected the performance (for 30°, 60°, 90°); Uniform channel PHP is more sensitive to inclination compared to non-uniform.
Hathaway et al. [66] (2012)	2-layer PHP with uneven turns: Evaporator: 20 turns; Condenser: 14 full turns + 6 half turns;	Water; Acetone	The uneven 2-layer channels can start the oscillating motion in THM ¹ even though at low power did not perform as well as in the BHM; Both water and acetone PHPs were able to reduce the effect of gravity on heat transport capability;
Mameli et al. (2014) [48]	CLPHP 31 turns I.D. 1.1 mm,	FC-72; FR 50% and 70%;	The CLPHP in the horizontal position is less effective, but it does not undergo any performance drop until the maximum heat input level is reached; The start-up regime ranges from 10W to 20W without a clear dependence on the tilting level (gravity head); The effect of gravity is less evident for FR 70%

3.6 Role of the liquid film

The liquid–vapour interface controlled by the surface tension and meniscus radius plays a fundamental role in fluid flow and thus in heat transfer of a capillary based devices. The heat provided to the solid substrate of the two-phase cooling device, is conducted through a thin liquid film to its free surface to take advantage of the high heat transfer rates associated with phase change at the liquid-vapour interface. Starting

¹ THP: Top Heating Mode

from initial equilibrium condition, the heating process may lead to a disruption of the interface equilibrium, characterised by rupture or collapse of the thin film structure upon the solid wall [67]. The combination of factors governing the instability of an evaporating liquid film have been analysed by Polansky et al. [67] and Sefiane et al. [68]:

- Mass loss due to evaporation;
- Long-range molecular forces;
- Vapour recoil is due to a non-uniform pressure acting down on the liquid-vapour interface [27], forcing the liquid towards the wall and amplifying the disturbance. Vapour recoil effect could be neglected in case of moderate evaporation rates;
- Thermo-capillarity: a temperature gradient arises when there is a spatial change in the thickness of the interface. As a consequence, a surface tension instability arises (Marangoni Instability);
- Viscous forces;
- Geometric constrains.

Gravitational effects and liquid inertia are estimated to not affect the process, given the small flow rate involved and the scales of the phenomenon. Capillary forces have been defined as the principal stabilising mechanism. These can force the system back towards an equilibrium condition as their intensity increases with a reduction of the thickness of the interface. A similar rolling cell structure is observed during Bénard-Marangoni fluid instability. A second potential stabilising mechanism is the local cooling of the regions with reduced film thickness given by an excess of evaporation, resulting in a reducing vapour recoil and thermocapillary effect. The dynamic of the liquid film can be estimated coupling experimental information on temporal movement of the triple line and signals from sensors placed in the vapour zone with the adoption of the ideal gas equation, given the superheated condition in that zone [28].

3.6.1 Dynamics of menisci

Vapour plugs and liquid slugs are not symmetrical. Under capillary conditions, the slug flow encounters additional friction (the capillary resistance), due to the capillary pressure difference between the plug front (advancing meniscus, in the moving direction) and the plug end (receding meniscus, against movement). This pressure

difference is given by the two different curvatures (Figure 29a), resulting in dynamic contact angle hysteresis [29]. Water for instance ($\sigma = 0.0072$ N/m at 25° C), when flowing into a 2 mm internal diameter glass capillary tube, has to overcome an additional capillary resistance of $F=0.26 \cdot 10^{-3}$ N, given $\alpha_{front}|_{dynamic} \approx 80^\circ$ and $\alpha_{back}|_{dynamic} \approx 42^\circ$. For ethanol, the two dynamic contact angles are about the same and less than 10° ; in this case the capillary resistance is negligible. In a train of slugs and plugs (Figure 29b) this phenomenon is amplified because the resistance is additive and therefore the combination of fluid-solid determines the cumulative pressure gradient to overcome [31].

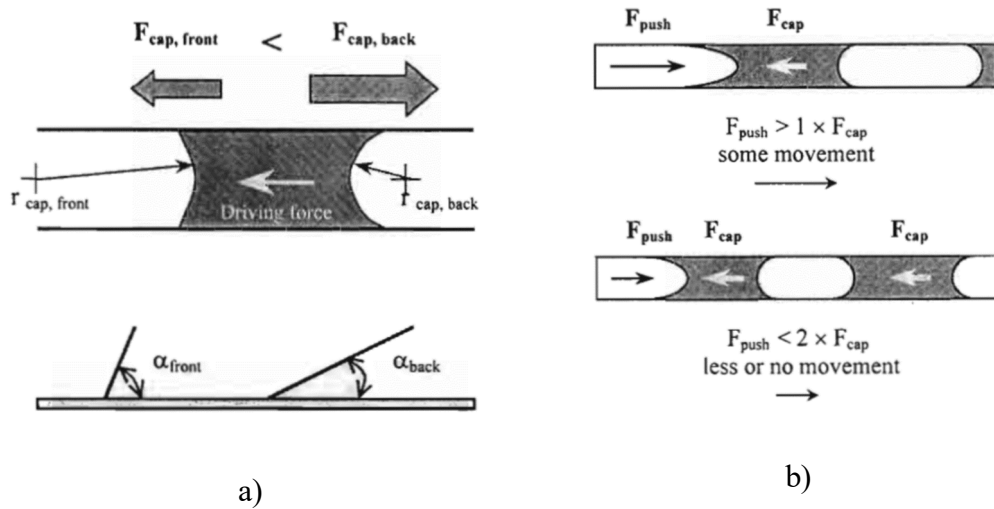


Figure 29: a) Capillary resistance due to dynamic contact angle; b) Influence of several plugs in a tube on resistance to movement [69]

In the experimental work conducted by Srinivasan et al. [69], the dynamics of a single, small and partially wetting liquid plug (with known length L and wettability), pushed by a flow of injected air inside a long, dry, circular capillary tube has been investigated in order to assess the effects of capillary pressure difference on oscillation. The dynamic advancing and receding angles resulted being weakly related to the length of the liquid plug and a major contribution to the total pressure drop is due to the contact angle hysteresis.

3.6.2 Observing oscillatory component

Evaporator and condenser wall temperatures follow the fluctuations of vapour plugs and liquid slugs and operating conditions of the PHP, such applied heat flux, liquid filling ratio, two-phase flow distribution influence the oscillation amplitude and

frequency. The amplitude of the oscillations not only depends on temperature difference between heat sink and heat source but also on the absolute temperature levels and heat input. For a range of temperature, the oscillations are quasi-static, and these oscillations become more regular in period as the temperature gradient (ΔT_{e-c}) decreases. Three stages of flow oscillations are generally observed while the heat load is increased, each one with a peculiar frequency spectrum:

- a) Low amplitude oscillation
- b) Oscillation
- c) Unstable oscillation with circulation and direction reversals
- d) Unidirectional flow circulation

An oscillatory component is sometimes overlapping the circulating component resulting in a case of circulating flow with local flow direction switch [70]. Experimental studies have been performed for the characterization of the frequency content of steady state of thermal oscillations on different geometries PHPs combined with a wide range of operating conditions (working fluid, heat input, filling ratio and inclination). Several studies have shown that a rise in the heat flux increases the chaotic nature of the overall motion, because there is no clear frequency of the oscillation. No regular oscillation has been detected from the frequency spectrum of the pressure signal in the work of Mameli et al. [43]² done on a full scale PHP. Some researchers (Cai et al. [71]), found a connection between the viscosity of the working fluid and the temperature fluctuation of the self-sustained flow in PHPs, observing frequency increase for low viscosity fluids.

An experimental investigation on a single channel in conditions very close to the actual functioning of a PHP has been carried out by Lips et al. in 2010 [72] on a flow consisting of only one oscillating liquid slug. The test bench, shown in Figure 30, is comprised of two tanks connected by a 2.4mm I.D./4mm O.D glass capillary tube. A variable frequency electric motor imposes a quasi-sinusoidal volume variation on the vapour pentane contained inside the upstream tank, whereas the downstream tank is filled liquid pentane in equilibrium with its vapour phase. The flow is visualized by means of a high-speed camera. This single tube experimental campaign has been

² The same FFT analysis has been conducted in this research work on a different device (Single Loop Pulsating Heat Pipe) with different working fluids (Ethanol and FC72) under varying gravity level (Parabolic Flight) and power input (9W up to 30W) with no univocal oscillation frequency shown, as observed by Mameli in [43].

carried out to highlight, and in some cases reveal, phenomena that are usually overlapped with others when they occur in real PHPs, but whose analysis is easier in a single tube.

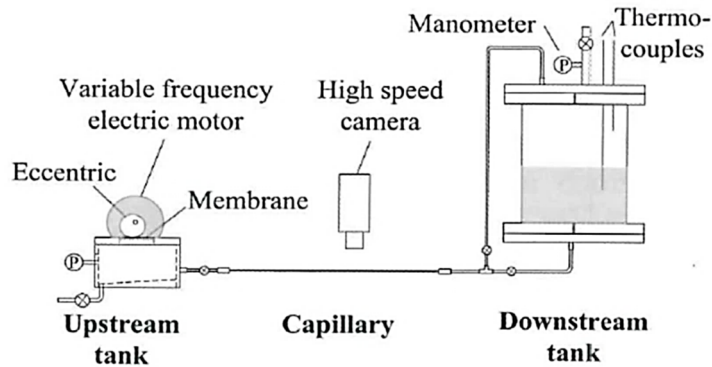


Figure 30: Experimental set-up for investigation of capillary pressure difference effects on oscillations [72]

The main outcome of the mentioned work is related to the importance of taking into account the differences between the advancing and receding meniscus radii surrounding the liquid plug in advanced models, because the induced capillary pressure difference is of the same order of magnitude as the friction losses. Another interesting phenomenon observed is the presence of instabilities wavelet-type in the region of the advancing meniscus. The authors linked the generation of the instabilities to a critical velocity and they suggest further investigations on the effects of the wavelet instability on evaporation and stability of the vapour bubble. Most correlations are available for steady motion of the meniscus of wetting fluids at low Capillary number (Ca), a correlation for a meniscus moving with at constant acceleration has been proposed taking into account the effects of Bond number (Bo) by Han and Shikazono [73]. The assumption of constant meniscus acceleration is however quite restrictive and leads to an empirical correlation bias of $\pm 15\%$ when evaluated in the most appropriate region to apply this equation, when the meniscus commences its downward journey, laying the liquid film in the heat source section. It is able to give reasonable estimations when compared with complex models. With evaluation of Bond number (Bo) and Capillary number (Ca), the initial film thickness is in the range of 80-90 μm .

3.6.3 Evaporation and condensation associated with a self-sustained thermally driven oscillation

Referring to the set-up presented in Figure 31, the experiments provided the instantaneous location of the meniscus inside the capillary tube during a full cycle of its self-induced oscillatory motion between the maximum height reached in the evaporator (L_e) and the minimum height reached at the condenser (L_c), starting from an intermediate position 0 and back. Four contributions to the total vapour mass have been identified and their variation is depicted in Figure 32 together with the correspondent position of the interface in the channel (black line in Figure 32). The four contributions can be described as follows:

- *Condensation at the meniscus*: the vapour temperature at the meniscus does not vary considerably and the difference between T_{sat} and T_C remains nearly constant resulting in an almost linear contribute. This mass contribution is negligible compared to others;
- *Condensation at the liquid film*: it is a critical and highly variable component. When the heat sink section is completely full of fluid its contribution is zero, while it reaches its maximum when the liquid film length deposited on the wall of the cooling section is high (meniscus at the bottom position);
- *Evaporation at the triple-line*: significant contribution considered almost constant;
- *Evaporation/Condensation between the liquid film and the vapour*: component highly dependent on the position of the meniscus inside the capillary tube.

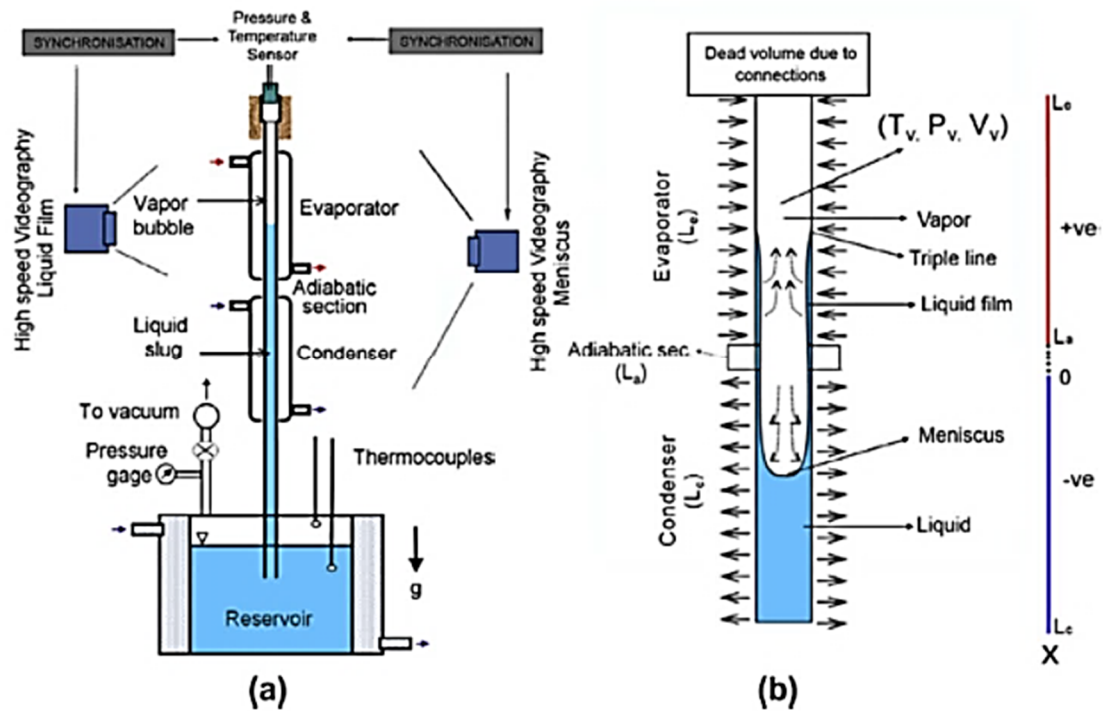


Figure 31: a) Schematic of the experimental set-up for self-sustained thermally driven oscillating flow in a “unit-cell”; b) Unit-cell details and relevant parameters [74]

The bottom position of the meniscus corresponds to the highest vapour mass rate, while tends to zero or became slightly negative (condensation rate is higher than evaporation rate) when the vapour is being compressed at the topmost position by the upward moving meniscus. During each of these cycles, the thickness of the liquid film in the evaporator is varying from a constant value δ_0 , when the meniscus begins its journey towards the condenser, to zero at the end of the cycle.

Interfacial dynamics of the oscillations that arise during the unsteady behaviour of PHP are a fundamental parameter to investigate, directly linked with the nature of the liquid film laid by the meniscus while moving away from evaporator. Referring to the experiments conducted by Rao et al. [74], the downward motion of the meniscus from the heat source to the heat sink is responsible of a large vapour generation obtained from the liquid film laid down on the tube wall, as previously described.

The meniscus carries out one full stroke along the whole tube followed by two incomplete strokes limited to the heat sink area because it is not able to re-enter the heating section until the liquid film is completely evaporated. The meniscus dynamic is depicted in Figure 33, and the highest value of pressure is not reached when the meniscus is at the top-most position (point E) but at the point J, just before the meniscus enters into the condenser.

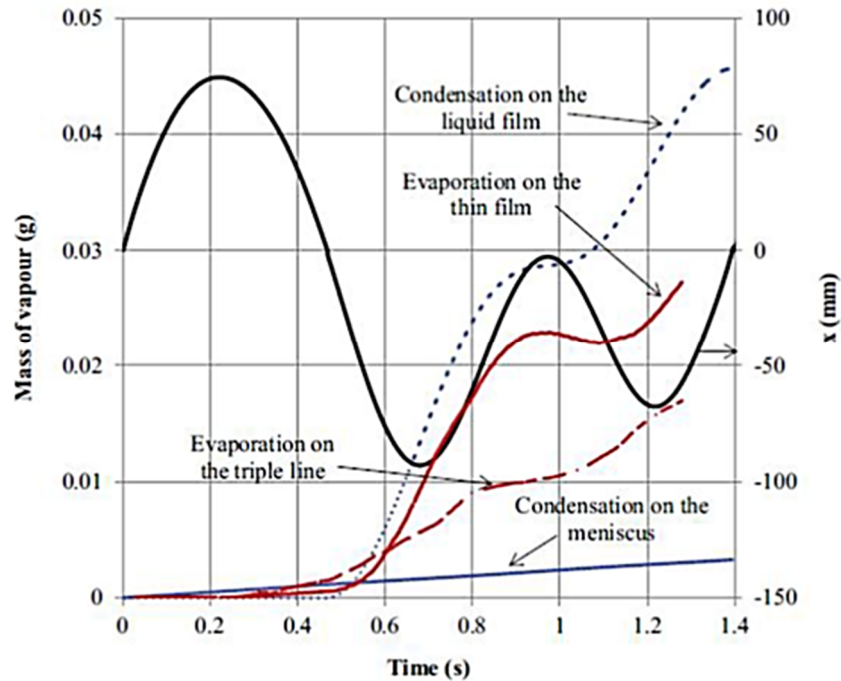


Figure 32: Variation of vapour mass during one cycle of induced oscillation, separating the four different contributions, and position of the interface in the channel [74]

The system cannot thus be compared with a gas compression cycle. When the meniscus is moving downwards the pressure begins to decrease due to the combined effect of vapour bubble expansion and vapour condensation and the meniscus reaches the first bottom-most level (point M). During the next up-ward period (N-P) the pressure rises again implying a residual vapour production from the remaining liquid films that overcomes the rate of liquid condensed. The presence of liquid film in the evaporator area force the meniscus downwards again (P-R) until the evaporation process is complete and the vapour pressure is too low to obstacle the meniscus rise. This cyclic process is repeated with regular repeatable oscillations.

It is therefore clear the key role of the thin liquid film and of the evaporation phenomena on the thermal auto-oscillation of the meniscus. The lifespan of the liquid film in the heating section is rather long compared to the entire time of the oscillation and the remnants of evaporating liquid restrict the entry of the meniscus in the evaporator pushing it back to the heat sink section. The complete process of film appearing and vanishing, takes typically a period between 1.0 and 1.4 s.

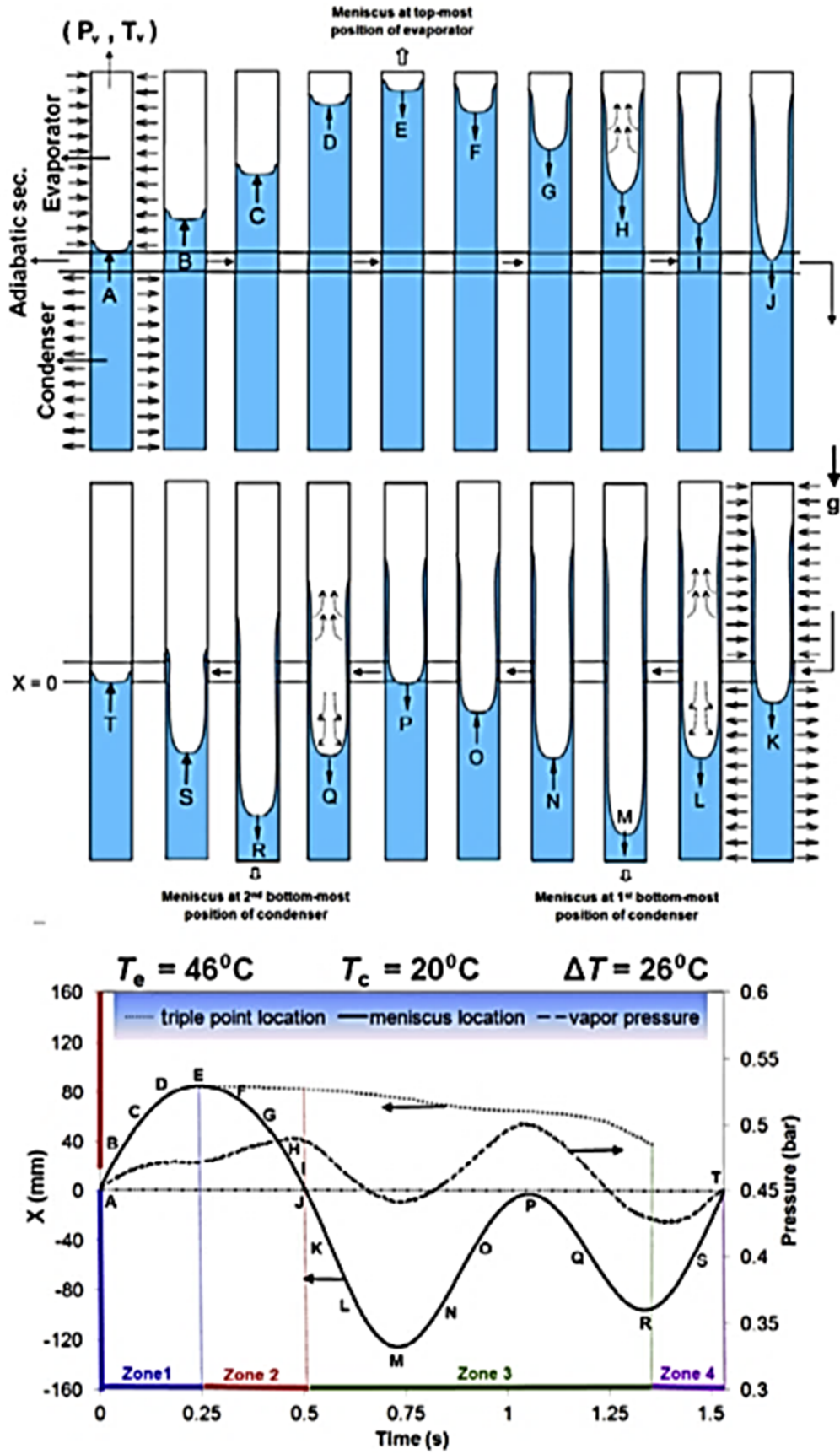


Figure 33: a) Schematic of one cycle of the meniscus motion b) Time evolution of the meniscus position related to the pressure field [74].

3.7 PHP research for Space applications

For a PHP to operate, the inner diameter must be sufficiently small so that the vapour phase can form vapour bubbles and the liquid phase encapsulated between two vapour bubbles along the axis of the tube and a liquid film between the tube walls. The maximum channel diameter that can allow the slug-plug in reduced gravity should increase compared to on ground operation, given the increasing role of surface tension. Starting from the Bo number, a balance of forces for reduced gravity has been proven predicting unrealistic high channel diameters (e.g $d_{crit} = 15\text{mm}$ at $0.01g$ and 150mm at $10^{-4}g$ for R114), and it could wrongly lead to the assumption that a PHP can operate with any diameter in micro-gravity.

The first investigation of the effect of reduced gravity on the functioning of the PHP has been performed by Gu et al.[75] with an aluminium flat plate PHP $250 \times 60 \times 2.2$ mm with a 1×1 mm cross section and filled at 50-60% with R114 as working fluid. The serpentine pattern is composed of 48 turns at both ends. In this work, the PHP tested in vertical and horizontal orientations, support the hypothesis that the PHPs with larger channel diameters can operate under microgravity.

The lack of buoyancy in μg leads to a simpler flow pattern than those on the ground: only three main two-phase flows have been reported to exist under μg [2]:

- Bubbly;
- Slug;
- Annular/Semi-flow;

The work of Mameli et al.(2014) [76] investigated for the first time the transition of regime due to the change of gravity and the complex interplay of gravitational field, inertial forces and viscous forces, showing the possibility to exploit the micro-gravity to increase the diameter of a PHP for higher heat transfer rates.

These considerations opened the way to a novel concept of PHP, a hybrid thermosyphon/PHP with a diameter bigger than the static threshold level on ground and around the dynamic threshold level in microgravity conditions. The first attempt of testing such a hybrid device has been made by Mangini et al. (2015) [32] and by Mameli et al. (2016) [58]. The result is a device that works on ground as a Closed Loop Two Phase Thermosyphon, where the fluid flow motion is due to the “bubble lift” principle:

- The expanding vapor phase pushing batches of fluid (both liquid and vapor) towards the condenser section
- In the cooled zone, vapor condenses and the tube is completely filled by the liquid phase that is returned back to the evaporator by gravity.

During microgravity periods, it operates instead in a completely different way: a transition from the Thermosyphon mode to the PHP working mode is detected. A slug/plug pulsating flow is observed also when the PHP is in the horizontal position. Figure 34 describes the change in working principles due to the effect of internal diameter and, for a fixed diameter, of the gravity level.

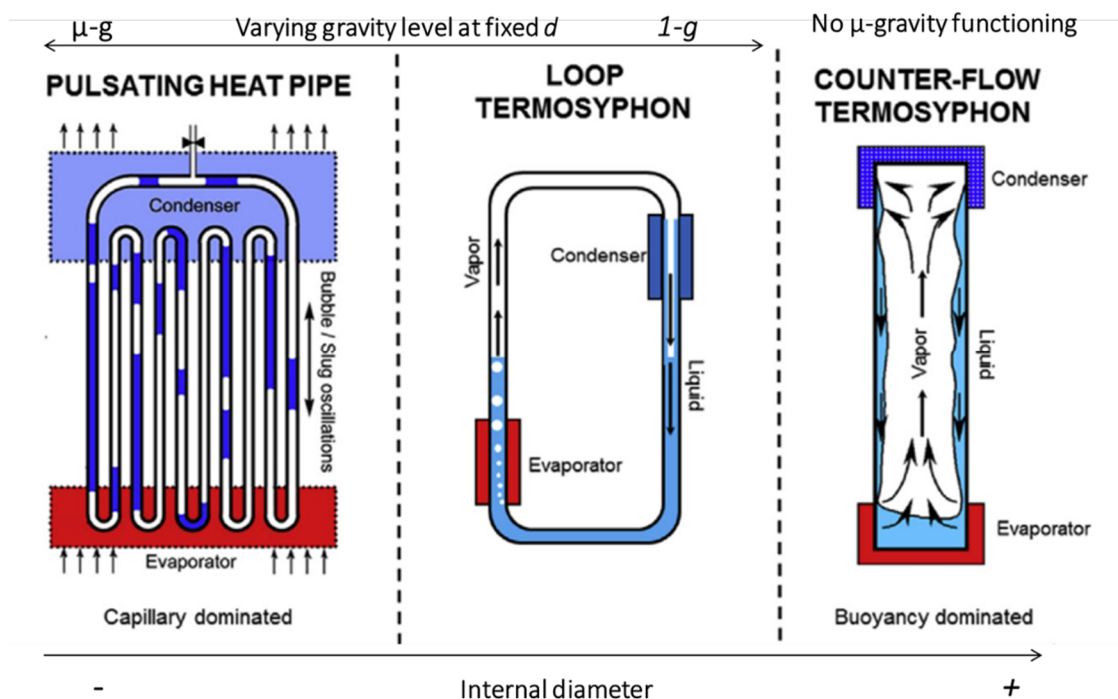


Figure 34 Wickless heat pipe working principles variation increasing the internal diameter and decreasing the gravity level

The role of the hyper-gravity phase ($\approx 2g$) has been investigated and proved to assist the flow motion, helping in re-activating the fluid motion after a dry-out [77]. The hyper-gravity period is able to eliminate partial dry-outs restoring the correct operation until the occurrence of the next microgravity period, highlighting a limit given by the nature of parabolic flight as a platform for short reduced gravity investigation.

Table 11 Relevant works done on PHP in Micro-g and Hyper-g

Author	PHP Description	μ g Platf. ³	WF	Main Outcome
Gu et al. [75] (2004)	Aluminium Flat PHP (250×60×2.2 mm 1×1mm cross section)	PF	R114	<ul style="list-style-type: none"> • PHPs can operate satisfactorily under long-term microgravity
Mameli et al. [77] (2014)	Copper tube PHP (I.D./O.D. 1.1 mm/2.0 mm) bended into a planar serpentine (32 parallel channels)	PF	FC-72	<ul style="list-style-type: none"> • 20s of μ-g are not enough to make statements on the PHP thermal performance, but only about its thermal dynamic response • Hyper-gravity slightly assists the flow motion, while during microgravity the PHP undergoes sudden temperature increase in the evaporator zone • The thermal dynamic response to the occurrence of micro-gravity resembles the thermal dynamic response of a vertical-to-horizontal manoeuvre on ground
Mangini et al. [32] (2015)	Aluminium Hybrid Thermosyphon/PHP (I.D. 3mm)	PF	FC-72	<ul style="list-style-type: none"> • The device switch working principle from Thermosyphon to PHP while in μ-g • During μ-g, slug/plug pulsating flow is observed also in horizontal position
Ayel et al. [78] (2015)	Copper Flat Plate PHP (1.6x1.7mm cross section, 12 bends)	PF	FC-72	<ul style="list-style-type: none"> • The device reaches a μ-g steady state regime in 22s • The device tested in horizontal is not influenced by variation of gravity level
Creatini et al. [79] (2015)	2 aluminium PHP tested: Large diameter (3 mm/5 mm I.D./O.D., double layer 14 turns); Small diameter (1.6 mm/3.2 mm I.D./O.D.)	SR	FC-72	<ul style="list-style-type: none"> • A malfunctioning in the de-spin system didn't allow to reach μ-g conditions • Small diameter PHP: hyper-gravity conditions have a beneficial effect on the overall thermal performance with respect to horizontal orientation; • Large diameter PHP: hyper-gravity conditions have a negative effect. Device more sensitive to the centrifugal acceleration due to stratification
Nannipieri et al. [80] (2017)	Aluminium PHP (3 mm/5 mm I.D./O.D., double layer 14 turns)	SR	FC-72	<ul style="list-style-type: none"> • All the temperature signals (evaporator and condenser) exhibit an oscillating component for the whole zero gravity duration • Fluid pressure signal increased in amplitude during μ-g • No stop-over phase shown during μ-g • Steady-state not reached due to the inertia of the heat sink
Ando et al. [81] (2018)	Stainless steel PHP (0.8 mm, /1.59mm I.D./O.D.) with check valves	SAT	R134a	<ul style="list-style-type: none"> • 4 years test with performances matching that on ground • Start-up difficulties due to the initial phase distribution;

The enhancement of performance associated with hyper-gravity is conditional to a minimum heat input though: up to 3g at 50W, up to 4g at 70W and up to 6g at 100W, according to the experiments conducted by Mameli et al. [82] on Large Diameter

³ Microgravity platform. PF: Parabolic Flight; SR: Sounding Rocket; SAT: Satellite

Centrifuge (LDC). Table 11 resumes the relevant experimental works done in reduced gravity, reporting the main characteristics of the device tested and the main outcomes of the investigation.

A study of PHP in weightlessness condition could further advance the following issues:

- Thermal and hydrodynamic characterization of two-phase oscillating/circulating flows in mini-channels during transitions between normal, Hyper and Micro gravity conditions;
- Gravity influence on the oscillation start-up and stop;
- Gravity influence on the flow pattern transition.

Chapter 4

Experimental set-up and Methods

4.1 Introduction

The investigation performed in this research project encompasses two main parts: an extensive experimental characterisation of a simplified “unit cell” of a Pulsating Heat Pipe, easier to instrument and to observe the causal effect of a selected list of varying parameters and a post-processing of the produced data (visual and signals) aiming to estimate the thermo-dynamic parameters necessary to obtain a new insight of the system PHP. The experimental investigation of the characteristic fluid flow has been carried out varying three relevant conditions to the system: working fluid, heating power input and gravity level. Two phase heat transfer in PHPs is a complex matter due to the strong coupling of the hydro-dynamics with the thermal phenomena that occur inside the evacuated serpentine. A further development of PHPs can only be achieved through a deep understanding of these governing principles with the support from experimental activities focused on reconstructing the overall physics, in order to provide useful data for the validation of theoretical and numerical model. This will help to predict the behaviour of even more complex devices (full scale PHP) and, eventually, obtain a tool for the design of the most suitable PHP given a specific application.

The most appealing field for PHPs is the space industry where the spectrum of *thermal management solutions* is required to be widened, and for the PHP technology to play a role, a range of performance stability needs to be defined and its reliability increased. This implies that the experimentation on ground must be followed by experimentation in a similar environment to that present in space. The first obvious difference is the gravity field; from previous investigation on gravity dependence of PHPs, it is easy to foresee the complexity in the design of a thermal management system for space applications but also the potential of these devices.

In this chapter, the selected apparatus for the experimental investigation will be presented, alongside the post-processing methods developed. Part of the research program has been dedicated to the design and realisation of the necessary facilities to implement the test-cell onboard of the parabolic flight, the selected microgravity platform. A description of the resulting parabolic flight rack will be provided.

4.2 Local scale investigation and single loops

The aim of the following activity is to review what is available in literature in terms of investigation of the phenomena involved in the two-phase thermally-induced flow and justify the selection of the set up proposed. The number of relevant parameters to consider for a characterisation of a PHP is so elevated that it is difficult to obtain information on the effect of one parameter against the others. The design of a simplified geometry for the test cell, able to conserve the peculiar functioning characteristic of the PHP but reducing the complexity and the number of parameters involved, is a common approach in research. The investigations done on single channels or single loops (Table 12) suggest an increase in the interest of the research at the local scale (i.e., at the scale of one bubble and one liquid plug) or a reduced geometry, in order to focus on basic phenomena which are responsible for the oscillations and the heat transfer in PHPs with both qualitatively and quantitatively results.

What emerged from the first approaches to this method is that even though a single loop can replicate many of the phenomena observed in a full-scale PHP, the performance is not comparable, and the operating range is not the same (i.e. if a PHP works horizontally, this does not imply that the extracted single loop is able to work horizontally).

Table 12 Simplified geometry approach in Pulsating Heat Pipe research. Geometry: Single Loop (SL), Single Channel (SC). Flow type: Pulsating (P), Mechanically induced oscillation (MIO). Area of study: Entire Loop (EL), Evaporator (EVA), Condenser (COND), Adiabatic section (ADB).

Author	Measurement technique	Geom.	Flow type	Channel cross-section	Fluid	g	Aim of the study	Area of study
Khandekar et al. [42] (2003)	Pressure and wall temperature	SL	P	Cu tube, I.D./O.D.=2mm/3 mm	Ethanol	1 g	Compare with multi-turn CLPHP	EL
Gully et al. [83] (2013)	Direct micro-TC ⁴	SC	P	SS tube, I.D./O.D.=2mm/3 mm	Liquid oxygen	1 g	Vapour temp.	EVA
Nine et al. [22]	TC and visual	SL	P	Cu/Acrylic tube 2.4mm I.D.	Water nanofl. (Cu)	1 g	Thermal perform., Pressure frequency spectrum	CON
Rao et al. [74]	High-speed videography	SC	P	Glass 2mm I.D.	FC-72	1 g	Physics of triple line Flow	EVA, CON
Spinato et al. [84]	Time-strip image processing	SL	P	Square 1x1mm	R245fa	1 g	regimes, Interface dynamics	EVA, CON
Srinivasan et al. [85]	Micro PIV	SC	MIO	Glass 1x1mm	Air-Water	1 g	Meniscus behaviour during oscillation	ADB
Fourgeaud et al. [86]	Grid deflection, Interferom.	SC	P	Rectangular, 2x22mm ²	Ethanol	1 g	Film Dynamic	EVA

4.3 The Single Loop Pulsating Heat Pipe (SLPHP) test rig

The test cell, consisting of a closed loop with four 90 degree turns, has been designed to facilitate high speed imaging and high-accuracy, high-frequency pressure investigation coupled with temperature measurement. The main components of the system are shown in Figure 35. The evaporator and the condenser are made of copper tubes (I.D./O.D. 2 mm/4 mm) and are connected by means of two sapphire tubes (110 mm axial length, same I.D./O.D. of the copper tubes). Twelve T-type thermocouples (10Hz acq. freq.) that monitor the external wall temperature are placed both in the heated and in the cooled sections. Two high-accuracy pressure transducers (1 bar absolute, accuracy 0.05% FSO, 100Hz acq. freq.), mounted at both ends of one of the

⁴ TC: Thermocouple

sapphire inserts. The high-speed camera (resolution 1280x1024 pixel) records images of both the channels at 100 fps, with perfect synchronisation with the pressure and temperature data. Three electrical heaters are coiled around the evaporator in three sections, providing a nominal wall-to-fluid heat flux of 6.5 W/cm^2 at 10 W. The heaters are controlled independently, to vary the heating distribution along the heated zone. The independent control of the heating elements allows non-symmetrical heating with respect to the gravity field. As previously demonstrated [87], for a similar multi-turn two-phase passive heat transfer device, a non-uniform heating pattern, promotes circulation in a preferential direction, with a subsequent improvement of the overall thermal performance when the device is gravity assisted.

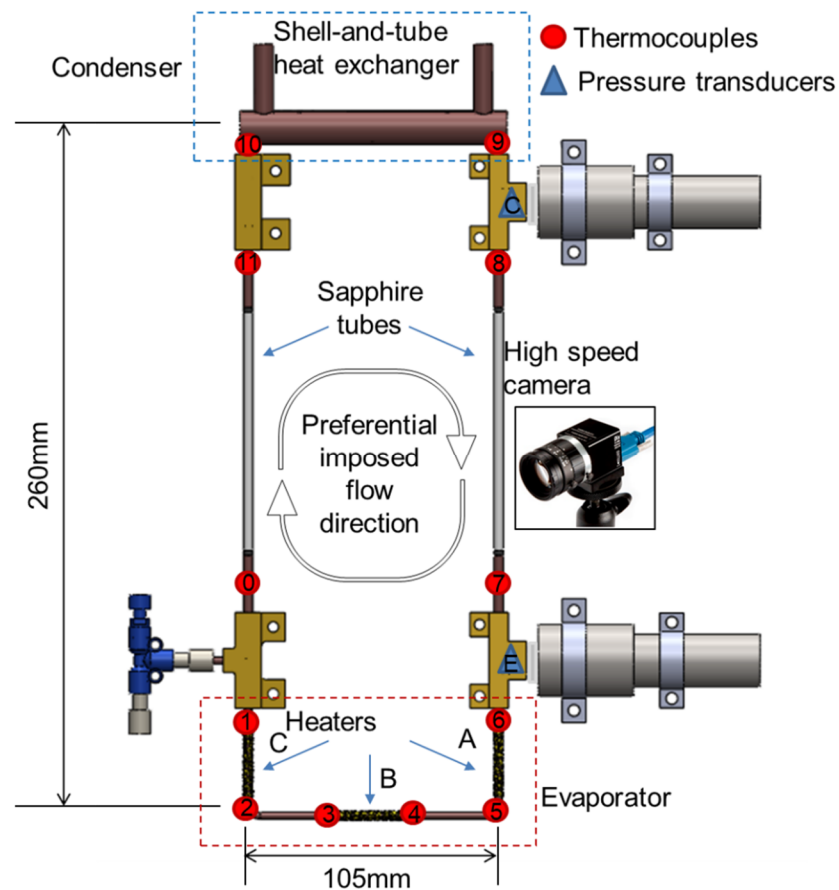


Figure 35 Single Loop Pulsating Heat Pipe (SLPHP) with position and numbering of thermocouples and pressure transducers

Two working fluid have been tested: Ethanol and FC- 72⁵. The SLPHP was first evacuated to 0.3mPa and then partially filled with the selected fluid, with a filling ratio of 0.6, corresponding to a fluid volume of 1.45 ml. After the ground characterization [88], the SLPHP has been tested under varying gravity conditions during the ESA 66th Parabolic Flight Campaign. Given the presence of delicate components, like the pressure transducer, during all tests, on ground and during parabolic flights, the working point of the device has been kept as far as possible from the dry-out conditions.

During dry-out, the sudden increase of pressure from the evaporator side can cause the rupture of the sensing membrane of the transducer. The highest power input safely operable by the device has been set at 30W. This means being able to operate quite close to the dry-out point characteristic of the combination device\working fluid, without occurring in the phenomenon.


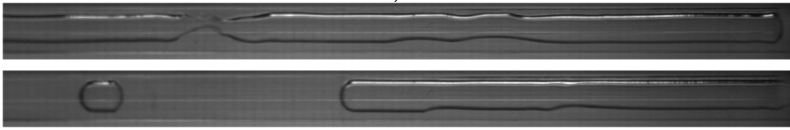

4.4 Liquid bulk velocity estimation method

In this work, a high-speed visual investigation has been performed on both transparent sections of the SLPHP (please refer to the apparatus description provided in 4.3). After the instauration of the circulation, three different regimes were observed in the visualisation sections of the channel with preferential direct flow following the direction condenser-to-evaporator (commonly called down-comer). The other channel (up-riser) is constantly showing a clear annular flow pattern (Table 13, frame c) while the down-comer shows transitions between Taylor flow (Table 13, frame a) and semi-annular (Table 13, frame b) depending on the thermo-hydraulic conditions.

The velocity of the liquid phase has been evaluated by processing high-speed imaging via a multiple-position, liquid phase sensitive, PIV-based velocimetry method. The method is an adaptation of an open source time-resolved particle image velocimetry (PIV) software developed at the University of Western Ontario (Canada) [89], which allows for resolution in time, paired with the capability of long recording periods.

⁵ For a detailed discussion on the rationale behind the selection of the fluid, please refer to Chapter 5

Table 13 Samples of the main flow patterns identified during the experimental campaigns

Flow pattern sample	Flow pattern definition
<p style="text-align: center;">a)</p> 	Taylor bubble\Slug-plug
<p style="text-align: center;">b)</p> 	Transitional\Elongate bubble\ Semi-Annular
<p style="text-align: center;">c)</p> 	Annular

In this study, the fluid is not seeded with tracer particles but the difference in pixel intensity, characteristic of a meniscus, has been exploited to track the velocity of the bubbles. In order to track a meniscus, each frame is segmented into a grid where I is the number of nodes in the y direction and J the number of nodes in the x direction (Figure 36). The spacing of the nodes along the radial dimension has been fixed to 8 pixels after sensitivity analysis. The PIV software allocates a value for each component of velocity (x and y) to each node and for every frame, reacting to the variation in pixels intensity characteristic of a liquid/vapour interface.

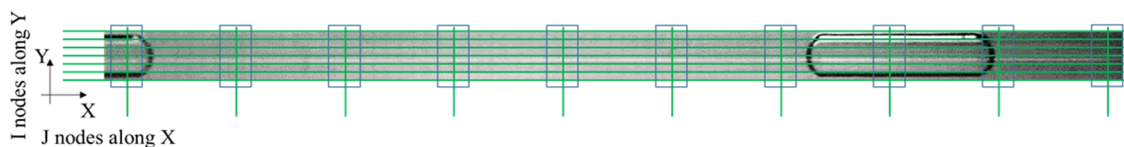


Figure 36 Velocity nodes grid overlapped on a frame and position of the radial averaging sections.

The raw data produced by the PIV software have been postprocessed with a Matlab® routine developed for the present study, in order to obtain a relevant velocity of the interfaces for every frame analysed. In every J position, the values of v_x has been averaged in the radial direction (y), excluding node 1 and node I to avoid wall effects for all the images of the sequence analysed, in order to obtain the temporal trend of the interface's velocity.

The procedure adopted for estimating the velocity is as follows:

- 1) *Radial Averaging*: Average of the I nodes excluding the four nodes nearest to the wall (two nearest to the upper wall, two nearest to the lower wall) at every J position;
- 2) *Axial Averaging*: The maximum average is considered the most relevant to define the overall motion of the fluid;
- 3) *Time*: The procedure is repeated for each frame in order to have a trend of the average velocity in a selected interval;
- 4) *Validation*: The software has been validated against seven imposed-velocity frame series, in the range of velocity between 0.05 and 0.5 m/s. The error (Figure 37) is lower than 5% for velocities lower than 0.15m/s. With the increase of the velocity up to 0.3 m/s, a 10% error has to be taken into account. For velocities greater than 0.4 m/s, the error increases significantly. A fixed axial discretization has been used for every velocity tested, after a sensitivity analysis. This simplification causes a reduction of the accuracy for high velocity and an increase of accuracy for medium-low range velocity. The actual error with a continuous flow at speed greater than 0.4 m/s can be considered reduced, given the smoother transition of frames in the sequence to be processed and not an artificial reconstruction of a moving bubble that can lead to unphysical transitions within frames. A further validation against frames belonging to a two-phase flow with known actual velocity rather than artificially imposed velocity in the range 0.4-0.8 m/s is needed.

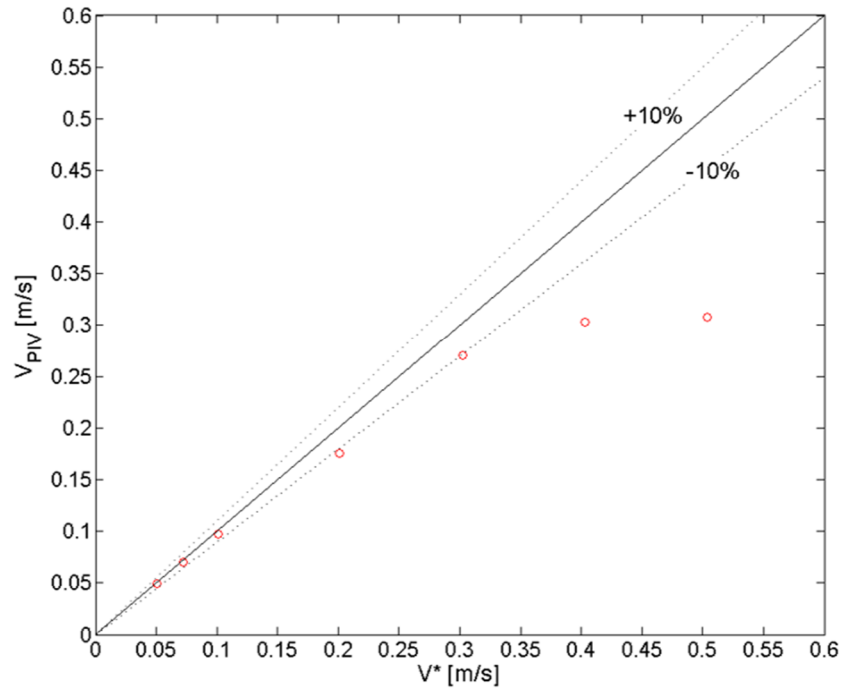


Figure 37 Error between the imposed velocity (V^*) and the velocity estimated by the filtered PIV method (V_{PIV})

The available data for full scale PHP (ammonia, 2mm/6mm I.D/O.D) [90], report of maximum velocity ranges of 0.4-0.6 m/s for slug/plug and 0.6-0.8m/s for semi-annular flow tested with heating power up to 500W.

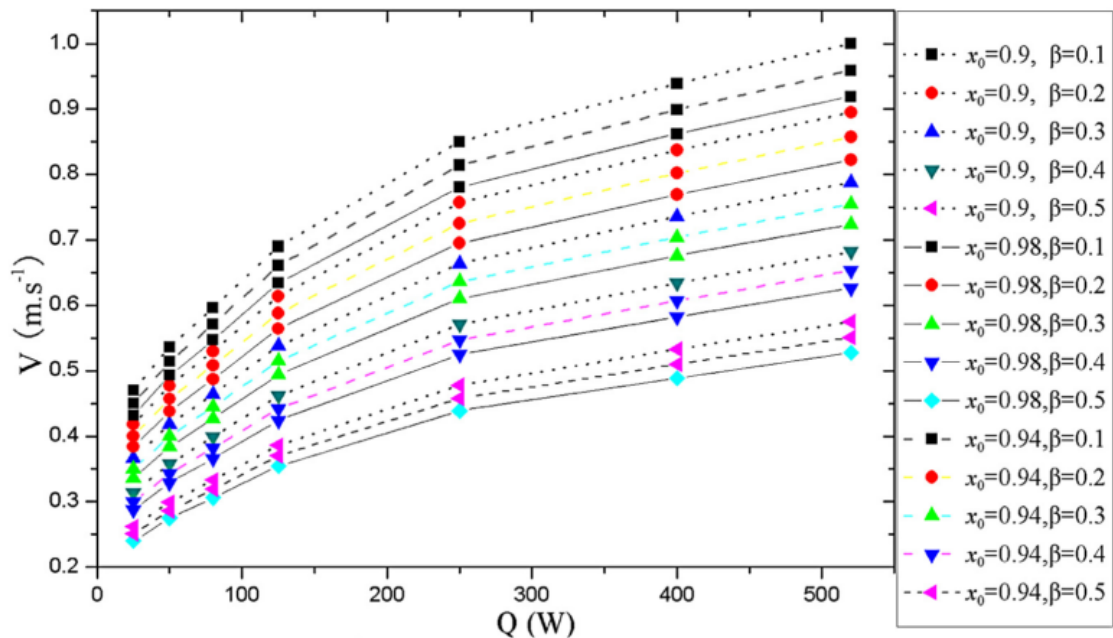


Figure 38 Prediction of fluid velocity variation with the heating power input, for different liquid quality (x_0) and ratio of evaporative heat to the total heat (β) from the analytical model presented in [90]

In the same paper [40], the authors show via analytical modelling a high dependency of the velocity with the power input (Figure 38). Due to the specific characteristic of the single loop, the maximum power tested is limited to 30W, implying limited fluid velocities. As shown in Figure 38, for power input lower than 50W the expected maximum velocities are in the range 0.2-0.45m/s making the velocity code applicable in the specific range with known accuracy. Tests conducted on a single loop pulsating heat pipe by Spinato et al. [70] for power input varying between 30W and 65W, shows a velocity range of 0.07 and 0.15 m/s, graphically evaluated from a time-strips method at the evaporator. This confirms the applicability of the code in the specific range of velocity, also from comparison with experimental data from similar geometry.

4.5 Void fraction and bubble length estimation method

The void fraction is a fundamental quantity in the description and analysis of two-phase flows; in the case of transition from slug to semi-annular flows the void fraction at any point varies dramatically with time, therefore, a continuous record of void fraction is desirable to describe the flow. The volume average void fraction, α , in a two-phase mixture is defined as:

$$\alpha = \frac{\text{Volume of gas in the mixture}}{\text{Total volume of the gas and liquid}}$$

Void fraction estimation via direct visualization of the fluid flow is the most common approach. Other innovative techniques have been applied to milli and micro-channels. A brief selection of interesting and innovative void fraction measurement and estimation techniques is reported in Table 14.

Normally, in considering void fraction, the time-average value (taken over a long period of time) is used, but the void fraction is fluctuating with time and instantaneous values are of great interest. To the knowledge of the author, this is the first attempt of estimation of the void fraction in the adiabatic section of a working PHP-like device.

The void fraction has been estimated starting from the high-speed imaging acquired during the 66th ESA Parabolic Flight campaign and during an On-Ground campaign. The 100 fps sequences has been processed via Matlab® routine developed in the context of the present study, in order to obtain a binarization of the starting images (Figure 39).

Table 14 Void fraction estimation and measure techniques selection

Author	Estimation\Measurement technique	Channel specifics
Costigan et al. [91]	Impedance void fraction probe	32mm I.D. tube
Triplett et al. [92]	Images analysis, resolution and fps not specified	Circular (1.1mm and 1.45mm) and semi-triangular (1.09mm and 1.49mm hydraulic diameter)
Ji et al. [93]	High-speed capacitance measurement	Glass micro-pipes 3.96, 2.65 and 1.56 mm
Kawahara et al. [94]	Images analysis, 1024 × 1024 pixels@30fps; 648 × 484pixels@125fps	Circular microchannels of 50, 75, 100, and 251 μm diameter
Masiukiewicz at al. [95]	Stereological visual investigation	From 2.08x1.90mm to 4.94x4.89mm
Liu et al. [96]	Multi-vision technique, two cameras @200fps	Circular 2.1, 2.9, and 4.0 mm I.D.
Gerbino et al. [97]	Single optical probe and Image analysis (up to 4000 fps)	Circular 1.91mm/4mm I.D./O.D.

The lighting conditions was adjusted prior to every test campaign but some reflections on the tube affected the processing of the data. Furthermore, the structure of the sapphire insert used is less clear than borosilicate glass, making necessary the use of morphological operators after the binarization to obtain bubbles with a close shape. During a morphological operation, the value of each pixel in the output image is based on a comparison of the corresponding pixel in the input image with its neighbours. The extension of the correction is characterised by size and shape of the neighbourhood. The main assumption of the code is considering the vapour bubble symmetrical with respect to the channel axis. This approximation has been considered sufficient for the purposes of this work, where not the liquid film thickness nor the interface shape are object of investigation. Also, any lens effect has not been taken into account during the estimation of the void fraction. The magnifying effect, linked to the dioptric power of a cylindrical lens, is maximum in the direction perpendicular to the central axis of the cylinder; along the central axis, the magnifying effect is one, being the dioptric power zero. The measure of the length of the bubble is carried out along the central axis and therefore not affected by lensing effect. The measure of the extension of the bubble in the radial direction is indeed affected by lensing effects. In

the case of slug/plug flow, the fluid is completely filling the cross-section of the channel, except from twice the thickness of the liquid film ($\delta \cong 80\text{-}100\mu\text{m}$) not appreciable with this technique and not object of this investigation. The radial extension of the slug/plug has been fixed to $D-2\delta$, where D is the diameter of the channel and δ a value of the liquid film thickness obtained from literature. Again, this is considered acceptable given the level of detail required for this analysis. For the specific purposes of determining with good accuracy the shape of the bubble, the techniques presented by Liu et al. [96] and Masiukiewicz et al. [95] are recommended. The process of binarization starts with a background frame subtracted from the sequences of interest. In the campaign performed with MW-IR Hi-speed camera, a portion of the tube had to be painted with high-emissivity black paint. The morphological operators used, suppress any non-bubble element in the frame, creating a closed series of white pixels where bubbles are present.

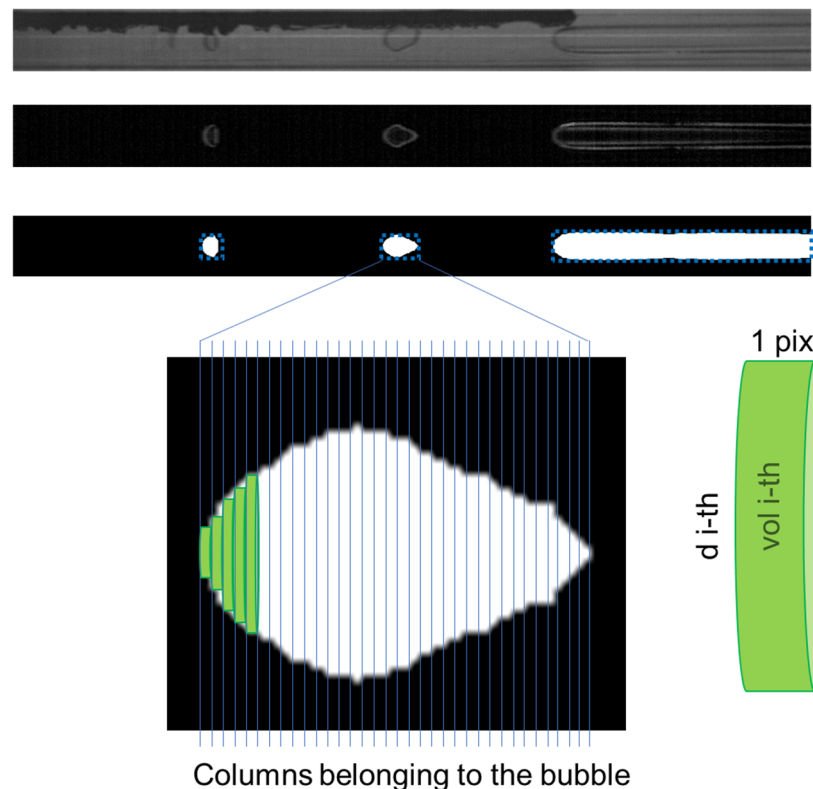


Figure 39 Binarization process of the original frame and successive estimation of a bubble volume as sum of infinitesimal disks

With the same code, the length of each bubble in each frame has been estimated and used in the determination of a novel concept of flow pattern map (Chapter 6). For the estimation of α , every bubble has been divided in columns spaced 1 pixel each.

Along each column belonging to the same bubble, the script count the number of white pixels and calculate the volume of a disk with diameter the number of the white pixels along the column and height 1 pixel. The volume of the i -th bubble is then given by the sum of the volume of each disk. The total volume of vapour in each frame is then the sum of the volume of each bubble detected. The code used, has been included in Appendix A.

A validation of the code has been performed on a series of frame produced via VOF simulation of slug-plug flow in a 3 mm channel, with known void fraction. The error has been estimated to be less than 2% for the case of bubbles with no liquid penetration, which is the dominant case for the combination of adopted I.D. of the pipe, heat power input and working fluid.

4.6 Parabolic flight investigation

Aircraft parabolic flight is one of the platforms scientists have to perform experiments in weightlessness. Orbiting spacecraft and free-falling objects experience near weightless conditions. For a spacecraft orbiting Earth, the gravitational attraction force is balanced by the centrifugal force at the location of the centre of mass. Objects inside the spacecraft will therefore experience weightlessness. The common reference to zero gravity, although incorrect, is widely used and will be used throughout this document in all its derivations (micro-gravity, hyper gravity, etc.). The best place to conduct microgravity research would be aboard the Space Shuttle, where a longer duration of microgravity can be attained. However, conducting research in space is very expensive, complex, and time-consuming. As shown in Figure 40, different flight opportunities are available for research in weightlessness. The main differences are the weightlessness period available and the possibility of direct interaction with the experiment whilst on flight (manned or unmanned flights). A parabolic flight campaign is the easiest and cheapest way to conduct verification tests prior to space experiments in order to improve their quality and success rate. It is the only micro-gravity platform (at the moment) allowing the research team responsible of the experiment to directly interact with the test-rig rather than demanding controlling functions to a non-expert of the experiment, as happens on the ISS with astronauts.



Figure 40 Weightlessness platforms available and their principal characteristics [98]

An aircraft in parabolic ballistic manoeuvre, provides investigators with a laboratory for scientific experimentation where the gravity levels are changed repetitively, giving successive periods of reduced gravity, preceded and followed by periods of hyper gravity. Flying a parabolic trajectory (Figure 41) in an aircraft is one of the few ways to obtain reduced gravity on Earth, which is important for astronaut training and scientific research. Typically, the aircraft performs parabolic arcs that produce approximately 20 seconds of freefall (0 g) anticipated and followed by 20 seconds of enhanced force (1.8 g), repeated 30–60 times. Despite the aircraft trajectory including large (45°) pitch-up and pitch-down attitudes, the occupants experience a net force perpendicular to the floor of the aircraft. This is because the aircraft generates appropriate lift and thrust to produce the desired vertical and longitudinal accelerations, respectively, although a moderate (0.2 g) aft-ward accelerations during certain parts of these trajectories is measured [98].

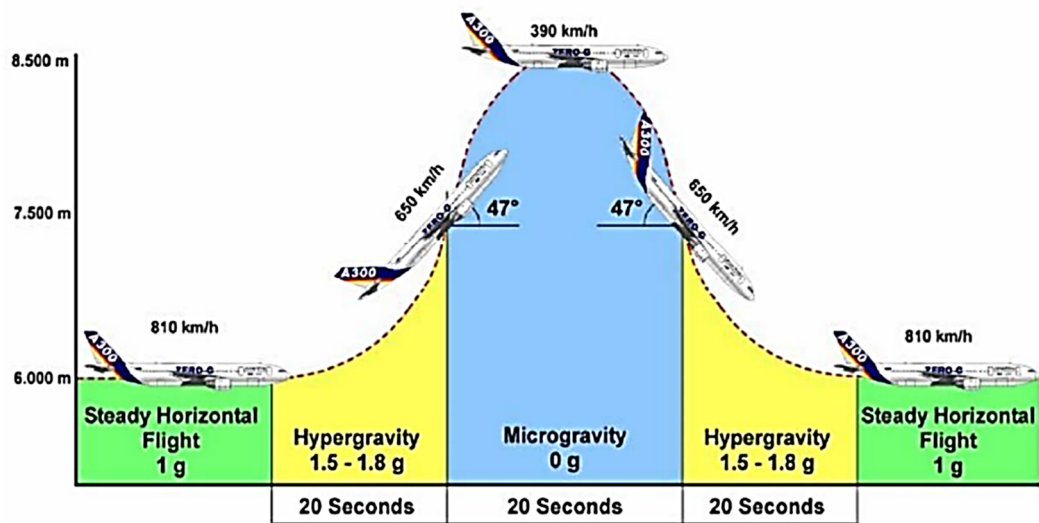


Figure 41 Parabolic flight manoeuvre description [98], [99]

4.6.1 Platform for Parabolic Flights investigation

In order to perform research aboard a Zero-g flight, the experiment and the structure containing the payload and acting as interface between the experiment and the aircraft, has to be designed (Figure 42) and realised following requirements based on good practices of aeronautical and space safety, according to French and European safety directives.

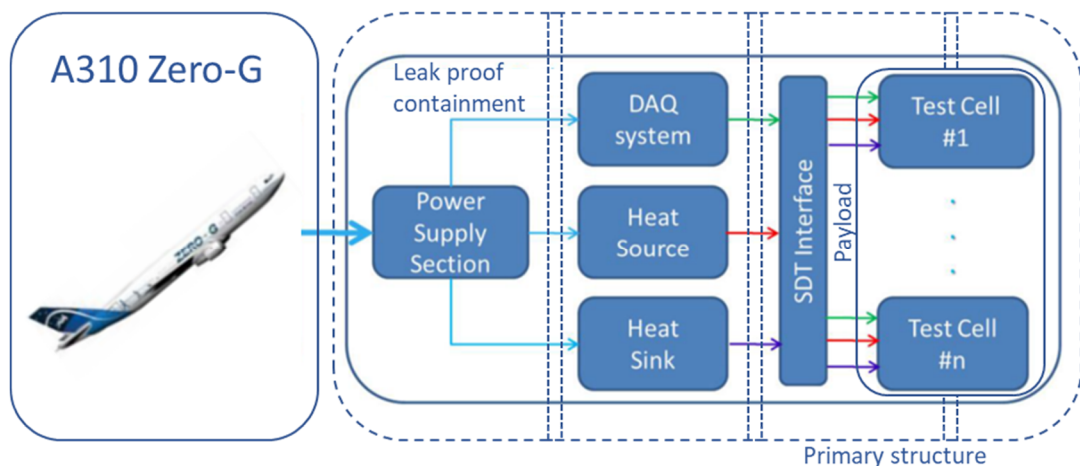


Figure 42 Logic of the Experimental Rack

Novespace, the owner of the plane and organiser of the flight on behalf of the European Space Agency, provides technical support in matching the safety requirements and is responsible for checking that the experiment design, construction and experiment organization procedures comply with the safety requirements. All the constraints and safety requirements for the design of the experiment are listed in the

official documentation provided by Novespace [100], including how to design and verify the primary structure [101] and how to interface the experimental rack with the aircraft [102]. As shown in Figure 42, the aircraft provides the electrical power to the rack, that is supported by a primary structure, secured to a series of rails on the plane. For PHP-related experiments, heat source and heat sink are necessary to activate the motion of the fluid. Operational data (P, T, visual imaging, IR imaging) are acquired and stored via the DAQ system. Given the presence of fluids, a leak proof containment is required.

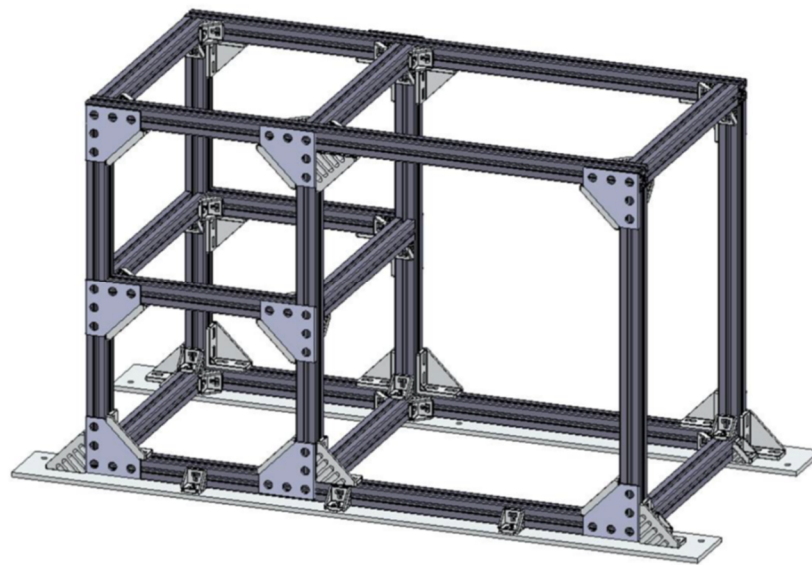


Figure 43 Rendering of the primary structure

The primary structure described, in Figure 43, has been designed and realized with the aim of hosting all the future thermo-fluid-dynamic two-phase related experiments that the University of Brighton is going to test under reduced gravity conditions. The chosen footprint is 1200x610mm with a two levels structure.

Referring to Table 15 and Figure 45, the experimental equipment in flight configuration consists of a test cell (1) equipped with electric heating elements in the evaporator zone. The condenser zone temperature is controlled by a Peltier cells array, coupled with a cold plate where distilled water is recirculated and cooled by a secondary cooling loop (2) able to dissipate the whole heating power. A fast camera (3) synchronized with an infrared Camera (4) allow to record the flow regimes and the fluid temperature distribution through the transparent section made of sapphire. Signals (up to 24 temperatures channels, two high-frequency fluid pressure channel, two auxiliary loop pressure transducers) are acquired using a National Instrument

Compact RIO (5) and several modules. The subsystems containing fluids are inserted in a double containment (6) and finally, all the systems described above are mounted on the rack structure utilized successfully for the first time during the 66th Parabolic Flight Campaign (7).

Table 15 Parabolic flight rack sub-system description in its final configuration as per PFC67th and PFC68th

Sub-syst.	Description	Type	Function
1	Test cell	Thermal	Tested device, evap. electric heating and cond. temperature control
2	Cooling Loop	Thermal	Global heat sink
3	Camera System	Diagnostic s	Visualization of the transparent section
4	INFRARED System	Diagnostic s	Visualization and temperature meas. of the transparent section
5	POWER, DAQ, PC	Power and Signal acq.	Power supply, Data acquisition, system and safety control
6	Rack Structure	Structural	Primary structure
7	Exp. box	Structural	Double containment and vibration damping

A detailed description of all the general layout of the connections as per configuration approved for the 67th ESA PFC can be found in Figure 44.

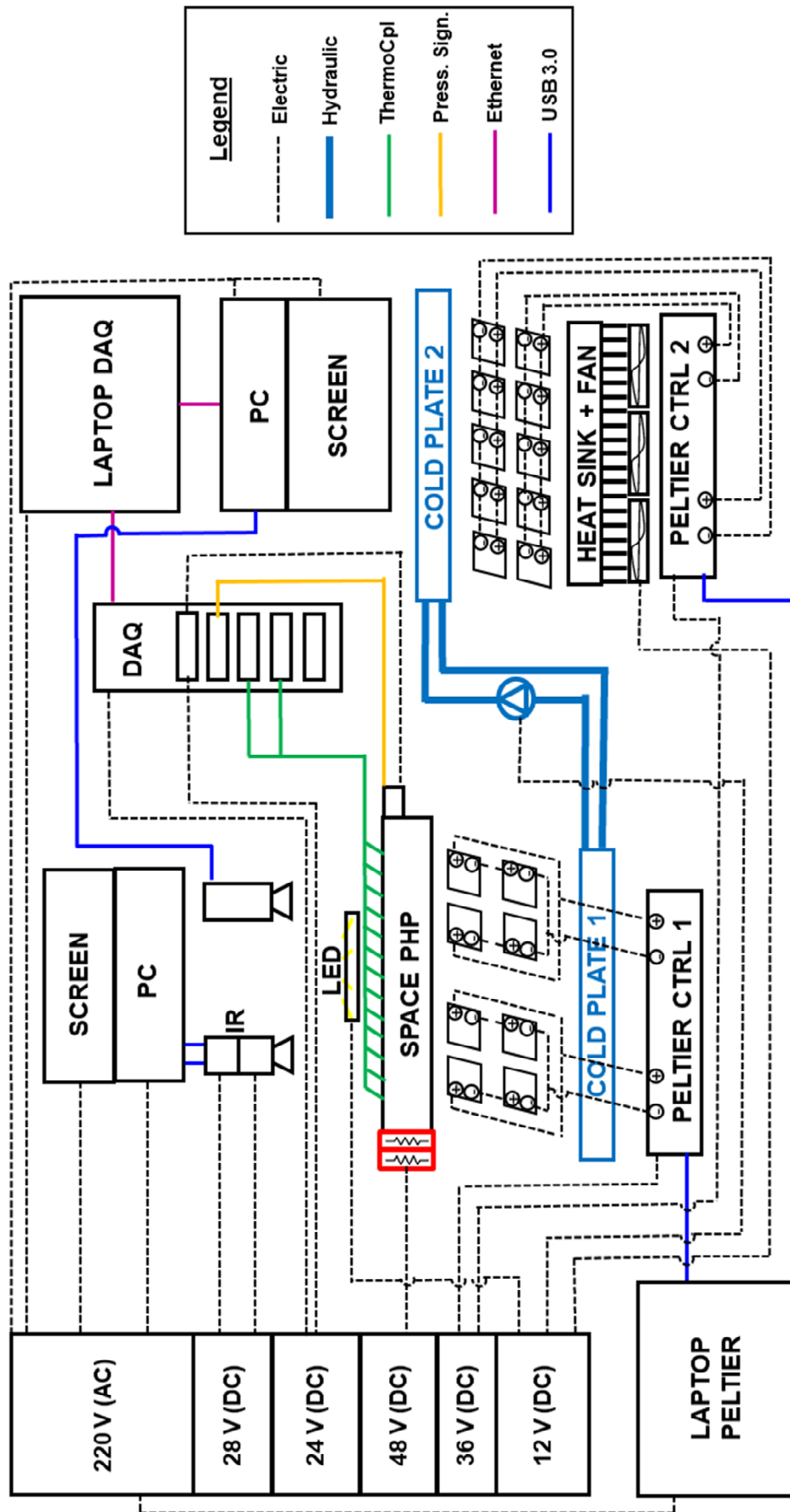


Figure 44 General layout of connections as per PFC67th

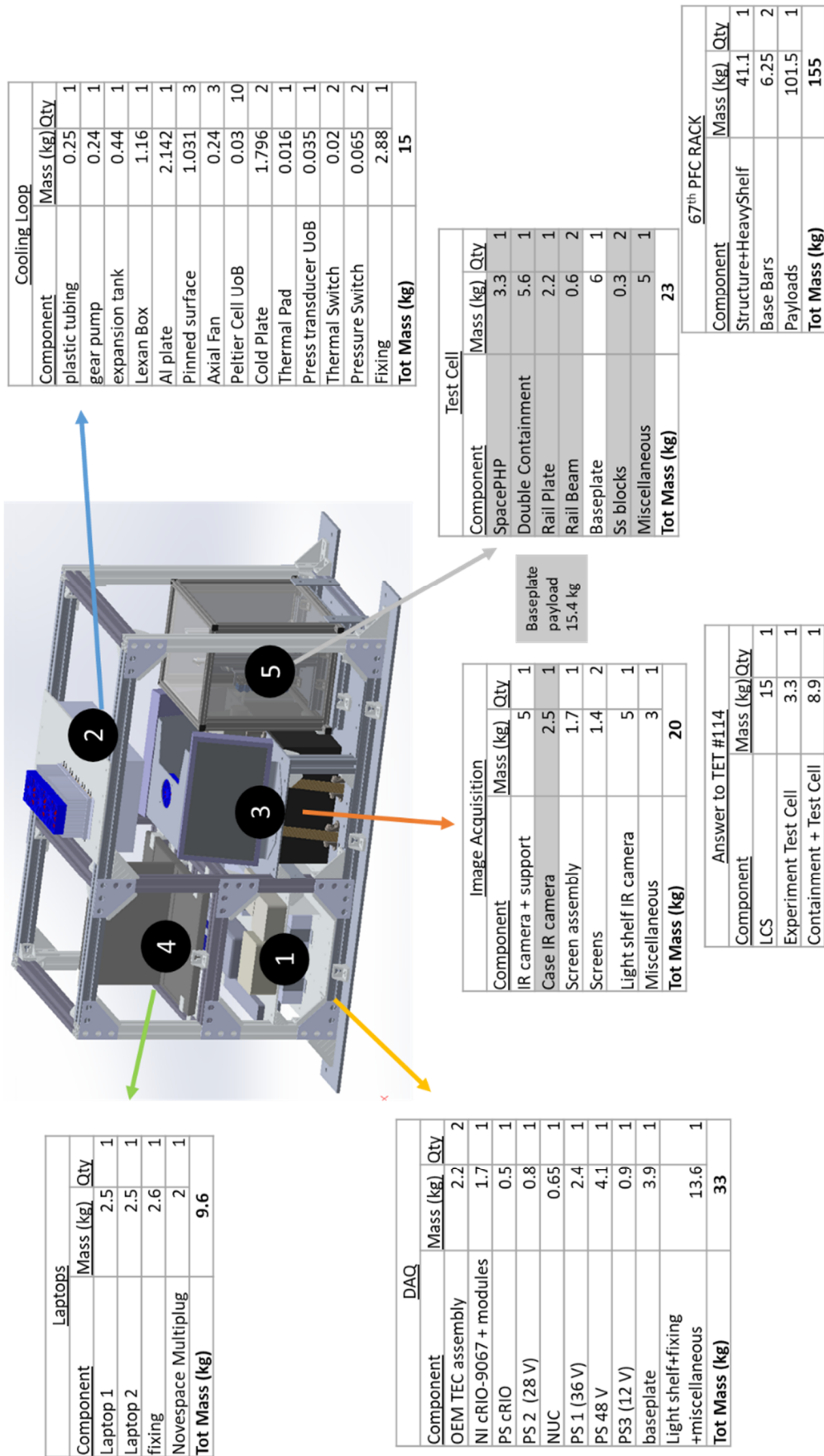


Figure 45 Rack modules description. All sub-systems included in the rack, as per 67th ESA PFC, with a weight breakdown as required by Novespace.

4.6.1.1 Liquid Cooling System (LCS)

The Liquid Cooling System (LCS), described in Figure 46. The cooling stage is called Thermo-Electric Cooling Stage, (TECS); a series of 10 Peltier cells is coupled with a liquid cold plate on the cold side of each module. The maximum temperature estimate for the hot side of each module is around 50°C. The heat exchange is made possible throughout the coupling of the assembly fans and heat sinks with a liquid cold plate. The three 92mm fans are mounted on pinned heat sinks, where the cooling fluid flows through (detail in Figure 47). The entire system will be double contained in a box made with Lexan® prospects. The minimum temperature on the cold side can vary between 5C and 30C when the Peltier pack will operate in reverse mode. A double staged thermo-switch has been implemented in the system. The working fluid cooled by the Liquid Cooling System will be pushed by a gear pump to a cold plate responsible of cooling the hot side of 8 Peltier cells attached directly to the condenser of the test cell.

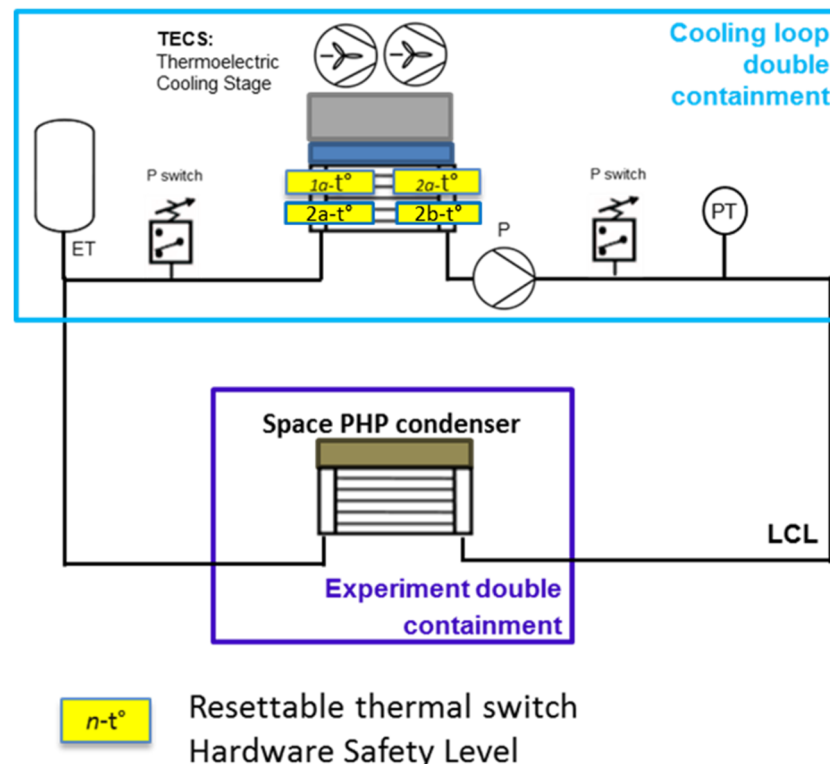


Figure 46 Description of the Liquid Cooling System

The double-level thermal switch system is placed in contact with the cold plate, inside the cooling loop double containment (light blue area in Figure 46 and rendering

in Figure 48). A maximum operating temperature of 90 °C has been selected for the switches. They act directly on the Peltier power supply system, via a relay. An additional safety level is provided by the commercial software used, in which a maximum temperature control value can be set. A double-stage pressure switch system is placed in the cooling loop double containment and calibrated to 500mBar g. They are operating on the pump via a relay, electrically connected in line with the 12 Vdc power supply. Note that the cooling loop water will never exceed 90°C because of the first safety level on the Peltier array of the test cell condenser. A pressure transducer has been placed in the loop, to also allow a software safety level. Pressure oscillations and potential expansions of the fluid will be controlled by means of an expansion tank. The cooling loop has been tested and the internal pressure never rises above 1.3 bar abs during normal operations. In case of fluid overpressure, hydraulically induced, the pressure switches will stop the pump. The hot side of the test cell Peltier array is the hottest zone for the cooling loop and it is maintained at $T < 90^{\circ}\text{C}$ by the thermal switches. So, the water in the cooling loop will never rise above 90°C.

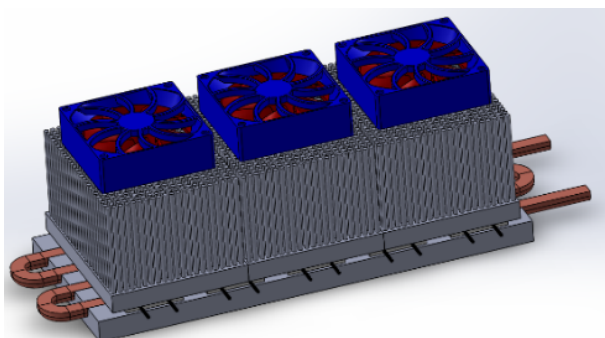


Figure 47: Description of the TECS assembly

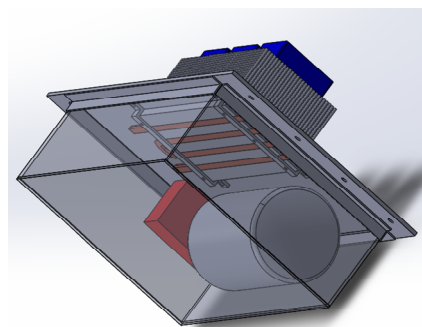


Figure 48: LCS assembly and double containment

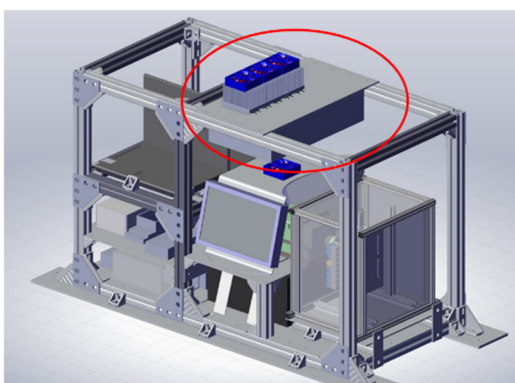


Figure 49: Position of the cooling stage assembly in the rack

Table 16: Description of the Liquid Cooling System main components

Description	Function	Qty.
Loop tubing-Flexible tubing	Contain and transport the working fluid	3 m
Liquid Cold Plate, Aavid Thermalloy, 305x127x17mm, Al-Cu	Heat exchanger	2
Pinned Heat Sink, Cooling Innovation, 95.5x127x75mm designed for 92mm fan	Heat dissipation	3
Axial Fan, 35W, 12 Vdc 92x38.15x 92mm, 270m ³ /h	Heat dissipation	3
Peltier cooler module APH-199-14-15-E, European Thermodynamics, 88.4W nominal power, 44x40x3.9mm	Active Cooling	10
Gear Pump (P), 12Vdc. Max discharge pressure (without pressure drops of the loop) 1.5 bar @ 0.86 l/m;	Fluid Circulation	1
Expansion Tank (ET)- Jabsco Mini Accumulator Tank 0.65l	Fluid fluctuation compensation	1
OEM Dual channel TEC Controller	Loop Peltier cells Controller	1
Peltier cooler module ETC-288-10-05-E European Thermodynamics, 193.5W nominal power, 44x40x32.8mm	Direct cooling of the test cells condensers	2
Pressure transducer- Cell Pressure (Keller M5 Series)	Software Level Safety & Data Acquisition	2
Pressure Transducer- Water Loop Pressure (Honeywell PX3 Series)	Software Level Safety	1
Pressure switch - 0.5 bar gauge setting: ES-41 Diaphragm Pressure Switch, Euroswitch	Hardware Level Safety	2
Pt100 probe, 100 Ohm	PID control	1
NTC thermistor	PID control	1
Resettable thermal switch, 2.5 A +90°C (cooling loop)	Hardware safety level	4

The maximum cooling capacity of the system is 300W. For the 67th PFC, the lower temperature output for the Liquid Cooling Loop has been fixed at 18°C. Given the presence of fans that need to operate without any risk of obstruction, the cooling module has been placed on top of the highest frames of the rack (Figure 49). All the components of the module are listed in Table 16.

For pressurised components, additional information is required for safety reason. The ratio between the maximum design pressure (in operating condition) and the maximum working pressure as per datasheet has to be specified (Table 17).

Table 17: LCS hydraulic pressure components list.

Description	Function	MDP [bar rel]	MAWP [bar rel]	MAWP/ MDP
Gear Pump (P), 12Vdc.	Fluid Circulation	0.5	1.45	2.91
Loop tubing-Flexible tubing	Fluid Containment	0.5	5	10
Shell and fined tube Heat Exchanger	Heat exchanger	0.5	2.3	4.6
Expansion Tank (ET)- Jabsco Mini Accumulator Tank 0.65l	Pressure compensation	0.5	7.6	15.2
Ultrasonic Flow Meter UF08B (FM)	Mass flow rate acquisition	0.5	9	18
Pressure Transducer (Honeywell Px3 Series)	Software Level Safety	0.5	6.8	11.6
Pressure switch - 0.5 bar gauge setting (calibrated 10/05/17): PS-41 Diaphragm Pressure Switch, Gems	Hardware Level Safety	0.5	9	18

4.6.1.2 Visualization (High speed visible spectrum camera)

The liquid flow evolution is recorded with a compact high-speed camera, able to reach up to 100 fps (Ximea XiQ® Figure 50 High-speed visible spectrum Ximea XIQ camera). The camera is connected via USB3 to a laptop that at the same time powers up the camera.

Table 18: Fast speed visualization system elements.

Component	Dimension	Description	Function
USB camera	26x26x24mm 26 grams	Ximea MQ013MG-ON	Flow visualization
Camera lens	55 grams	Pentax Cosmocar C2514-M F25mm C mount	Flow visualization
Led (2)	46x16x3mm	3W COB, 12V, waterproof enclosure (COTS)	Flow illumination
Infrared filter	(2) 50x25 mm	Cut off wavelength 700-1100 nm	Filters the LED IR light
NUC nano PC	117x112x35mm, 600g	Intel NUC mini PC mod D34010WYK	USB3 camera data stream acquisition



Figure 50 High-speed visible spectrum Ximea XIQ camera

4.6.1.3 Visualization (infrared)

Liquid dynamics through the sapphire tube and opaque body temperatures are visualised and acquired with the fast Medium-Wave Infra-Red camera described in Figure 51.

Optics	1280MW
Focal Length	25mm
Speed	F/2.3
FOV	21.0mm
Bandwidth	3 - 5 μm
Transmission	~93%
Resolution	40 μm
Sensor	1280x1024
Format	1280 x 1024

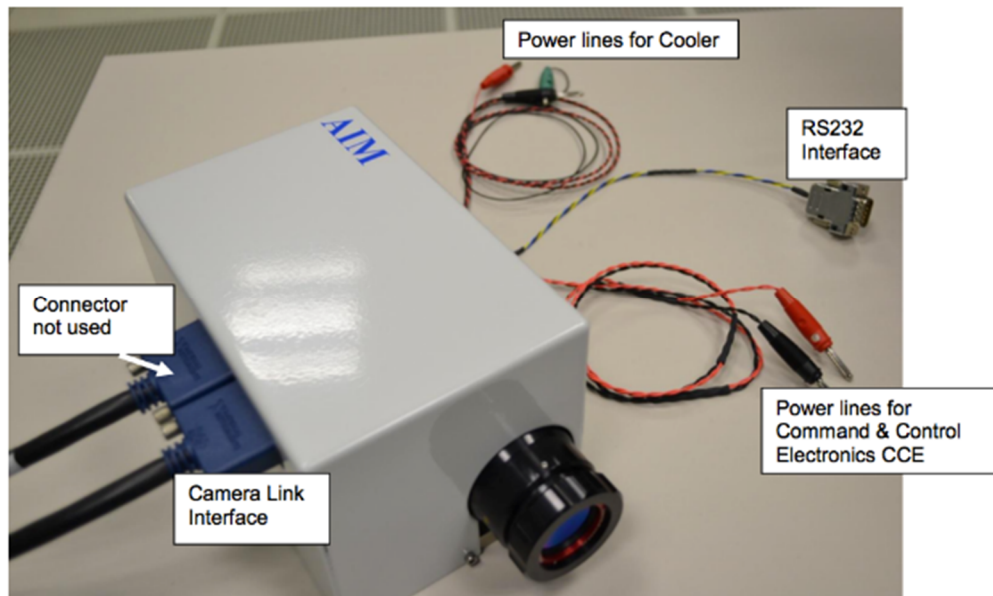


Figure 51: ESA MWIR Camera specifics

4.6.1.4 Results of the rack design and construction

The modular parabolic flight rack designed during the second year of this research program, has been qualified in the 66th ESA Parabolic Flight Campaign, highlighting its functionality and high adaptability of the system to third part payloads and suggested improvement for future flights. The improved rack, in Figure 52 shows it in its final configuration, has been used during the 67th and 68th ESA PFC. A tool for microgravity thermo-fluid dynamic related experiments is available for the scientific community and has been presented during the 15th UK Heat Transfer Conference [103].

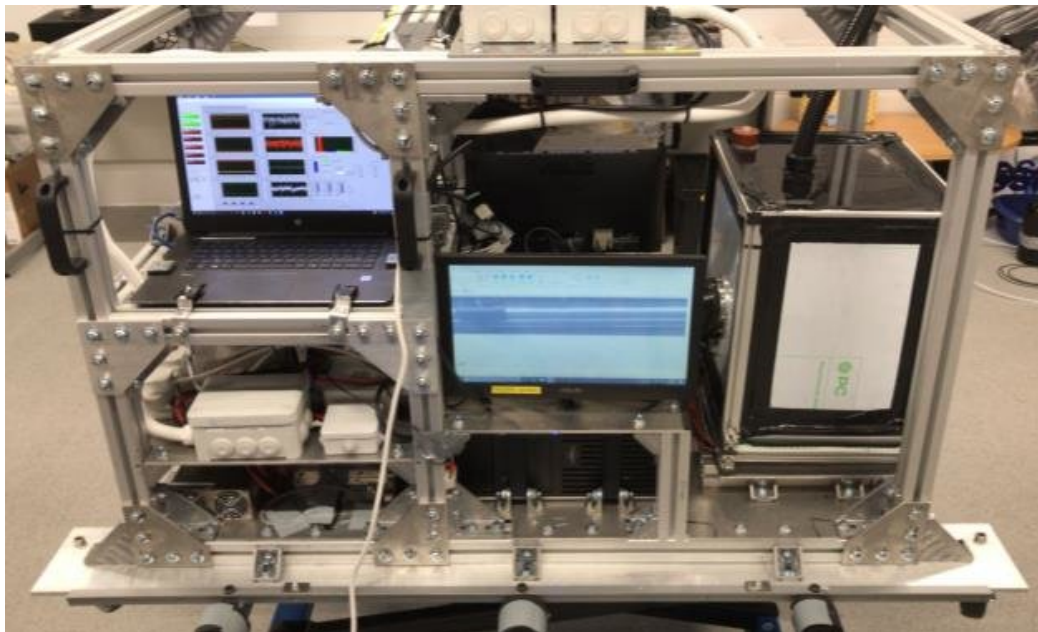


Figure 52 The University of Brighton parabolic flight rack in its final configuration

Chapter 5

1-g, Micro-g and Hyper-g tests

5.1 Introduction

In this chapter, the data extracted from the work done both on-ground and during two parabolic flight campaigns (the 66th ESA Parabolic Flight Campaign and 68th ESA Parabolic Flight Campaign) to characterise the device Single Loop Pulsating Heat Pipe, will be presented.

The characterisation will be presented in terms of pressure and temperature trends at the start-up for different fluids, power input and gravity level. The evolution of the void fraction in the “down-comer” channel will be presented and discussed, comparing the different behaviours when varying the gravity level and the working fluid. The equivalent thermal resistance, usually always reported as one of the main parameters to describe the thermal performance of a Pulsating Heat Pipe, will not be reported in this case. The simplified nature of the device does not allow to obtain equivalent thermal resistance data comparable with the best performing design available in literature given the reduced number of turns and the heat input that it can cope with. As previously mentioned, it is not the intention of the author to rely on a “unit cell” design to evaluate performances but to investigate the physical phenomena that occur in a “unit cell” as well as in a full-scale device.

5.2 SLPHP: On ground characterisation

The working fluid selected for all the experimental campaigns are ethanol (ethyl alcohol C_2H_5OH) and perfluorohexane (tetradecafluorohexane C_6F_{14}), commonly known as FC-72.

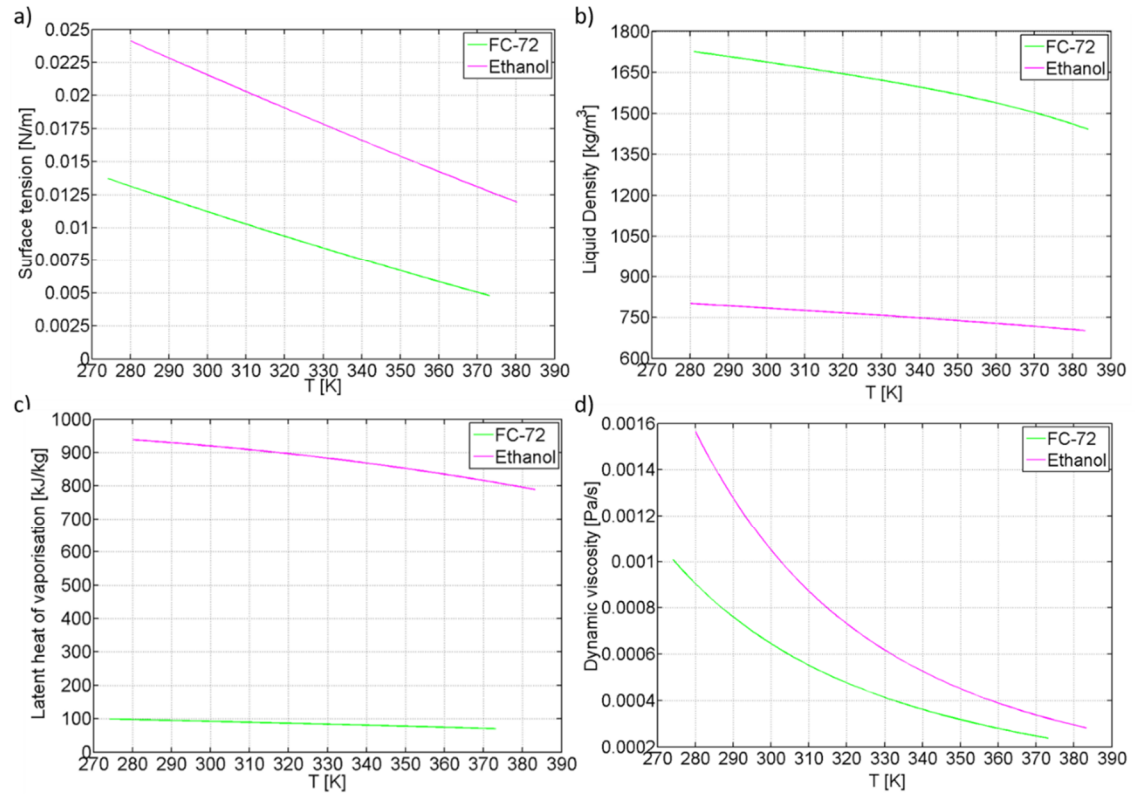


Figure 53 Relevant thermophysical properties of the selected working fluids in a temperature range of interest. a) Surface tension b) Liquid density, c) Latent heat of vaporisation, d) Dynamic viscosity

The two fluids present relevant differences in thermophysical properties (Figure 53), representing a good reference for a campaign that seeks to cover a wide range of cases. The internal diameter has been kept at 2mm throughout all the experimental campaigns, in order to obtain two completely different behaviours of the fluid at varying gravity levels. That means, according to the Bond criterion for critical diameter at 1g, the device filled with ethanol is always operating in critical conditions whilst FC-72 is operating in sub-critical conditions for 1g and Hyper-g with a transition to critical in micro-g. From Figure 54 it can be seen that the temperature should not trigger transitions in the range of interest for this work, so any transition will be triggered only by a change in the gravity level. From the classification previously described of two-phase passive systems, the device filled with Ethanol will

then act as a PHP on ground and in flight whilst FC-72 will act as a closed loop thermosyphon on ground and as a PHP when in conditions of reduced gravity.

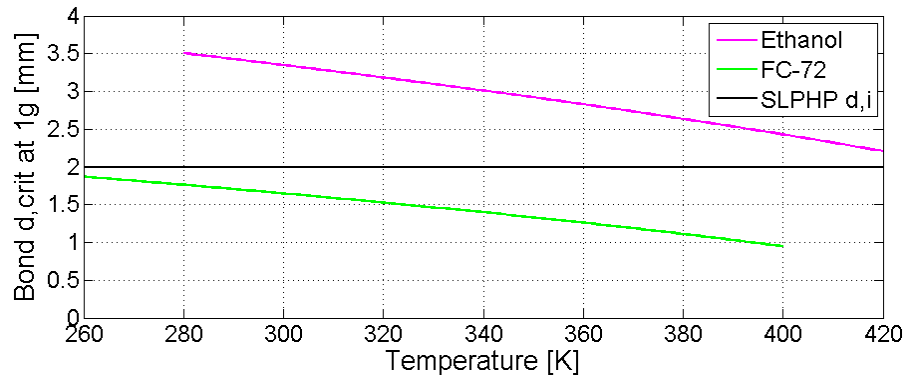


Figure 54 Comparison of critical diameter according to Bond criterion for ethanol and FC-72 varying the temperature in a relevant range for the tested device.

The thermal characterisation tests, described in [88], were performed at four inclination angles (0° , 30° , 60° and 90°). The heating power was varied providing a global power of 1 W, 3 W, 6 W, 12 W and 18 W. Different heating configurations were tested where the heating power was split among the three heaters to obtain a specific heating distribution. Pseudo-steady state conditions were reached in approximately 3 minutes, due to the low thermal inertia of the system. Heating configuration tested were kept constant for 15 minutes, to ensure that a pseudo-steady state conditions was reached for every case. Given the nature of reduced loop, the thermal performance in terms of equivalent thermal resistance are not considered. This because the simplified geometry of the Single Loop will not give any values comparable with multi-turns PHP designs available form literature.

High-speed imaging was performed during the last minutes of each case. Refer to section 4.3 for test rig description. Table 19 lists the cases tested in Bottom Heated Mode. Ilinca et al. [88] reported that 1 W is not sufficient to activate a self-sustained two-phase flow and the temperatures at the evaporator increases, while the pressure, close to the saturation pressure of ethanol at 20°C , exhibits a flat trend. All the other power inputs were sufficient for showing peaks of pressure that result in a slight decreasing of the evaporator temperatures even though a full start-up of the system, with oscillation of the fluid, is detectable from 6W. The activation is now followed by an abrupt decrease of the evaporator temperatures. Some combinations of the power input were able to establish circulation of the fluid in a preferential direction, clockwise or anti-clockwise. The two visualisation sections showed two clearly distinguishable different flow patterns during an established circulation, depending on the position of

the source of power: the up-riser channel (direction evaporator to condenser) always in annular flow and the down-comer (direction condenser to evaporator) in preferential slug/plug flow.

Table 19 Cases tested during ground test characterization [88]

Configuration	Heater Left	Heater Middle	Heater Right
1	0	1	0
3a	0	3	0
3b	1	1	1
3c	0	1	2
3d	0	1.5	1.5
3e	1.5	1.5	0
6a	0	6	0
6b	2	2	2
6c	1	2	3
6d	0	3	3
6e	3	3	0
12a	0	12	0
12b	4	4	4
12c	6	6	0
12d	0	6	6
12e	6	6	0
18a	9	9	0
18b	0	9	9
18c	4	6	6
18d	6	6	6

Config	Power input (Watt)				FC-72				Ethanol				
	Left	Mid	Right	Total	Pivot angle				Pivot angle				
					0°	30°	60°	90°	0°	30°	60°	90°	
1a	0	1	0	1	-	-	-	-	-	-	-	-	-
3a	0	3	0	3	S	S/C	C	-	S	-	-	S	-
3b	1	1	1	3	O	C	C	C	S	-	-	S	-
3c	0	1	2	3	O	C	C	C	S	-	-	-	-
3d	0	1,5	1,5	3	O	C	C	C	S	-	-	-	-
3e	1,5	1,5	0	3	O	C	S	C	S	-	-	S	-
6a	0	6	0	6	O	C	C	C	C	S	S	S	S
6b	2	2	2	6	O	C	C	C	C	S/O	S	C	C
6c	1	2	3	6	O	C	C	C	-	S	S	C	C
6d	0	3	3	6	C	C	C	C	O	S	C	C	C
6e	3	3	0	6	C	C	C	C	O	S	S	C	C
12a	0	12	0	12	C	C	C	C	C	C	C	C	S
12b	4	4	4	12	C	C	C	C	C	C	C	C	C
12c	2	4	6	12	C	C	C	C	C	C	C	C	S
12d	0	6	6	12	C	C	C	C	C	C	C	C	S
12e	6	6	0	12	D	C	C	C	C	C	C	C	C
18e	9	9	0	18		C	C	C	C	C	C	C	O
18d	0	9	9	18		C	C	C	O	C	C	S	-
18c	4	6	8	18		C	C	C	D	C	C	C	C
18b	6	6	6	18		C	C	C		C	C	C	C
18a	0	18	0	18		C	C	D		C	C	D	-
12a'	0	12	0	12		C	C	C		C	C	C	C
6a'	0	6	0	6		C	C			C	C	C	C

Figure 55 Global thermohydraulic behaviour of the system varying power distribution, working fluid and inclination angle of the SLPHP: no symbol = not tested; - = no fluid motion in the transparent tube; S = start-up or shut down (unstable); O = oscillating (stable); C= circulating (stable); D = dry-out risk.

For power input higher than 18W, the dry-out condition is approached, and the test stopped. Establishing a preferential circulating direction, avoids bubble stagnation, increasing the velocity in one direction. This will lead to an increase in the CHF.

5.2.1 SLPHP start-up with different fluids

The reaction to a power input sufficient to activate the system, filled with different fluids, has been investigated in this work. The initial conditions of distribution of phases in the channel clearly affects the start-up of the device, given the different heat transfer properties of liquid phase compared to the vapour. What is of interest in this phase of the work, is to define quantitative methods to measure the performance at the start-up of a PHP device. What can be qualitatively deduced from two cases of start-up with different fluids (Figure 56, the configuration adopted is 9W, distributed as 6W, 3W, 0W from left heater to right heater), with a good experimental repeatability, is that FC-72 responds quicker than Ethanol to a power input. In some cases, this quicker process results in a stage-activation, function of the phase distribution in the evaporator. A general trend for this behaviour cannot be deduced, being linked to a random distribution parameter; what is of interest, is developing tools to estimate the effect that it might have on practical values like the overheating at the evaporator before an activation that will then lead to a sudden drop in temperature. In the specific case of Figure 56, the two behaviours lead to different phenomena. A flattening of T2 (A-B), followed by overall temperature reduction when the pressure shows oscillatory trend (after B) in FC-72; this causes also fluid displacement due to expansion of vapour bubble. The pressure oscillation following point B can be described as a sequence of sinusoidal positive half-waves that slowly attenuates its amplitude and frequency. Ethanol shows a sudden and simultaneous decrease of temperature in the entire evaporator (point C), caused by a pulsating activity. After that, pressure signals show a rapid damping in the amplitude value. What changes is the energy supplied to the fluid and an index of how the device, as a cooling system, is performing.

In order to relate the energy absorbed by the fluid to the thermal performance of the device, a *start-up overheating index* can be defined as the increase in temperature in sensible locations (evaporator), before the cooling effect of the activation of the pulsating motion takes place. Knowing the power input and the delay before a full start-up, the energy supplied to the system for the activation can be estimated. The ratio between the energy supplied to the system Q and the $Max(\Delta T_{evap})$ and (last

column in Table 20), gives an idea of the *equivalent thermal capacity* of the system composed by PHP and fluid, including the random initial distribution of phases in the evaporator.

Table 20 Start-up performance comparison between working fluids

Fluid	\dot{Q} [W]	Δt [s]		Q [J]		ΔT_{evap}^{max} [K]	$\frac{Q}{\Delta T_{evap}}$ [J/K]
		First Stage	Second Stage	First stage	Second Stage		
FC-72	9	14.9	6.5	134	58	12.2	13.7
Ethanol	9	19.5		175		14	14.3

As shown in Table 20, FC-72 has a lower *start-up overheating index* or *equivalent thermal capacity*, a sign of better performance at the start-up. The acquisition frequency used for both the power input and temperature signals is 10Hz. The power supplied (Q) is electronically selected and current values are acquired by means of a dedicated electronic board with known datasheet uncertainty for the total electric resistance (δR_{ds}) and current supplied (δI_{ds}), respectively 0.2Ω and $0.003A$. According to Moffat [104], the uncertainty interval of the power supplied has been evaluated following the (5-1):

$$\delta Q = \sqrt{\left(\frac{\delta Q}{\delta I} \delta I\right)^2 + \left(\frac{\delta Q}{\delta R_{ds}} \delta R_{ds}\right)^2} \quad (5-1)$$

and listed in Table 21 for different values of power input; for what concerns the temperatures value, the uncertainty from datasheet δT_{ds} is $0.86^\circ C$.

Table 21 Uncertainty calculated on different heat input steps

Q [W]	δQ [W]
10	0.58
20	0.91
30	1.21

Looking at the thermodynamic properties of the fluids (Table 22), different behaviour at the start-up is certainly caused by the thermal capacity of the fluid alongside with the latent heat of evaporation, significantly higher for ethanol, and the thermal diffusivity of the liquid phase, which defines how quickly the transient conduction processes will happen in the liquid phase.

Table 22 Fluids properties at the start of the heating period

Fluid at 20°C	ρ [kg/m ³]	c_p [kJ/kgK]	Δh_{lv} [kJ/kg]	α [m ² /s]
FC-72	1700	1.03	94	3.32
Ethanol	790	2.5	962	8.38

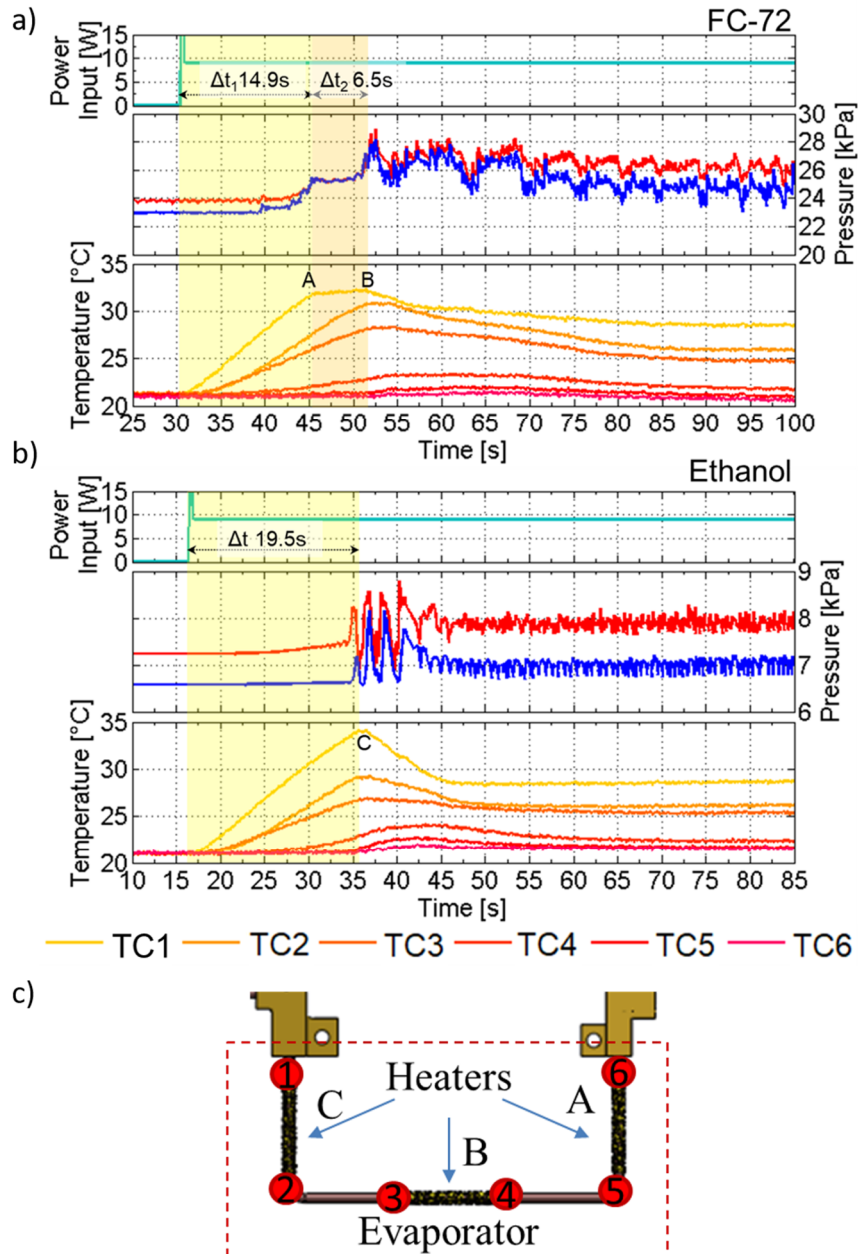


Figure 56 Start-up characteristics of the SLPHP with a) FC-72 and b) Ethanol. From top to bottom of each figure: Power input, Pressure signals, Evaporator temperatures. Activation delay reported. c) Position of the thermocouples in the evaporator zone.

The high latent heat of vaporisation of Ethanol compared to a refrigerant fluid like FC-72 seems to be responsible for the slower start-up. A slightly higher thermal

diffusivity of the ethanol, with a better spreading of the thermal load, could explain the simultaneous temperature drop in the entire evaporator (Table 22). Even though similar trends have been observed, the effect of the initial distribution of phases in the evaporator zone has to be taken into account because it affects the start-up time and therefore the energy required for an activation.

5.3 SLPHP: μ -g and Hyper-g characterisation

The micro and hyper gravity characterisation of the SLPHP has been undertaken during the 66th and the 68th ESA-Novespace Parabolic flight campaign. The present section of the research is focused on:

- Analysing Temperature and Pressure signals from the PFC
- Investigating the start-up in microgravity
- Estimating the energy required for having pulsations in μ -g
- Studying the effect of the thermodynamic properties of the working fluid on the μ -g activation
- Visual investigation of flow regime transitions in a PHP-like device under varying gravity level
- Estimation of the fluid velocity under varying gravity level and power input
- Void fraction estimation under varying g levels and heating power

5.3.1 Experimental procedure

Two different fluids were tested over the three days of flight: Ethanol and FC-72. The device has been tested in a vertical position, bottom heated mode (BHM) under different heating configurations. The same experimental matrix has been adopted for both fluids. The flight test procedure, in terms of power input to the evaporator, has been reported in Table 23. Details on the power allocated to the three heaters has also been reported, to show the configuration selected to impose a preferential direction to the flow.

At the occurrence of microgravity (injection phase) of the first parabola of each series, the selected power has been provided to the heaters to investigate the start-up in microgravity conditions. For the other parabolas of the series, the power input has been kept constant throughout the sequence normal gravity – hyper gravity – microgravity – hyper gravity – normal gravity and in the gaps between parabolas.

During the breaks between each series (5'-5'-15'- 5'-5') the power was switched off completely.

Table 23 PFC 66th experimental matrix

Parabola N.	Ethanol (Day I) and FC-72 (Day II) Total Power	Heater A	Heater B	Heater C
Parabola 0	15W	0	6	9
Parabola 1-5	9W	0	6	3
Parabola 6-10	15W	0	6	9
Parabola 11	15W	0	6	9
Parabola 12-15	18W	0	6	12
Parabola 16	18W	0	6	12
Parabola 17-20	24W	0	9	15
Parabola 21	18W	0	6	12
Parabola 22-25	21W	0	9	12
Parabola 26	15W	0	3	12
Parabola 27-30	27W	6	9	12

5.3.2 Temperature, pressure and visual data

As a reference, the complete track of temperatures, pressures and z-axis acceleration for the ethanol and FC-72 fluid has been reported in Figure 57 and Figure 63 respectively. Samples of flow pattern at different gravity level and power input are provided in Figure 60, Figure 61 and Figure 62 for ethanol whilst.

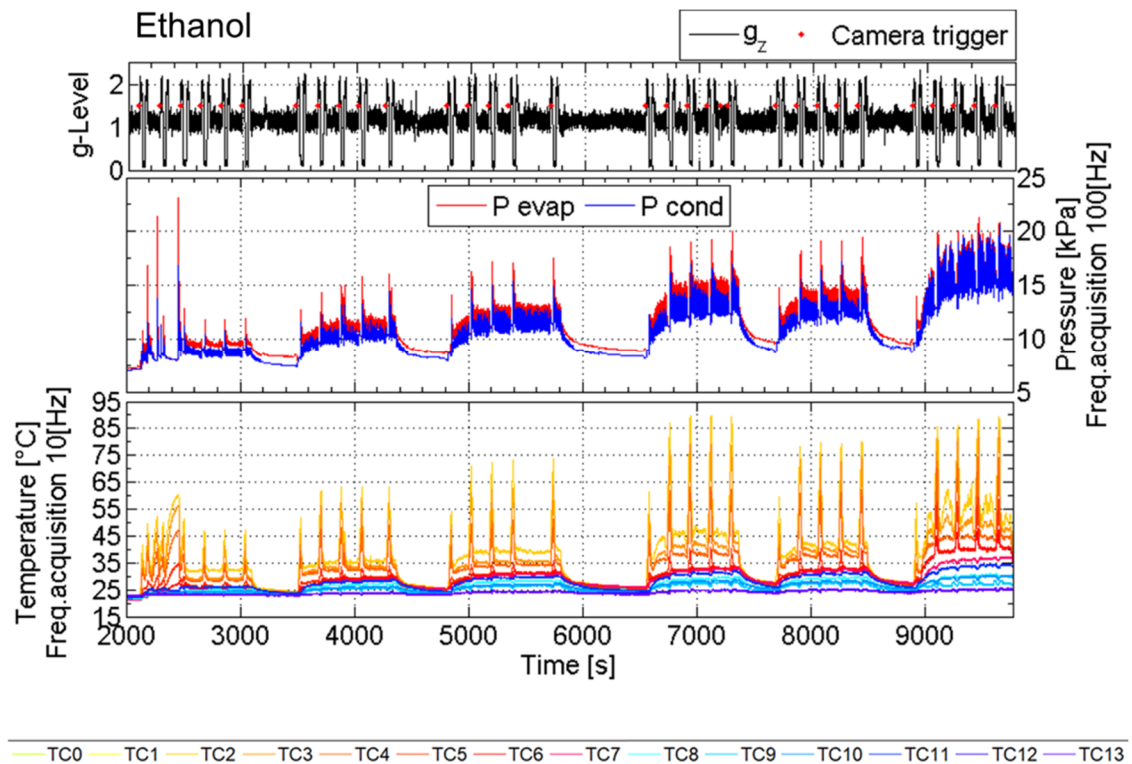


Figure 57 Complete track of temperature, pressure and z-axis acceleration for ethanol during the 66th ESA PFC. In the temperature plot, Yellow/red colour shade = Evaporator temperatures; Blue colour shade = Condenser temperatures

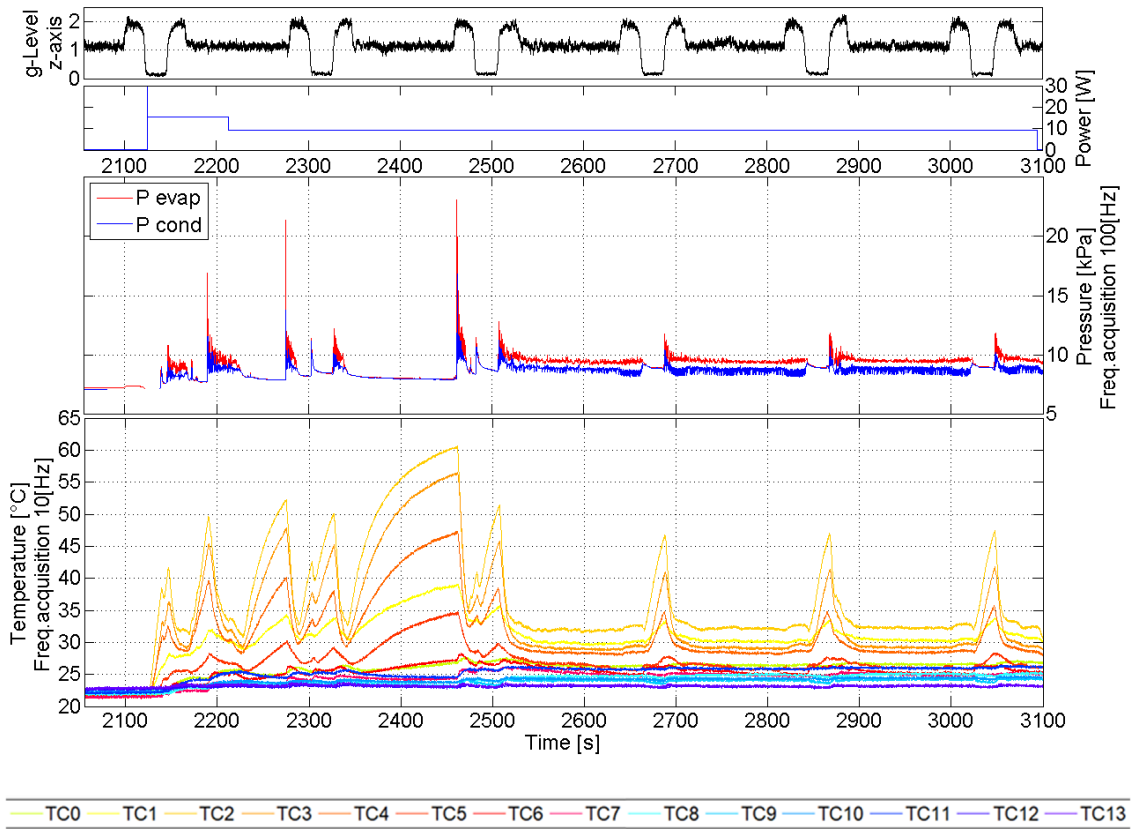


Figure 58 Ethanol, detail of parabolae 0 to 6, low heating power. From top to bottom: z-axis acceleration, heating power, pressure signals, temperature signals.

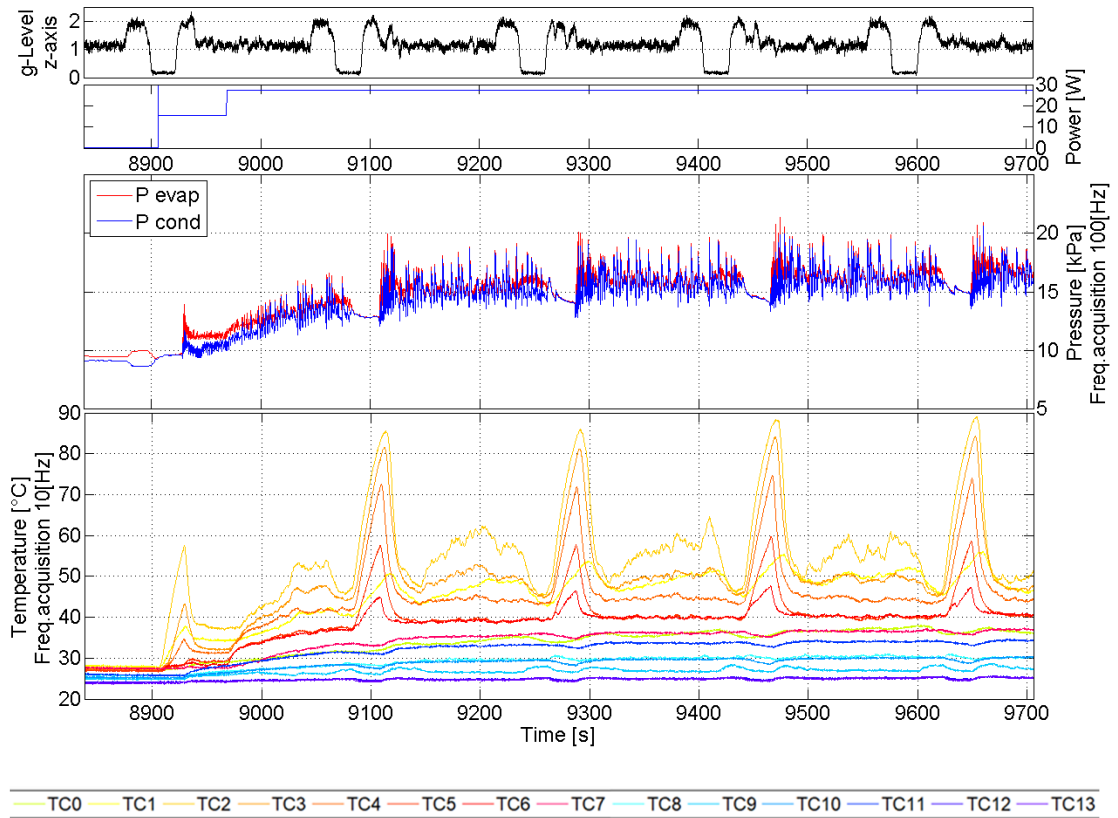


Figure 59 Ethanol, detail of parabolae 26 to 30, low heating power. From top to bottom: z-axis acceleration, heating power, pressure signals, temperature signals.

The asymmetric heating configuration is able to establish a continuous core flow of vapour (annular flow) in the central part of the cross section of the tube at which end the heater supplied with the highest power is coiled.

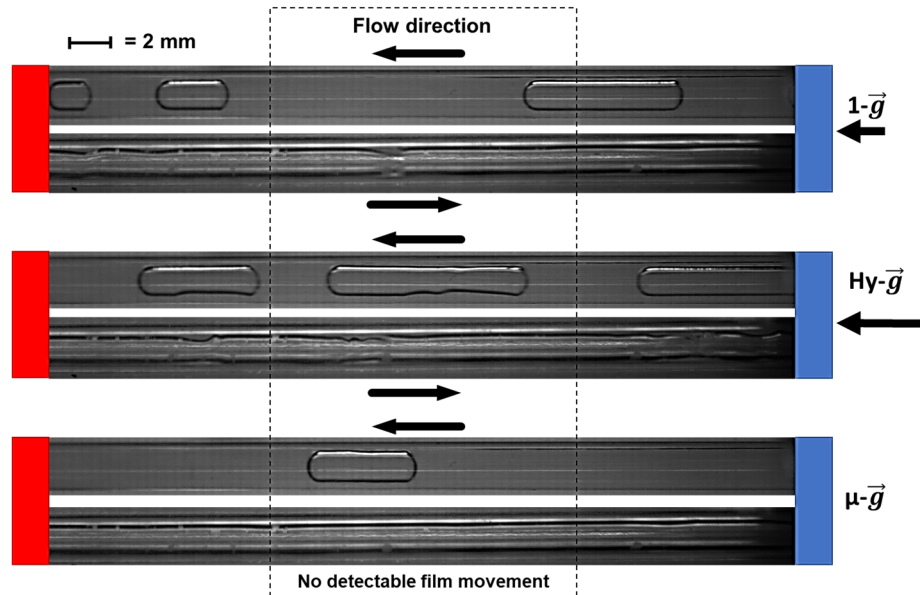


Figure 60 Typical flow pattern obtained with ethanol for low power input (9W). Evaporator side in red, condenser side in blue

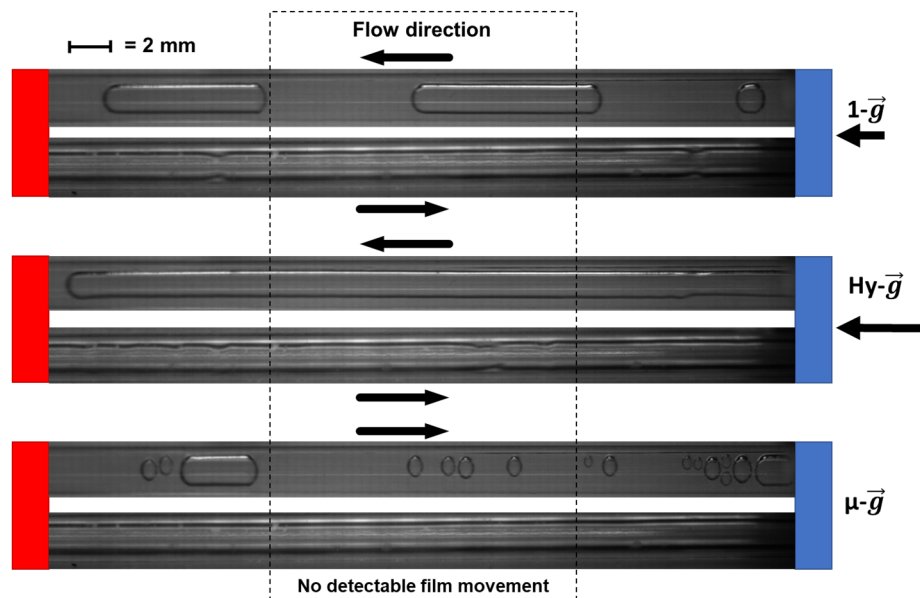


Figure 61 Typical flow pattern obtained with ethanol for medium power input (18W). Evaporator side in red, condenser side in blue

This pushes the liquid towards the periphery of the tube cross section and forces it to move against gravity due to the velocity difference across the interface between two fluids (creating liquid ridges due to the Kelvin-Helmholtz instability); some liquid

droplets appear also to be entrapped in the core vapour flow and lifted to the condenser. This overview of the two flights can be used for a simple comparison, suggesting interesting qualitative differences and quantitative indications in terms of temperature and pressure. For instance, the temperature reached at low power input and high power input by the working fluids: for high heating power level, ethanol (flow pattern examples for different gravity levels in Figure 62; temperature and pressure trends in Figure 59) shows lower overheating either in pseudo-stationary states (regimes conditions obtained during 1-g and Hy-g) and in transitional regimes of micro-gravity than at low power input (flow pattern examples at different gravity level in Figure 60; temperature and pressure trends in Figure 58) when the device shows a difficult activation and sustaining of the pulsation.

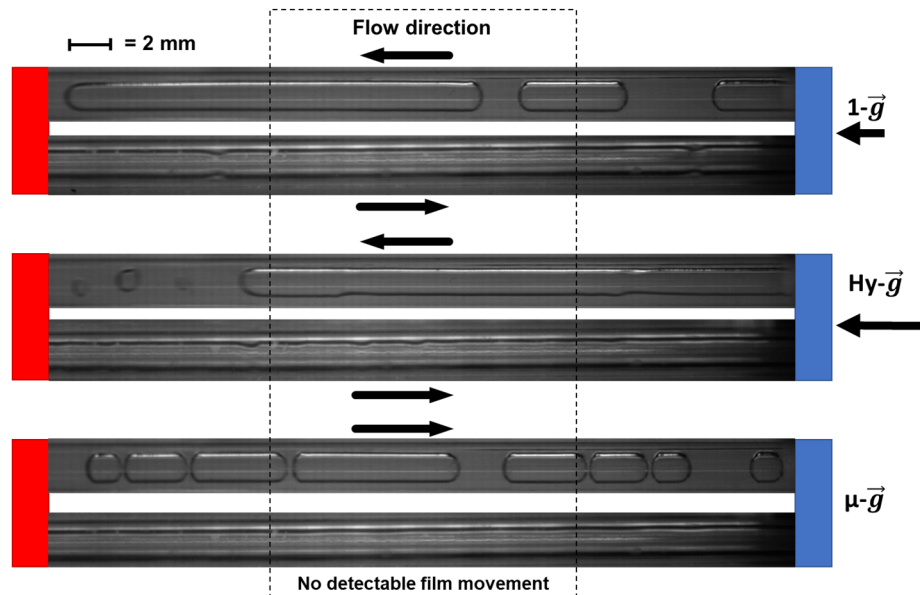


Figure 62 Typical flow pattern obtained with ethanol for high power input (24W). Evaporator side in red, condenser side in blue

From what can be seen from the examples of flow pattern at different power input and gravity level (Figure 60, Figure 61, Figure 62), an overall circulation of the fluid is always present. The slug/plug flow pattern, with increasing characteristic length, is detected in 1g for all power inputs whilst the hyper gravity tends not to show clear slug/plug for medium and high power, where the length of the bubble increases resembling more a semi-annular flow; qualitatively, the motion of the fluid is characterised by a visible increase in reverse flow events frequency. During micro-g phases, the slug/plug is always present, with a sensible reduction in the flow velocity

and acceleration; the power input seems affecting the number of bubbles observed in the channel.

FC-72, on the other hand, shows better performances at low power input (Figure 64) rather than at high power input (Figure 65) where signs of an incipient thermal crisis are shown by TC1, TC2 and TC3. The temperature peaks in the graphs correspond to a μ -gravity period. The abrupt temperature rise is mainly due to two factors: the sudden stop of the fluid caused by the lack of gravitational head, which was able to distribute the less dense part (vapour) towards the top section of the device and the denser part (liquid) towards the bottom, and the transition to a surface tension dominate regime, hindering the movement of the liquid phase.

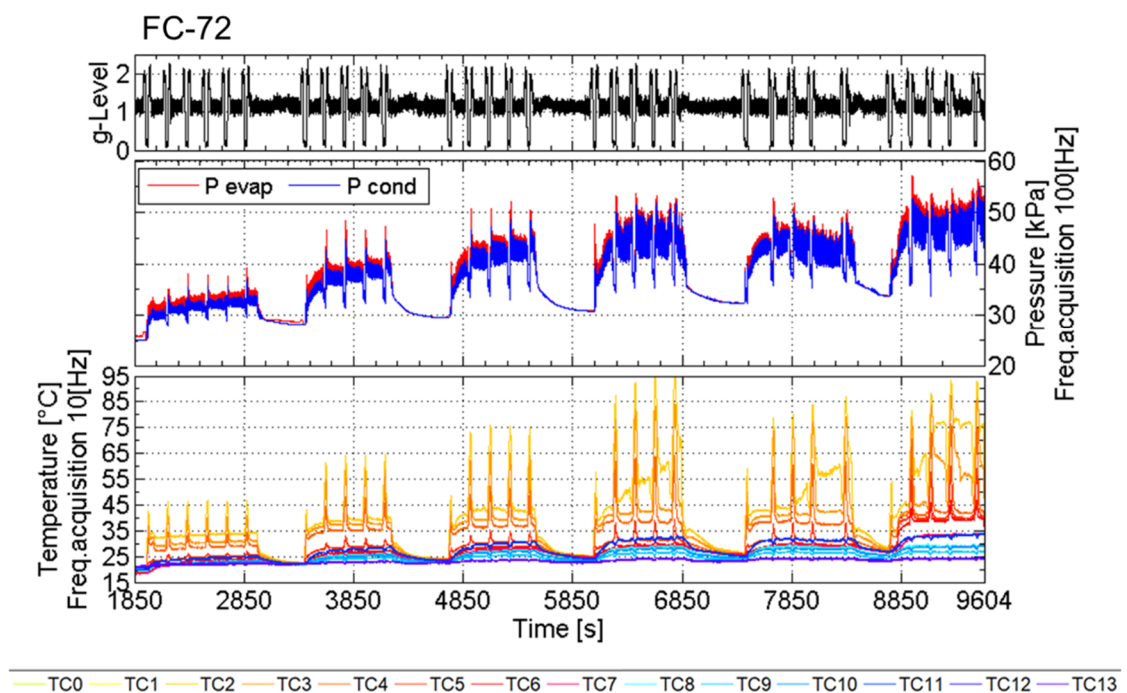


Figure 63 Complete tack of temperature, pressure and z-axis acceleration for FC-72 during the 66th ESA PFC. In the temperature plot, Yellow/red colour shade = Evaporator temperatures; Blue colour shade = Condenser temperatures

If the thermal gradient between evaporator and condenser acts as a promotor of the instabilities that are the base of the PHP functioning, the increased importance of surface tension compared to body forces, seems to be acting as an inhibitor of the thermo-hydrodynamic instabilities governing the PHP. During this phase, dry spots can be obtained in the evaporator region for the combined effect of localised evaporation phenomena and scarce feeding with fresh working fluid. However, this micro-g deterioration of performance, is recorded during a transition phase and not a steady-state functioning of the device.

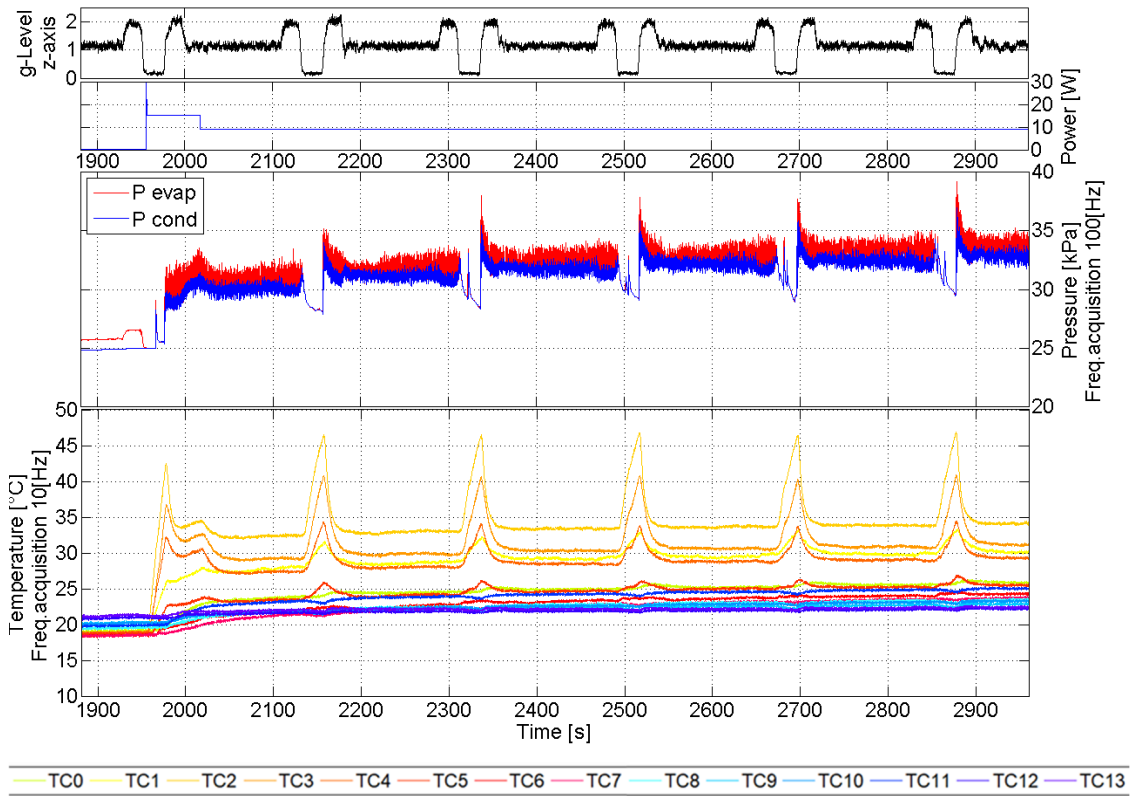


Figure 64 FC-72, detail of parabolae 0 to 6, low heating power. From top to bottom: z-axis acceleration, heating power, pressure signals, temperature signals.

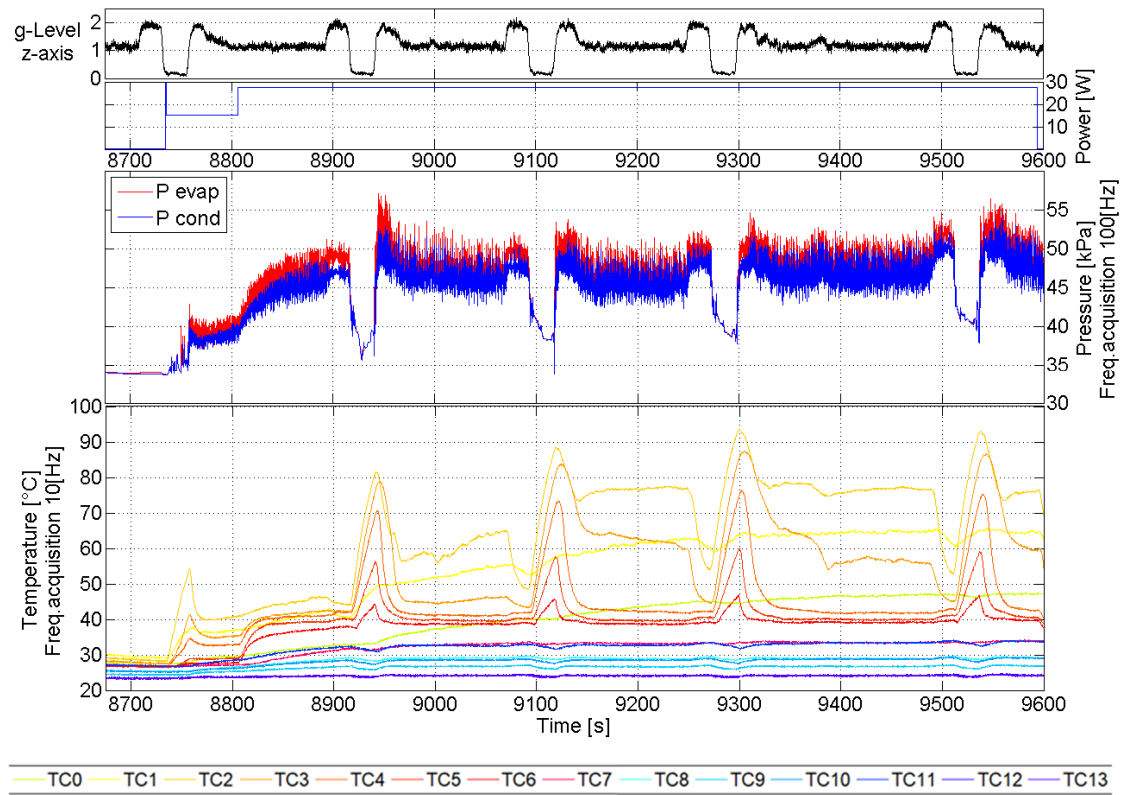


Figure 65 FC-72, detail of parabolae 26 to 30, high heating power. From top to bottom: z-axis acceleration, heating power, pressure signals, temperature signals.

From what can be seen from the examples of flow pattern at different power input and gravity level (Figure 66, Figure 67, Figure 68), an overall circulation of the fluid is always present, similarly to the ethanol.

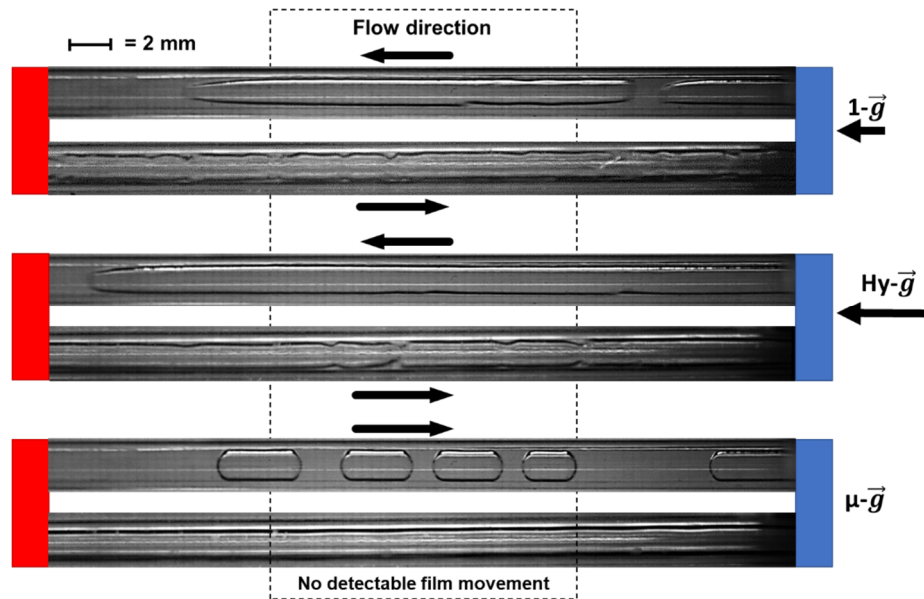


Figure 66 Typical flow pattern obtained with FC-72 for low power input (9W). Evaporator side in red, condenser side in blue

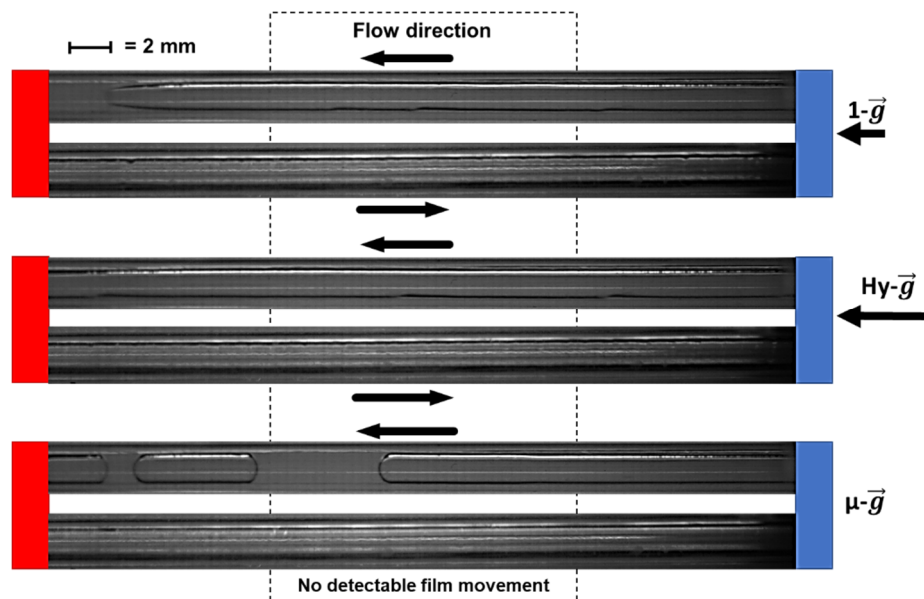


Figure 67 Typical flow pattern obtained with FC-72 for medium power input (18W). Evaporator side in red, condenser side in blue

A clear slug/plug flow pattern is never detected in 1g or hyper-g, where elongated bubbles with deformed interfaces due to the inertial effects evolve in a semi-annular flow pattern; increasing power and gravity seems having an effect on the length of the elongated bubbles, increasing their characteristic length. A clear transition to slug/plug

is triggered by the micro-g phases; a slight increase in the length of the bubbles can be linked to the increase in power input. Qualitatively, the motion of the fluid is characterised by a visible increase in reverse flow events frequency when the gravity and the power increase. During micro-g phases, a sensible reduction in the flow velocity and acceleration is qualitatively appreciable; the increase in power input seems affecting the number of bubbles observed in the channel, evolving towards longer bubbles and an overall higher void fraction. In the next chapters, quantitative values for bubble length, flow velocity, acceleration and void fraction will be provided, in order to define correlations between these parameters and the resulting flow pattern.

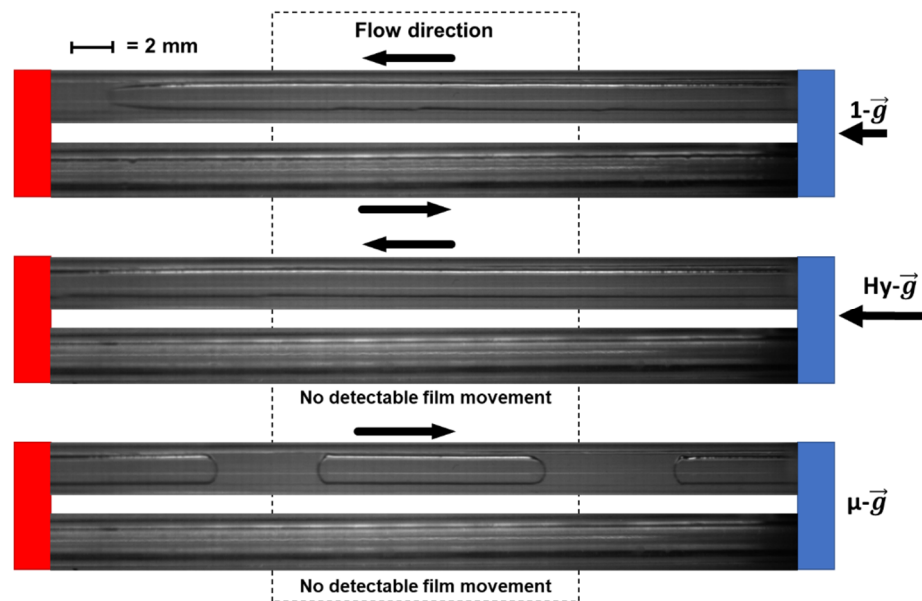


Figure 68 Typical flow pattern obtained with FC-72 for high power input (24W). Evaporator side in red, condenser side in blue

It can be argued that the 20s circa of microgravity, available on a parabolic flight, are not enough to reach a fully developed pulsating fluid flow and what we are observing is just the first part of the transient heating process of this specific combination device-working fluid. We may speculate on this, arguing that at the end of the transient period a full activation will be achieved, but only long-term microgravity experimentation can confirm that, providing information about the time required for the activation, the overheating level of the evaporator reached before the activation and the thermal resistance characteristic of a micro-gravity steady-state.

5.3.3 Start-up in micro-gravity

Estimating the start-up performance of the two working fluid was one of the major aims of the parabolic flight campaign. For this reason, at the occurring of the micro-g, the same power has been provided to the system, previously cooled down to cabin temperature during breaks. As a measure to compare the performance, the energy required to cause a strong pulsation (if achieved), has been estimated as the product of the heating power and the time between the power has been provided and a significant pulsation. Table 24 shows how difficult it is to achieve pulsations in microgravity for ethanol due to the dominant role of surface tension, where the specific heat flux has been calculated as:

$$q'' = \frac{Q}{2\pi d_{in} L_e} \text{ [W/m}^2\text{]} \quad (5-2)$$

where Q is the heat power input in W, d_{in} is the inner diameter of the tube, L_e is the length of the evaporator section. Looking at the FC-72 a pulsation is always recorded, and the energy transferred to the fluid (considering negligible the losses towards the ambient) is shown to be in a narrow range, function of the random distribution of phases in the evaporator at the instant of the power switch on, as confirmed also by the recent work published by Ando et al. [81] in 2018.

Table 24 Activation energy detail in micro-gravity conditions for ethanol and FC-72

Parabola Number	Heat Flux Input [W/m ²]	Microgravity Start-up quality		Start-up energy [J]	
		Ethanol	FC-72	Ethanol	FC-72
0	3.18·10 ⁴	Strong pulsation	Strong pulsation	220	156
6	3.18·10 ⁴	No activation	Strong pulsation	-	166
11	3.18·10 ⁴	No activation	Weak pulsation	-	265
16	3.82·10 ⁴	No activation	Weak pulsation	-	223
21	3.82·10 ⁴	No activation	Strong pulsation	-	161
26	3.18·10 ⁴	No activation	Weak pulsation	-	217

Examples of “Strong” pulsation can be found in Table 25. A pulsation similar to the one obtained with FC-72 at 1.91·10⁴ W/m², with at least one pressure peak equal or above 1kPa can be considered strong. Anything below is considered weak. No activation is when no significative pulsation is detected, and the pressure trend is decreasing.

Table 25 reports pressure trends and consequent temperature trends for the simulated start up in reduced gravity at different heat flux input.

Table 25 Start-up behaviour during a micro-gravity period for ethanol and FC-72

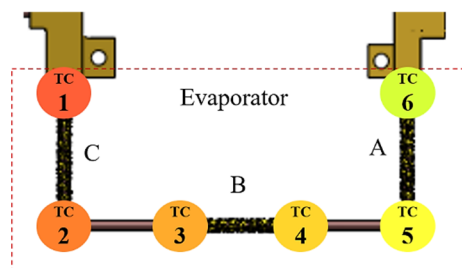
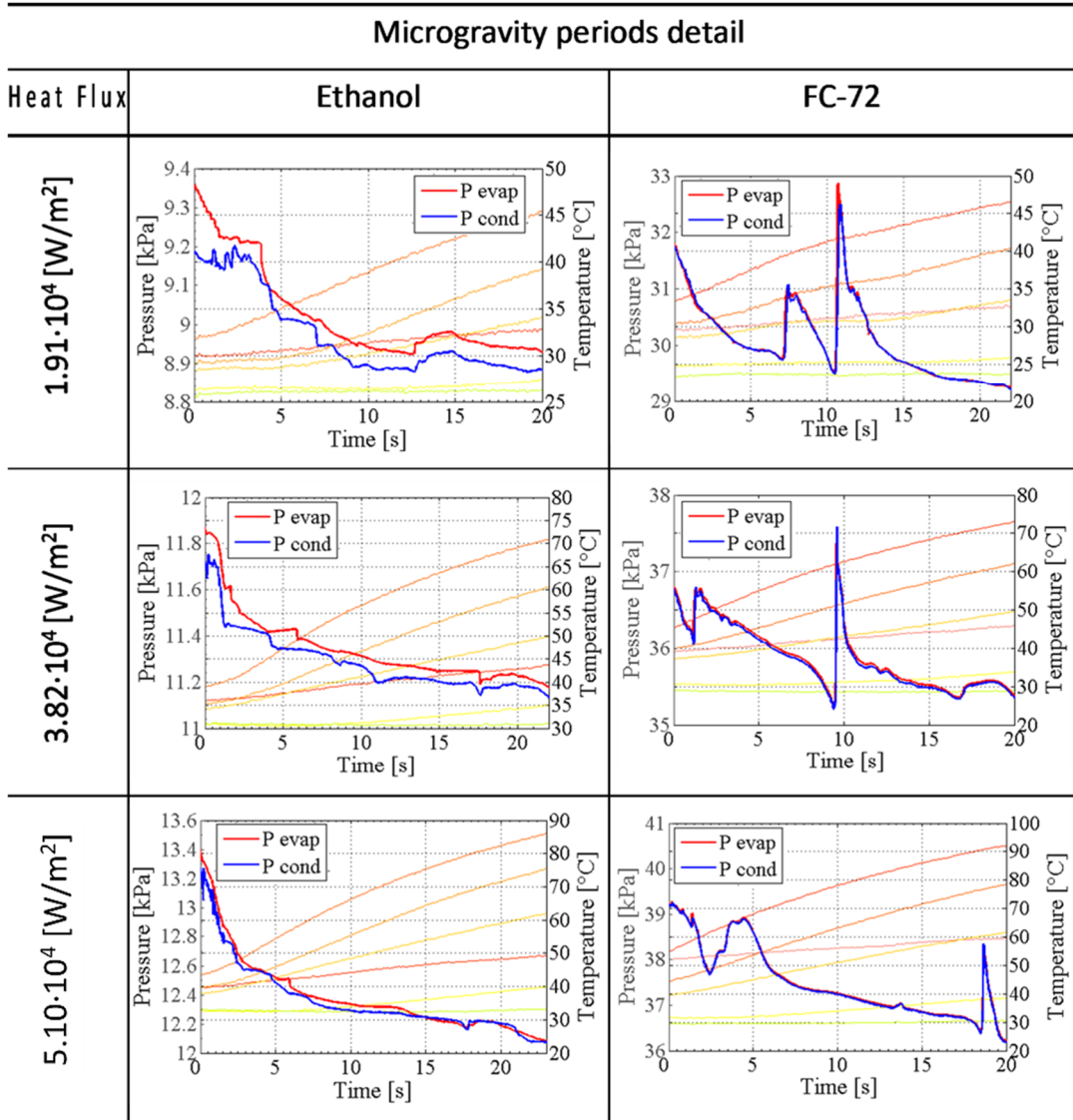


Figure 69 Position of evaporator thermocouples and colours adopted in Table 25

Referring to the schematic of the test cell described in Figure 35, a close up of the evaporator zone with position and colours adopted in Table 25 is provided in Figure 69.

The effect of the pulsation on the temperature is clearly visible in the FC-72 at $1.91 \cdot 10^4$ W/m² case: a change of the slope of TC1, TC2 and TC3 indicates fluid movement in the evaporator.

5.3.4 Void fraction evolution in the SLPHP

The volume averaged void fraction has been estimated processing the high-speed (100fps) imaging acquired during the 66th PFC with the method described in section 4.5. The data from the three gravity levels available on flight have been plotted against the heat power input provided to the test-cell.

As can be seen from Figure 70, the two working fluids establish fluid flows with very different levels of void fraction. A stable slug flow exists when the void fraction is lower than 35%-40%; a transitional flow can be characterised by $35\% < \alpha < 60\%$ while $\alpha > 60\%$ characterises a semi-annular flow. FC-72 shows higher values of α at every gravity level, an indication of a prevalent semi-annular flow pattern as expected for a fluid that is not verifying the static Bond confinement criterion (please refer to Figure 54 for evolution of confinement diameter at 1-g). With ethanol always confined (on ground and consequently also in micro-gravity) in a 2mm channel, a slug/plug flow pattern is guaranteed unless disrupted by inertial effects. FC-72 shows a clear increasing trend of α with the power input while ethanol seems less affected by Q.

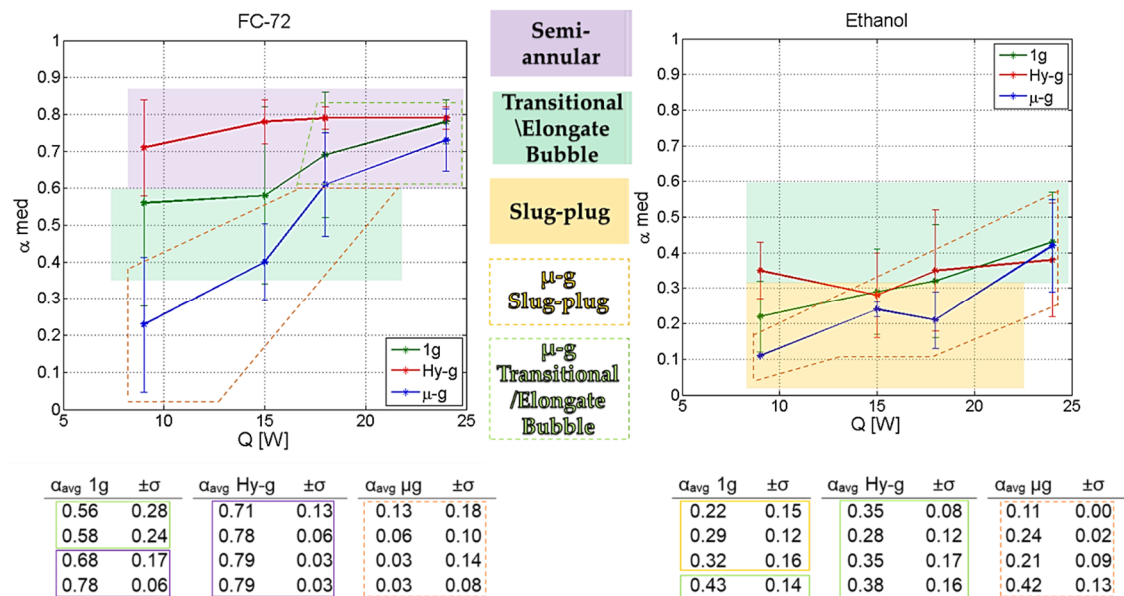


Figure 70 Comparison of evolution of average void fraction with standard deviation during parabolic flight for two working fluids.

The thresholds between flow patterns, as a function of α and Q , have been implemented in a script able to identify the flow pattern from an input of raw high-speed imaging, making the identification process fast and not affected by subjectivity of the operator.

Chapter 6

Developing flow pattern maps of an accelerated two-phase flow

6.1 Flow pattern in two-phase flows

When gas-liquid mixtures flow in a tube, the two phases may distribute through a number of patterns, each characterizing the distribution of liquid and gas. The flow is usually quite chaotic, and these phase distributions are quite difficult to describe. Many descriptions of the flow pattern are available in literature with differences in the name of the flow and number of classes. The nature of the flow patterns varies with channel geometry and size (macro and microscale), fluid physical properties, flow orientation, flow parameters, adiabatic or diabatic condition, etc. For the purposes of this work, we will refer to a basic four regime classification for vertical tubes. For horizontal macro-tubes a fifth pattern is possible, that is the stratified.

- Bubble Flow: The gas phase is approximately uniformly distributed in the form of discrete bubbles in a continuous liquid phase;
- Slug Flow: Most of the gas is located in large bullet shaped bubbles which have a diameter almost equal to the pipe diameter. They move uniformly and are also indicated as “Taylor bubbles.” Taylor bubbles are separated by slugs of continuous liquid which bridge the pipe and contain small gas bubbles.
Between

- the Taylor bubbles and the pipe wall, liquid flows downward in the form of a thin falling film. At low flow rates, the gas-liquid boundaries are well defined:

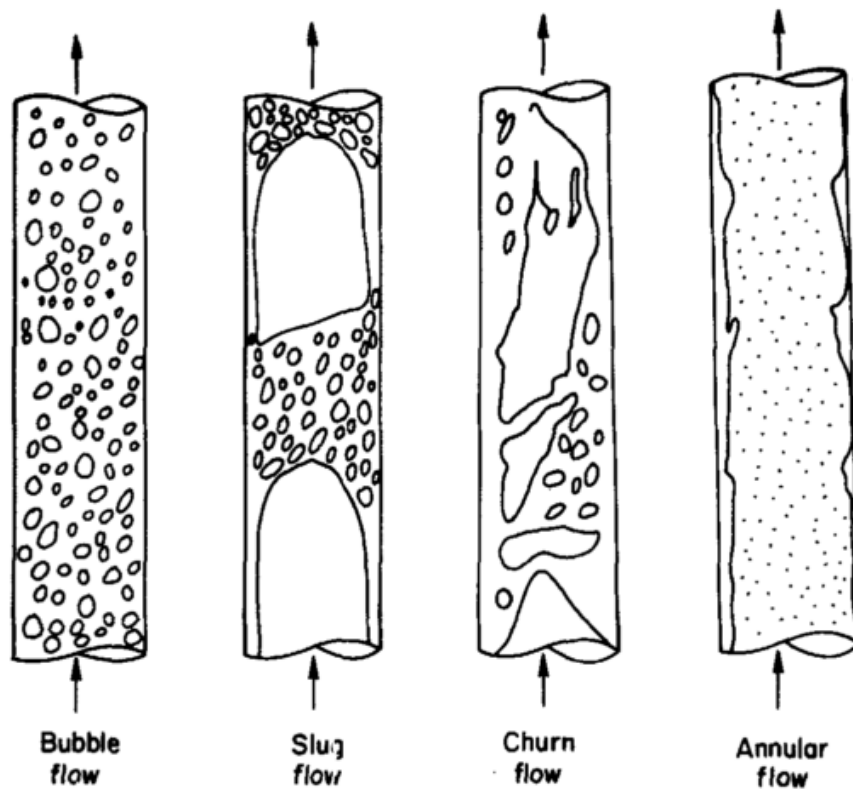


Figure 71 Basic flow pattern in vertical tubes [105]

- Churn Flow: Is similar to a slug flow but much more chaotic and frothier. The bullet-shaped Taylor bubble becomes narrow, and its shape is distorted. The continuity of the liquid in the slug between successive Taylor bubbles is repeatedly interrupted by a high local gas concentration in the slug;
- Annular Flow: Is characterized by the continuity of the gas phase along the pipe in the core. The liquid phase moves along the channel partly as wavy liquid film and partially in the form of drops entrained in the gas core.

The physical mechanisms controlling two-phase pressure drops and heat transfer coefficients are intrinsically related to the local flow patterns and thus flow pattern prediction is an important aspect for heat transfer devices (Figure 72). Therefore, flow patterns and flow-pattern maps play an important role in improving the prediction models for two-phase heat transfer coefficients.

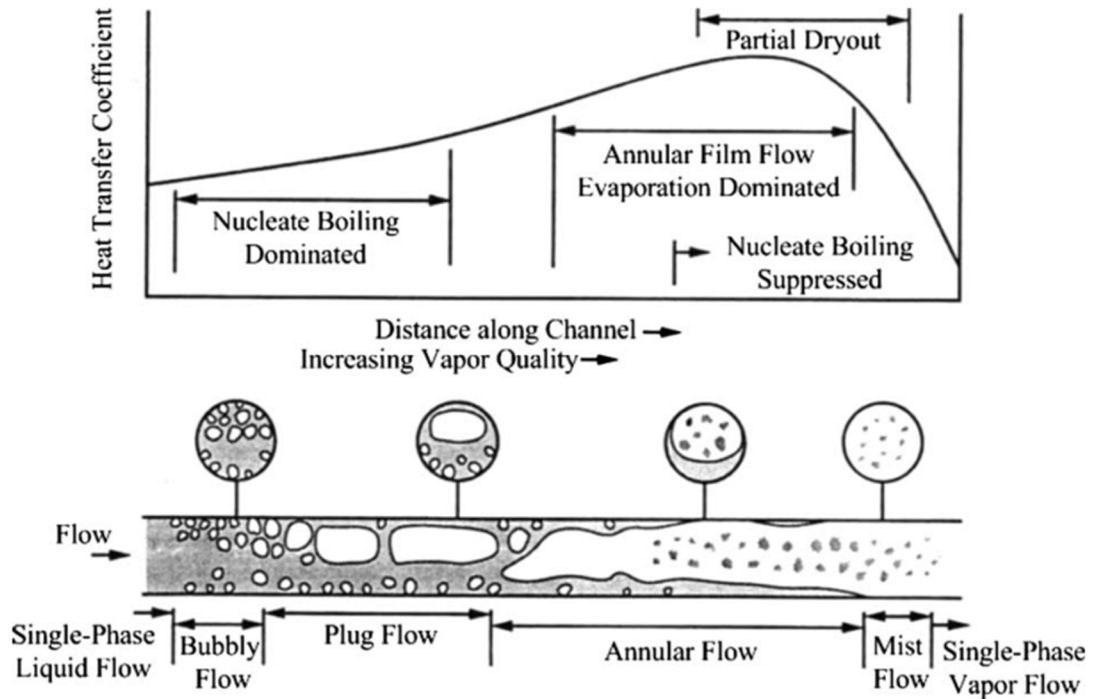


Figure 72 Schematic of flow patterns and the corresponding heat transfer mechanisms and qualitative variation of the heat transfer coefficients for flow boiling in a horizontal tube [106]

6.1.1 Two-phase flow pattern maps

The studies on two-phase flow pattern transitions have led to the development of “macroscale” and “microscale” flow pattern prediction maps for adiabatic and diabatic flow conditions to help in the prediction of which type of flow will exist in a tube for some given boundary conditions. Generally, the gas and liquid flow rates are constant for adiabatic flow and the typical approach to generate those predictions is purely empirical, based on experiments at the specific flow conditions. For a controlled mass flow rate experiment (e.g. rising of injected air in a vertical tube, pump regulated and measured flow in flow boiling), flow pattern observation results are usually plotted on a two-dimensional map in terms of the superficial liquid and gas velocities or in terms of mass flow rate of the two phases with transition criteria to separate the areas corresponding to the various flow regimes. Less frequently, dimensionless numbers are used. Extension of such flow pattern maps to other flow conditions and cross section geometries and sizes is of uncertain reliability since they strongly depend on the particular flow conditions at which they were generated.

Many two-phase flow pattern maps have been proposed. Among them, the most widely used maps for transitions in macroscale vertical, upward flows has been

proposed by Taitel et al. [107] (Figure 73). They suggested physically based transition mechanisms and modelled the transitions on these mechanisms.

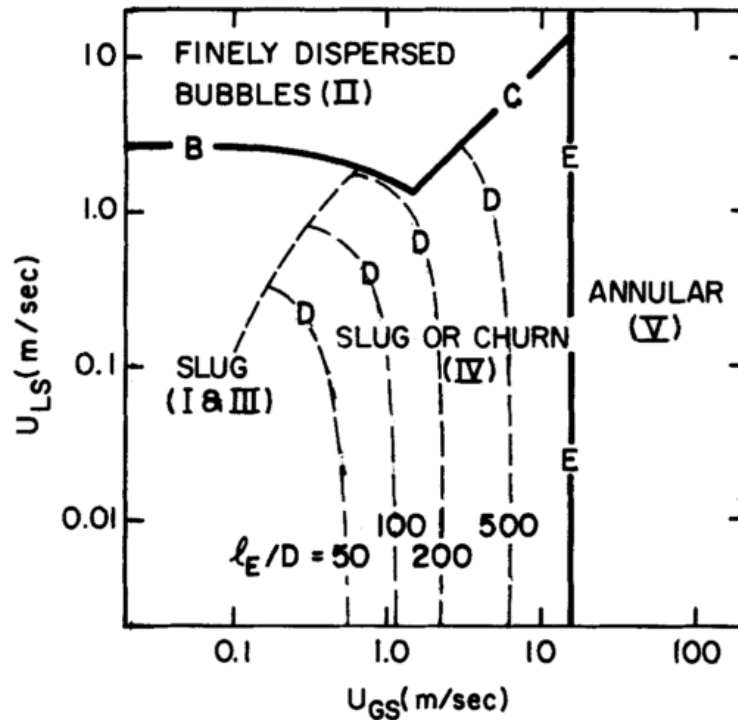


Figure 73 Flow pattern map in 1-g vertical upward air–water flow in 25mm i.d. tube [105]

Experimental activities supported the transition mechanisms with velocity ranges of the liquid and of the vapour phase. The liquid flow rate was investigated in regard to its effect on coalescence on small disperse bubbles, at low-medium velocities, and on the turbulent break-up of large bubbles into.

For millimetric and micrometric channel, the investigation of the transition limit between confined and unconfined flow is of great interest. An alternative definition of microchannel refers to a channel for which the heat transfer coefficient and pressure drop deviate from the predictions from widely accepted models for conventional-sized channels. Ong and Thome [108] proposed a macroscale (Figure 74) and microscale (Figure 75) flow pattern map expressed in terms of mass velocity and vapour quality. From the image processing results, it was observed that the gravity forces are fully suppressed and overcome by the surface tension forces when the confinement number approaches 1. The two-phase flow patterns and transitions have been observed to be a function of channel confinement, mass velocity, saturation temperature. Fluid properties such as surface tension, phase densities, and viscosity were found to affect the flow pattern transitions. The applicability of the maps from Ong and Thome is still restricted to a controlled flow.

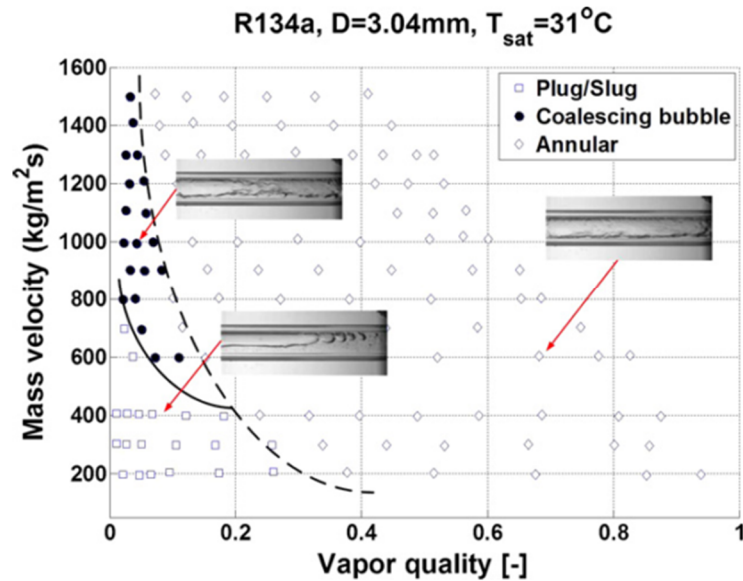


Figure 74 Experimental flow pattern map with transition curves for R236fa, $D = 1.03\text{mm}$ channel at $T_{\text{sat}}=31\text{ C}$, $T_{\text{in}}=27\text{ C}$ and $Co = 0.83$ [108]

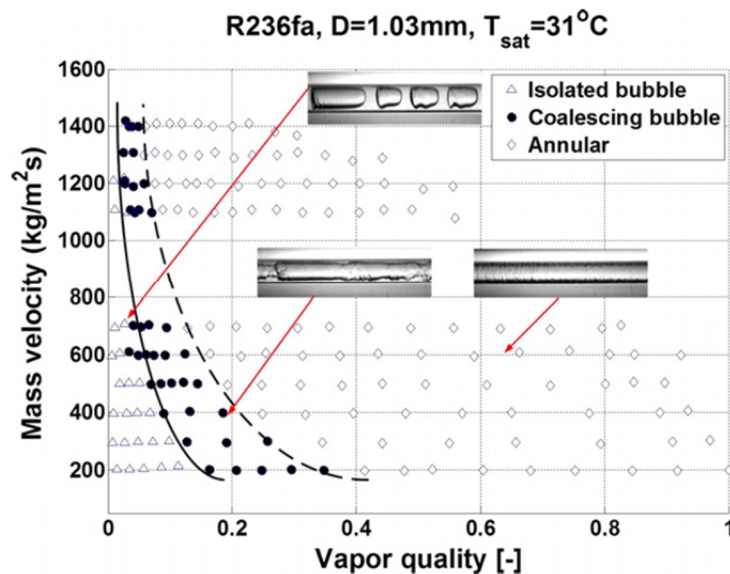


Figure 75 Experimental flow pattern map with transition curves for R134a, $D = 3.04\text{mm}$ channel at $T_{\text{sat}}=31\text{ C}$, $T_{\text{in}}=27\text{ C}$ and $Co = 0.27$ [108]

Transient two-phase flows and flow oscillations, characteristic of the functioning of a Pulsating Heat Pipe, are yet to have a flow pattern map able to describe the flow pattern induced transitions, expressed in function of dimensionless number for a general and wide application.

In their work, Harirchian and Garimella [109], in relation to the conditions under which vapour confinement occurs in micro-channels, stated that channel dimensions and flow properties alone, as proposed in past studies, are insufficient for determining

confinement effects in microchannel boiling. They introduced the new *convective confinement number*, that includes effects of mass flux, inertia, channel cross-sectional area and fluid properties. As a result, a new comprehensive flow regime map valid over a wide range of experimental parameters and channel dimensions has been developed. A quantitative transition criterion, based on non-dimensional boiling parameters, has been proposed.

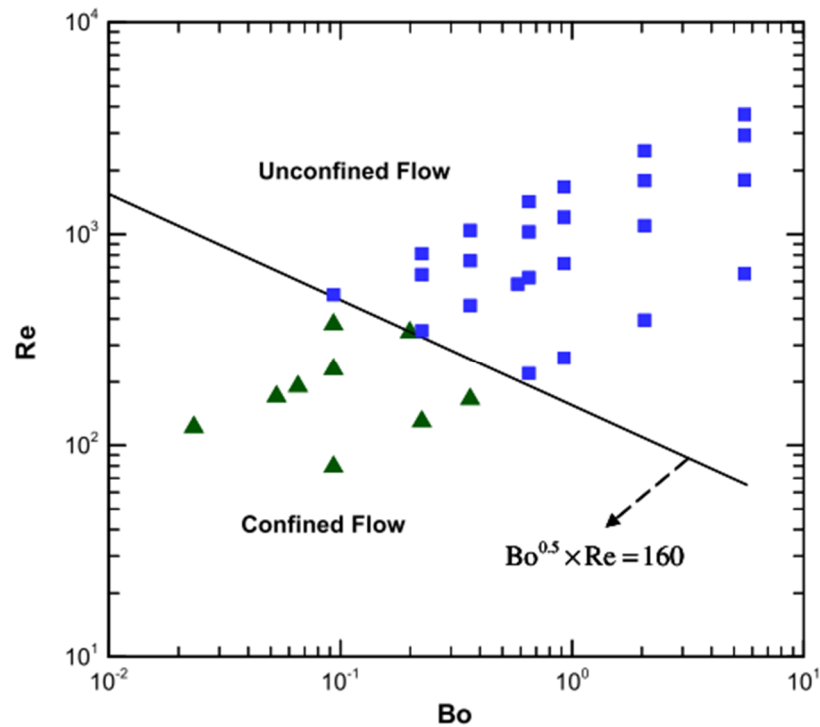


Figure 76 The quantitative transition criterion for physical confinement in flow boiling in relation to Bo and Re number proposed by Harirchian and Garimella [109]

This new flow boiling transition criterion suggested that for $Bo^{0.5} \times Re < 160$, vapor bubbles are confined and the channel should be considered as a microchannel. For larger convective numbers, a physical confinement is not experienced, and the flow can be analysed with conventional correlation for macro scale. As can be seen, the criterion doesn't include terms related to the power heating input; that make it independent from the heat flux.

This is one of the first criterion presented in terms of non-dimensional groups, easily extendable to PHPs. In section 6.2, an attempt of validation of this criterion against experimental data extracted from a PHP-like device is proposed.

6.2 Flow pattern transition in the context of Pulsating Heat Pipe

The thermal performance evaluated as the equivalent thermal resistance of a PHP, is not only dependent on the numerous parameters linked to geometry and working fluid but also strongly coupled with the two-phase flow patterns existing while in operation. A major dependency on the filling ratio (FR) and the heat power input has been found in literature [43].

The interaction between gravitational, interfacial, inertial and viscous forces defines the form of a two-phase flow in micro-channels. Referring to non-dimensional numbers allows one to understand the role of these forces. When surface tension forces dominate gravitational forces, a channel is conventionally defined as capillary and a stratified flow is not observed anymore. A critical Bond number value of 4 [30] has been derived by balancing surface tension and gravitational forces and has been commonly accepted by the PHP community as transition threshold between slug/plug flow to stratified flow typical of thermosyphons, only referring to static conditions obtained in a channel, without considering inertial effects. The corresponding critical diameter is:

$$d_{crit}(Bo) \leq 2\sqrt{\sigma Bo_{crit} / g(\rho_l - \rho_v)} \quad (6-1)$$

The resulting critical diameter for some common working fluids used in PHP has been plotted in Figure 77. For each fluid, the region above the critical curve represents non-confined conditions on ground whilst the region below the critical curve indicates that the fluid is confined in static conditions and in the specific range of temperature; being the term of gravity acceleration g at the denominator of the (6-1), it is easy to understand that for values of g approaching zero, it provides unreasonably high critical diameter values (see Chapter 3.7). The Weber number (We) has been used in the past to mark the transition between confined and unconfined flows; it can be easily rearranged to provide a diameter as output. The same rearrangement can be done with Garimella's (Ga) criterion [109]. They make a step forward compared to the static Bo number, since both consider inertial effects.

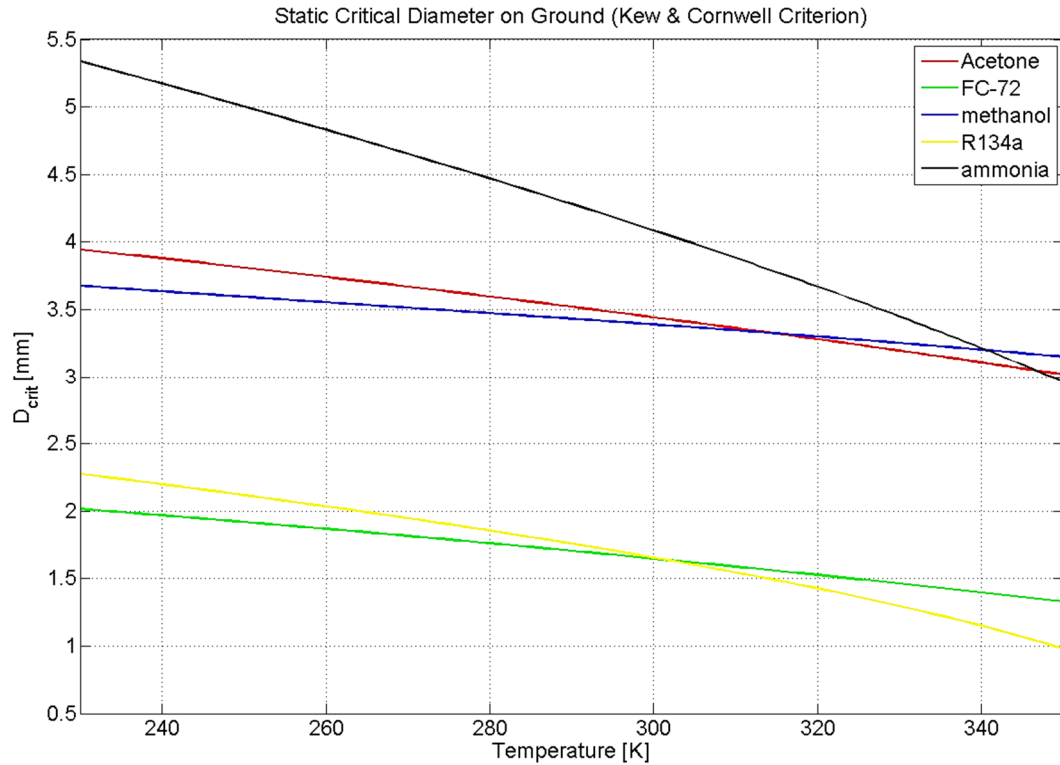


Figure 77 Critical diameter curve for common working fluids in static conditions and in a 230 K to 350 K temperature application range

Inertial effects play an important role on the flow confinement and flow pattern, in the sense that when the velocity is high, the menisci are deformed and a possible rupture of the vapor bubble can be achieved, due to a disruption of the equilibrium liquid-vapour interface. Weber and Garimella criteria are also applicable to define limits for Space applications, as thoroughly explained by Mameli et al. [76]. The corresponding critical diameters are given by (6-2) and (6-3).

$$d_{crit}(We) \leq 4 \sigma / \rho_l u_l^2 \quad (6-2)$$

$$d_{crit}(Ga) \leq \sqrt{160 \mu_l / \rho_l v_l \sqrt{\sigma / g(\rho_l - \rho_v)}} \quad (6-3)$$

To understand the actual meaning of Weber and Garimella criteria for the critical diameter, a 3-axis map, indicating the dependency of d_{cr} from temperature and velocity has been elaborated. For the same pair of values of temperature and estimated average velocity, the information on the critical diameter given by the We criterion (Figure 78a) is extremely high for the lowest liquid bulk velocity compared to the value returned by Ga criterion (Figure 78b), because the Weber criterion does not take into

account the viscous effect and does not provide any information in case of varying gravity field.

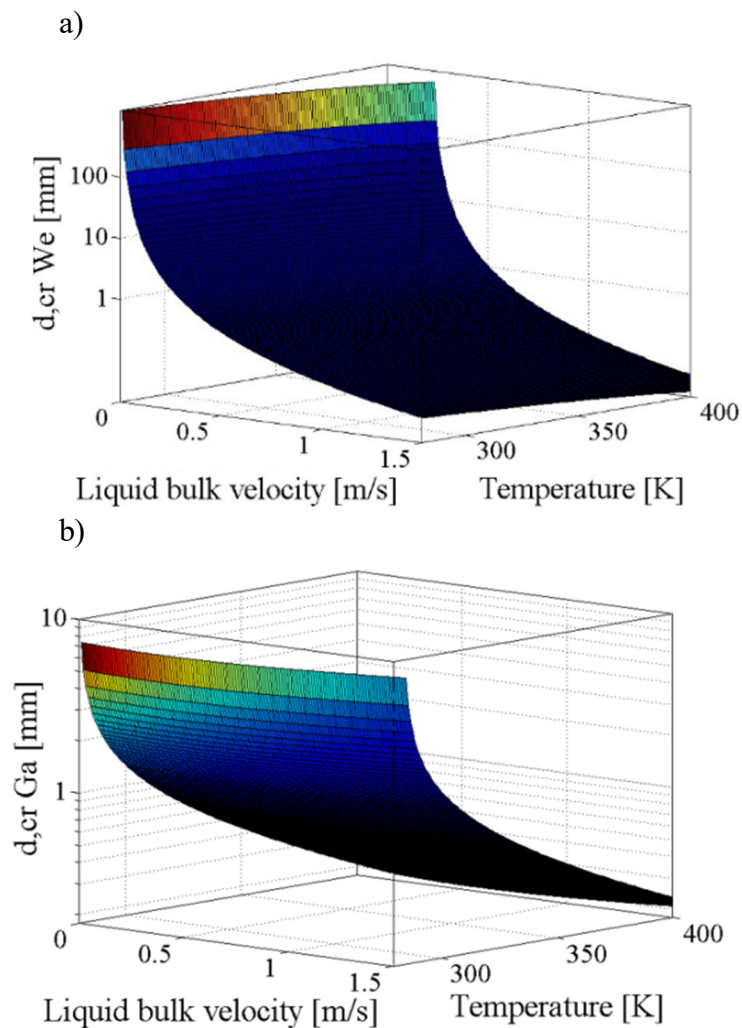


Figure 78 a) Map of critical diameter according to Weber number criterion and b) Garimella number criterion for Ethanol at Earth gravity level.

Garimella's critical diameter equation has been formulated correlating experimental data obtained at Earth gravity conditions and keeping constant mass flow rate, flow boiling conditions and never validated against very specific experimental data on a PHP device, operating under varying gravity level. Given the continuously varying conditions (velocity, temperature, acceleration, gravity field) inside the channels of a PHP designed for space applications, the idea of a static critical diameter might not be the most appropriate for predicting the flow distribution. Since the inertial force plays an important role on the menisci rupture and vapor bubble merging during PHP operation, a critical velocity, derived for a given diameter, has been extracted from Garimella's confinement criterion (6-3):

$$v_{crit}(Ga) = 160 \frac{\mu_l}{\rho_l d^2} \sqrt{\sigma/g(\rho_l - \rho_v)} \quad (6-4)$$

The resulting critical velocity is then a function of the gravity field and temperature. An estimation of the critical velocity for the two fluids object of the investigation, is reported in Figure 79 (Ethanol) and in Figure 80 (FC-72).

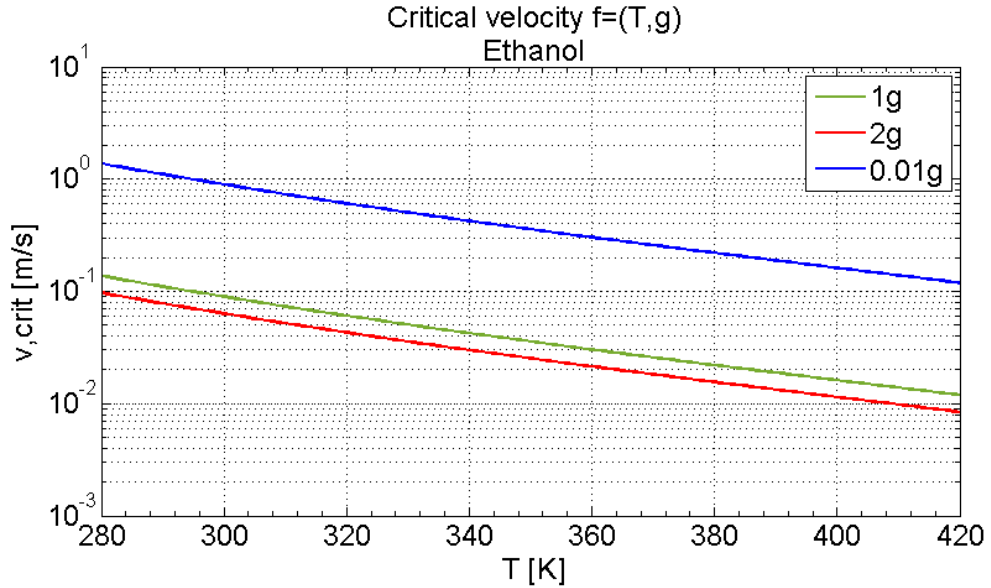


Figure 79 Critical velocity according to Garimella criterion for a 2 mm I.D. tube filled with Ethanol at varying gravity level and over a 140K temperature range

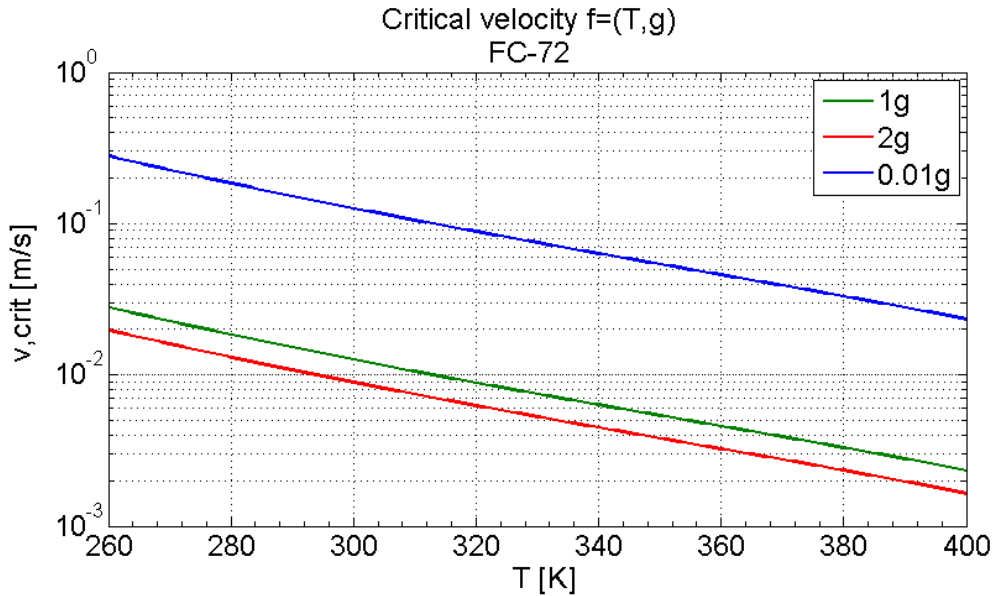


Figure 80 Critical velocity according to Garimella criterion for a 2 mm I.D. tube filled with FC-72 at varying gravity level and over a 140K temperature range

6.2.1 Critical velocity theory verification - Inertial effects on the flow pattern transitions

The role of flow velocity in influencing the flow pattern and the relative importance of body forces is significant. Low flow velocities allow surface tension forces to play a more important role. High velocities cause flow inertia to dominate any surface tension or gravity effect, producing similar flow patterns for all gravity level. Lips et al. [72] highlighted the importance of fluid velocity on the definition of flow conditions ($Bo > 2$, flow governed by hydrodynamics and $Bo < 2$, flow governed by capillary effects), setting a first constant critical value of 0.3 m/s as a threshold. A more accurate attempt to identify the continuous transition between flow patterns in a PHP can be obtained from the ratio between the velocity estimated at a generic time i and the value of critical velocity derived from the Garimella criterion (6-3), for a given and constant value of temperature characterising the i -th timestep:

$$\phi_i = \frac{v_{l,i}}{v_{crit}} \Big|_{T=const.} \quad (6-5)$$

Looking at (6-5), a ratio greater than the unity, should mark the transition to a semi-annular or annular regime (i.e. a deformation of the slug-plug that leads to a break-up of the liquid/vapor interface). Higher velocities are needed to destabilise the slug\plug flow for Ethanol compared to FC-72 due to the higher surface tension. For a given temperature, increasing the g level, leads to a reduction of the critical velocity. In other words, it is more difficult to preserve the slug\plug condition when surface tension is dwarfed by inertial forces. Liquid inertia and surface tension dictate the slug to annular transition.

To check the validity of this criterion, the velocity of the liquid phase has been evaluated in 12 cases via the method presented in section 3.3, for two fluids (FC-72, ethanol) under varying gravity levels and heat power input. The resulting velocity temporal trends have been related to the critical velocity (two red lines representing the critical velocity thresholds for positive and negative fluid velocities) calculated at the fluid temperature and gravity field values characteristic of each case. Figure 81 reports the velocity fields for FC-72 during the three phases of a parabola (1g, Hy-g and μ -g) for the lowest two levels of power input (9W and 15W) while the highest power levels tested (18W and 24W) are shown in Figure 82. Figure 83 and Figure 84

show the same information for Ethanol. As expected, the FC-72 tends to work outside the thresholds or close to it more than the Ethanol for a 2mm I.D. tube given the higher critical diameter according to Bond criterion. For every case, the zones where $|v| > v_{cr}$ have been compared with the high-speed imaging, looking for a transition in the flow pattern. An example is shown in Figure 85, in the form of the ratio introduced in (6-5). Frames a) and c) show examples of non-accurate prediction of the slug-plug flow whilst frames b) and d) show an accurate prediction.

Table 26 Statistic of prediction accuracy of semi-annular flow pattern and slug-plug flow pattern with the presented velocity code (considering a 10% error on the velocity estimation) and according to the critical velocity criterion. 'N/A'= Flow pattern not present; '-'='Data not available.

Fluid	Power input [W]	Gravity Level	Verit [m/s]	Semi-annular and $v > v_{cr}$ predicted [%]	Slug-plug and $v < v_{cr}$ predicted [%]
Ethanol	9	1g	0.087	3	89
Ethanol	9	Hy-g	0.067	36	56
Ethanol	9	μ -g	0.714	N/A	100
Ethanol	15	1g	0.073	46	30
Ethanol	15	Hy-g	0.063	38	37
Ethanol	15	μ -g	0.708	N/A	100
Ethanol	18	1g	0.078	42	46
Ethanol	18	Hy-g	0.06	60	11
Ethanol	18	μ -g	0.64	N/A	100
Ethanol	24	1g	0.077	18	38
Ethanol	24	Hy-g	0.058	-	-
Ethanol	24	μ -g	0.62	N/A	100
FC72	9	1g	0.012	87	
FC72	9	Hy-g	N/A	-	-
FC72	9	μ -g	0.103	0	94
FC72	15	1g	0.012	82	N/A
FC72	15	Hy-g	0.0093	74	N/A
FC72	15	μ -g	0.0965	N/A	99
FC72	18	1g	0.0011 7	56	N/A
FC72	18	Hy-g	0.008	52	N/A
FC72	18	μ -g	0.093	N/A	99
FC72	24	1g	0.011	47	N/A
FC72	24	Hy-g	0.009	35	N/A
FC72	24	μ -g	0.099	N/A	99

FC-72

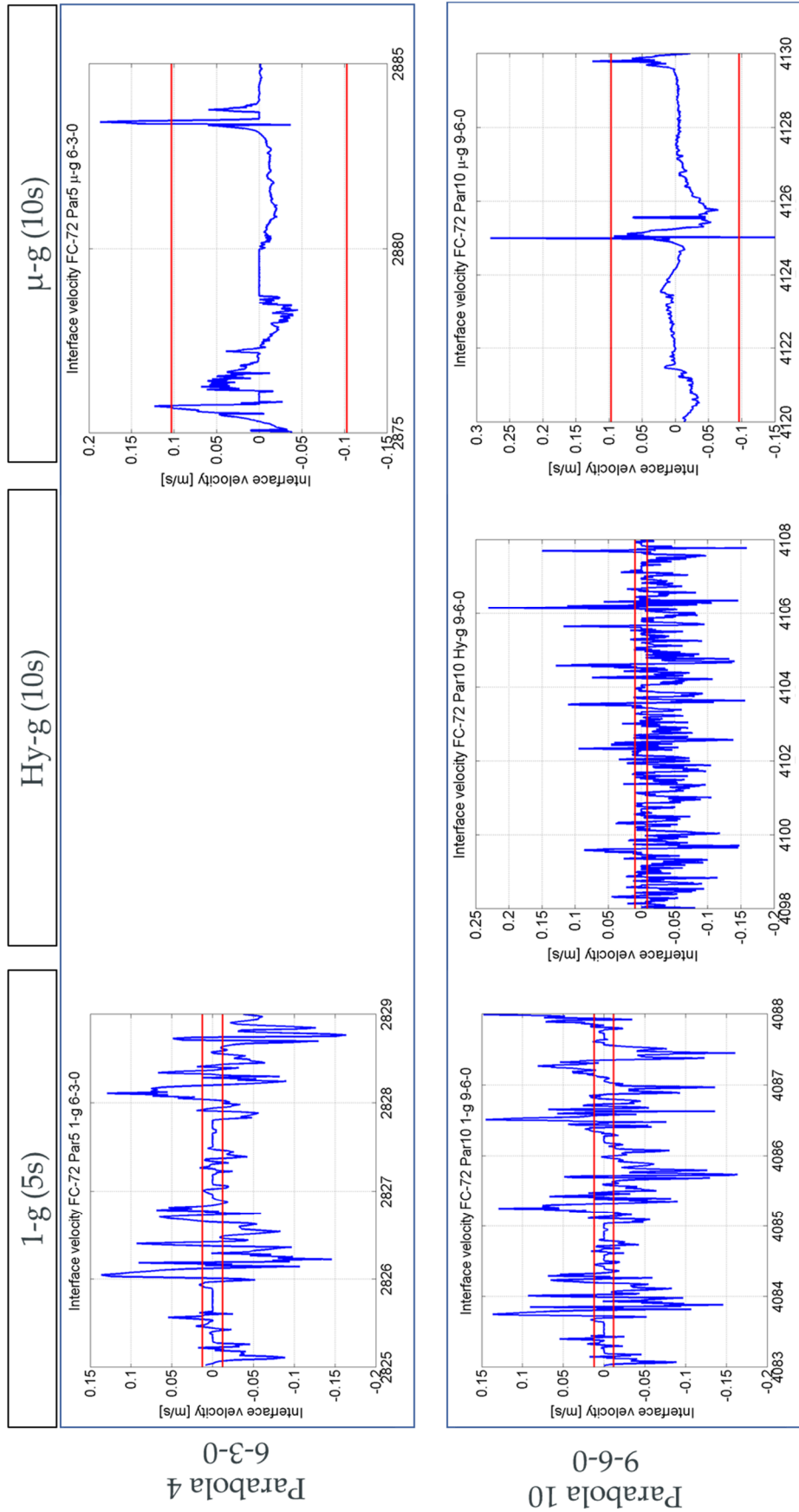


Figure 81 Velocity signal obtained for FC-72 at 9W and 15W under varying gravity levels and critical velocity thresholds (in red)

FC-72

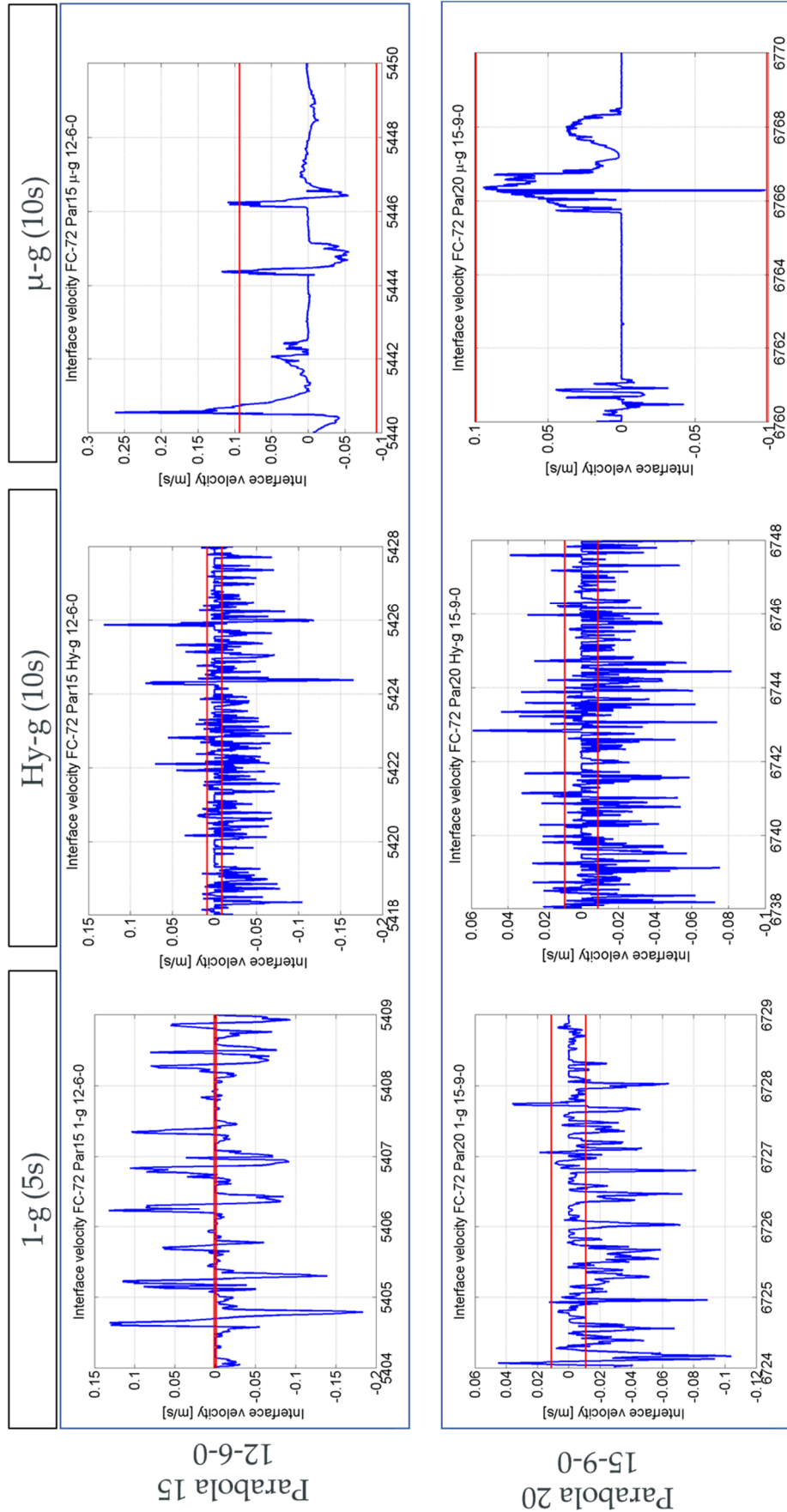


Figure 82 Velocity signal obtained for FC-72 at 18W and 24W under varying gravity levels and critical velocity thresholds (in red)

Ethanol

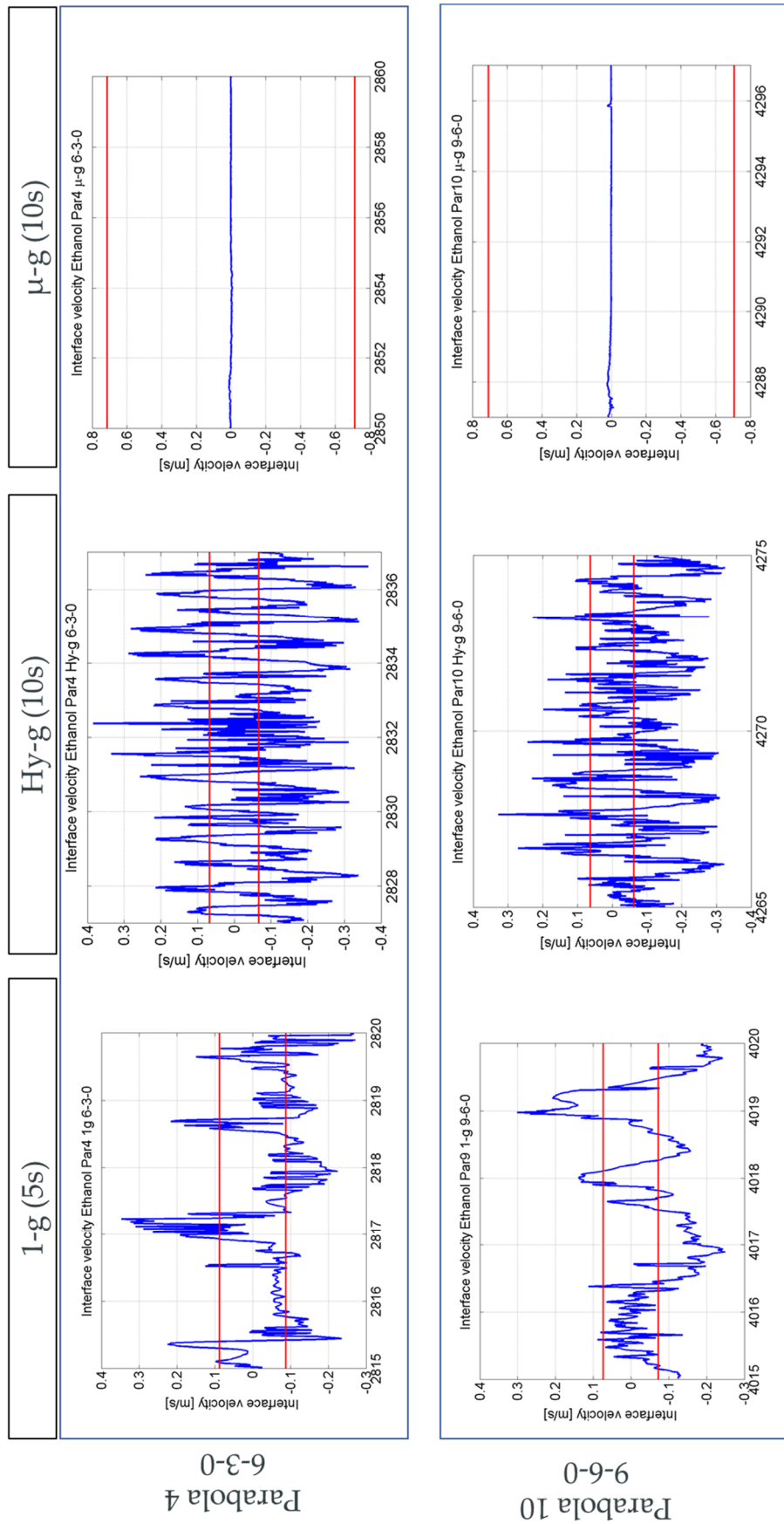


Figure 83 Velocity signal obtained for Ethanol at 9W and 15W under varying gravity level and critical velocity thresholds (in red)

Ethanol

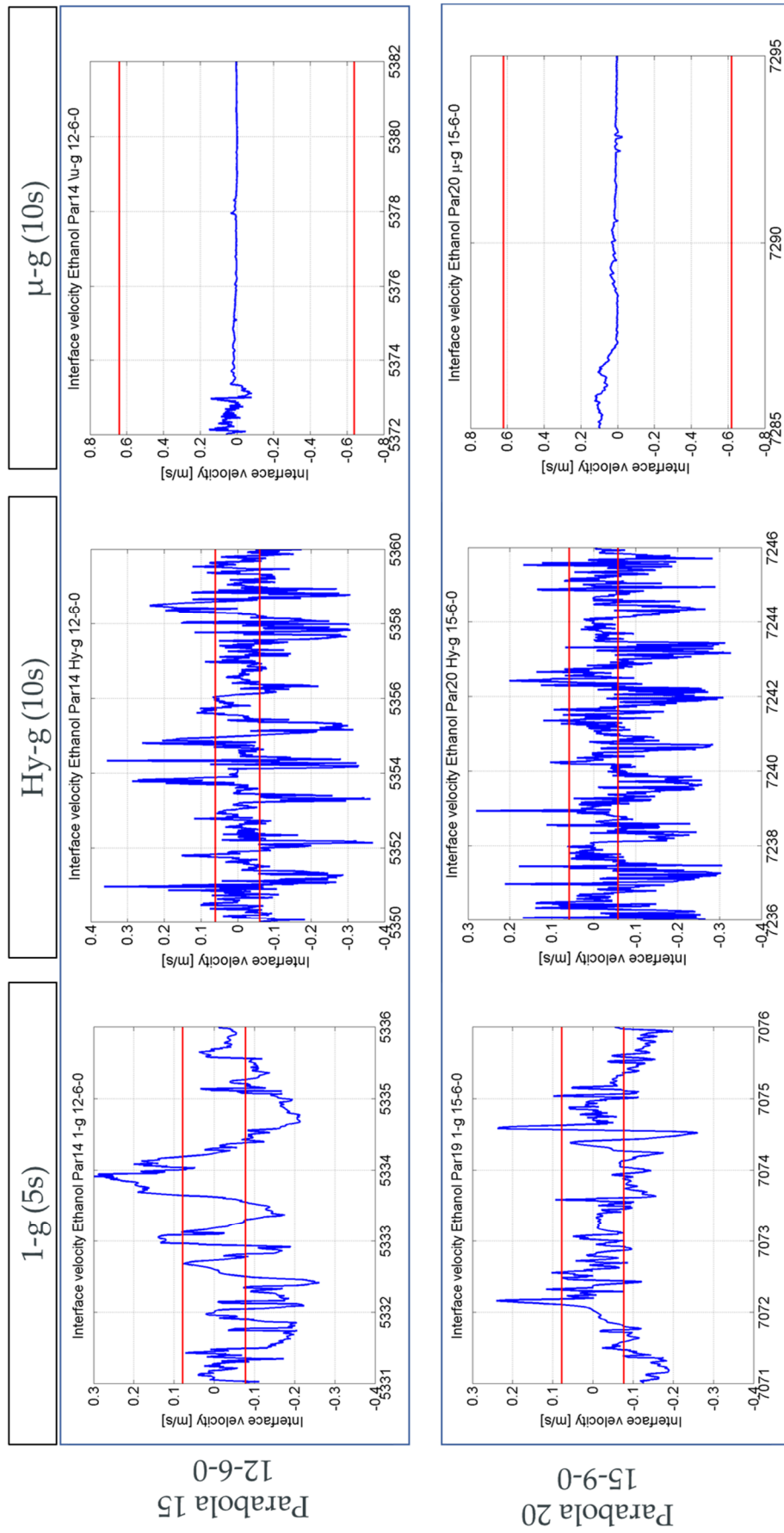


Figure 84 Velocity signal obtained for Ethanol at 18W and 24W under varying gravity levels and critical velocity thresholds (in red)

This novel analysis led to the conclusion that, although in some cases a value of $\phi > 1$ indicates a condition of transitional flow pattern or a semi-annular flow pattern, it cannot be extended to every case and therefore cannot be used as a general rule to define the flow pattern in a PHP.

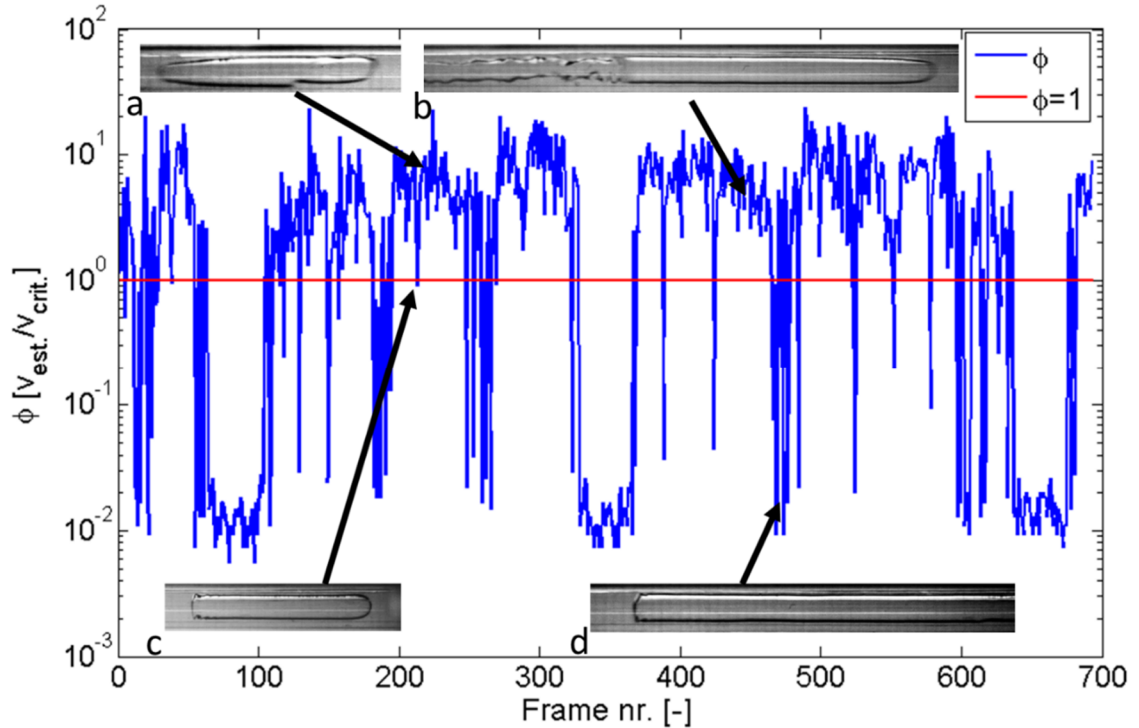


Figure 85 Ratio between estimated velocity and critical velocity for 2mm sapphire tube filled with FC72, during 1g period; all properties evaluated at 23°C. Frames a) and d) shown non-accurate prediction while frames b) and c) truly describe the flow pattern. Acquisition frequency: 100fps.

6.2.2 Role of velocity, acceleration and bubble length in flow pattern transitions and bubble break up

The cause of the low accuracy of the previously presented criterion may be found in the role of the actual acceleration of the liquid, as a result of all the forces acting on the fluid (gravitational and body forces induced by thermal phenomena) not taken into account in the Garimella criterion that just considers the gravitational acceleration field. Among the parameters affecting the two-phase flow pattern, acting especially on the coalescence of bubbles and then on the resultant void fraction, the literature available includes the length of the bubble as one of the most relevant. Thome et al. [25] proposed a mechanistic multiscale mapping of two-phase flow pattern in microchannels illustrating the strong dependency of heat transfer on bubble frequency, lengths of the bubbles and liquid slugs, and the liquid film thickness δ . Xu et al. [110],

while investigating a PHP filled with water and methanol, related the length of the vapour bubble to break-up affirming that very long vapor plugs were observed for methanol PHP but not observed for the water PHP, due to the vapor plug break-up mechanism. A numerical study conducted on the effect of different parameters on confined bubble break-up [111], based on the VOF model developed by Georgoulas et al. [112] [113], suggests the length of the bubble is affecting the resulting liquid dynamics and the consequently the break-up mechanism responsible for flow regime transitions within PHPs (Figure 86).

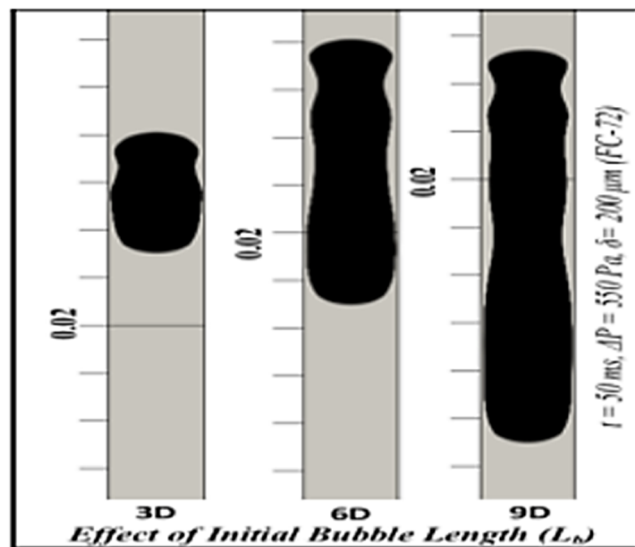


Figure 86 Effect of initial bubble length on the liquid dynamics, responsible for break-up phenomena [111]

To the best knowledge of the author, the role of the vapour plug length has not been correlated to velocity and acceleration of the fluid in the context of PHP or flow boiling. Batchelor [114], studying interfacial disturbances resulting from gravitational instabilities around the upper surface of a unconfined bubble rising through liquid, describes the growing process of infinitesimal disturbances to an extent where they may become large enough and proceed at a rate fast enough to overcome the smoothing action of extensional motion of the interface and cause finite-amplitude effects leading to break-up of the bubble. There is not a unique value of the break-up radius for a given gas-liquid system, but it depends on the initial magnitude of the disturbance generated by external causes. In this work, an attempt to extend this concept to a confined flow has been made. However, a detailed study of the disturbance propagation is not the objective of this study.

The difference in density between the two phases and the flow conditions (velocity and acceleration), are then responsible for the generation and propagation of disturbances. In a confined flow, disturbances generated on the advancing interface are transported down the side of the bubble into the liquid film due to the movement of the rising\descending bubble. In a PHP this mechanism is even more complicated, given the frequent inversion of the flow direction. In this study, break up events have been recorded during direct and reverse flow phases proper of a PHP device. The two break up mechanisms can be described as follow:

- During a direct flow phase, a co-current liquid-vapour flow with slip ratio generally greater than 1, causes propagation of small disturbances from the advancing meniscus into the liquid film. Local thickening of the liquid film (ridge) is observed with spatial distribution and radial extension linked to the amplitude and frequency of the initial disturbance with consequent ununiform liquid entrapment between vapour bubble and wall. The frequency of the ridges tends to increase with the increase of the gravity field (1-g and Hyper-g level of a parabolic flight), in agreement with [114];
- During a reverse flow phase (Figure 87), when a short period of counter-current liquid-vapour flow occurs, given the inertia of the liquid bulk, intense disturbances are generated causing local thickening of the liquid film with spatial distribution and radial extension linked to the amplitude and frequency of the initial disturbance with consequent ununiform liquid entrapment between vapour plug and wall. This condition is generally more likely to lead a break up.

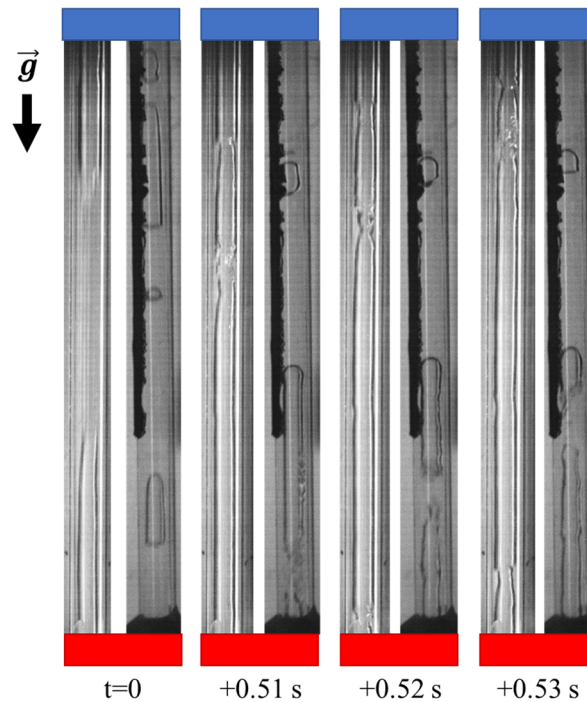


Figure 87 Break up event during a reverse flow. Ethanol, 1g, 18W power input.

For a stationary bubble confined in a channel, in a condition of dominance of surface tension over viscous forces (low Ca number), a steady shape exists. This shape no longer exists when the viscous forces elongate the bubble. The elongation of the bubble in adiabatic conditions leads to a decrease in the vapour pressure, allowing the ridges to locally penetrate in the body of the vapour plug, locally narrowing the cross section. The break up takes place when the local balance of forces due to the surface tension (calculated with the radius of the ridge) overcomes the vapour pressure. When the vapour pressure becomes lower than the saturation pressure at the specific temperature of the fluid flow, condensation phenomena might arise along the liquid film-to-vapour interface creating a more favourable environment for break-up events. Elongated bubbles allow the disturbances to travel longer along the tube with a vapour pressure field reduced compared to the stationary case, increasing the probability of a break up event and affecting the transport phenomena in the Taylor flow. The evolution of bubble length and its relevant role in transport phenomena has been investigated in flow boiling conditions by Laboire et al. [115]. This suggests the necessity to introduce the length of the vapour plug as characteristic length in the conventional non-dimensional numbers.

6.2.3 The proposed flow pattern map

Following the rationale proposed in the previous section 6.2.2, three modified non-dimensional numbers that consider velocity of the fluid, actual acceleration of the fluid and vapour bubble length have been introduced to obtain a flow map for the very specific case of oscillating thermally-induced two-phase flow inside a PHP-like device:

$$Bo_l^{*0.5} = \left[\frac{\rho}{\sigma} \left(\frac{dv}{dt} \right) \right]^{0.5} D \left(\frac{l_b}{D} \right) \quad (6-6)$$

$$Fr_l^* = \frac{v}{\sqrt{\left(\frac{dv}{dt} \right) D \left(\frac{l_b}{D} \right)}} \quad (6-7)$$

$$We_l^* = \frac{\rho v^2 D}{\sigma} \cdot \left(\frac{l_b}{D} \right) \quad (6-8)$$

where the subscript l indicates the well-known numbers are considering the length of the vapour bubble as characteristic length; du/dt is the actual acceleration of the liquid phase replacing the fixed value of g , already adopted for the estimation of the liquid film thickness in micro tubes slugs by Moriyama and Inoue [73] (where the acceleration is easily derived from the velocity estimation method described in section 3.3); D is the internal diameter of the channel; l_b is the length of the longest bubble in the channel for every frame analysed, considered the most relevant length. In order to quantify the conditions that lead to a break up events, the modified Bond number (Bo_l^*) and a combination of Fr_l^* and We_l^* has been evaluated, to relate the effect of interface disturbance propagation and the ability of the flow to create and preserve bubbles (if the surface tension of the fluid decrease its importance because of higher momentum transfer between the phases) to the effect of the actual acceleration on the confinement conditions. For two fluids, four power inputs and the three gravity levels available on a parabolic flight, a novel flow pattern map with indication on the break up limit and coalescence limit, has been proposed. The internal diameter of the pipe has been kept constant to 2mm. As expected, the fluid in sub-critical diameter condition ($d_{cr,Bo} > D$, ethanol in Figure 88) is mainly working in slug-plug regime. Transition to semi-annular are obtained at the highest power input and in Hy-g, alternated with slug-plug. Two zones of slug-plug are easily recognisable:

- Micro-gravity Slug-Plug: the region approximately contained in the rectangle delimited horizontally by $Fr_l^{0.5}We_l^{0.25} < 10^0$ and vertically by $Bo_l^{0.5} < 10^0$ belongs to μ -g conditions, characterised by non-activation of the devices (no pressure oscillation detected and quasi-constant increase of the evaporator temperature) and therefore low velocities of the fluid and low accelerations. The modified Bond number is the lowest registered among all cases analysed, also influenced by the short length of the vapour plugs, as shown in Figure 91. Surface tension is dominating over inertia and the length of the bubble is comprised between $2xD$ and $6xD$ for most of the time. Only at 24W, bubble length seems to increase drastically up to $22xD$. That can be explained with the sudden decrease of ΔP at the ends of the bubble, allowing the bubble to expand, decreasing the vapour pressure of the bubble.
- Fully activated Slug-Plug: the velocities involved are one order of magnitude higher than the micro-g cases. The range of modified Bo number goes up to 40 and the group $Fr_l^{0.5}We_l^{0.25}$ slightly decreases with $Bo_l^{0.5}$ suggesting a decreasing in the dominance of surface tension and a limitation of the dynamic of the bubble linked to its length. High concentration of bubble coalescence events, events that lead to a sensible increase in bubble length, have been noted along the line marking the upper limit of the operational points nebula.

Semi-annular operational points, magenta square markers in Figure 88, occupy the right-hand side of the nebula. Long bubble length is expected from Hy-g and 1-g high power input conditions. The slug-plug flow, in facts, tends to increase its length with the power input at 1-g and Hy-g gravity levels. Perturbations can travel more along a bubble weakened by its length, a high slip ratio between the two phases and sudden peaks of acceleration during inversion phases, typical of the oscillating/pulsating motion. An anomaly in the distribution of break-up events has been noticed along the line that marks the right limit of the semi-annular operational points nebula. The slope of the right boundary line defines a decrease of the modified Bond number with a reduction of the velocity of the flow or a reduction of the bubble length due to a less harsh dynamic of the fluid. A clear transition zone, between slug-plug and semi-annular is visible.

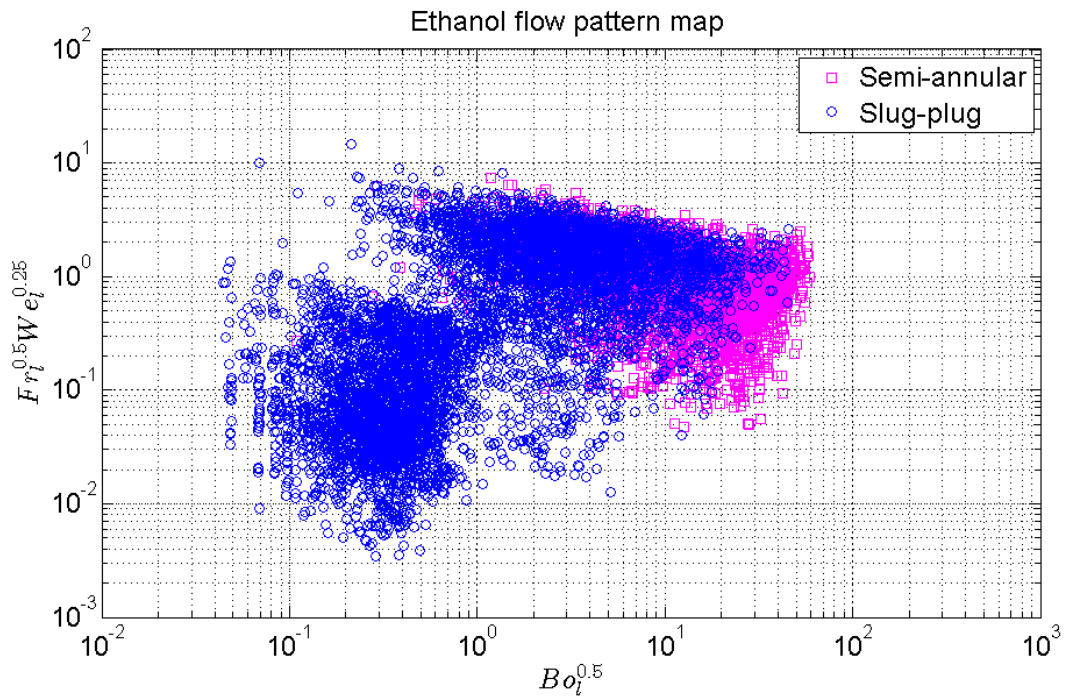


Figure 88 Ethanol flow pattern map in terms of dynamic non-dimensional groups with bubble length as characteristic; adiabatic section of a single loop PHP

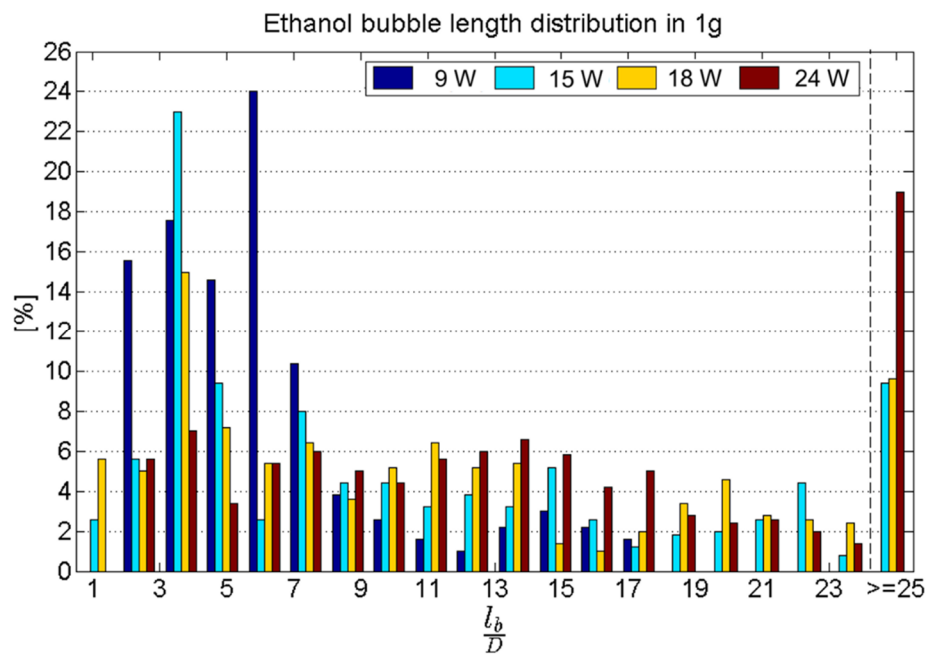


Figure 89 Statistic of the bubble length to diameter ratio for ethanol in 1g at four power level. Sampling period 5 s at 100 fps, HFOV = 50mm

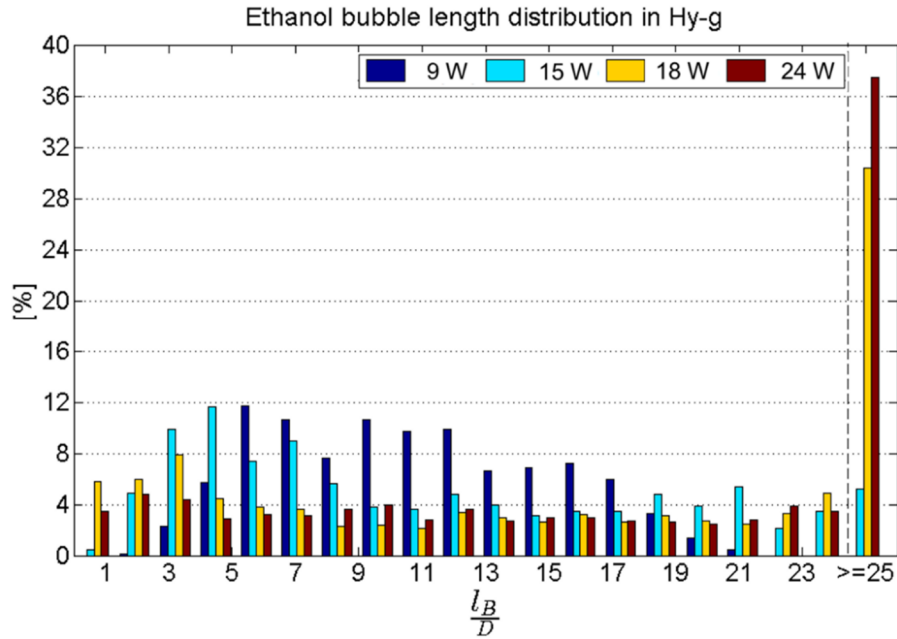


Figure 90 Statistic of the bubble length to diameter ratio for ethanol in Hy-g at four power level. Sampling period 10 s at 100 fps, HFOV = 50mm

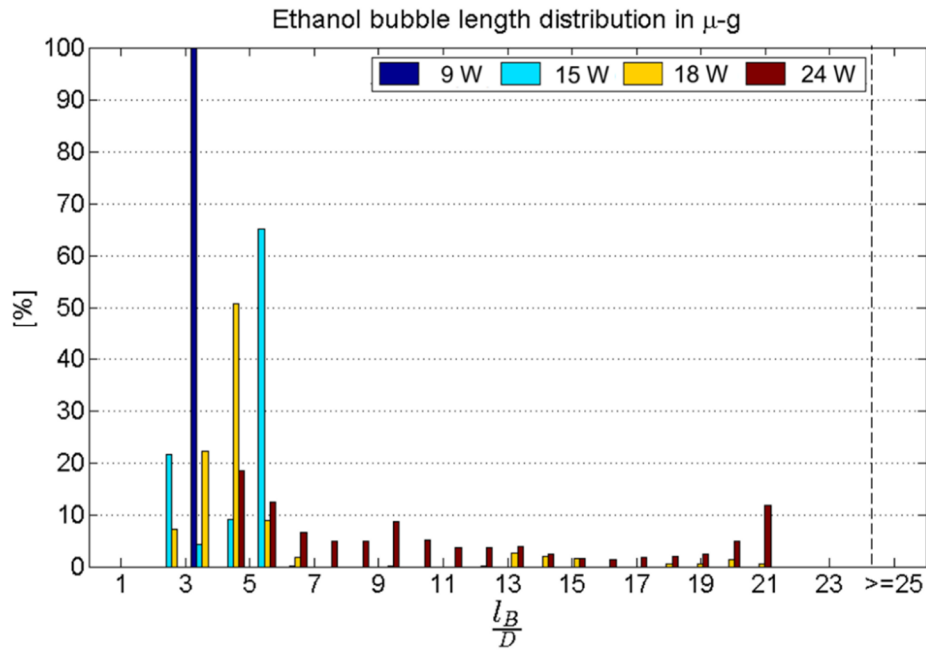


Figure 91 Statistic of the bubble length to diameter ratio for ethanol in μ -g at four power level. Sampling period 10 s at 100 fps, HFOV = 50mm

The fluid in non-critical diameter condition ($d_{cr,Bo} < D$, FC-72 in Figure 92) is mainly working in semi-annular regime, being subject to stratification under gravity levels greater than that of Earth. Slug-plug conditions are exclusively obtained in μ -g. The distinction between the two regimes is clearer when compared to the case with

ethanol. A transition zone is still visible but is narrower than is the case with ethanol. The lower surface tension and higher dynamic of the flow seem deterring coalescence phenomena characteristic of the upper limit of the nebula. From Figure 95, we can observe the effect of a partial activation (isolated pulsation) on the bubble length during a μ -g period. At 24W, the bubble length is the highest compared to the other power levels, indicating a vapour production activity. The flow pattern observed is still slug-plug, meaning that we are still in surface tension dominant conditions. In the other regimes, Figure 93 and Figure 94, the dominant semi-annular\annular flow pattern can be described by the length of the bubble equal to the length of the channel for most of the frames analysed at any power level.

Overlapping the two operational points maps, a generalised map independent from the working fluid can be obtained (Figure 97). That map shows a general accordance on the flow pattern transition boundaries and operational limits given by the break up and coalescence events.

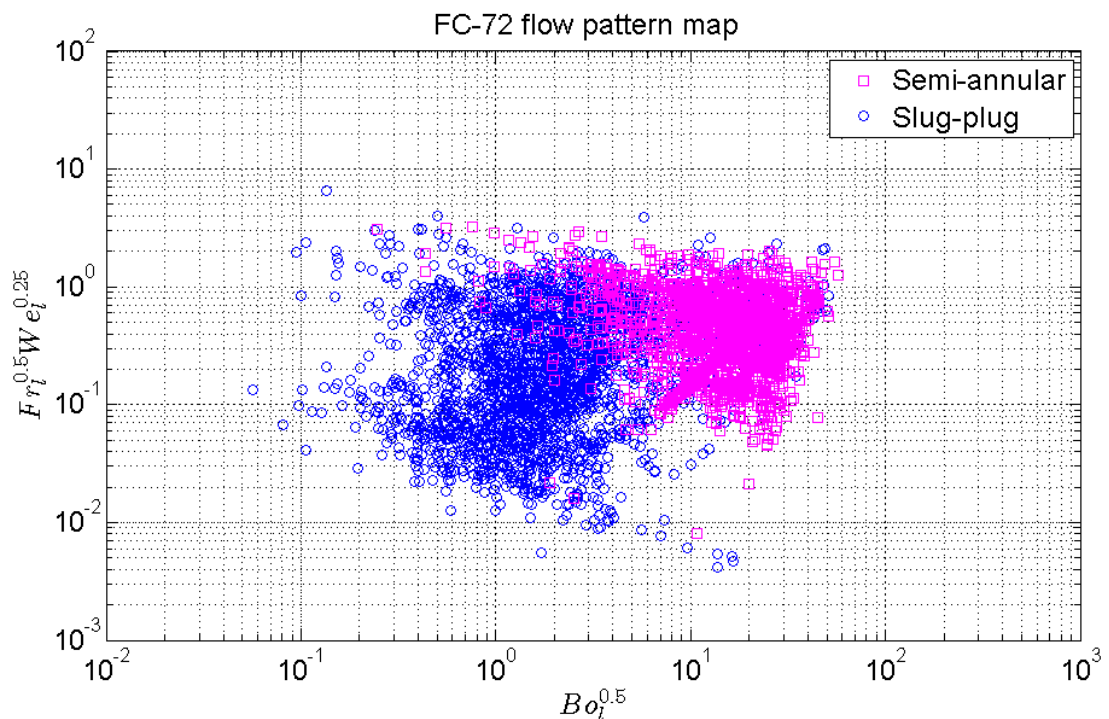


Figure 92 FC-72 flow pattern map in terms of dynamic non-dimensional groups with bubble length as characteristic length; adiabatic section of a single loop PHP

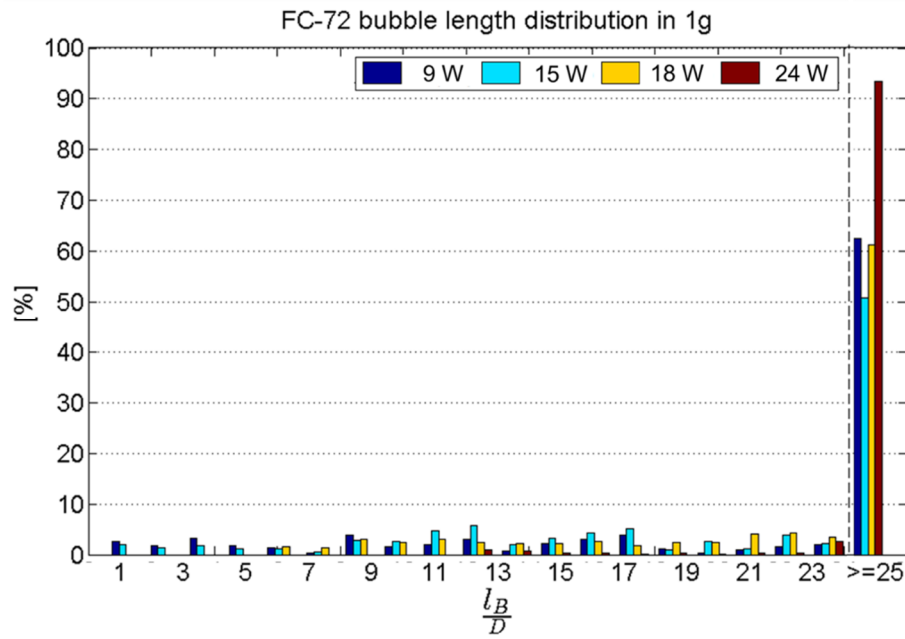


Figure 93 Statistic of the bubble length to diameter ratio for FC-72 in 1g at four power level. Sampling period 5 s at 100 fps, HFOV = 50mm

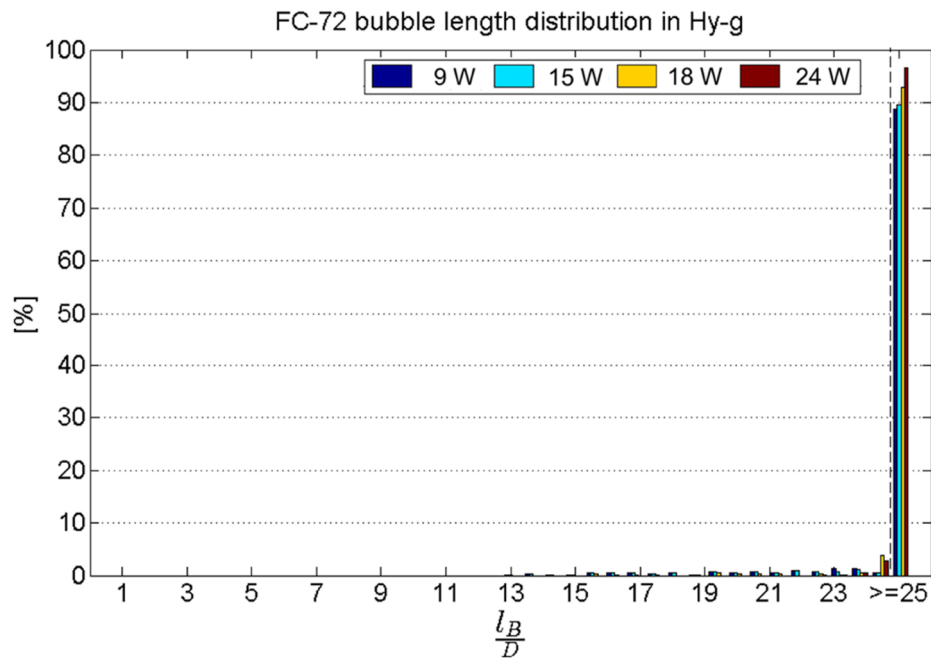


Figure 94 Statistic of the bubble length to diameter ratio for FC-72 in Hy-g at four power level. Sampling period 10 s at 100 fps, HFOV = 50mm

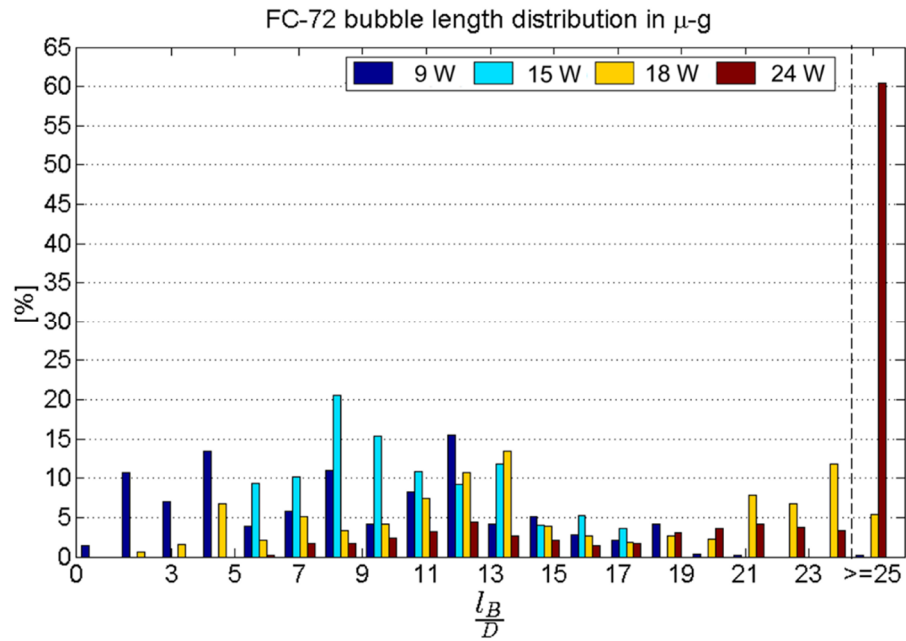


Figure 95 Statistic of the bubble length to diameter ratio for FC-72 in μ -g at four power level. Sampling period 10 s at 100 fps, HFOV = 50mm

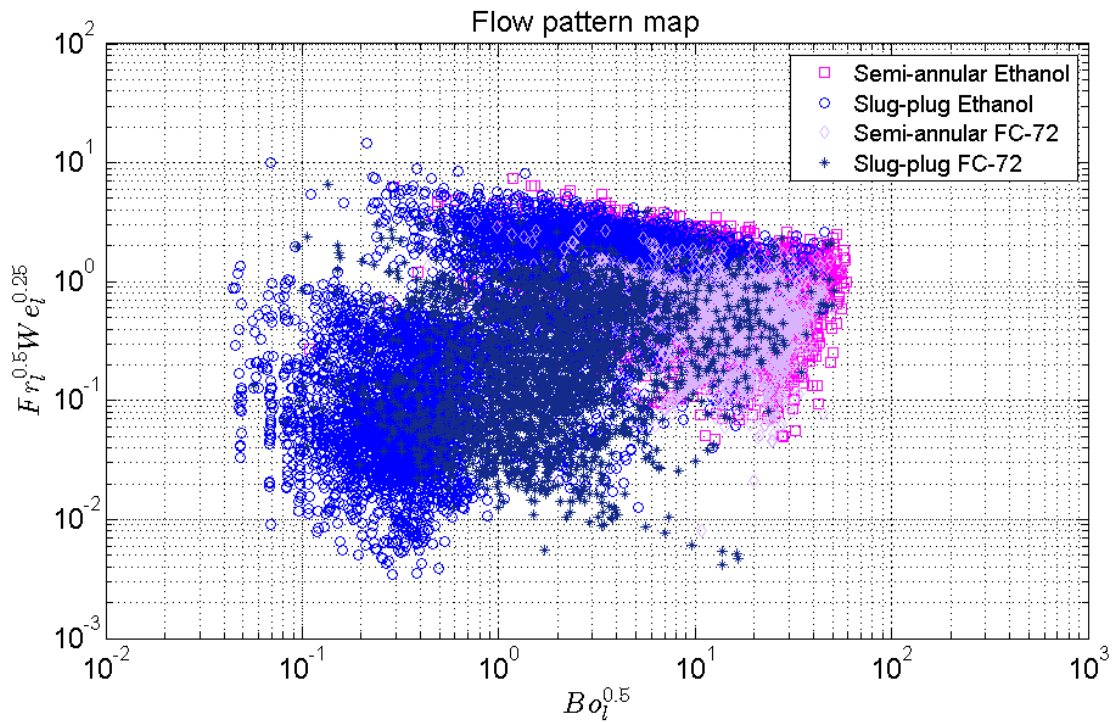


Figure 96 Flow pattern map for Ethanol and FC-72 in terms of dynamic non-dimensional groups with bubble length as characteristic length; adiabatic section of a single loop PHP

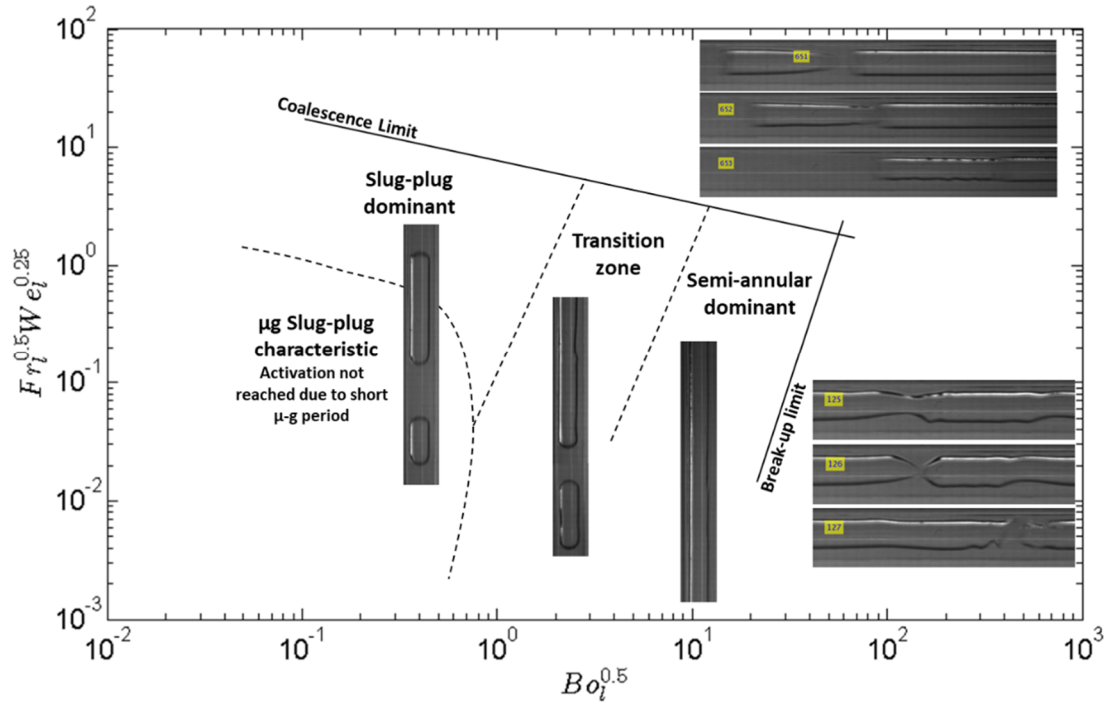


Figure 97 Flow Pattern map of an accelerated slug-plug flow independent from the fluid and the diameter of the tube obtained under three different gravity level

A first attempt to obtain an operational map able to predict the flow pattern and the bubble break-up of a two-phase flow in a thermally driven PHP-like devices is proposed in Figure 97. This novel theory considers velocity, actual acceleration of the fluid and the length of the bubble having active role in defining the evolution of the fluid flow towards a slug-plug condition or a semi-annular condition and in predicting break-up events. The proposed flow pattern map includes new dimensionless numbers accounting for body forces, inertia and surface tension. These dimensionless numbers also account for the transition from surface tension dominated isolated bubble flow to shear dominated annular flow. The proposed new flow pattern transition lines are as follows:

- a) Slug-plug dominant to transitional regime:

$$Fr^{*0.25} We^{*0.25} = 0.11 \ln Bo^{*0.5} - 0.65 \quad (6-9)$$

- b) Transitional regime to Semi-annular dominant:

$$Fr^{*0.25} We^{*0.25} = -1.57 \ln Bo^{*0.5} - 0.57 \quad (6-10)$$

- c) Superior limit (Coalescence):

$$Fr^{*0.25} We^{*0.25} = -0.96 \ln Bo^{*0.5} + 5.02 \quad (6-11)$$

d) Right limit (Break-up):

$$Fr^{*0.25}We^{*0.25} = -3.21 \ln Bo^{*0.5} + 0.17 \quad (6-12)$$

The proposed flow pattern transition map, after a further validation against experimental data, can be implemented in advanced numerical codes to help the design of a PHP devices, defining potential operating limit due to break-up events and bubble merging/coalescence, together with the flow pattern transition limit.

Chapter 7

Conclusions and future developments

7.1 Conclusions

The oscillating/pulsating thermally induced flow motion characteristic of Pulsating Heat Pipes is difficult to characterise due to its extremely complex dynamics linked to the evaporation and condensation of the working fluid. The lack of understanding of the local characteristic of a slug flow has limited the modelling of PHPs. The aim of this investigation was to observe and characterise the flow regime transitions in a millimetric channel when the mass flow rate is not controlled neither constant and results from thermally induced phenomena like in a Pulsating Heat Pipe. This study is based on the output of the post-processing of high-speed imaging collected on ground and on the European Space Agency parabolic flight microgravity platform to assess the effect of gravity on flow pattern and to support the development of space applications. The original outcomes are listed below:

- The inertial effect on flow pattern transitions have been reviewed and discussed. The fluid acceleration and velocity have been identified having a determinant role on the confinement conditions, confirming that a static confinement criterion cannot fully represent an oscillating flow over a range of operating condition;

- The actual velocity of the liquid phase has been estimated and for the first time compared with a critical velocity value that derived from the most reliable empirical non-dimensional criterion developed for flow boiling conditions in milli-channels; the investigation shows limited accuracy of flow pattern prediction, leading to the conclusion that the velocity is not the only responsible for the transitions;
- The vapour phase characteristic length has been investigated and is clearly affected by the power input and the varying gravity level besides the working fluid;
- A new flow pattern map with modified Bond, Weber and Froude numbers including the parameters that were not considered yet in the literature such as the actual acceleration of the fluid rather than a constant value of g and the length of the bubbles as characteristic length, has been proposed. The distribution of more than 1200 operating points on the new system of coordinates, clearly marks the transitions from surface tension dominated slug/plug flow to shear dominated annular flow, based on comparison with high-speed imaging. The proposed flow pattern transition map is independent from the working fluid and the gravity level and shows also neat borders associated with the coalescence limit and break-up limits.

Flow pattern maps are an important tool to describe the internal fluid-dynamic of a passive two-phase system for thermal management because of the critical impact of the flow pattern on the heat transfer coefficient. So far, the prediction the flow pattern of a PHP have been made extending theories developed in conditions of flow boiling, where a controlled mass flow rate is imposed, and a flow reversal is not contemplated. This extension to the PHP field is quite an approximation and has proven to not assist with any further development of the technology. Even harder is extending the correlation to a reduced gravity environment for future space applications. This work can be used to implement the flow pattern phenomena in advanced modelling tools that support the design phase of PHP for both ground and space applications.

7.2 Future developments

The map presented in this work, has now to undergo a wider validation process based on data obtained from different PHP and evaluate the possible extension to generic two-phase flows like in flow boiling conditions and to more accurate velocity estimations, especially in the range 0.4-0.8 m/s. The actual accuracy of the proposed

code in the mentioned range is still uncertain and has to be estimated with a flow of known characteristics.

The development of flow pattern maps for PHPs is a first step towards the reduction of the complexity of the thermo-hydraulic problem given by an oscillating thermally-induced two-phase flow. Being able to identify the flow pattern means being one step closer to the ultimate objective of the estimation of the local heat transfer coefficient in time of a working full-scale PHP. The empirical transition limit proposed, will be implemented in an existing 1D PHP simulation code that at the moment assumes the existence of a slug/plug regime *a priori*. In parallel, the measure of the HTC has to be improved, to provide each flow pattern with the most accurate values. To achieve this goal, a promising technique, based on infrared analysis, can be perfected and applied to the field of PHPs: a direct, non-intrusive, liquid temperature measurement via Medium Wave Infrared investigation will provide the input for the solution of the Inverse Heat Conduction Problem which will give an .

7.2.1 Liquid direct temperature measurement via MWIR imaging

An attempt to perform Medium Wave Infra-Red direct visualization of a fluid with known and sufficiently high emissivity through a sapphire insert has already been made on ground and, for the first time on a PHP, aboard of a parabolic flight during the 68th ESA Parabolic Flight by this research team (University of Brighton) in collaboration with the University of Pisa [116]. This parabolic flight campaign has been carried out with the aim of further analysing the thermo-fluid dynamic behaviour of the SLPHP through conventional pressure and temperatures measurements and high-speed imaging with the innovative support of infrared visualization.

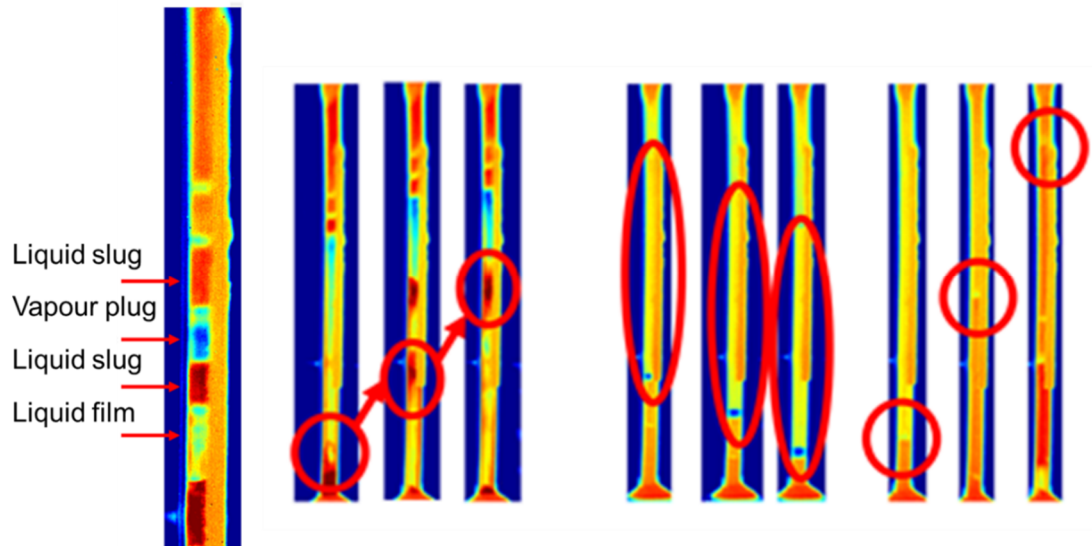


Figure 98 MWIR visualization of a FC-72 slug-plug flow through a sapphire insert during the 68th ESA parabolic flight campaign

The ability to detect liquid phase, vapour phase and zone with reduced thickness of liquid (liquid film) in a pulsating flow is clear (Figure 98).

The relation between pressure and temperature measurements and the flow patterns observed, has been shown by extrapolating time-space maps of the fluid temperature from the IR analysis, and correlating them with the liquid slug velocity and the void fraction for the three gravity levels available (Figure 99). The liquid film dynamics can be investigated with the proposed IR technique alongside the liquid bulk temperature within the sapphire insert. An important test on the feasibility of accurate temperature distribution measurements along liquid slugs during normal gravity, hyper-gravity and micro-gravity phases has been carried out showing some interesting qualitative data [116].

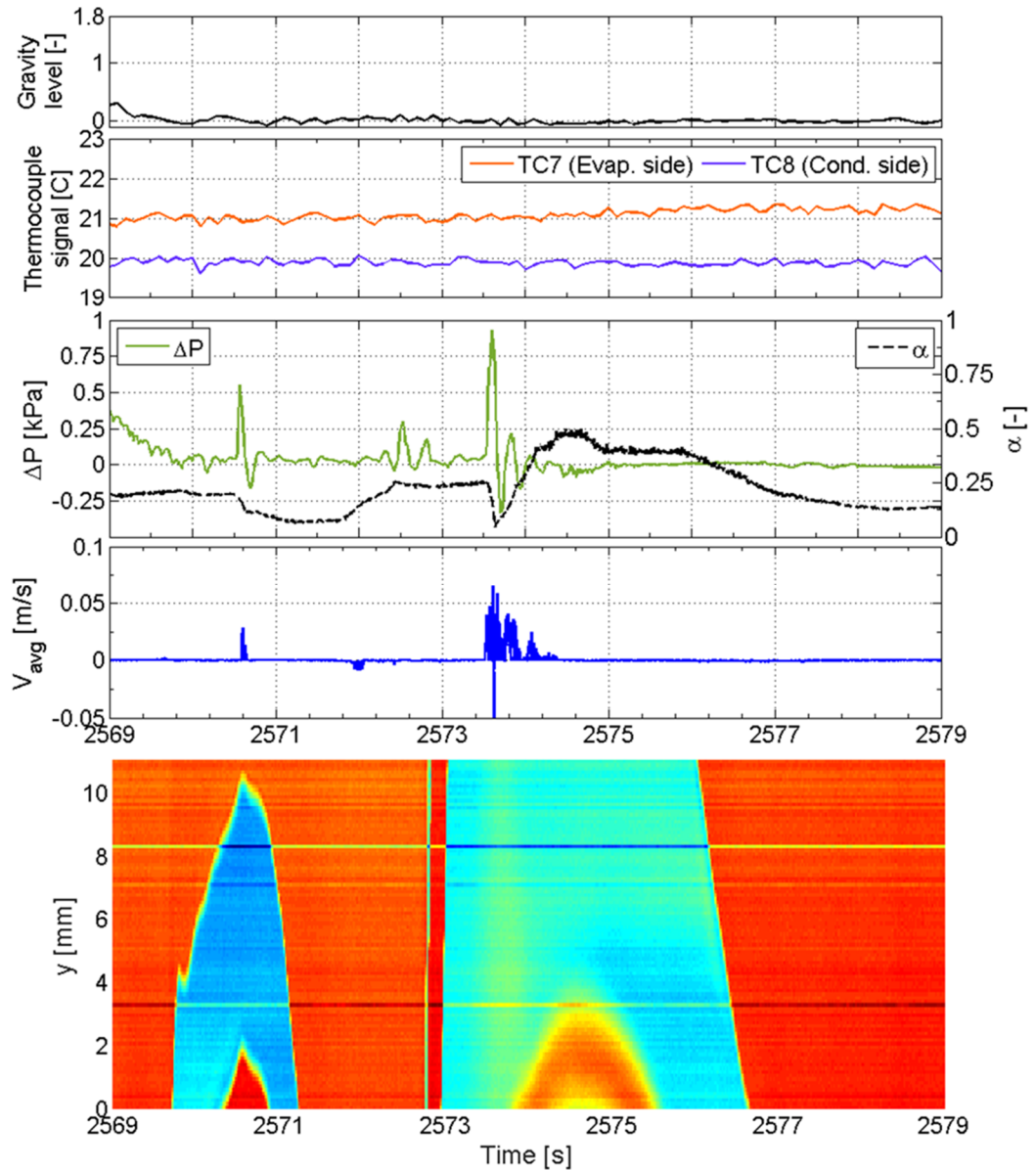


Figure 99 a) Gravity level, b) External tube temperatures at the edges of the sapphire, c) Pressure difference, d) Liquid velocity and void fraction and e) time-space temperature map of the fluid synchronized during microgravity oscillations

Still open is the question of the decoupling the contribution to the overall emissivity given by temperature and thickness of the liquid, if the latter is not enough to guarantee high emissivity. Please refer to Appendix A: Infrared analysis in the context of PHP for a description of the method.

7.2.2 Inverse heat conduction problem in the context of Pulsating Heat Pipes

Although the heat flux in PHP has been extensively investigated, almost all the works presented the results only in terms of the mean values over the evaporator or the

condenser area. The external wall temperature of the adiabatic zone is affected by the temperature of the fluid flowing inside due to the conduction of the material of the tube. Heat is released from the fluid to the wall when a two-phase flow is rising with a high temperature from the evaporator to the condenser, increasing the wall tube temperature. The opposite happens when the fluid leaves the condenser directed to the evaporator: the cold fluid flowing from the condenser receives part of the heat previously accumulated in the tube, decreasing its temperature. An innovative method to estimate the local heat flux during PHPs operation has been presented in the conference paper by Cattani et al. [117] result of the recent collaboration of this research team (University of Brighton) with the University of Parma and the University of Pisa. Two consecutive seconds at 50 fps of IR images, extracted during either an oscillating slug-plug period and annular period, have been investigated. In the region between the evaporator and the condenser, the local heat flux can reach values of up to 4000 W/m² in the case of annular flow and 2000W/m² in the case of an oscillating slug/plug flow. This method can be improved by using an internal high-emissivity thin coating, to have a measure of temperature on the inner surface of the tube that is not affected by the conduction on the sapphire insert and implemented in new experiments for the estimation of the local heat flux and heat transfer coefficient at the condenser and at the evaporator.

Bibliography

- [1] NASA, 'NASA Technology Roadmaps TA 14: Thermal Management Systems', 2015.
- [2] C. Nadjahi, H. Louahlia, and S. Lemasson, 'Sustainable Computing: Informatics and Systems', *Sustain. Comput. Informatics Syst.*, vol. 19, no. May, pp. 14–28, 2018.
- [3] S. Khandekar and M. Groll, 'On the definition of pulsating heat pipes: an overview', in *5th Heat Pipes, Heat Pumps and Refrigerators International Seminar*, Minsk, 2003, vol. 3.
- [4] D. Reay and P. Kew, *Heat Pipes: theory, design and applications*, 5th ed. Oxford: Butterworth-Heinemann, 2006.
- [5] M. S. El-Genk and H. H. Saber, 'Heat Transfer Correlations for Liquid Film in the Evaporator of Enclosed, Gravity-Assisted Thermosyphons', vol. 120, no. 2, 1998.
- [6] F. Zhou, G. Ma, Z. Liu, F. Li, and X. Yan, 'Heat transfer characteristics of thermosyphon heat exchanger for cooling electrical cabinet', pp. 1–7, 2018.
- [7] H. Jouhara and A. J. Robinson, 'Experimental investigation of small diameter two-phase closed thermosyphons charged with water, FC-84, FC-77 and FC-3283', *Appl. Therm. Eng.*, vol. 30, no. 2–3, pp. 201–211, 2010.
- [8] D. Jafari, A. Franco, S. Filippeschi, and P. Di Marco, 'Two-phase closed thermosyphons: A review of studies and solar applications', vol. 53, pp. 575–593, 2016.
- [9] A. Franco and S. Filippeschi, 'Closed loop two-phase thermosyphon of small dimensions: A review of the experimental results', *Microgravity Sci. Technol.*, vol. 24, no. 3, pp. 165–179, 2012.
- [10] J. M. Ochterbeck, 'Heat Pipes', in *Heat transfer handbook*, A. Bejan and A. D. Kraus, Eds. John Wiley & Sons, 2003, pp. 1181–1230.
- [11] Y. F. Maidanik and Y. G. Fershtater, 'Theoretical Basis and Classification of Loop Heat Pipes and Capillary Pumped Loops', in *Proc. 10th International Heat Pipe Conference*, 1997

-
- [12] Y. F. Maydanik, 'Loop heat pipes', *Appl. Therm. Eng.* 25 635–657.
- [13] H. Akachi, 'Structure of a micro-heat pipe', US005219020A, 1993.
- [14] H. Yang, S. Khandekar, and M. Groll, 'Operational limit of closed loop pulsating heat pipes', *Appl. Therm. Eng.*, vol. 28, no. 1, pp. 49–59, 2008.
- [15] R. M. Davies and G. Taylor, 'The Mechanics of Large Bubbles Rising through Extended Liquids and through Liquids in Tubes', *Proc. R. Soc. A Math. Phys. Eng. Sci.*, vol. 200, no. 1062, pp. 375–390, 1950.
- [16] M. Mameli, 'Pulsating Heat Pipes: Numerical Modeling and Experimental Assessment, PhD Thesis', University of Bergamo, 2012.
- [17] ECSS, 'Adoption Notice of ISO 16290, Space systems – Definition of the Technology Readiness Levels (TRLs) and their criteria of assessment'.
- [18] ECSS, 'Thermal design handbook - Part 8: Heat Pipes'.
- [19] D. G. Gilmore, *Spacecraft Thermal Control Handbook Volume I: Fundamental Technologies*, vol. Second Edi. 2002.
- [20] H. Akachi, 'Structure of a heat pipe', 4921041, 1990.
- [21] Y. Zhang and A. Faghri, 'Advances and Unsolved Issues in Pulsating Heat Pipes', *Heat Transf. Eng.*, vol. 29, no. 1, pp. 20–44, 2008.
- [22] M. J. Nine, M. R. Tanshen, B. Munkhbayar, H. Chung, and H. Jeong, 'Analysis of pressure fluctuations to evaluate thermal performance of oscillating heat pipe', *Energy*, vol. 70, pp. 135–142, 2014.
- [23] M. Mac Giolla Eain, V. Egan, J. Howard, P. Walsh, E. Walsh, and J. Punch, 'Review and extension of pressure drop models applied to Taylor flow regimes', *Int. J. Multiph. Flow*, vol. 68, pp. 1–9, 2015.
- [24] P. M.-Y. Chung and M. Kawaji, 'The effect of channel diameter on adiabatic two-phase flow characteristics in microchannels', *Int. J. Multiph. Flow*, vol. 30, no. 7–8 SPEC. ISS., pp. 735–761, 2004.
- [25] J. R. Thome, A. Bar-Cohen, R. Revellin, and I. Zun, 'Unified mechanistic multiscale mapping of two-phase flow patterns in microchannels', *Exp. Therm. Fluid Sci.*, vol. 44, pp. 1–22, 2013.
- [26] P. M.-Y. Chung, M. Kawaji, A. Kawahara, and Y. Shibata, 'Two-phase flow through square and circular microchannels - Effects of channel geometry', vol. 126, no. 4, pp. 546–552, 2004.
- [27] S. G. Kandlikar, S. Garimella, D. Li, S. Colin, and M. R. King, *Heat Transfer and Fluid Flow in Minichannels and Microchannels*. 2014.
- [28] J. R. Thome, 'Boiling in microchannels: a review of experiment and theory', vol. 25, pp. 128–139, 2004.

- [29] P. Cheng and H. Y. Wu, 'Mesoscale and Microscale Phase-Change Heat Transfer', *Adv. Heat Transf.*, vol. 39, pp. 461–463, 2006.
- [30] P. A. Kew and K. Cornwell, 'Correlations for the prediction of boiling heat transfer in small-diameter channels', *Appl. Therm. Eng.*, vol. 17, no. 8–10, pp. 705–715, 1997.
- [31] C. Baldassari and M. Marengo, 'Flow boiling in microchannels and microgravity', *Prog. Energy Combust. Sci.*, vol. 39, no. 1, pp. 1–36, 2013.
- [32] D. Mangini, M. Mameli, A. Georgoulas, L. Araneo, S. Filippeschi, and M. Marengo, 'A pulsating heat pipe for space applications: Ground and microgravity experiments', *Int. J. Therm. Sci.*, vol. 95, pp. 53–63, 2015.
- [33] B. Mehta and S. Khandekar, 'Measurement of local heat transfer coefficient during gas–liquid Taylor bubble train flow by infra-red thermography', *Int. J. Heat Fluid Flow*, vol. 45, pp. 41–52, 2014.
- [34] S. Nukiyama, 'The maximum and minimum values of the heat Q transmitted from metal to boiling water under atmospheric pressure', *J. Japan Soc. Mech. Engrs*, vol. 37, pp. 367–374, 1934.
- [35] D. D. Hall and I. Mudawar, 'Critical heat flux (CHF) for water flow in tubes-II . Subcooled CHF correlations', *Int. J. Heat Mass Transf.*, vol. 43, pp. 2605–2640, 2000.
- [36] C. Konishi, I. Mudawar, and M. M. Hasan, 'Investigation of localized dryout versus CHF in saturated flow boiling', *Int. J. Heat Mass Transf.*, vol. 67, pp. 131–146, 2013.
- [37] J. A. Boure', A. E. Bergles, and L. S. Tong, 'Review of two-phase flow instabilities', *Nucl. Eng. Des.*, vol. 25, pp. 165–192, 1972.
- [38] S. Kakac and B. Bon, 'A Review of two-phase flow dynamic instabilities in tube boiling systems', vol. 51, pp. 399–433, 2008.
- [39] L. Ruspini, C. Marcel, and A. Clausse, 'Two-phase flow instabilities: A review', *Int. J. Heat Mass Transf.*, vol. 71, pp. 521–548, 2014.
- [40] S. K. Saha and G. P. Celata, *Instability in Flow Boiling in Microchannels*, Springer. 2016.
- [41] P. Charoensawan, S. Khandekar, M. Groll, and P. Terdtoon, 'Closed loop pulsating heat pipes - Part A: Parametric experimental investigations', *Appl. Therm. Eng.*, vol. 23, no. 16, pp. 2009–2020, 2003.
- [42] S. Khandekar and M. Groll, 'An insight into thermo-hydrodynamic coupling in closed loop pulsating heat pipes', *Int. J. Therm. Sci.*, vol. 43, no. 1, pp. 13–20, Jan. 2004.
- [43] M. Mameli, M. Marengo, and S. Khandekar, 'Local heat transfer measurement and thermo-fluid characterization of a pulsating heat pipe', *Int. J. Therm. Sci.*, vol. 75, pp. 140–152, 2014.

-
- [44] V. M. Patel, Gaurav, and H. B. Mehta, 'Influence of working fluids on startup mechanism and thermal performance of a closed loop pulsating heat pipe', *Appl. Therm. Eng.*, vol. 110, pp. 1568–1577, 2017.
- [45] V. S. Nikolayev, 'Effect of tube heat conduction on the single branch pulsating heat pipe start-up', *Int. J. Heat Mass Transf.*, vol. 95, pp. 477–487, 2016.
- [46] V. S. Nikolayev, 'Effect of tube heat conduction on the single branch pulsating heat pipe start-up Vadim Nikolayev', *Int. J. Heat Mass Transf.*, vol. 95, pp. 477–487, 2016.
- [47] H. Yang, S. Khandekar, and M. Groll, 'Performance characteristics of pulsating heat pipes as integral thermal spreaders', *Int. J. Therm. Sci.*, vol. 48, no. 4, pp. 815–824, 2009.
- [48] M. Mameli, V. Manno, S. Filippeschi, and M. Marengo, 'Thermal instability of a Closed Loop Pulsating Heat Pipe: Combined effect of orientation and filling ratio', *Exp. Therm. Fluid Sci.*, vol. 59, pp. 222–229, Nov. 2014.
- [49] R. T. Dobson, 'Theoretical and experimental modelling of an open oscillatory heat pipe including gravity', *Int. J. Therm. Sci.*, vol. 43, no. 2, pp. 113–119, 2004.
- [50] S. R. Sahu and M. K. Moharana, 'Two-dimensional numerical analysis of common header pulsating heat pipe', 2018.
- [51] H. Han, X. Cui, Y. Zhu, and S. Sun, 'A comparative study of the behavior of working fluids and their properties on the performance of pulsating heat pipes (PHP)', *Int. J. Therm. Sci.*, vol. 82, no. 1, pp. 138–147, 2014.
- [52] X. Liu, Y. Chen, and M. Shi, 'Dynamic performance analysis on start-up of closed-loop pulsating heat pipes (CLPHPs)', *Int. J. Therm. Sci.*, vol. 65, pp. 224–233, 2013.
- [53] A. Brusly Solomon, V. K. Karthikeyan, K. Ramachandran, and B. C. Pillai, 'Effect of number of turns on the temperature pulsations and corresponding thermal performance of pulsating heat pipe', *J. Enhanc. Heat Transf.*, vol. 20, no. 5, pp. 443–452, 2013.
- [54] Y. Song and J. Xu, 'Chaotic behavior of pulsating heat pipes', *Int. J. Heat Mass Transf.*, vol. 52, no. 13–14, pp. 2932–2941, 2009.
- [55] M. Mameli, M. Marengo, and S. Zinna, 'Numerical model of a multi-turn Closed Loop Pulsating Heat Pipe: Effects of the local pressure losses due to meanderings', *Int. J. Heat Mass Transf.*, vol. 55, no. 4, pp. 1036–1047, 2012.
- [56] J. Wang, H. Ma, and Q. Zhu, 'Effects of the evaporator and condenser length on the performance of pulsating heat pipes', *Appl. Therm. Eng.*, vol. 91, pp. 1018–1025, 2015.
- [57] J. Qu and Q. Wang, 'Experimental study on the thermal performance of vertical closed-loop oscillating heat pipes and correlation modeling', *Appl. Energy*, vol. 112, pp. 1154–1160, 2013.

- [58] M. Mameli, D. Mangini, G. F. T. Vanoli, L. Araneo, S. Filippeschi, and M. Marengo, 'Advanced multi-evaporator loop thermosyphon', *Energy*, vol. 112, pp. 562–573, 2016.
- [59] Y. Ji, H. Chen, Y. J. Kim, Q. Yu, X. Ma, and H. B. Ma, 'Hydrophobic Surface Effect on Heat Transfer Performance in an Oscillating Heat Pipe', *J. Heat Transfer*, vol. 134, no. 7, p. 074502, 2012.
- [60] T. Hao, X. Ma, Z. Lan, N. Li, and Y. Zhao, 'Effect of superhydrophobic and superhydrophilic surfaces on heat transfer and oscillating motion of an oscillating heat pipe', *J. Heat Transfer*, vol. 136, no. 8, 2014.
- [61] X. Cao and P. Cheng, 'A novel design of pulsating heat pipes with improved performance', in *13th International Heat Pipe Conference*, 2004.
- [62] Y. Ji, C. Chang, G. Li, and H. Ma, 'An investigation of operating limits for oscillating heat pipes', in *15th International Heat Transfer Conference*, 2014.
- [63] P. Charoensawan and P. Terdtoon, 'Thermal performance correlation of horizontal closed-loop oscillating heat pipes', *Appl. Therm. Eng.*, pp. 460–466, 2008.
- [64] S. Khandekar, M. Schneider, and M. Groll, 'Thermofluid dynamic study of a flat plate CLPHP', 2002.
- [65] K.-H. Chien, Y.-T. Lin, Y.-R. Chen, K.-S. Yang, and C.-C. Wang, 'A novel design of pulsating heat pipe with fewer turns applicable to all orientations', *Int. J. Heat Mass Transf.*, vol. 55, no. 21–22, pp. 5722–5728, 2012.
- [66] A. A. Hathaway, C. A. Wilson, and H. B. Ma, 'Experimental Investigation of Uneven-Turn Water and Acetone Oscillating Heat Pipes', *J. Thermophys. Heat Transf.*, vol. 26, no. 1, pp. 115–122, 2012.
- [67] C. Marcel, L. Carlos, C. Pablo, and A. Clause, 'Two-phase flow instabilities : A review International Journal of Heat and Mass Transfer Two-phase flow instabilities : A review', *HEAT MASS Transf.*, vol. 71, no. April, pp. 521–548, 2014.
- [68] K. Sefiane, D. Benielli, and a. Steinchen, 'A new mechanism for pool boiling crisis, recoil instability and contact angle influence', *Colloids Surfaces A Physicochem. Eng. Asp.*, vol. 142, no. 2–3, pp. 361–373, Dec. 1998.
- [69] V. Srinivasan, S. Khandekar, N. Bouamrane, F. Lefevre, and J. Bonjour, 'Motion of an isolated liquid plug inside a capillary tube: effect of contact angle hysteresis', *Exp. Fluids*, vol. 56, no. 1, 2015.
- [70] G. Spinato, N. Borhani, and J. R. Thome, 'Understanding the self-sustained oscillating two-phase flow motion in a closed loop pulsating heat pipe', *Energy*, vol. 90, pp. 889–899, 2015.
- [71] Q. Cai, C.-L. Chen, and J. F. Asfia, 'Operating Characteristic Investigations in Pulsating Heat Pipe', vol. 128, no. 12, pp. 1329–1334, 2006.
- [72] S. Lips, A. Bensalem, Y. Bertin, V. Ayel, C. Romestant, and J. Bonjour,

- ‘Experimental evidences of distinct heat transfer regimes in pulsating heat pipes (PHP)’, *Appl. Therm. Eng.*, vol. 30, no. 8–9, pp. 900–907, 2010.
- [73] Y. Han and N. Shikazono, ‘Measurement of the liquid film thickness in micro tube slug flow’, *Int. J. Heat Fluid Flow*, vol. 30, no. 5, pp. 842–853, 2009.
- [74] M. Rao, F. Lefèvre, S. Khandekar, and J. Bonjour, ‘Heat and mass transfer mechanisms of a self-sustained thermally driven oscillating liquid–vapour meniscus’, *Int. J. Heat Mass Transf.*, vol. 86, pp. 519–530, 2015.
- [75] J. Gu, R. Futamata, and M. Kawaji, ‘Effects of Gravity on the Performance of Pulsating Heat Pipes’, *J. Thermophys. Heat Transf.*, vol. 18, no. 3, pp. 370–378, 2004.
- [76] M. Mameli, L. Araneo, S. Filippeschi, L. Marelli, R. Testa, and M. Marengo, ‘Thermal response of a closed loop pulsating heat pipe under a varying gravity force’, *Int. J. Therm. Sci.*, vol. 80, pp. 11–22, 2014.
- [77] J. Gu, M. Kawaji, and R. Futamata, ‘Microgravity performance of micro pulsating heat pipes’, *Microgravity - Sci. Technol.*, vol. 16, pp. 181–185, 2005.
- [78] V. Ayel, L. Araneo, A. Scalambra, M. Mameli, C. Romestant, A. Piteau, M. Marengo, S. Filippeschi, and Y. Bertin, ‘Experimental study of a closed loop flat plate pulsating heat pipe under a varying gravity force’, *Int. J. Therm. Sci.*, vol. 96, pp. 23–34, Oct. 2015.
- [79] F. Creatini, G. M. Guidi, F. Belfi, G. Cicero, D. Fioriti, D. Di Prizio, S. Piacquadio, G. Becatti, G. Orlandini, A. Frigerio, S. Fontanesi, P. Nannipieri, M. Rognini, N. Morganti, S. Filippeschi, P. Di Marco, L. Fanucci, F. Baronti, M. Mameli, M. Manzoni, and M. Marengo, ‘Pulsating Heat pipe Only for Space (PHOS): results of the REXUS 18 sounding rocket campaign’, *J. Phys. Conf. Ser.*, vol. 655, 2015.
- [80] P. Nannipieri, M. Anichini, L. Barsocchi, G. Becatti, L. Buoni, F. Celi, A. Catarsi, P. Di Giorgio, E. Ferrato, P. Guardati, E. Mancini, G. Meoni, F. Nesti, S. Piacquadio, E. Pratelli, L. Quadrelli, A. Viglione, S. Zanaboni, M. Mameli, F. Baronti, L. Fanucci, S. Marcuccio, C. Bartoli, P. Di Marco, and S. Filippeschi, ‘Upgraded Pulsating Heat Pipe only for space (U-PHOS): results of the 22nd Rexus sounding rocket campaign’, in *World Conference on Experimental Heat Transfer, Fluid Mechanics and Thermodynamics*, 2017.
- [81] M. Ando, A. Okamoto, K. Tanaka, M. Maeda, H. Sugita, T. Daimaru, and H. Nagai, ‘On-orbit demonstration of oscillating heat pipe with check valves for space application’, *Appl. Therm. Eng.*, vol. 130, pp. 552–560, 2018.
- [82] M. Mameli, M. Manzoni, L. Araneo, S. Filippeschi, and M. Marengo, ‘Experimental investigation on a closed loop pulsating heat pipe in hyper-gravity conditions’, pp. 1–13, 2014.
- [83] P. Gully, F. Bonnet, V. S. Nikolayev, N. Luchier, and T. Q. Tran, ‘Evaluation of the vapor thermodynamic state in PHP’, in *17th International Heat Pipe Conference*, 2013, pp. 1–6.
- [84] G. Spinato, N. Borhani, B. P. D’Entremont, and J. R. Thome, ‘Time-strip

- visualization and thermo-hydrodynamics in a Closed Loop Pulsating Heat Pipe’, *Appl. Therm. Eng.*, vol. 78, pp. 364–372, 2015.
- [85] V. Srinivasan, S. Kumar, M. Asfer, and S. Khandekar, ‘Oscillation of an isolated liquid plug inside a dry capillary’, in *Joint 18th IHPC and 12th IHPS*, 2016, pp. 9–15.
- [86] L. Fourgeaud, V. S. Nikolayev, E. Ercolani, J. Duplat, and P. Gully, ‘In situ investigation of liquid films in pulsating heat pipe’, *Appl. Therm. Eng.*, vol. 126, pp. 1023–1028, 2017.
- [87] D. Mangini, M. Mameli, D. Fioriti, S. Filippeschi, L. Araneo, and M. Marengo, ‘Hybrid Pulsating Heat Pipe for space applications with non-uniform heating patterns: Ground and microgravity experiments’, *Appl. Therm. Eng.*, vol. 126, no. I, pp. 1029–1043, 2017.
- [88] A. Ilinca, D. Mangini, M. Mameli, D. Fioriti, S. (University of P. Filippeschi, L. Araneo, N. Roth, and M. Marengo, ‘Fluid-flow pressure measurements and thermo- fluid characterization of a single loop two-phase passive heat transfer device Fluid-flow pressure measurements and thermo-fluid characterization of a single loop two-phase passive heat transfer device’, *J. Phys. Conf. Ser.*, 2017.
- [89] Z. J. Taylor, R. Gurka, G. A. Kopp, and A. Liberzon, ‘Long-Duration Time-Resolved PIV to Study Unsteady Aerodynamics’, *IEEE Trans. Instrum. Meas.*, vol. 59, no. 12, pp. 3262–3269, 2010.
- [90] Z. H. Xue and W. Qu, ‘Experimental and theoretical research on a ammonia pulsating heat pipe: New full visualization of flow pattern and operating mechanism study’, *Int. J. Heat Mass Transf.*, vol. 106, pp. 149–166, Mar. 2017.
- [91] G. Costigan and P. B. Whalley, ‘Slug flow regimes identification from dynamic void fraction measurement in vertical air-water flows’, vol. 23, no. 2, pp. 263–282, 1997.
- [92] K. A. Triplett, S. M. Ghiaasiaan, A. LeMouel, and B. N. McCord, ‘Gas-liquid two-phase flow in microchannels Part II : void fraction and pressure drop’, *Int. J. Multiph. Flow*, vol. 25, pp. 395–410, 1999.
- [93] H. Ji, H. Li, Z. Huang, B. Wang, and H. Li, ‘Measurement of Gas-Liquid Two-Phase Flow in Micro-Pipes by a Capacitance Sensor’, *Sensors*, vol. 14, pp. 22431–22446, 2014.
- [94] A. Kawahara, M. Sadatomi, K. Okayama, M. Kawaji, and P. M.-Y. Chung, ‘Effects of Channel Diameter and Liquid Properties on Void Fraction in Adiabatic Two-Phase Flow Through Microchannels’, *Heat Transf. Eng.*, vol. 26, no. 3, pp. 13–19, 2006.
- [95] M. Masiukiewicz and S. Anweiler, ‘Two-phase flow phenomena assessment in minichannels for compact heat exchangers using image analysis methods’, vol. 104, pp. 44–54, 2015.
- [96] H. Li, X. Zheng, H. Ji, Z. Huang, B. Wang, and H. Li, ‘Particuology Void fraction measurement of bubble and slug flow in a small channel using the multivision technique’, *Particuology*, vol. 33, pp. 11–16, 2017.

-
- [97] F. Gerbino, M. Mameli, P. Di Marco, and S. Filippeschi, 'Local void fraction and fluid velocity measurements in a capillary channel with a single optical probe', *Interfacial Phenom. Heat Transf.*, vol. 5, no. 1, pp. 1–20, 2017.
- [98] V. Pletser, 'European aircraft parabolic flights for microgravity research, applications and exploration: A review', *Reach - Rev. Hum. Sp. Explor.*, vol. 1, pp. 11–19, 2016.
- [99] Novespace, '67 th ESA parabolic flight campaign: Practical and technical information', 2017.
- [100] Novespace, 'Experiment Design Requirements for Parabolic Flights', 2016.
- [101] Novespace, 'Standard primary structure catalog', 2015.
- [102] Novespace, 'A310 ZERO - G Interface Document', 2016.
- [103] L. Pietrasanta, N. Miche, D. Fioriti, L. Araneo, and M. Marengo, 'A modular test-rig for shared thermo-fluid dynamics experiments in reduced gravity environment', in *15th UK Heat Transfer Conference, UKHTC2017*, 2017.
- [104] R. J. Moffat, 'Describing the Uncertainties in Experimental Results', *Exp. Therm. Fluid Sci.*, vol. 1, pp. 3–17, 1988.
- [105] Y. Taitel, D. Bornea, and A. E. Dukler, 'Modelling Flow Pattern Transitions for Steady Upward Gas-Liquid Flow in Vertical Tubes', *AIChE J.*, vol. 26, no. 3, pp. 345–354, 1980.
- [106] L. Cheng, G. Ribatski, and J. R. Thome, 'Two-Phase Flow Patterns and Flow-Pattern Maps : Fundamentals and applications', *Appl. Mech. Rev.*, vol. 61, 2008.
- [107] K. S. Gabriel, *Microgravity two-phase flow and heat transfer*. Microcosm Press and Springer, 2007.
- [108] C. L. Ong and J. R. Thome, 'Macro-to-microchannel transition in two-phase flow : Part 1 – Two-phase flow patterns and film thickness measurements', *Exp. Therm. Fluid Sci.*, vol. 35, pp. 37–47, 2011.
- [109] T. Harirchian and S. V. Garimella, 'A comprehensive flow regime map for microchannel flow boiling with quantitative transition criteria', *Int. J. Heat Mass Transf.*, vol. 53, no. 13–14, pp. 2694–2702, 2010.
- [110] J. L. Xu, Y. X. Li, and T. N. Wong, 'High speed flow visualization of a closed loop pulsating heat pipe', *Int. J. Heat Mass Transf.*, vol. 48, no. 16, pp. 3338–3351, 2005.
- [111] L. Pietrasanta, D. Mangini, D. Fioriti, N. Miche, A. Georgoulas, M. Andredaki, L. Araneo, and M. Marengo, 'A single loop pulsating heat pipe in varying gravity conditions: experimental results and numerical simulations', in *16th International Heat Transfer Conference, IHTC-16, Beijing, China, 10-15 August, 2018*, 2018.
- [112] A. Georgoulas, P. Koukouvinis, M. Gavaises, and M. Marengo, 'Numerical investigation of quasi-static bubble growth and detachment from submerged

- orifices in isothermal liquid pools: The effect of varying fluid properties and gravity levels', *Int. J. Multiph. Flow*, vol. 74, pp. 59–78, 2015.
- [113] A. Georgoulas, M. Andreadaki, and M. Marengo, 'An Enhanced VOF Method Coupled with Heat Transfer and Phase Change to Characterise Bubble Detachment in Saturated Pool Boiling', *Energies*, vol. 10, no. 3, p. 272, Feb. 2017.
- [114] G. K. Batchelor, 'The stability of a large gas bubble rising through liquid', *J. Fluid Mech.*, vol. 184, pp. 399–422, 1987.
- [115] S. Laborie, C. Cabassud, and J. M. Laine, 'Characterisation of gas-liquid two-phase flow inside capillaries', *Chem. Eng. Sci.* 54 5723-5735.
- [116] D. Mangini, M. Pozzoni, M. Mameli, L. Pietrasanta, and M. Marengo, 'Infrared analysis and pressure measurements on a single loop pulsating heat pipe at different gravity levels', in *Joint 19th IHPC and 13th IHPS, Pisa, Italy, June 10-14S*, 2018.
- [117] L. Cattani, D. Mangini, F. Bozzoli, L. Pietrasanta, N. Miche, M. Mameli, S. Filippeschi, S. Rainieri, and M. Marengo, 'An original look into Pulsating Heat Pipes: Inverse heat conduction approach for assessing the thermal behavior', in *Joint 19th IHPC and 13th IHPS, Pisa, Italy, June 10-14*, 2018.
- [118] S. Luciani, D. Brutin, and C. Le Niliot, 'Boiling heat transfer in a vertical microchannel: local estimation during flow boiling with a non intrusive method', *Multiph. Sci. Technol.*, vol. 21, no. 4, pp. 297–328, 2009.
- [119] G. Hetsroni, A. Mosyak, E. Pogrebnyak, and R. Rozenblit, 'Infrared temperature measurements in micro-channels and micro-fluid systems', *Int. J. Therm. Sci.*, vol. 50, no. 6, pp. 853–868, 2011.
- [120] B. Mehta and S. Khandekar, 'Infra-red thermography of laminar heat transfer during early thermal development inside a square mini-channel', *Exp. Therm. Fluid Sci.*, vol. 42, pp. 219–229, 2012.
- [121] V. K. Karthikeyan, S. Khandekar, B. C. Pillai, and P. K. Sharma, 'Infrared thermography of a pulsating heat pipe: Flow regimes and multiple steady states', *Appl. Therm. Eng.*, vol. 62, no. 2, pp. 470–480, 2014.
- [122] N. Chauris, V. Ayel, Y. Bertin, and C. Romestant, 'Evaporation of a liquid film deposited on a capillary heated tube: Experimental analysis by infrared thermography of its thermal footprint', *Int. J. Heat Mass Transf.*, vol. 86, pp. 492–507, 2015.
- [123] T. L. Liu and C. Pan, 'Infrared thermography measurement of two-phase boiling flow heat transfer in a microchannel', *Appl. Therm. Eng.*, vol. 94, pp. 568–578, 2016.
- [124] B. Sobac and D. Brutin, 'Thermocapillary instabilities in an evaporating drop deposited onto a heated substrate', *Phys. Fluids*, vol. 24, no. 3, 2012.
- [125] A. Scammell and J. Kim, 'Heat transfer and flow characteristics of rising Taylor bubbles', *Int. J. Heat Mass Transf.*, vol. 89, pp. 379–389, 2015.

- [126] A. Catarsi, D. Fioriti, M. Mameli, S. Filippeschi, and P. Di Marco, ‘Accuracy analysis of direct infrared temperature measurements of two-phase confined flows’, in *Proceedings of the 16th International Heat Transfer Conference, IHTC-16 August 10-15, 2018, Beijing, China*, 2018.

List of publications

Conference Papers

L. Pietrasanta, M. Mameli, A. Georgoulas, N. Miche', S. Filippeschi, M. Marengo, *Towards the Development of Flow Pattern Maps for Thermally-Induced Pulsating Two-Phase Flows*, Accepted Paper - 10th International Conference on Multiphase Flow, ICMF Rio de Janeiro, Brazil, May 19 – 24, 2019

R. Perna, M. Mameli, L. Pietrasanta, M. Marengo, S. Filippeschi, *Time-Frequency Analysis of a Thermally Induced Pulsating Slug Flow*, Accepted Paper - 10th International Conference on Multiphase Flow, ICMF Rio de Janeiro, Brazil, May 19 – 24, 2019

L. Pietrasanta, D. Mangini, D. Fioriti, N. Miche, M. Andredaki, A. Georgoulas, L. Araneo, M. Marengo, *A single loop pulsating heat pipe in varying gravity conditions: experimental results and numerical simulations*, Proceedings of the 16th International Heat Transfer Conference, IHTC Beijing, China, 16 August 10-15, 2018

M. Andredaki, A. Georgoulas, D. Mangini, L. Araneo, L. Pietrasanta, M. Mameli, N. Miché, M. Marengo, *Computational study on break-up mechanisms of isolated vapour slugs during saturated flow boiling conditions*, Proceedings of the 16th International Heat Transfer Conference, IHTC Beijing, China, 16 August 10-15, 2018

M. Mameli, A. Catarsi, D. Mangini, L. Pietrasanta, D. Fioriti, M. La Foresta, L. Caporale, N. Miche, M. Marengo, P. Di Marco, S. Filippeschi, *Large Diameter Pulsating Heat Pipe for Future Experiments on the International Space Station: Ground and Microgravity Thermal Response*, Joint 19th IHPC and 13th IHPS, Pisa, Italy, June 10-14, 2018

L. Cattani, D. Mangini, F. Bozzoli, M. Mameli, L. Pietrasanta, N. Miche', S. Filippeschi, M. Marengo, S. Rainieri, *An original look into Pulsating Heat Pipes: Inverse heat transfer approach for assessing the thermal behaviour*, Joint 19th IHPC and 13th IHPS, Pisa, Italy, June 10-14, 2018

D. Mangini, M. Pozzoni, M. Mameli, L. Pietrasanta, M. Bernagozzi, D. Fioriti, N. Michè, L. Araneo, M. Marengo, S. Filippeschi, *Infrared analysis and pressure measurements on a single loop pulsating heat pipe at different gravity levels*, Joint 19th IHPC and 13th IHPS, Pisa, Italy, June 10-14, 2018

V. Ayel, L. Pietrasanta, G. Lalizel, B. Medrinal, C. Romestant, Y. Bertin, M. Marengo, *Thermo-hydraulic analysis of semi-transparent Flat-Plate Pulsating Heat Pipes Tested Under Normal and Microgravity Regimes*, Joint 19th IHPC and 13th IHPS, Pisa, Italy, June 10-14, 2018

W. Tzevelecos, L. Pietrasanta, D. Fioriti, N. Miché, P. Queeckers, S. Van Varemberg, M. Marengo, *Self-rewetting liquid vein stability*, ISPS-7 & ELGRA-25 Joint Conference Juan-les-Pins, France, 2-6 October 2017

L. Pietrasanta, N. Miché, D. Fioriti, L. Araneo, M. Marengo, *A modular test-rig for shared thermo-fluid dynamics experiments in reduced gravity environment*, 15th UK Heat Transfer Conference, UKHTC2017, Brunel University London, 4-5 September 2017

Submitted Journal Papers

L. Pietrasanta, M. Mameli, A. Georgoulas, D. Mangini, N. Michè, S. Filippeschi, M. Marengo, *Developing flow pattern maps of accelerated two-phase flow in the context of Pulsating Heat Pipe*, Experimental Thermal and Fluid Science.

M. Mameli, A. Catarsi, D. Mangini, L. Pietrasanta, N. Michè, M. Marengo, P. Di Marco, S. Filippeschi, *Start-up during Microgravity and Local Thermodynamic States of a Hybrid Loop Thermosyphon/Pulsating Heat Pipe*, Applied Thermal Engineering.

V. Ayel, L. Pietrasanta, G. Lalizel, B. Medrinal, C. Romestant, Y. Bertin, M. Marengo, *Thermo-hydraulic analysis of semi-transparent Flat-Plate Pulsating Heat Pipes tested under normal and microgravity regimes*, Microgravity Science and Technologies.

L. Cattani, D. Mangini, F. Bozzoli, L. Pietrasanta, N. Miche', M. Mameli, S. Filippeschi, S. Rainieri, M. Marengo, *An Original Look into Pulsating Heat Pipes: Inverse Heat Conduction Approach for Assessing the Thermal Behaviour*, Thermal Science and Engineering Progress.

Appendix A: Infrared analysis in the context of PHP

PHP's governing phenomena are not yet completely fully understood. Almost all of the tests performed on PHPs aim to study the thermal working principles and the overall heat transfer rate between evaporator and condenser area or the thermal resistance of the system. This approach comes from the practical difficulty of measuring local heat flux on the internal wall surface of these pipes. The size of most common probes compared to the dimension of the device makes accessibility of the inner surface considerable difficult. Since in the recent years Infra-Red (IR) sensors have become more accurate and reliable, the Infra-Red (IR) analysis represents a breakthrough for the non-intrusive measurement of the fluid temperature distribution evolution.

A review of the last 10 years cutting edge techniques applicable in local scale, milli/micro-channels fluidic investigation is resumed in Table 27. The main advantages of the IR technique are the high sensitivity, the low response time and a non-intrusive measurement. There is a compelling necessity of direct measurements on the fluid that do not affect the fluid-dynamics, thus Infrared (IR) techniques are getting the attention of many research groups. Frequently are coupled with an IR transparent media (Germanium or Sapphire inserts) that allow the direct fluid temperature field measurement. Difficulties and constrains linked to adapting an experiment to a μg platform, like a Parabolic Flight (PF), have slowed down the integration of promising techniques.

Table 27 Innovative techniques of temperature measurement applicable in local scale, milli/micro-channels

Author	Measurement technique	Geometry	Flow type	Channel cross-section	Fluid	g level	Aim of the investigation	Investigated area
Luciani et al. [118]	Indirect TC	Single Channel	Flow Boiling	Rectangular, Hy-Diam.: 0.49, 0.84, and 1.18 mm	HFE-7100	PF ⁶	Inverse Heat Conduction Problem	Evaporator
Hetsroni et al. [119]	Direct IR	Multi-channels	Laminar single phase	Rectangular, 320x750 um	Water	1g	Fluid temperature	Heated
Mehta and Kandekar [120]	Indirect IR	Single channel	Laminar single phase	Square 5mm	Water	1g	Heat flux	Heated
Gully et al. [83]	Direct micro-TC	Single channel	Pulsating	Stain-less steel tube, I.D/O.D=2mm/3mm	Liquid oxygen	1g	Vapour temperature	Evaporator
Karthikeyan et al. [121]	Indirect IR	CLPHP	Pulsating	Copper tube, I.D/O.D=2mm/3mm	Water	1g	Flow regimes	Evaporator, Adiabatic
Chauris et al. [122]	Indirect IR	Single channel	Flow boiling	Copper tube, I.D/O.D=2mm/2.4mm	Water	1g	Film Heat transfer	Adiabatic
Liu and Pan [123]	Direct IR	Single channel	Flow boiling	Germanium\Aluminium, rectangular 250umx1mm	Ethanol	1g	Fluid temperature, Flow regimes	Evaporator

The aim of this section of the work is to perform an innovative direct high-speed Mid- Wave infrared (MWIR) analysis at different gravity levels, of the fluid temperature distribution thanks to two sapphire inserts on the adiabatic region of different PHP devices. In this section of the research, a non-intrusive spatial and temporal measurement of the fluid temperature by high-speed Mid-Wave Infra-Red (MWIR) thermography is presented, as a method for understanding the coupling between the fluidic motion and the resulting temperature oscillations which drive the system dynamics. The advantage of this technique is the absence of contact with the working fluid, which makes possible observing thermal phenomena without interfering with the processes.

However, the difficulty is then to correctly interpret the infrared information measured with the camera considering the radiative properties of the observed fluid. The working fluid is generally a semi-transparent media in a specific spectral range of measurement, making it difficult to convert the radiation emitted into a temperature value.

⁶ Gravity levels available on a parabolic flight: ~1g, ~1.8g and ~0.01g

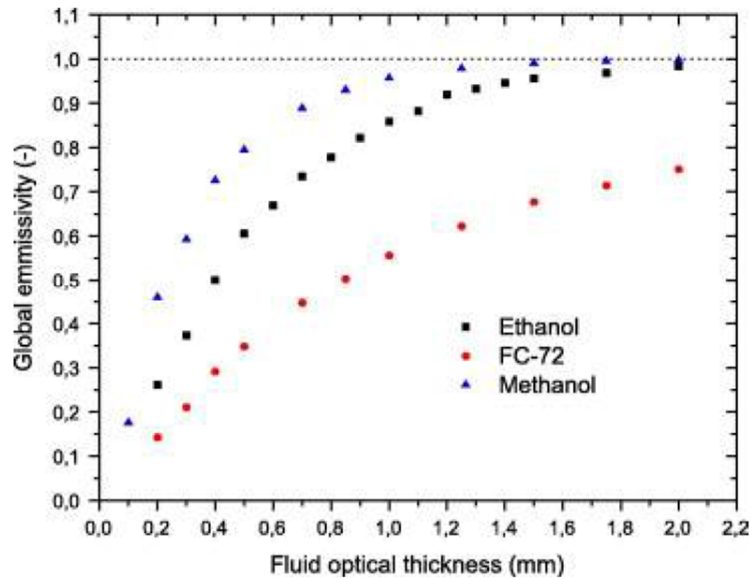


Figure 100 Global emissivity of FC-72, methanol and ethanol as a function of the optical thickness of the fluid in a wavelength of 3–5 μm [124]

To reduce the interference given by the tube containing the fluid, a material with total or high transparency in the range of the IR investigation, must be used. Sapphire glass or CaF₂ can achieve 85-90% of transparency in the range of 3-5 μm . Since most of the common working fluids are a semi-transparent fluid between 3 and 5 μm , their global emissivity ε does not depend only on the temperature, but also on the liquid thickness. Sobac and Brutin, measured the global emissivity of some fluids of interest, like Ethanol, FC-72 and Methanol between 3 and 5 μm , as a function of the liquid thickness by means of a spectrophotometer [124].

Previous works pointed out the possibility to visualize by means of a MWIR camera the liquid flow evolution within sapphire inserts. Scammel et al. [125] performed an analysis of the heat transfer profiles around bubbles of a Taylor type flow, identifying turbulent mixing in the bubble wake due to vortex shedding as the main contributor to the heat transfer. To characterize the heat transfer and dynamics of rising Taylor bubbles, a flow boiling experiment was conducted in which measurements of the local wall heat transfer and film thickness along with high speed images were obtained as single bubbles of varying length rose in a vertical column containing upward flowing liquid.

The infrared camera used for the investigation is an AIM® non-commercial camera, property of the European Space Agency which detects radiation in the medium infrared, wavelength 3-5 μm . The main specifications are listed in Table 28.

Table 28 Medium Wave Infra-Red camera specifics

Parameter	Value
Focal Length	25 mm
Speed	50 Hz
FOV	21.0 mm
Bandwidth	3 – 5 μm
Transmission	$\approx 93\%$
Resolution	40 μm
Sensor	1280x1024

An in-situ calibration of the camera is mandatory, even though the accuracy is highly-dependant from the procedure and the specific experimental conditions which may differ from the calibration conditions. Catarsi et al. [126], using the same MWIR that has been used in this work, performed an accuracy analysis of direct infrared temperature measurements of two-phase confined flows. A lumped parameter IR model has been developed and adopted for the present work (Figure 101). The authors declared that a reliable and accurate direct fluid temperature measurements can be performed by means of infrared analysis after a proper calibration process with a maximum error on an actual application $\pm 2\text{K}$.

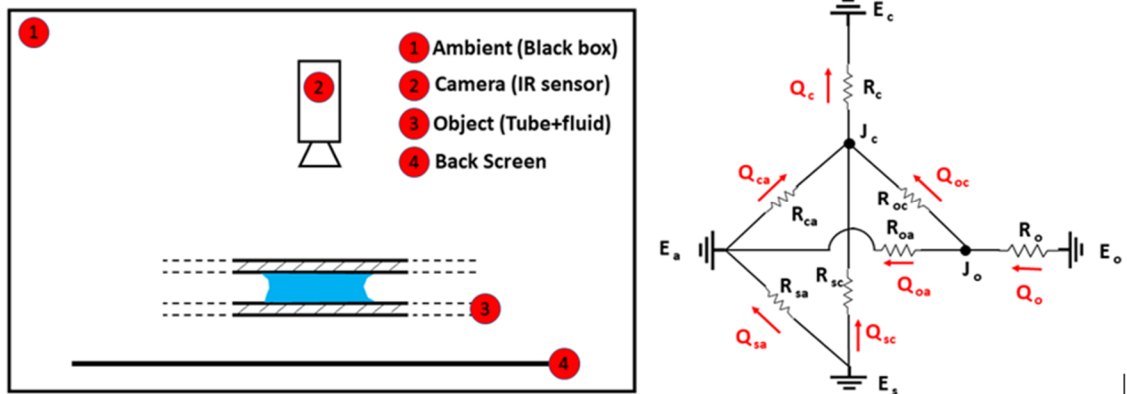


Figure 101 Schematisation of the problem and equivalent electric scheme for the lumped parameter model resolution

Appendix B: The Inverse Heat Conduction Problem (IHCP)

For modern complex materials, having thermo-physical properties strongly varying with temperature and position, the use of conventional methods for determining these properties have become unsatisfactory. Moreover, many modern industrial processes are becoming more and more sophisticated, requiring an accurate in situ estimation of thermo-physical properties under actual operating conditions. The inverse heat transfer problem approach can provide satisfactory answers for such situations. The main advantage of the IHCP is enabling experiments as close to the real conditions as possible. Practical applications of the technique are:

- Estimation of thermo-physical properties of materials: properties of heat shield material during its re-entry into the earth's atmosphere, and estimation of temperature dependence of thermal conductivity of a cooled ingot during steel tempering;
- Estimation of bulk radiation properties and boundary conditions in absorbing, emitting and scattering semi-transparent materials;
- Control of the motion of the solid-liquid interface during solidification;
- Estimation of inlet condition and boundary heat flux in forced convection inside ducts;
- Estimation of timewise varying unknown interface conductance between metal solidification and casting;
- Estimation of interface conductance between periodically contacting surfaces;
- Monitoring radiation properties of reflecting surfaces of heaters and cryogenic panels

The estimation of such quantities with conventional techniques is an extremely difficult or impossible matter.

One limitation of the method is given by the sensitivity of the solution. In order to estimate the boundary heat flux, a sensor must be located within a depth below the surface where the amplitude of the temperature oscillation is much greater than the measurement errors. Otherwise it is impossible to distinguish if the measured temperature oscillation is due to changes in the boundary condition or due to errors in the measurement process. This results in the non-uniqueness of the solution.

B.1 Formulation of the problem

The schematisation of the problem is reported in Figure 102 with its mathematical formulation.

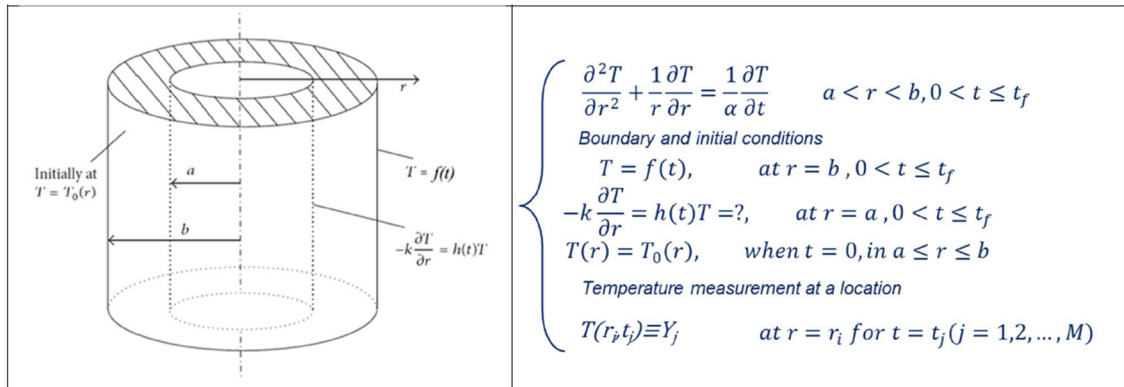


Figure 102 Schematisation and formulation of the IHCP

A successful solution of an inverse problem generally involves the transformation of the inverse problem into a well posed-approximate solution. The existence of an inverse solution is guaranteed by requiring that the inverse solution minimize the least squares norm rather than make it necessarily zero. The establishment of the direct solution is obviously basic to the procedure. The analytical solutions are strictly applicable to linear problems. To extend the technique to nonlinear problems, the numerical methods such as FDM and FEM have been used in the solution of IHCP. The object of the research is, by utilizing the measured temperature data, to estimate the unknown surface heat flux function $h(t)$, over the whole time domain. Since no prior information is available regarding the functional form, the problem may be regarded as a problem of function estimation (Figure 103). The analysis and solution of this inverse problem are presented in the following basic steps:

- The formulation of direct and inverse problems
- The transformation of the inverse problem into a system of least-squares equations
- Physical significance of sensitivity coefficients
- The solution of the least-squares equations
- The determination of the sensitivity coefficients
- Numerical results

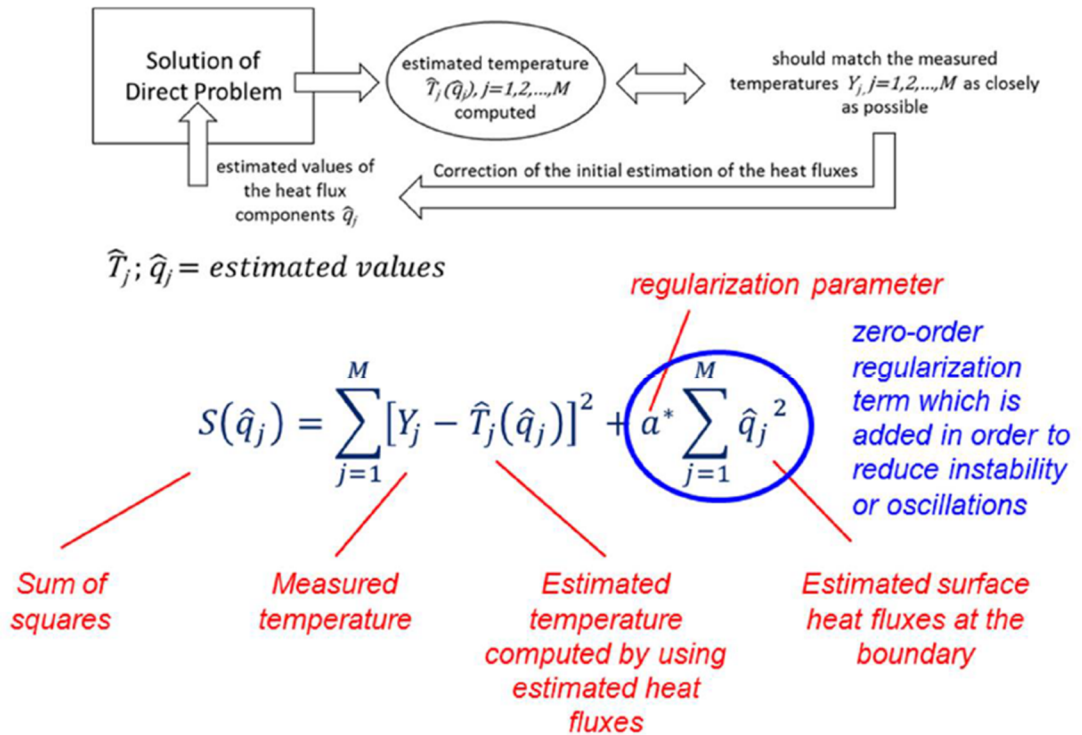


Figure 103 Schematisation of the resolution procedure

Appendix C: Code for the estimation of Void Fraction and bubble length

```
warning off
%           close everything
clear all

PATH = 'G:\VOID FRACTION - Prove\PFC66_ETHANOL\12-6-
0_5s_Par14 1g';           % Change every time
IMAGE = '09-57-18.555.tif';
% Change every time

PATHvel = 'G:\LIQUID VELOCITY\ETHANOL\12-6-0_5s_Par14
1g\Source';           % Change every time
cd (PATHvel)
open('workspace_vcrit.mat');
TrP = ans.TrP;
strV = open('Med_combo_mod.mat');
V = strV.Med_combo_mod;
PATHtp = 'G:\LIQUID VELOCITY\ETHANOL\GLOBAL';
% DA CAMBIARE OQUANDO CAMBIA IL FLUIDO
cd (PATHtp)
open('T_Pdata.mat');
gz = ans.gz;
TC7 = ans.TC7;
TC8 = ans.TC8;
cd (PATH)
TrP=input('Trigger position: ');           % Initial
acquisition trigger position
SA=input('Seconds of acquisition: ');
%%CREATE FOLDERS FOR TYPES OF IMAGES
cd (PATH
```

```

mkdir('Crop');
mkdir('Adjusted');
mkdir('Binarised');
mkdir('Source');
rmdir('Crop','s');
rmdir('Adjusted','s');
rmdir('Binarised','s');
mkdir('Crop');
mkdir('Adjusted');
mkdir('Binarised');

FirstFrame = 1; %select the first and the last of the
frame
FrameCheck = imread([PATH, '\', IMAGE]);
D = dir('*.*tif');
[Num NUMH] = size(D); %length(D(not([D.isdir])));
% N=Num -2; %Num+1;
LastFrame = Num;

% INITIALISATION VARIABLES
dpg = zeros(Num,1);
d_PHP = 0.002; % m
fps = 200; %frame per second (depends on dimesion
1024x1024->462fps ; 1024x512->923fps ; 1024x923->1825fps
%the value of brightness is evaluate using imtool gui
BrightLow = 10/256; %10/256 from imtool
BrightHigh = 50/256; %50/256 from imtool

%% BACKGROUND
BG=imread('G:\VOID FRACTION -
Prove\PFC66_ETHANOL\BackGround.tif');
BGcrop=imcrop(BG,[0.5 9.5 1278 90]); %[0.5 19.5 1280
61] [0.5 9.5 1280 77]

%open the filepath to select the file
[fileBack,filepath] =
uigetfile({'*.jpg;*.tif;*.png;*.gif','All Image
Files';...
'*..*','All Files' },'Choose multipage tif',PATH);

filename = [filepath fileBack ]; %create the file name

i = [];
for i = FirstFrame:LastFrame %do for all the images
FileName = D(i,:).name;
TL=imread(FileName); %read the image
TLcrop=imcrop(TL,[0.5 9.5 1278 90]); %
TLdiff=BGcrop-TLcrop;
TLadj=imadjust(TLdiff, [BrightLow; BrightHigh],[],
[]);

```

```

        im = im2bw(TLadj, 0.05);           % Initial
value 43/255
        [dim DIM] = size(im);
        Bound(1:3*dim+1,1:(DIM+101))=0;
        Bound(92:182,51:1329)=im;      %(FirstRow:[(nr.
elements- 1)+FirstRow] , FirstColumn:[(nr. elements-
1)+FirstColumn])
        I=Bound;
        Iflip = flipud(I);
        I(1:0.5*size(I),:) = Iflip(1:0.5*size(I),:);
        I=bwmorph(I,'clean',16);      %8
        %Cycle for slicing the image for easier elimination
of long axial reflections
        passo = 10;
        cc = floor(size(I,2)/passo);
        for c = 1 : cc
            c100 = c*passo;
            I(:,c100)=0;
        end
        % MORPHOLOGICAL OPERATORS
        I = bwareaopen(I, 28,4);
        SE0 = strel('Disk',12,0);
        I = imclose(I, SE0);
        SE1 = strel('Line',32,90);
        I = imclose(I, SE1);
        SE2 = strel('Disk',20,6);
        I = imclose(I, SE2);      % This can be removed if
the other two are enough
        % Removing the extra frame
        I = I(92:182,51:1329);
        tic
        % ESTIMATION OF AREAS AND VOLUMES
        [ll, BubbNum] = bwlabel(I);
        BubbNum_tot(i,:) = BubbNum;
        %BlackArea = regionprops(imcomplement(I),'Area');
        VolChannelTot = ((pi/4)*(50)^2)*1279;
        AreasProp = regionprops(ll,'Basic');
        VolArea = [];
        x_width_i = BubbNum;
        if BubbNum >0           % If there is more than one
bubble
            for j=1:BubbNum     % Operations to do for each
bubble
                bubbID_i = [i*100+j];
                bubbID(i,1) = bubbID_i;
                coord = [];
                x = [];
                dx = [];
                xf = [];
                x_width_j = [];
                y_width_j = [];
            end
        end
    end
end

```

```

VolUnitario = [];
coord(1,:) = AreasProp(j).BoundingBox; %
Create a matrix with Bounding Box values for each bubble.
BoundingBox --> [x y dx dy] --> x y (of the most external
pixel, left to right); dx dy (to reach the most external
pixel on the right)
x = round(coord(:,1));
dx = round(coord(:,3));
xf = x+dx;
x_width_j = coord(:,3);
y_width_j = coord(:,4);
x_width_i = cat(2,x_width_i,x_width_j);
NrW = [];
for k= x : xf-1 % Check each of the
k columns
    z=k-x+1;
    NrW(z,1) = sum(I(:,k)); % Number of
white elements along the column = Diameter
in pixels of the i-th disk
    if NrW (z,1) > 45
        NrW(z,1)=45;
    end
    VolUnitario(z,1) =
((pi/4)*(NrW(z))^2)*1; % Volume of
the k-th disk. 1 is the height of the
disk (1 pix)
end
VolArea(j,1) = sum(VolUnitario);
end
VolTotFrame(i,1) = sum(VolArea);
Tab(i,1:size(x_width_i,2)) = x_width_i;
else VolTotFrame(i,1) = 0;
Tab(i,:) = 0;
toc
end

%% SAVE IMAGES CROPPED
cd Crop
FileNameCrop = [FileName(1:end-4), '_Crop.tif'];
imwrite(TLcrop,FileNameCrop);
imwrite(TLcrop,'Crop_FINAL.tif');

cd ..

%% SAVE IMAGES ADJUSTED

cd Adjusted
FileNameAdjusted = [FileName(1:end-
4,'Adjusted.tif)];

```

```

imwrite(TLadj,FileNameAdjusted);
imwrite(TLadj,'Adjusted_FINAL.tif');

cd ..

%% SAVE IMAGES BINARISED
cd Binarised
FileNameBinarised = [FileName(1:end-4),'_Bin.jpg'];
imwrite(I,FileNameBinarised);
imwrite(I,'Bin_FINAL.jpg');

cd ..

end
beep
alfa = VolTotFrame./VolChannelTot;
alfaM = mean(alfa,1)
astd = std(alfa,1)
avar = var(alfa,1)
for i=1:size(Tab,1) % Max length on
each row
    L(i,:) = max(Tab(i,:));
end
% l=1';
path = [PATH,'\Source'];
cd (path)
save('L.mat','L');
save('Tab.mat','Tab');
cd ..

TC7i = TC7(TrP*10:TrP*10+SA*10);
TC8i = TC8(TrP*10:TrP*10+SA*10);
gi = gz(TrP*10:TrP*10+SA*10);
%Tmed = zeros(Num,1);
Tmed = (mean(TC7i)+mean(TC8i))/2;
gmed = mean(gi);
theta = 90; % Angle of inclination of the device in
deg. 90 = Vertical

% Properties calculation for ETHANOL

%g = ones(num,1);
if gmed>0.5
    g = gmed*9.81;
else g = (gmed./100)*9.81;
end

x=Tmed; % N.B. ALL TEMPERATURES IN C!!

```

```

Psat = 0.0002*x^3 - 0.0076*x^2 + 0.3923*x - 0.842;
rho_l = -0.0013*x^2 - 0.7819*x + 805.86;
rho_v = 2e-08*x^4 + 3e-07*x^3 + 9e-05*x^2 + 0.0019*x +
0.0335;
sigma = 1e-07*x^2 - 0.0001*x + 0.0251;
mu_li = 8e-12*x^4 - 3e-09*x^3 + 4e-07*x^2 - 4e-05*x +
0.0018;
hlv = -0.0115*x^3 - 4.383*x^2 - 788.56*x + 944332;
% sr=sigma/(Drhoi*g);
% a2=160*mu_li;
% b2=rho_l*(d_PHP^2);
% q2=a2/b2;
% v_cr=(q2)*sr;
h = 0.195;          % [m] altezza canale
for ii=1:Num
    dpG(ii,1) = g*(alfa(ii,1)*rho_v+(1-
alfa(ii,1))*rho_l)*1*h/1000;      % kPa
end
tp = linspace(TrP, (TrP+SA), size(dpg,1));
tp =tp';

%% Effect of bubble lenght calculation
a = diff(V)./0.01;
V = V(1:size(a));
L = L(1:size(a));
V = abs(V);
a = abs(a);
mpix = 0.00004;          % [m/pix]
Lm = L.*mpix;          % [m]

```